

An Investigation on Acoustic Metamaterial Physics to Inspire the Design of Novel Aircraft Engine Liners

Benjamin E. Hubinger

Thesis submitted to the faculty of the
Virginia Polytechnic Institute and State University
in partial fulfillment of the requirements for the degree of

Master of Science

in

Mechanical Engineering

Christopher R. Fuller, Chair

Douglas M. Nark

Steve C. Southward

Zhenhua Tian

October 12, 2023

Blacksburg, VA

Key words: Acoustic Meta Material (AMM), Acoustic Liner, Turbofan Engine, Helmholtz Resonator, Transfer Matrix Method (TMM), Bloch Wave Theory

An Investigation on Acoustic Meta Material Systems For Quieting Aircraft Turbofan Engines

Benjamin E. Hubinger

Christopher R. Fuller, Chair

Center for Aerospace Acoustics

(ABSTRACT)

Attenuation of low frequency turbofan engine noise has been a challenging task in an industry that requires low weight and tightly-packed solutions. Without innovative advancements, the technology currently used will not be able to keep up with the increasingly stringent requirements on aircraft noise reduction. A need exists for novel technologies that will pave the way for the future of quiet aircraft. This thesis investigates acoustic metamaterials and their ability to achieve superior transmission loss characteristics not found in traditional honeycomb liners. The acoustic metamaterials investigated are an array of Helmholtz resonators with and without coupled cavities periodically-spaced along a duct wall. Analytical, numerical, and experimental developments of these acoustic metamaterial systems are used herein to study the effects of this technology on the transmission loss. Particularly focusing on analytical modeling will aid in understanding the underlying physics that governs their interesting transmission loss behavior. A deeper understanding of the physics will be used to aid in future acoustic metamaterial liner design. A parameter study is performed to understand the effects of the geometry, spacing, and number of resonators, as well as resonator cavity coupling on performance. Increased broadband transmission loss, particularly in low frequencies, is achieved through intelligent manipulation of these parameters. Acoustic metamaterials are shown to have appealing noise cancellation characteristics that prove to be effective for aircraft engine liner applications.

An Investigation on Acoustic Meta Material Systems For Quieting Aircraft Turbofan Engines

Benjamin E. Hubinger

Christopher R. Fuller, Chair

Center for Aerospace Acoustics

(GENERAL AUDIENCE ABSTRACT)

Aircraft noise reduction is an ongoing challenge for the aerospace industry. Without innovative advancements, the next generation of aircraft will not be able to keep up with increasingly stringent noise regulations; novel acoustic technology is needed to pave the way for a future of quieter aircraft. This thesis investigates acoustic metamaterials and their ability to achieve superior noise reduction over traditional methods. Modeling techniques were developed, and experimental tests were conducted to quantitatively evaluate the effectiveness of a new acoustic metamaterial system. The acoustic metamaterial design explored herein was proven to reduce noise effectively and shows promise for a world of quieter aircraft.

Acknowledgements

I would like to thank my advisor, Dr. Christopher Fuller, for mentoring me, guiding me in this project, and showing support. I would also like to thank my committee members Douglas Nark, Dr. Steve Southward, and Dr. Zhenhua Tian for their help and support.

I would like to thank Collins Aerospace and NASA Langley Research Center for providing financial support. At Collins, I would specifically like to thank Jose Alonso for guiding me in the project and providing support. At NASA Langley, I would specifically like to thank the Structural Acoustics Branch and the branch head, Randolph Cabell, for providing me with branch resources and a place to work. I would also like to thank Michael Jones, Brian Howerton, Max Reid, Chelsea Dodge, and Martha Brown for providing support.

I would like to thank Virginia Tech for providing me with the opportunity to study at their university, and I would like to thank the National Institute of Aerospace for providing distance learning capabilities in Hampton Roads. I would like to thank Cathy Hill, Corina Sandu, and Mandy Collins for providing support and guidance at Virginia Tech. I would also like to thank Arthur Wiedemann for support with this project. I would like to thank Alexis Talbot and Casey Radigan at Hexagon for providing access to Actran for my numerical work. I would also like to thank the Center for Aerospace Acoustics at the National Institute of Aerospace for access to their equipment and laboratories.

Table of Contents

Acknowledgements	iii
List of Tables	vi
List of Figures.....	vii
1. INTRODUCTION.....	1
1.1. Motivation.....	1
1.2. Introduction to turbofan engine acoustic liners	3
1.3. Physics principles guiding metamaterial design.....	8
1.4. Introduction to acoustic metamaterials	29
1.5. Objectives.....	32
1.6. Outline.....	33
2. ARRAY OF HELMHOLTZ RESONATORS.....	35
2.1. Analytical modeling of an infinite array of Helmholtz resonators	35
2.2. Analytical modeling of a finite array of Helmholtz resonators.....	44
2.3. Numerical modeling array of Helmholtz resonators	51
2.4. Conclusions.....	59
3. CONNECTED HELMHOLTZ RESONATORS	61
3.1. Analytical modeling of an infinite array of connected Helmholtz resonators	63
3.2. Analytical modeling of a finite array of connected Helmholtz resonators.....	79
3.3. Numerical modeling of an array of connected Helmholtz resonators.....	91
3.4. Parameter studies of an array of connected Helmholtz resonators.....	99
3.4.1. Change in neck length.....	102
3.4.2. Change in neck diameter	108
3.4.3. Change in cavity height	115
3.4.4. Change in length of coupling tubes.....	122
3.4.5. Change in spacing between the resonators	128
3.4.6. Change in diameter of the coupling tubes.....	134
3.4.7. Change in number of resonators	139
3.5. Conclusions.....	142
4. EXPERIMENTAL TESTING AND VALIDATION.....	146
4.1. Experimental setup of impedance tube.....	146
4.2. Results and validation using impedance tube.....	155

4.3. Conclusions.....	166
5. CONCLUSIONS AND FUTURE WORK	168
5.1. Conclusions.....	168
5.2. Future work.....	172
APPENDIX.....	173
A. MATLAB Codes.....	173
BIBLIOGRAPHY	199

List of Tables

Table 1. Connected Helmholtz Resonator Parameter Values to be Evaluated in Inches 100

List of Figures

Figure 1. Section View of a Sample Perforate-Over-Honeycomb Structure.....	4
Figure 2. Local-Reacting vs. Extended-Reacting Liners.....	4
Figure 3. Schematic of a Helmholtz Resonator and its Mechanical Analog, a Mass-Spring System	5
Figure 4. Schematic of an Array of Helmholtz Resonators Representative of a Perforate-Over-Honeycomb Liner	6
Figure 5. Schematic of Acoustic Wave Transmission Through Inhomogeneous Layers.....	7
Figure 6. Schematic of a Duct Periodically Loaded with N Identical Helmholtz Resonators.....	8
Figure 7. Example Sketch of a Crystalline Solid – A Lattice of Periodically Arranged Atoms.....	9
Figure 8. Schematic of Locally Resonant Electrons and the Equivalent Spring-Mass System.....	10
Figure 9. Locally Resonant Electrons Collectively Excited by a Sinusoidal Electric Field – Analogous to a Driven Spring Mass-System	11
Figure 10. Example Plot of the Normalized Displacement of a Forced Mass-Spring System vs. the Driving Frequency Normalized by the Natural Frequency of the System.....	12
Figure 11. Schematic of a Crystalline Solid Modeled as a Set of Periodically Spaced Parallel Planes of Atoms Exhibiting Bragg Reflection.....	14
Figure 12. An Example of a 1D Crystalline Solid Whose Stationary Ions Introduce a Periodic Potential Energy for a Traveling Electron.....	16
Figure 13. An Example Plot of a Bloch Wave – A Plane Wave Modulated by a Periodic Function	18
Figure 14. An Example Plot of Damped Oscillatory Motion	19
Figure 15. An Example Plot of an Evanescent Bloch Wave.....	19
Figure 16. Example Dispersion Plot for an Electron Propagating Through a Crystal as a Bloch Wave Exhibiting Stop Band Behavior.....	20
Figure 17. Example Schematic of Propagating and Evanescent Bloch Waves of a Beam on Periodically-Spaced Supports	23
Figure 18. Example Schematic of the Decaying Plane Wave Envelope of an Evanescent Bloch Wave Propagating through a Duct Lined with a Periodic Array of Helmholtz Resonators.....	24
Figure 19. Section View of an Array of Connected, Periodically-Spaced Helmholtz Resonators	25
Figure 20. Schematic of Two Inhomogeneous Waveguides with Different Wave Speeds Coupled by an Acoustically Transparent Sheet	26
Figure 21. Schematic of the Energy Transfer Between the Waves of the Duct and the Chain of Resonator Cavities.....	27
Figure 22. Schematic of a) Unconnected HRs Acting as a Local-Reacting System b) Connected HRs Acting as an Extended-Reacting System	28
Figure 23. Sketch of Phononic Crystals Concept Proposed by Liu (not to scale) [39] and the Equivalent Mass-Spring System.....	30
Figure 24. Sketch of the Top View and Isometric View of a) Solid-Cylinder Sonic Crystal and b) Split-Tube Sonic Crystal.....	31
Figure 25. Schematic of Incident, Reflected, and Transmitted Waves in a Duct with a Liner Sample	33
Figure 26: Infinite Array of Helmholtz Resonators Schematic	36
Figure 27. First Subsection of the Unit Cell used to Write the Transfer Matrix Across a Portion of the Duct Treated with a Resonator	37

Figure 28. Schematic of a Helmholtz Resonator Represented as a Mass-Spring System.....	38
Figure 29. Second Subsection of the Unit Cell used to Write the Transfer Matrix Across the Duct Between Resonators	39
Figure 30. Dispersion Plot for Infinite Array of Helmholtz Resonators.....	42
Figure 31. Dispersion Plot for Infinite Array of Helmholtz Resonators with Bragg and HR Frequencies Shown	43
Figure 32. Finite Array of Helmholtz Resonators	44
Figure 33. Transmission Loss Plot for Finite Array of Helmholtz Resonators	48
Figure 34. The Effect of Number of Resonators N on normalized transmission loss TL/N	49
Figure 35. Normalized transmission loss TL/N as $N \rightarrow \infty$	51
Figure 36. CAD Model of the Fluid Domain of the Grazing Impedance Tube Lined with Four Helmholtz Resonators	52
Figure 37. Different Types of Meshes: a) Structured mesh and b) Unstructured mesh.....	53
Figure 38. Example Schematic of a Multi-Block Structured Mesh with Eight Different Blocks Each Highlighted in a Different Color	53
Figure 39. Block Topology for a Unit Cell of the Helmholtz Resonator Array.....	54
Figure 40. Mesh of Grazing Impedance Tube Lined with Four Helmholtz Resonators	55
Figure 41. Numerical Solution for Transmission Loss Across Impedance Tube Lined with Four Helmholtz Resonators	56
Figure 42. Color Map of Acoustic Pressure in dB for the Impedance Tube Lined with Four Helmholtz Resonators at the First Bragg Reflection Frequency.....	56
Figure 43. Color Map of Acoustic Pressure in dB for the Impedance Tube Lined with Four Helmholtz Resonators at the Helmholtz resonant Frequency	57
Figure 44. Normalized Acoustic Impedance for Helmholtz Resonator Array Solved Using Actran – First Bragg Reflection Frequency	58
Figure 45. Normalized Acoustic Impedance for Helmholtz Resonator Array Solved Using Actran – Helmholtz Resonant Frequency	59
Figure 46. Schematic of the Connected Array of Helmholtz Resonator Concept.....	62
Figure 47. Schematic of the Energy Transfer Between the Two Waveguides Caused by the Interaction of the Two Travelling Waves at the Necks	62
Figure 48. Infinite Array of Connected Helmholtz Resonators Schematic	64
Figure 49. Symmetric and Asymmetric Cell for Infinite Array of Connected Resonators	65
Figure 50. Symmetric and Asymmetric Cells with Subsections Highlighted.....	66
Figure 51. First subsection of unit cell used to write the T_{ct} transfer matrix	67
Figure 52. Second subsection of unit cell used to write the T_c transfer matrix	69
Figure 53. Third subsection of unit cell used to write the T_n transfer matrix.....	70
Figure 54. Possible Scenarios for the Two Forward-Travelling Bloch Waves for any Given Frequency.....	75
Figure 55. Dispersion Plot for Infinite Array of Connected Helmholtz Resonators.....	77
Figure 56. Finite Array of Connected Helmholtz Resonators Schematic	80
Figure 57. Transmission Loss Plot for Finite Array of Connected Helmholtz Resonators	86
Figure 58. Finite Array of Connected Helmholtz Resonators with Non-Cellular Ends	87
Figure 59. Comparison Between All Unit Cells and Non-Cellular Ends Systems.....	88
Figure 60. Connected and Unconnected Resonator Systems Comparison	90
Figure 61. CAD Model of Grazing Impedance Tube Lined with Four Connected Helmholtz Resonators...	92

Figure 62. Block Topology for Part of the Coupled Helmholtz Resonator Array	92
Figure 63. Mesh of Grazing Impedance Tube Lined with Four Connected Helmholtz Resonators – Isometric View	93
Figure 64. Mesh of Grazing Impedance Tube Lined with Four Connected Helmholtz Resonators – Side View	93
Figure 65. Numerical Solution for Transmission Loss Across Impedance Tube Lined with Four Connected Helmholtz Resonators.....	94
Figure 66. Color Map of Acoustic Pressure in dB for the Impedance Tube Lined with Four Connected Helmholtz Resonators at First Bragg Reflection Frequency	94
Figure 67. Color Map of Acoustic Pressure in dB for the Impedance Tube Lined with Four Connected Helmholtz Resonators at Second Stop-Band Frequency	95
Figure 68. Color Map of Acoustic Pressure in dB for the Impedance Tube Lined with Four Connected Helmholtz Resonators at First Peak Frequency in Double-Propagation Band.....	95
Figure 69. Normalized Acoustic Impedance for Connected Helmholtz Resonator Array Solved Using Actran - First Bragg Reflection Frequency	97
Figure 70. Normalized Acoustic Impedance for Connected Helmholtz Resonator Array Solved Using Actran – Helmholtz Resonant Frequency	98
Figure 71. Normalized Acoustic Impedance for Connected Helmholtz Resonator Array Solved Using Actran - First Peak Frequency in Double-Propagation Band.....	99
Figure 72. Baseline Case used for Parameter Study – Finite Array of Connected Helmholtz Resonators with Non-Cellular Ends.....	101
Figure 73. Finite Array of Connected Helmholtz Resonators with Non-Cellular Ends	101
Figure 74. Neck Length = 0.125 in.....	102
Figure 75. Neck Length = 0.25 in.....	104
Figure 76. Neck Length = 0.375 in.....	105
Figure 77. Neck Length = 0.5 in.....	106
Figure 78. Neck Length = 0.625 in.....	107
Figure 79. Effect of Neck Length on Transmission Loss – All Plots Combined.....	108
Figure 80. Neck Diameter = 1.0 in.....	109
Figure 81. Neck Diameter = 1.25 in.....	111
Figure 82. Neck Diameter = 1.5 in.....	112
Figure 83. Neck Diameter = 1.75 in.....	113
Figure 84. Neck Diameter = 2.0 in.....	114
Figure 85. Effect of Neck Diameter on Transmission Loss – All Plots Combined.....	115
Figure 86. Cavity Height = 0.5 in.	116
Figure 87. Cavity Height = 1.0 in.	117
Figure 88. Cavity Height = 1.5 in.	118
Figure 89. Cavity Height = 2.0 in.	119
Figure 90. Cavity Height = 2.5 in.	120
Figure 91. Effect of Cavity Height on Transmission Loss – All Plots Combined	121
Figure 92. Coupling Tube Length = 2.75 in.....	122
Figure 93. Coupling Tube Length = 3.0 in.....	123
Figure 94. Coupling Tube Length = 3.25 in.....	124
Figure 95. Coupling Tube Length = 3.5 in.....	125

Figure 96. Coupling Tube Length = 3.75 in.....	126
Figure 97. Coupling Tube Length = 4.0 in.....	126
Figure 98. Coupling Tube Length = 4.25 in.....	127
Figure 99. Coupling Tube Length = 4.5 in.....	127
Figure 100. Effect of Coupling Tube Length on Transmission Loss – All Plots Combined	128
Figure 101. Resonator Spacing = 6.0 in.....	129
Figure 102. Resonator Spacing = 7.0 in.....	130
Figure 103. Resonator Spacing = 8.0 in.....	131
Figure 104. Resonator Spacing = 9.0 in.....	132
Figure 105. Resonator Spacing = 10.0 in.....	133
Figure 106. Resonator Spacing = 11.0 in.....	133
Figure 107. Effect of Resonator Spacing on Transmission Loss – All Plots Combined.....	134
Figure 108. Coupling Tube Diameter = 0.125 in.	135
Figure 109. Diameter of Coupling Tube = 0.375 in.	136
Figure 110. Diameter of Coupling Tube = 0.625 in.	137
Figure 111. Coupling Tube Diameter = 0.875 in.	138
Figure 112. Effect of Coupling Tube Diameter on Transmission Loss - All Plots Combined	139
Figure 113. Effect of Number of Resonators on Normalized Transmission Loss for the Connected Resonator System	140
Figure 114. Normalized Transmission Loss TL/N as $N \rightarrow \infty$ for the Connected Resonator System	141
Figure 115. Example of a Practical AMM Liner with Coupled Quarter-Wave Resonators Forming a Waveguide	143
Figure 116. Exploded View of a Practical AMM Liner Example with a Larger Spacing Between the Resonators and Larger Coupling Tube Diameter	144
Figure 117. Exploded View of a Practical AMM Liner Example with Coupled Quarter-Wave Resonators Forming a Waveguide Below the Resonators.....	145
Figure 118. Experimental Setup of Impedance Tube.....	147
Figure 119. A diagram of dimensions of the impedance tube.....	148
Figure 120. Schematic of the Unconnected Resonators with 7" Spacing Test.....	149
Figure 121. Exploded View Schematic of the Unconnected Resonators with 7" Spacing Test	150
Figure 122. Unconnected Resonators with 4.5" Spacing Test	150
Figure 123. Unconnected Resonators with 7" Spacing Test	151
Figure 124. Connected Resonators with 7" Spacing and 3/8" Coupling Tube Diameter Test.....	152
Figure 125. Connected Resonators with 7" Spacing and 5/8" Coupling Tube Diameter Test.....	153
Figure 126. Connected Resonators with 7" Spacing and 7/8" Coupling Tube Diameter Test.....	154
Figure 127. Hard Wall Test.....	155
Figure 128. Predicted Results for First Three Impedance Tube Tests	156
Figure 129. Predicted Results for the Three Connected Resonators Tests	157
Figure 130. Geometric Definitions used for Measured Transmission Loss Equations	158
Figure 131. Measured vs Predicted Results for the Unconnected Array with 4.5" Spacing.....	160
Figure 132. Measured vs Predicted Results for the Unconnected Array with 7" Spacing.....	161
Figure 133. Measured vs Predicted Results for the Connected Array with 7" Spacing and 3/8" Coupling Tube Diameter	162
Figure 134. Measured Results of First Three Impedance Tube Tests and the Hard Wall Case	163

Figure 135. Measured vs Predicted Results for the Connected Array with 7" Spacing and 5/8" Coupling Tube 164

Figure 136. Measured vs Predicted Results for the Connected Array with 7" Spacing and 7/8" Coupling Tube 165

Figure 137. Measured Results of the Three Connected Resonators Systems with Different Diameters . 166

1. INTRODUCTION

1.1. Motivation

Over the years, the Federal Aviation Administration (FAA) has continued to tighten the aircraft performance requirements placed on the aerospace industry, forcing flight technology to continue to improve and adapt to a world experiencing an ever-increasing reliance on air travel. As a result, the industry is faced with a pressing demand for safer, more efficient aircraft, all while leaving less of an impact on the environment. A large part of that environmental impact is noise pollution.

Since 2010, the FAA's principal effort to encourage the development of environmentally beneficial aircraft technologies has been the Continuous Lower Energy, Emissions, and Noise (CLEEN) Program [1]. For example, under CLEEN Phase III which began in 2021, the FAA and industry partners have been working to reduce cumulative noise by 25 dB relative to the current FAA Stage 5 standard. In response to these challenges, programs such as NASA's Advanced Air Transport Technology (AATT) Project have come into fruition. The overarching goal of the AATT Project is to explore technologies compatible for fixed wing subsonic transports that allow for cleaner, quieter, and more efficient aircraft [2]. For example, one of the technical challenges listed in the AATT Project is to reduce lateral and flyover fan noise on a component basis by 4 dB for aircraft by the 2035 – 2045 timeframe.

Aircraft noise can have adverse health effects on communities within the vicinity of frequent air traffic. Chronic aircraft noise exposure, particularly during sleep hours, has been shown to increase hypertension in adults [3]. Aircraft noise exposure at school and home have both shown to be associated with decreased reading comprehension for children [4]. Even aside from more serious health effects, community annoyance undoubtedly increases with excessive aircraft noise exposure; a claim that has been quantified by the Neighborhood Environmental Survey (NES) conducted by the FAA [5].

Despite modification of flight logistics and community noise barriers around airports to prevent as much exposure as possible, only so much can be done. Given that the majority of noise radiates from an aircraft's engines, the predominant focus has been on decreasing engine

noise specifically. The problem is not so easy to solve, as different noise characteristics arise from different parts of the engine including the fan, stator blades, the exhaust, turbine, and combustor. Overall noise reduction across the ranging frequencies of these components makes for a challenging task. Over time, different solutions have been implemented attempting to attenuate different noise sources throughout the engine. For example, the scarf inlet concept first investigated by NASA in 1979 featured a longer lower lip than upper lip, thus redirecting the noise radiating from the inlet upwards and away from the communities on the ground [6]. In 1992, NASA developed an active noise control test bed which detects the tones produced by the fan using feedback sensors in the nacelle and uses flush-wall-mounted actuators to emit waves out of phase with the fan tone in order to cancel the noise measured in the far field [7]. In more recent years, a NASA and industry joint effort produced chevron technology first implemented on General Electric's CF34 engine for regional jets and GEnx engines for Boeing 787 and 747-8 aircraft [8]. Chevrons are a sawtooth pattern found on the trailing edge of exhaust nozzles which aid in jet noise reduction. More recently still, as part of their CLEEN Program agreement, Collins Aerospace is developing advanced acoustic exhaust concepts with novel core geometries tuned to exhaust tones capable of a 0.9-1.5 Effective Perceived Noise decibel (EPNdB) reduction [9].

Ever since the turbofan engine was popularized, the inlet and bypass ducts have provided sufficient surface area for the implementation of acoustic liners. Acoustic liner technology continues to be employed on modern turbofan engines today. As the demand for quieter aircraft increases, so has the wish to develop acoustic liners that exhibit better attenuation across a larger frequency range. As the need for more efficient engines increases, these liners are also required to weigh less and take up less space. The traditional honeycomb liner employed in most aircraft has been effective up until now, but their ability to keep up with demand for quieter flight is being challenged. Interest in alternative acoustic liner technology has risen as standard honeycomb liner performance development approaches its asymptote.

The goal of this research is to explore a novel acoustic liner concept that shows promise in achieving attenuation at frequencies unattainable by conventional liners, particularly at lower frequencies. The new concept involves taking advantage of acoustic metamaterial technology [10]. This technology shows promise in achieving sound absorption and transmission loss across

a wider range of frequencies, including lower frequencies, without adding excessive additional weight or space. Traditional acoustic liners are first introduced, followed by an introduction on acoustic metamaterials and how traditional liners can be manipulated to take advantage of this technology. Finally, the objectives of this research are listed and an outline of the paper is provided.

1.2. Introduction to turbofan engine acoustic liners

Since the 1950's, acoustic liners have been used for aircraft noise reduction, generally mounted to the walls of the inlet and aft-bypass duct to absorb both tonal and broadband noise [11]. Modern research facilities such as the Liner Technology Facility (LTF) at NASA Langley Research Center are equipped with state-of-the-art test rigs to measure the acoustic impedance of liners. Rigs like the Grazing Flow Impedance Tube (GFIT) and the Curved Duct Test Rig (CDTR) have been critical for U.S. industry in the development of these acoustic liners. The predominate liner configuration in modern commercial nacelles has been the perforate-over-honeycomb structure (see Figure 1). As the engine bypass ratio has increased over the years, jet noise has subsequently decreased to a point in which the broadband fan noise now dominates [11]. With this trend, the expectation for acoustic liners has now shifted to absorbing sound over a wider frequency range at the inlet; the hardest of which to attenuate being low frequencies ($ka < 1$ where k is the wavenumber, and a is the maximum dimension of a cross-section of the duct [12]).

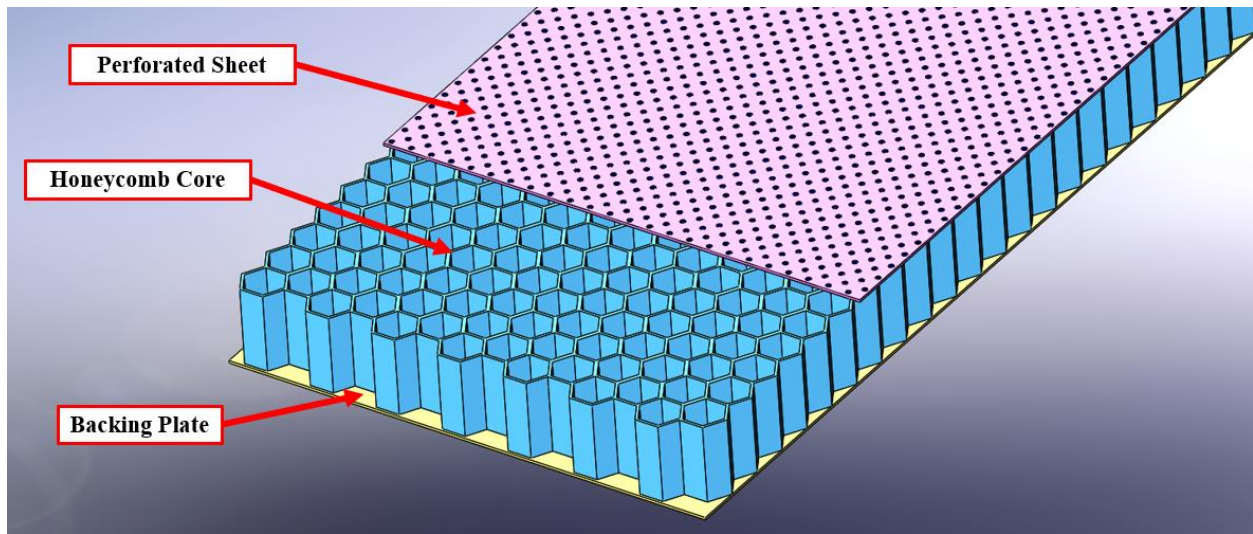


Figure 1. Section View of a Sample Perforate-Over-Honeycomb Structure

To date, acoustic liner research has mostly been conducted through the lens of local-reacting configurations (see Figure 2) [11]. Local-reacting liners use partitions to prevent sound transfer through the body of the liner while extended-reacting liners do not have partitions [11]. In the case of local-reacting liners, these partitions make up the “cells” of the liner where the cell volume is specifically chosen such that resonance occurs at desired frequencies. If those frequencies match the frequencies emitted from the engine, the noise will be attenuated. Due to limitations in liner thickness, however, the volume of these cells can only be but so large, meaning that lower frequencies are harder to attenuate [13].

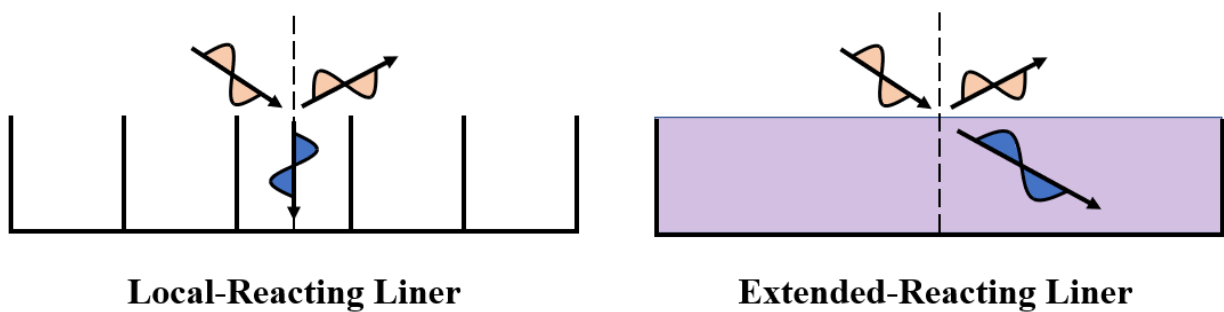


Figure 2. Local-Reacting vs. Extended-Reacting Liners

The industry standard perforate-over-honeycomb design is local-reacting and works based on the principle of Helmholtz resonators (HR). A Helmholtz resonator, in its simplest form, consists of a “neck” connected to a cavity (see Figure 3). In lumped-parameter analysis, if air is the working medium, then the neck can be modeled as a mass of air, and the cavity can be

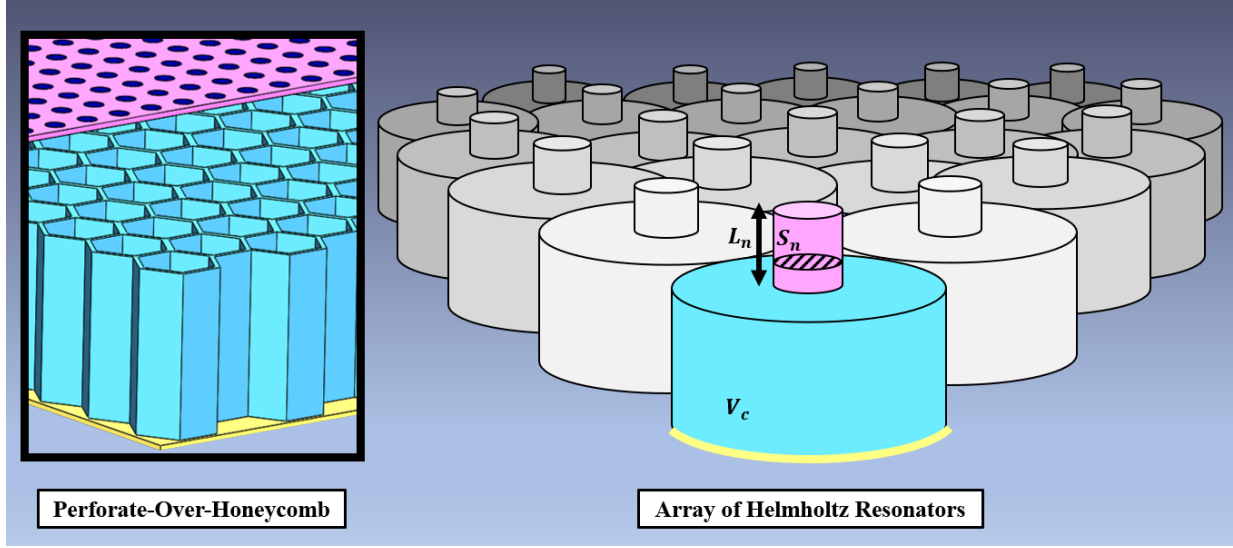


Figure 4. Schematic of an Array of Helmholtz Resonators Representative of a Perforate-Over-Honeycomb Liner

Since an array of Helmholtz resonators is then essentially a large mass-spring system, the number of equations of motion required to mathematically describe the system can become quite large. Large systems like these (especially repetitive ones) can instead be modeled using a transfer-matrix approach. The transfer-matrix method was first introduced in 1941 by Kramers and Wannier [14] and is used across multiple scientific fields that revolve around the study of waves propagating through layers of differing impedances (see Figure 5). If a wavefield is known at the beginning of a layer, then the wavefield at the end of the layer can be expressed as a simple matrix operation relating the end state to the beginning state. Transmission through a collection of layers with different impedances can then be expressed as the product of all of the matrix operations. In acoustics, the pressure and volume velocity states at opposite ends of the n^{th} layer of a multilayer system can be expressed as a transfer matrix via

$$\begin{bmatrix} p(x_n) \\ u(x_n) \end{bmatrix} = \begin{bmatrix} \cos(kL_n) & -iZ_n \sin(kL_n) \\ -i \frac{\sin(kL_n)}{Z_n} & \cos(kL_n) \end{bmatrix} \begin{bmatrix} p(x_{n-1}) \\ u(x_{n-1}) \end{bmatrix} = \mathbf{T}_n \begin{bmatrix} p(x_0) \\ u(x_0) \end{bmatrix} \quad (1)$$

where x_n and x_{n-1} are positions at the end of the n^{th} layer and at the beginning of the n^{th} layer respectively, p is the acoustic pressure, u is the acoustic volume velocity, k is the wavenumber, L_n is the length of the layer, $Z_n = \rho c/S_n$ is the acoustic impedance of the duct layer for a plane wave, S_n is the cross-sectional area of the layer, and i is the unit imaginary number [15].

Continuity conditions require that the pressures are equal immediately left and right of a

boundary between two layers of differing impedance (i.e., an impedance discontinuity) and likewise with the volume velocities; hence in Figure 5 for example, the pressures just to the left and right of the impedance discontinuity at x_1 are both written as p_1 and likewise with u_1 . The state variables across all three layers can thus be written as

$$\begin{bmatrix} p(x_3) \\ u(x_3) \end{bmatrix} = \mathbf{T}_3 \mathbf{T}_2 \mathbf{T}_1 \begin{bmatrix} p(x_0) \\ u(x_0) \end{bmatrix} \quad (2)$$

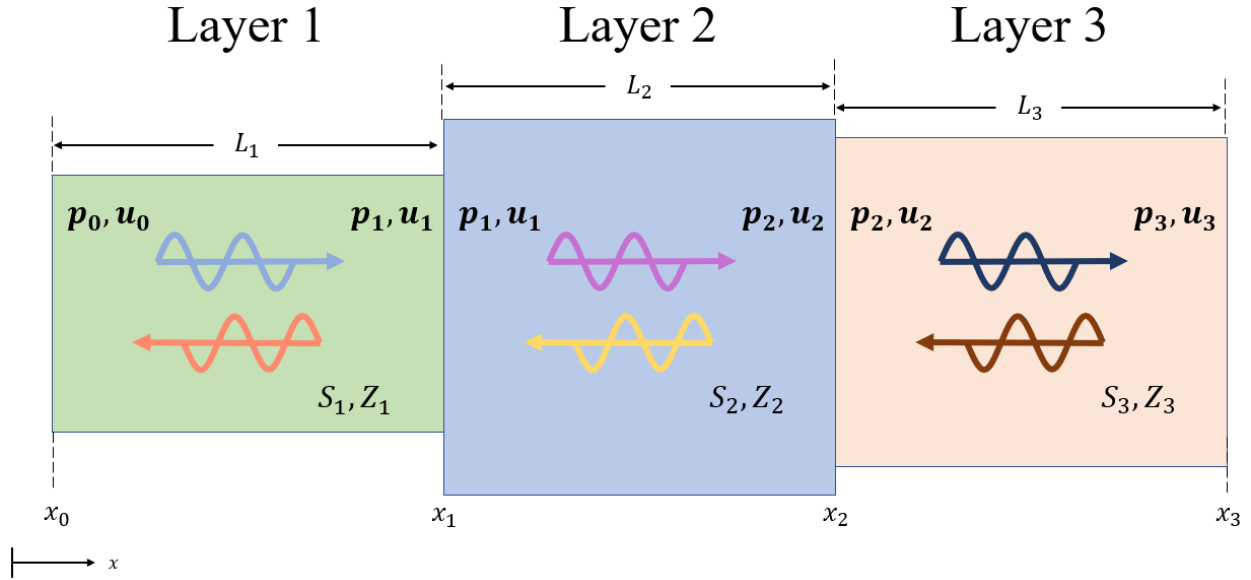


Figure 5. Schematic of Acoustic Wave Transmission Through Inhomogeneous Layers

In the case of a periodic array of impedance discontinuities such as a duct periodically loaded with identical Helmholtz resonators (see Figure 6), the system can be described by a repeating pattern of two alternating layers: one layer for an untreated portion of the duct between two resonators (shown in green) and one layer for a portion of a duct treated with a single Helmholtz resonator (shown in blue) [16]. That means that the relationship between the state variables across the entire duct lined with N periodically-spaced identical Helmholtz resonators can be expressed as

$$\begin{bmatrix} p(x_N) \\ u(x_N) \end{bmatrix} = (\mathbf{T}_d \mathbf{T}_r)^N \begin{bmatrix} p(x_0) \\ u(x_0) \end{bmatrix} \quad (3)$$

where T_d is the transfer matrix across an untreated duct layer and T_r is the transfer matrix across a duct layer containing a resonator. The product of these two matrices is exponentiated because these two layers repeat N times.

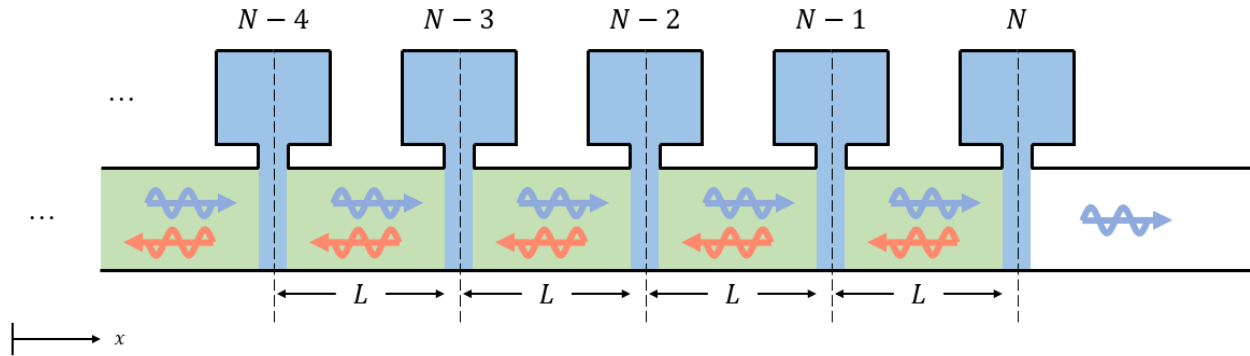


Figure 6. Schematic of a Duct Periodically Loaded with N Identical Helmholtz Resonators

When modeling a liner in this way, the periodic spacing of the cells becomes a parameter. Normally, cells are packed closely together in order to fit the maximum amount possible in the liner, but as will be shown in the following section on metamaterial physics, modifying the periodic spacing of the cells can greatly impact the sound absorption characteristics of a liner in a positive way. In practice, the performance of a liner is usually predicted via semi-empirical models, like the Goodrich perforate liner impedance model for example [17]. While this model is quite accurate in its characterization of the performance of a liner, the model is not tailored for the modification of the cell periodic distance without having to couple a duct propagation code with impedance boundary conditions to study these effects; hence, an alternate modeling approach is warranted to better study the effects of this parameter. By representing an acoustic liner as an array of periodically-spaced Helmholtz resonators, the effects of cell periodicity can be studied directly using the transfer-matrix method. It will be shown that designing liners with a focus on cell periodicity will enable the creation of more advanced liners that can attenuate a wider range of frequencies through the principles of metamaterial physics which essentially comes from solid-state physics (see next section).

1.3. Physics principles guiding metamaterial design

A metamaterial is a man-made structure engineered to alter wave propagation specifically via a periodic arrangement of discontinuities [18]. Their designs are inspired by naturally

occurring materials, particularly solids. All solid materials consist of a collection of atoms – more than 90% of all solids have a *periodic* arrangement of atoms, while the rest have an aperiodic atomic structure [19]. Solids with a lattice of periodically arranged atoms are known as crystalline solids or crystals (see Figure 7). A crystalline solid is capable of transmission, reflection, refraction, diffraction, absorption, and scattering of different kinds of waves at different frequencies. Crystals are able to manipulate wave behavior specifically because of two fundamental characteristics: the restoring forces within the solid and the periodic arrangement of the atoms [20]. This wave interaction within a solid at an atomic level determines the material’s electrical, magnetic, optical, thermal, and mechanical properties. Metamaterial engineering is thus the creation of artificial structures with periodically arranged discontinuities that alter wave propagation and work based on the same solid-state physics principles that are used to explain the alteration of wave propagation on an atomic scale in naturally-occurring crystalline solids [21]; hence, a review of these solid-state physics principles is warranted.

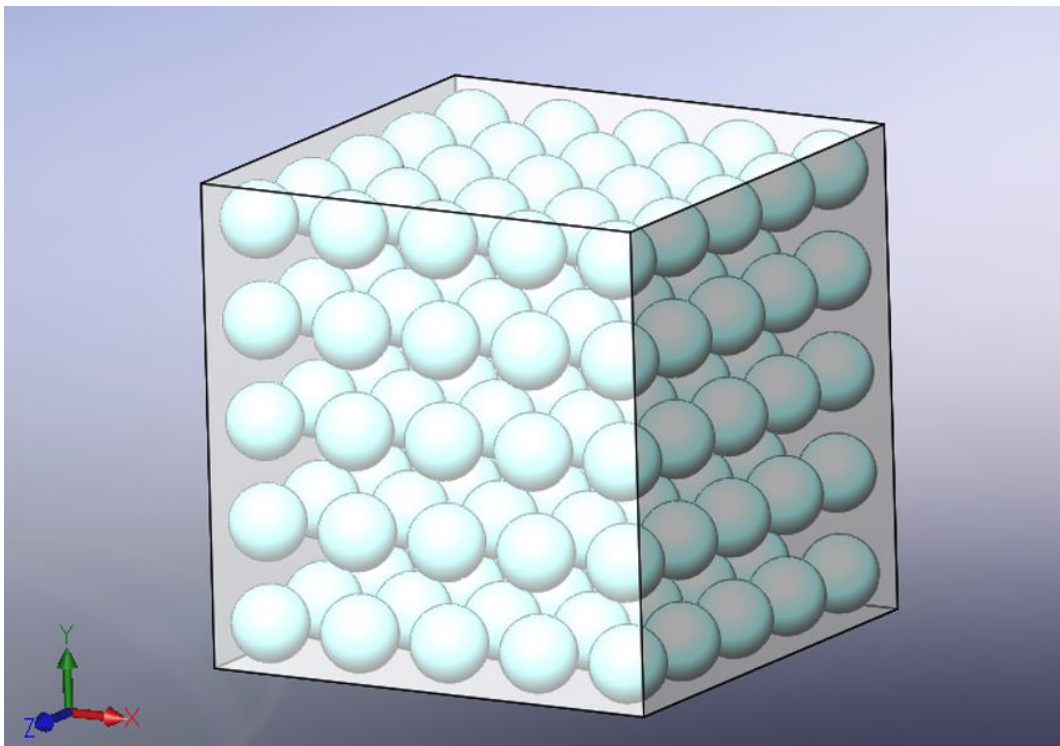


Figure 7. Example Sketch of a Crystalline Solid – A Lattice of Periodically Arranged Atoms

The two solid-state physics principles relevant to this thesis and to metamaterials in general are local resonances and Bragg reflection. The local resonances phenomenon occurs

naturally in metals under the influence of relatively low frequency waves like visible light, while the Bragg reflection phenomenon occurs naturally in metals under the influence of high frequency waves like X-rays [21].

Most metals are crystalline solids and thus consist of a lattice of periodically spaced atoms [19]. Atoms consist of negatively charged electrons that are bound to a positively charged nucleus. Valence electrons are the electrons that are most loosely bound to the nucleus. If a valence electron was displaced a certain distance away from the nucleus (see Figure 8a), the positively charged nucleus would exert a Coulomb restoring force on the electron pulling it back to its equilibrium position; however, the electron picks up so much speed in the process of returning to its equilibrium position (Figure 8b) that it actually passes the nucleus [21]. Upon reaching the other side of the nucleus, the Coulomb restoring force now pulls back on the electron enough to slow it down to a complete stop (Figure 8c), and the electron reverses its direction back toward the nucleus. This cycle repeats indefinitely assuming no damping in the system and thus behaves just like a classical harmonic oscillator (Figure 8d-f) where the electron is the mass and the Coulomb restoring force between the electron and the nucleus is the restoring force of the spring. The natural frequency of the oscillating electron is called the electron plasma frequency [21].

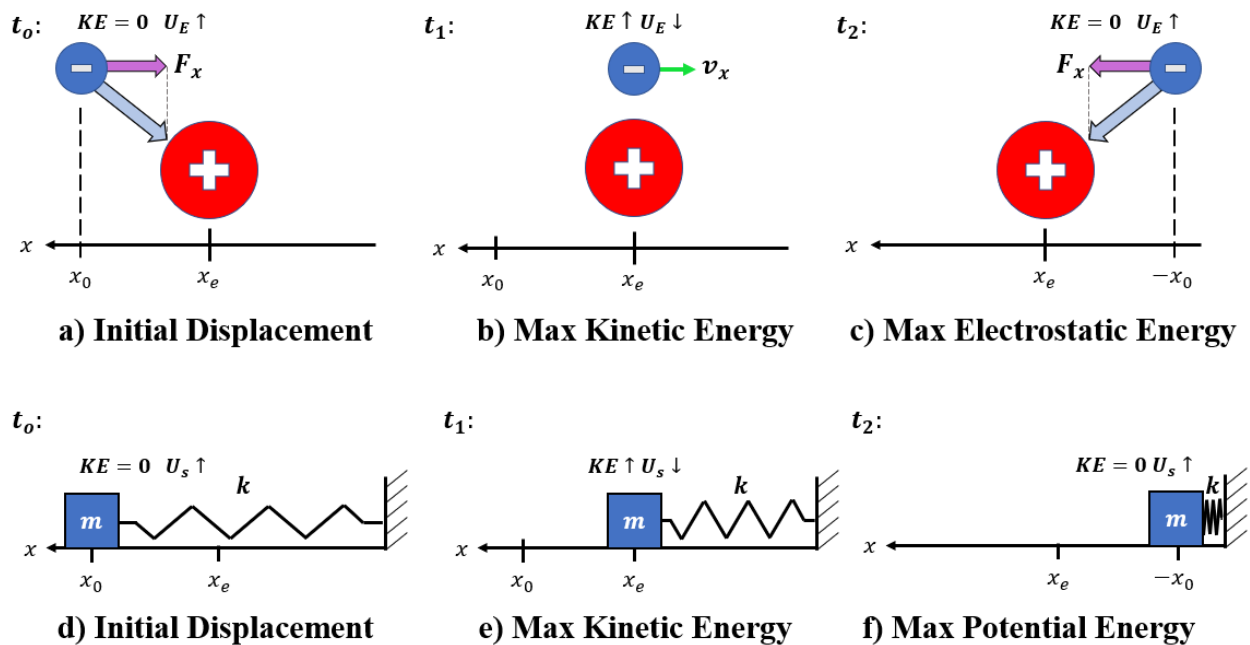


Figure 8. Schematic of Locally Resonant Electrons and the Equivalent Spring-Mass System

Any time two charges move in relation to each other, an electric field is generated [22]. If all the electrons are displaced by the same amount from their equilibrium positions, then all the electrons would resonate locally which collectively generates a strong sinusoidally-varying electric field. In the case where a sinusoidal electric field is applied on the surface of a metal (see Figure 9), the electrons on the surface will be excited such that they oscillate with the electric field but are also constrained by the electrostatic restoring forces from the positively charged nuclei; hence, this system as a whole behaves like a driven harmonic oscillator [20].

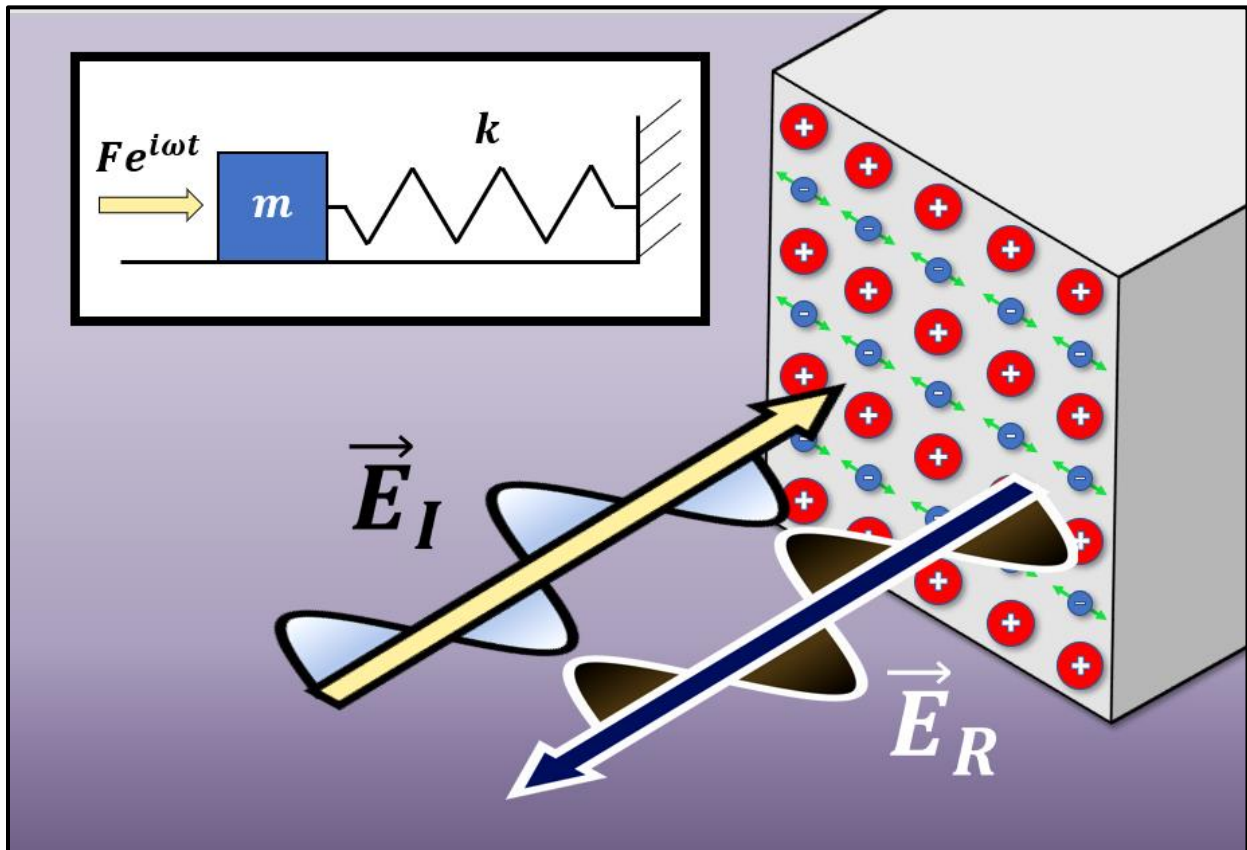


Figure 9. Locally Resonant Electrons Collectively Excited by a Sinusoidal Electric Field – Analogous to a Driven Spring Mass-System

An incident electric field acting on the metal with the same frequency as the plasma frequency will induce the maximum possible displacement of the electrons which in turn will generate the maximum amplitude possible for the reflected electric field (see Figure 10 for a displacement plot of an example mass-spring system) [21]. When the driving frequency is low (as in the stiffness-controlled region of a vibrational system), the displacement levels off to the static displacement. In this case, the electrons are still able to move and generate reflected

electric fields away from the metal. On the other hand, when the driving frequency is high (as in the mass-controlled region of a vibrational system), the electrons are unable to keep up and hence do not move much beyond their equilibrium positions and do not generate a reflected field. Since a reflected wave is not produced at these frequencies, the incident wave can propagate without interference and transmit through the metal [21]. The plasma frequency of most metals is somewhere in the ultraviolet region of the electromagnetic frequency spectrum, so metals can reflect visible light well since the frequencies of visible light are below the plasma frequency [21]. This phenomenon explains why metals are visibly opaque. There are some ultraviolet frequencies below the plasma frequency, so they also get reflected, which explains why metals appear shiny. Since the higher ultraviolet frequencies, X-rays, and gamma rays all have frequencies above the plasma frequency, they can penetrate the metal.

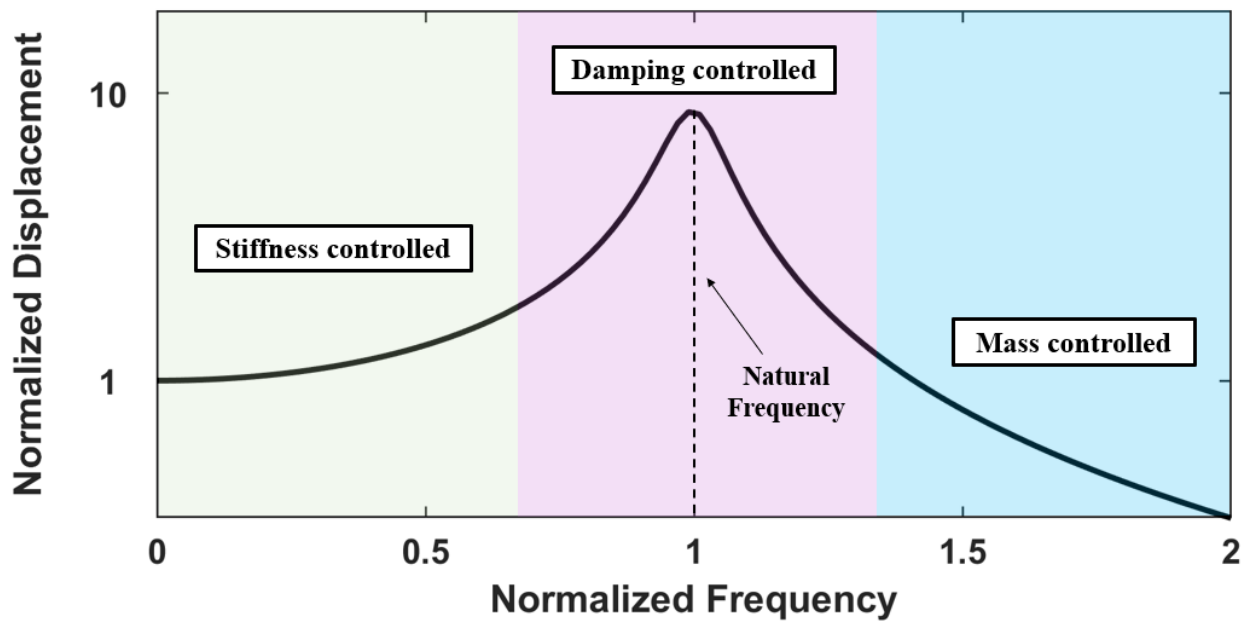


Figure 10. Example Plot of the Normalized Displacement of a Forced Mass-Spring System vs. the Driving Frequency Normalized by the Natural Frequency of the System

The idea of using locally resonant devices within a lattice to collectively reflect waves near and below the resonant frequency can be applied for any type of wave propagating through a periodic structure within a certain range of frequencies [21]. Many metamaterials that are designed for wave absorption are inspired by this phenomenon. Like metals, metamaterials often feature many periodically arranged local resonators [21]. In designing these metamaterials, the mass, stiffness, and damping of each local resonator can be tuned to achieve a desired overall

performance of the system, just like how the properties of metals are determined by the local resonances of their atoms.

Since an X-ray has a frequency higher than the plasma frequency of most metals, it can penetrate the metal surface. As an X-ray travels through a metal it gets scattered in all directions by the atoms [21]. Because there are so many atoms, the incident plane waves get scattered so much that neither constructive nor destructive interference patterns appear and collectively the X-ray can continue to transmit; however, not all frequencies of the X-ray spectrum can transmit. When the periodic distance of the atoms in a crystalline solid is a multiple of a half of a wavelength of an X-ray at normal incidence (see Figure 11), the scattered waves interfere constructively in the reverse direction and form an intense reflected wave [21]. This reflected wave will be out of phase with the incident wave, and thus destructively interfere and block the transmission of energy; the more planes of atoms, the more the waves get reflected. In solid-state physics, this phenomenon is called Bragg reflection [23], and it is not unique to X-rays in metals. This principle of physics applies to any type of wave that is traversing a periodic arrangement of discontinuities so long as the periodic distance between the discontinuities is a multiple of a half of a wavelength [21]. Inspired by this phenomenon, metamaterial designs often consist of periodic structures that are spaced a multiple of a half of a wavelength of the frequency of interest for attenuation.

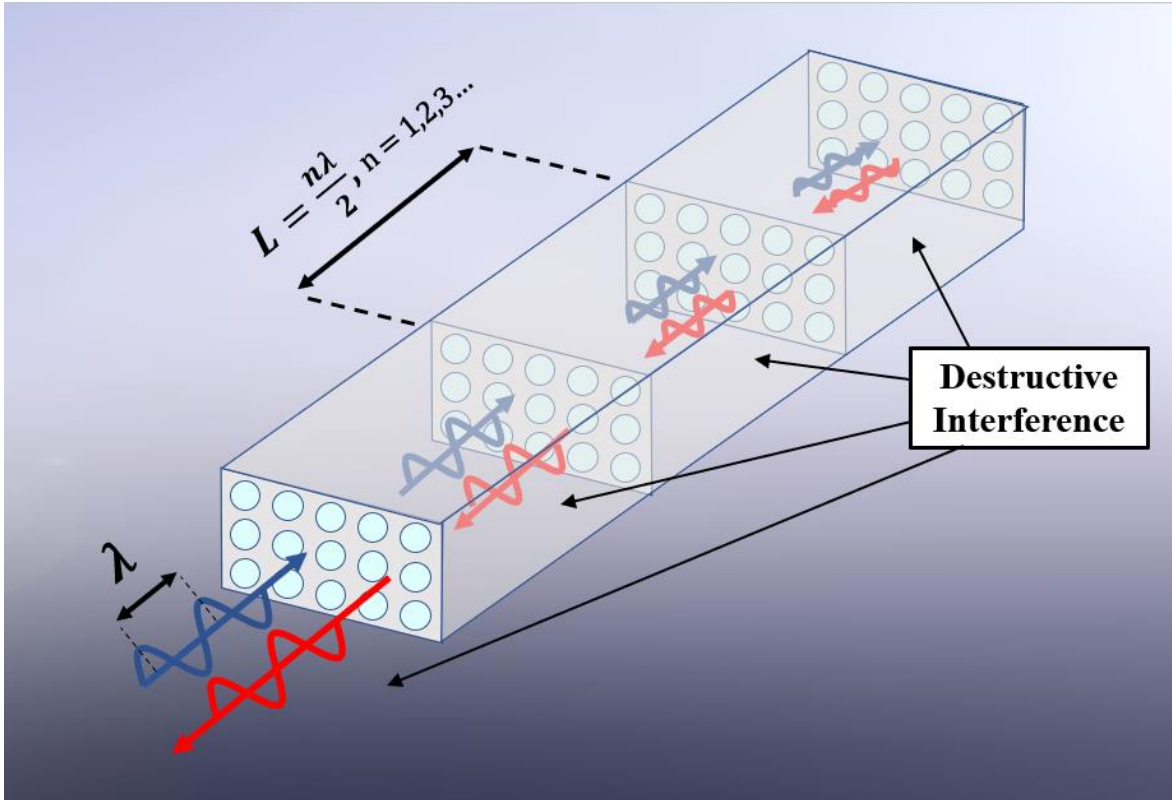


Figure 11. Schematic of a Crystalline Solid Modeled as a Set of Periodically Spaced Parallel Planes of Atoms Exhibiting Bragg Reflection

Before solid-state physics, no one had developed a wave equation to mathematically describe waves traveling through periodic media [24]. Periodic lattice systems in general were difficult to model. Isaac Newton was the first to ever attempt to model such a physical system when he modeled the propagation of sound waves through air as the vibration of a periodic lattice of masses and springs [25]. At that time, a continuous structure was an insoluble problem since partial differential equations did not yet exist; hence, that model could only be solved via simultaneous equations of motion. By the early 20th century, research of waves in periodic media was revisited in a new light thanks to the advent of quantum mechanics. In his PhD thesis in 1924 [26], Louis de Broglie developed the foundation of modern quantum mechanics when he inferred that all matter behave like waves. He showed that the energy of all matter can be expressed as a frequency and their momentum expressed as a wavelength using the Planck constant first postulated by Max Planck [27] in 1900:

$$\lambda = \frac{h}{p}, \quad f = \frac{E}{h} \quad (4)$$

where λ is the wavelength, h is Planck's constant, p is momentum, f is frequency, and E is the total energy [26].

Since all matter was found to behave like waves, a need to mathematically characterize different matter via unique wavefunctions arose in the scientific community. In 1926, Schrödinger [28] proposed that the time-independent wavefunction of an isolated quantum-mechanical system is governed by the following linear partial differential equation:

$$E\Psi(x) = -\frac{\hbar^2}{2m} \frac{d^2\Psi(x)}{dx^2} + V\Psi(x) \quad (5)$$

where E is the energy of the system, $\Psi(x)$ is the wavefunction, x is position, \hbar is the reduced Planck's constant ($\hbar = h/2\pi$), m is the mass of the particle, and V is the potential energy of the system.

Different quantum problems are described by different solutions to Schrödinger's equation. The most basic quantum problem is that of an electron propagating in free space with no external forces acting on it. This kind of electron is called a free electron [20]. The solution to Schrödinger's equation for the case of a free electron takes on the form of a plane wave:

$$\Psi(x) = Ae^{ikx} \quad (6)$$

where A is the amplitude of the wave, $k = 2\pi/\lambda$ is the wavenumber, and λ is the wavelength [28]. A more complex quantum problem of considerable interest at the time was the solution to the state of an electron propagating through a solid. A better understanding of this quantum problem would help to explain why some solids were better electrical conductors than others.

Generally, metals in a solid state have a low ionization energy, meaning that only a small amount of energy is required to remove the most loosely bound electron of an atom of the metal [22]. This ionization energy is so low, that these loosely bound electrons are relatively free to leave an atom, and now the atom will have become an ion with a net positive charge. Upon separating from the atom, these electrons are then able to be moved under the influence of an electric field, and the motion of these electrons constitutes an electric current [22]. The propagation properties of the electron are determined by the electric potential of the solid. In the case of crystalline solids, as an electron propagates through the crystal's periodic arrangement of

positively charged ions, the ions exert Coulomb attraction on the electron but not enough to bring the electron to a stop [20]. The electrons are much lighter than the ions, so the electrons move as a result of this force while the ions remain relatively immobile. Therefore, assuming the ions are not vibrating under the influence of thermal energy, the electron propagating through the periodic arrangement of stationary ions is subject to a periodic electric potential energy (see Figure 12) [20].

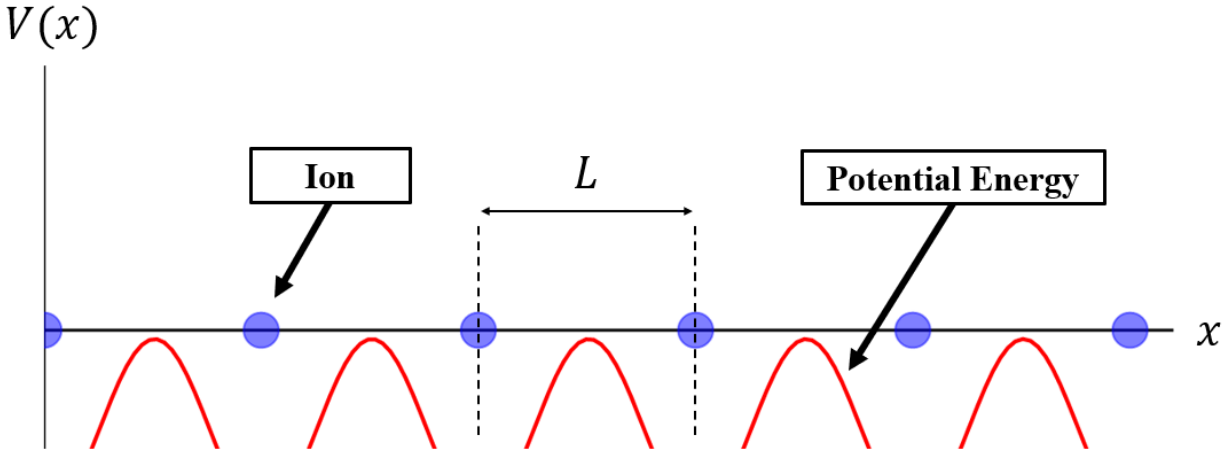


Figure 12. An Example of a 1D Crystalline Solid Whose Stationary Ions Introduce a Periodic Potential Energy for a Traveling Electron

Mathematically, the periodicity of the potential energy can be captured by

$$V(x) = V(x + R) \quad (7)$$

where $R = nL$, n is any integer, and L is the distance between two adjacent ions [20]. When the potential is periodic, then Schrödinger's Equation (Equation (5)) is no different than Hill's differential equation, a second-order linear differential equation in mathematics given by

$$\frac{d^2y}{dt^2} + f(t)y = 0 \quad (8)$$

where $f(t)$ is a periodic function obeying $f(t) = f(t + T)$ [29]. Since Schrödinger's equation with a periodic potential is essentially the same as Hill's equation, then the solution to the Schrödinger equation could be found in the same way as the solution to Hill's equation. By 1883, Floquet had already found the solution to Hill's equation using a process now known as

Floquet's theorem [30]. Floquet's theorem states that the fundamental matrix solution to a system of first-order differential equations written in the form

$$x'(t) = A(t)x(t) \quad (9)$$

is given by

$$\phi(t) = P(t)e^{tB} \quad (10)$$

where $x(t)$ is a column vector of length n , $x'(t) = dx/dt$, $A(t)$ and $P(t)$ are $n \times n$ periodic matrices with period T such that $A(t + T) = A(t)$ and $P(t) = P(t + T)$, and B is an $n \times n$ matrix of complex constants [30]. Essentially, this theorem states that the solution to a set of differential equations with a periodic coefficient matrix is another periodic matrix with the same periodicity modulated by a complex exponential term.

Recalling that second order differential equations can be written as a system of first order differential equations, Hill's equation (Equation (8)) can be rewritten in the form of Equation (9), and thus his equation could then be solved using Floquet theorem. Substituting $x_1 = y(t)$ and $x_2 = y'(t)$, Equation (8) can be rewritten as

$$\begin{bmatrix} x_1'(t) \\ x_2'(t) \end{bmatrix} = \begin{bmatrix} 0 & 1 \\ -f(t) & 0 \end{bmatrix} \begin{bmatrix} x_1 \\ x_2 \end{bmatrix} = A(t)x(t) \quad (11)$$

and hence, has a solution given by Equation (10).

Felix Bloch [31] had attended lectures given by Schrödinger at the University of Zürich during his undergraduate years, and in 1929, published the results of his PhD thesis in which he used Floquet's theorem to find the solution to Schrödinger's equation for electrons in a crystalline solid. The solution is given by

$$\Psi_{Bloch}(x) = e^{iqx}u(x) \quad (12)$$

where Ψ_{Bloch} is the Bloch wave function, x is position, $u(x)$ is a periodic function with the same periodicity as the ions in the crystal, and e^{iqx} is a plane wave with Bloch wavenumber q (which is just the wavenumber of the plane wave envelope of the Bloch wavefunction) [20]. This theorem essentially states that the wave behavior of an electron in a crystal differs from the plane

wave of a free electron only by a periodic modulation with the same periodicity as the crystal (see Figure 13). Such a wave is thus called a Bloch wave, and the exponent is negative ($e^{-iqx}u(x)$) when the wave is forward traveling, and the exponent is positive when backward traveling ($e^{+iqx}u(x)$).

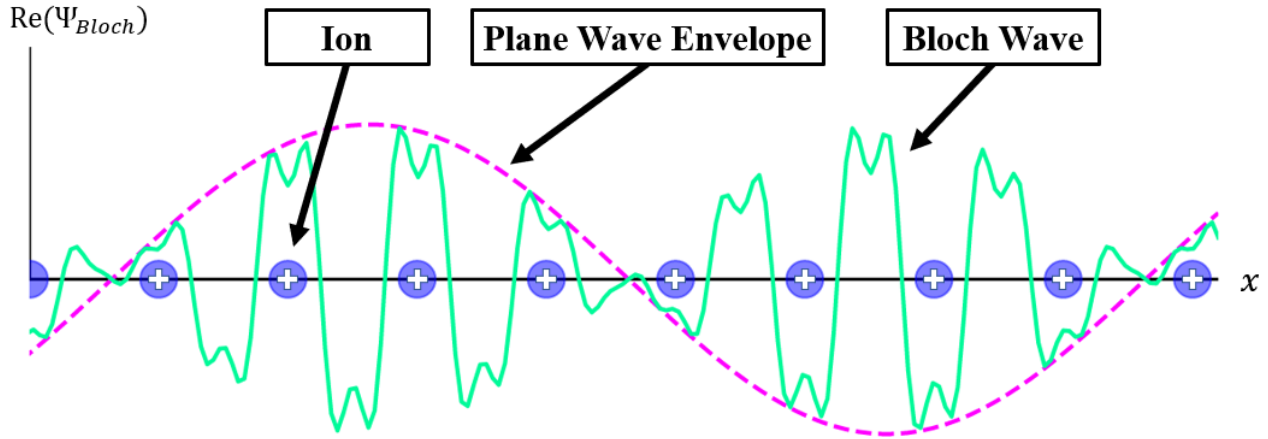


Figure 13. An Example Plot of a Bloch Wave – A Plane Wave Modulated by a Periodic Function

Observe from Figure 13 that the local wave motion between any two atoms is identical (i.e., described by a periodic function) except that the amplitude of the local wave motion between two atoms is controlled by the phase of the non-local plane wave envelope. In general, a wavenumber $k = 2\pi/\lambda$ is what characterizes a wave's phase difference between any two points at a unit distance apart [12]; however, the Bloch wavenumber q is a complex-valued wavenumber $q = q_r - iq_i$. Because the Bloch wavenumber is complex, the value mathematically describes both the phase change and the rate of decay of the plane wave envelope between two points at a unit distance apart [16]. This is because when an exponential function e^θ has a complex exponent $\theta = \theta_r + i\theta_i$, it can be split into $e^{\theta_r} \cdot e^{i\theta_i}$, where $e^{i\theta_i}$ is just Euler's form for simple harmonic motion, while e^{θ_r} changes the amplitude of that harmonic motion at an exponential rate.

Since forward traveling Bloch waves have a negative exponent ($e^{-iqx} = e^{-i(q_r - iq_i)x} = e^{-iq_r x} e^{-q_i x}$), the real component of the exponential $e^{-q_i x}$ is negative and thus decreases the amplitude of the Bloch wave exponentially with distance. The real component of the exponential $e^{-q_i x}$ has an effect on the Bloch wave that is analogous to viscous damping in oscillatory systems (see Figure 14) – if the real component of the exponential of a forward

traveling Bloch wave is sufficiently large, the amplitude of the plane wave envelope will decrease exponentially with distance, and the Bloch wave motion will become spatially “damped” (see Figure 15). Such a Bloch wave is thus evanescent, signifying that the electron will not propagate through the solid.

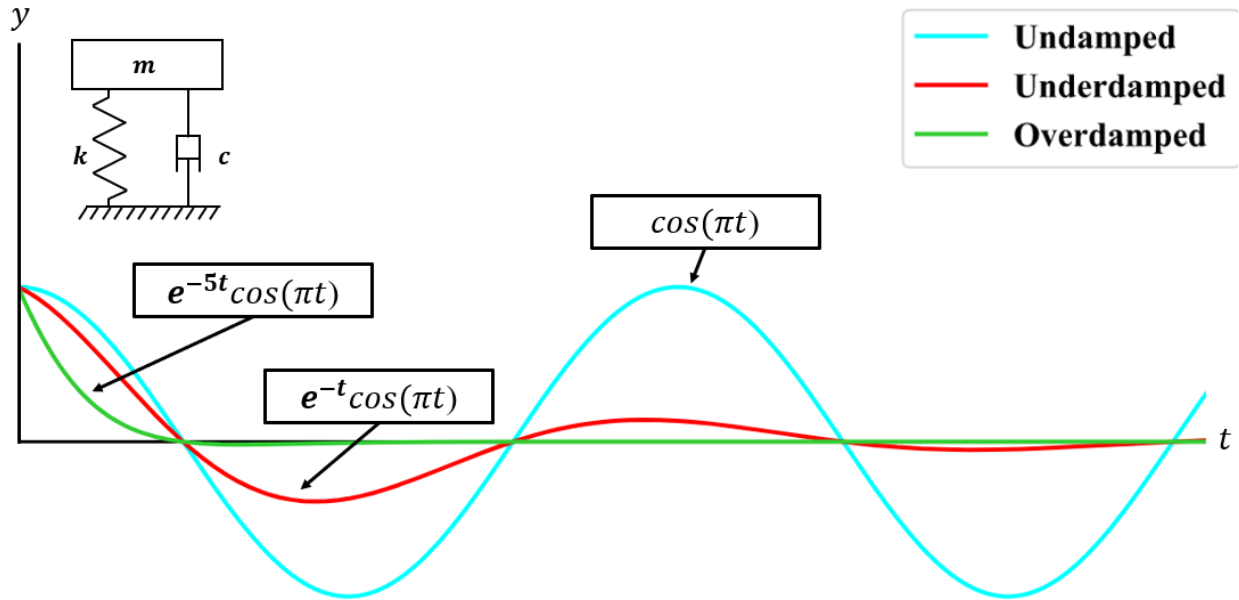


Figure 14. An Example Plot of Damped Oscillatory Motion

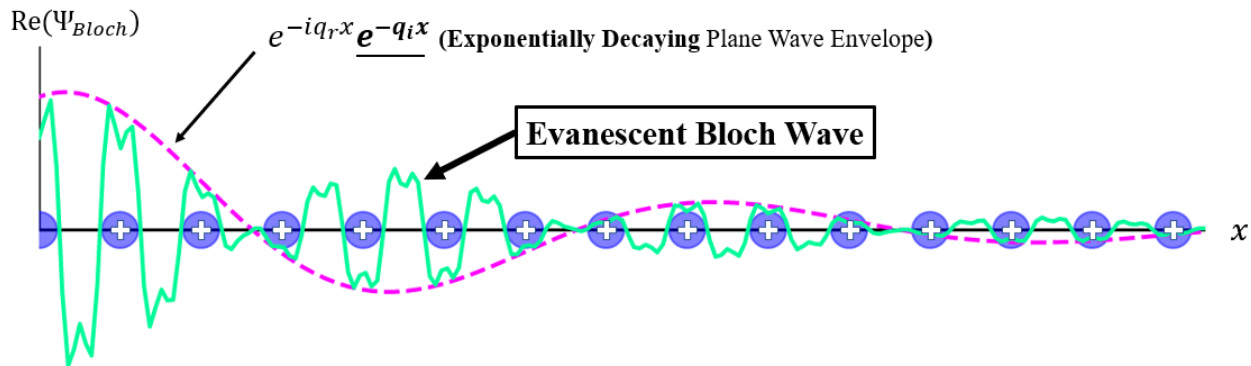


Figure 15. An Example Plot of an Evanescent Bloch Wave

At different electron energy levels (E in Equation (5)), the Bloch wavenumber q will take on different values [24]. At some energy levels of the electron, the Bloch wavenumber q will be purely real, meaning the exponential term of the forward traveling Bloch wavefunction e^{-iqx} will be purely imaginary $e^{-iq_r x}$, and hence the electron travels forward as a Bloch wave that

does not decay and will continue to propagate (as in Figure 13); at other energy levels, the Bloch wavenumber q will be complex, meaning the exponential term of the forward traveling Bloch wavefunction $e^{-iqx} = e^{-i(q_r - iq_i)x} = e^{-iq_r x} e^{-q_i x}$ will be complex, and hence the electron travels as a Bloch wave that decays exponentially with distance according to $e^{-q_i x}$ and is thus evanescent (as in Figure 15).

To visualize which energy levels result in propagating Bloch waves and which energy levels result in evanescent Bloch waves, dispersion plots are used (see Figure 16). Dispersion plots reveal that evanescent Bloch waves only occur in certain energy bands called “stop bands” [24]. These bands occur when the Bloch wavenumber q is complex and hence contains a decaying exponential term. Outside of these energy bands, the Bloch wavenumber q is purely real, and hence the Bloch waves propagate without decaying.

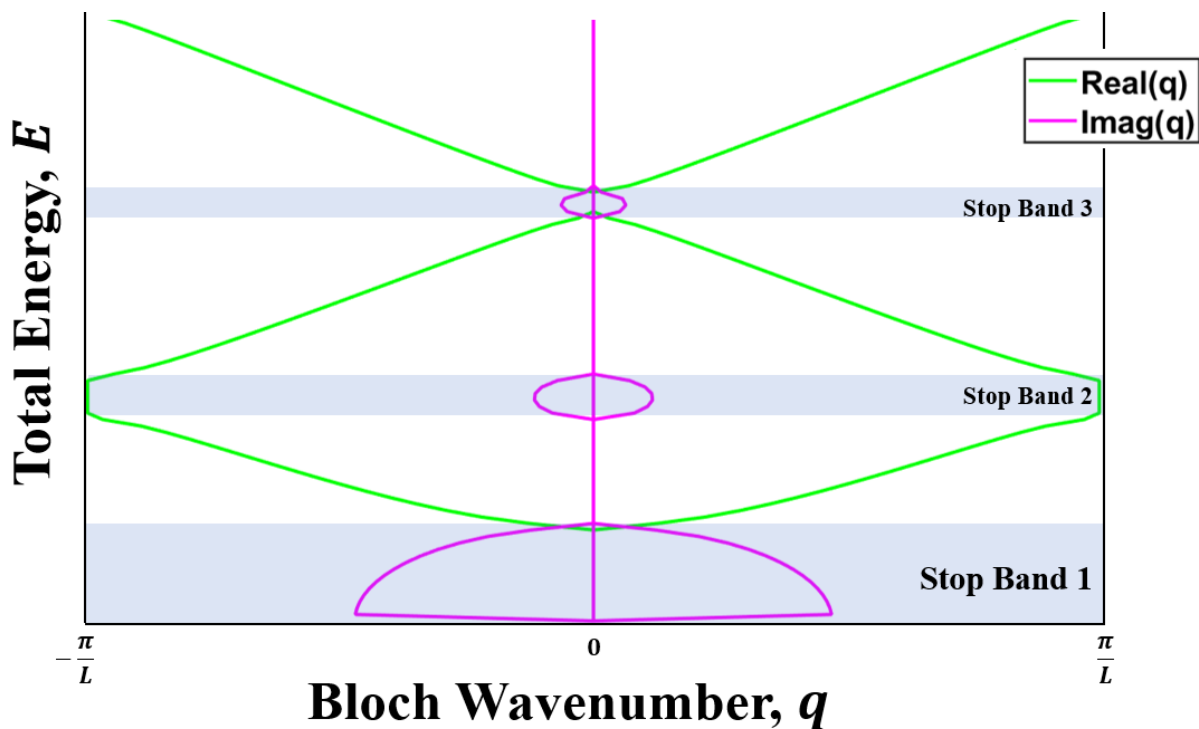


Figure 16. Example Dispersion Plot for an Electron Propagating Through a Crystal as a Bloch Wave Exhibiting Stop Band Behavior

Notice from Figure 16 that these stop bands occur when $q_r = \pm\pi/L$ where L is the periodic spacing of the ions. This observation is equivalent to saying that the stop bands occur when the periodic distance of the ions is equal to a half of a wavelength $L = \pm\lambda/2$ which is the

condition for Bragg reflection described in the beginning of this section [23]. In fact, if the bounds of the Bloch wavenumber q are extended in the dispersion plot shown in Figure 16, then the pattern would repeat such that stop bands occur at every multiple of a half of a wavelength equal to the periodic distance ($q = \pm n\pi/L$ where $n = 1,2,3, \dots$) [24]. Hence, when the periodic distance of the ions is equal to a multiple of a half of a wavelength, Bragg reflection occurs, and the Bloch wave is evanescent; otherwise, the Bloch wave can propagate freely without decaying and the crystalline solid will conduct electricity.

At this stage, it's helpful to introduce an alternative form of the Bloch wave equation given in Equation (12). The Bloch wave equation can alternatively be written as

$$\Psi_{Bloch}(x + L) = e^{iqL}\Psi_{Bloch}(x) = e^{\Gamma}\Psi_{Bloch}(x) \quad (13)$$

where L is the periodic spacing between the ions, and $\Gamma = iqL$ is the propagation constant of the Bloch wave [31]. The propagation constant of the Bloch wave acts as a convenient way of lumping the unit imaginary number i , the Bloch wavenumber q and the periodic spacing of the discontinuities L into one parameter that relates the states of a Bloch wave at two consecutive discontinuities [32]. Note that a propagation constant can be used to describe other wave types, not just Bloch waves, but it will only be used to describe Bloch waves in this thesis.

The term “propagation constant” is actually somewhat of a misnomer because it contains the Bloch wavenumber q which varies with the total energy E . Since the propagation constant varies with total energy E , the relationship between the two can also be visualized graphically via dispersion plots just like with the Bloch wavenumber q [33]. Because the propagation constant Γ contains the complex Bloch wavenumber $q = q_r - iq_i$, the propagation constant is also complex $\Gamma = \Gamma_r + i\Gamma_i$. A negative sign in front of the propagation constant Γ signifies a forward traveling Bloch wave, whereas a positive sign signifies a backward traveling Bloch wave. The imaginary component of the propagation constant $\Gamma_i = q_iL$ is often referred to as the phase constant because $e^{i\Gamma_i}$ is just Euler's form of simple harmonic motion which varies in phase as Γ_i varies [33]. The phase constant describes the phase change of the Bloch wave between the periodic discontinuities. The real component of the propagation constant $\Gamma_r = q_rL$ is referred to as the attenuation constant because it describes how a forward traveling Bloch wave decays exponentially according to $e^{-\Gamma_r}$ [33]. In other words, the attenuation constant describes the

decay rate between the periodic discontinuities. The propagation constant Γ inherently describes all the same information as the Bloch wavenumber q but is just a more convenient expression, as will be shown throughout the rest of this thesis.

The reason that the alternative form of Bloch's equation is provided in Equation (13) is because this form is similar to the form of the transfer-matrix method discussed in the previous section. Recall that the transfer-matrix method relates state variables at some distance apart L via

$$\begin{bmatrix} s_1 \\ s_2 \end{bmatrix}_{x+L} = \begin{bmatrix} A & B \\ C & D \end{bmatrix} \begin{bmatrix} s_1 \\ s_2 \end{bmatrix}_x = \mathbf{T} \begin{bmatrix} s_1 \\ s_2 \end{bmatrix}_x \quad (14)$$

where s_1 and s_2 are arbitrary state variables, and \mathbf{T} is the transfer matrix. Equation (13) can also be written in this form as

$$\begin{bmatrix} \Psi_{Bloch}(x+L) \\ \Psi'_{Bloch}(x+L) \end{bmatrix} = \begin{bmatrix} A & B \\ C & D \end{bmatrix} \begin{bmatrix} \Psi_{Bloch}(x) \\ \Psi'_{Bloch}(x) \end{bmatrix} = \mathbf{T} \begin{bmatrix} \Psi_{Bloch}(x) \\ \Psi'_{Bloch}(x) \end{bmatrix} = e^{\Gamma} \begin{bmatrix} \Psi_{Bloch}(x) \\ \Psi'_{Bloch}(x) \end{bmatrix} \quad (15)$$

where Ψ'_{Bloch} is the derivative of a Bloch wave with respect to x (note, however, that the choice of state variable is arbitrary). When written in this way, Equation (15) forms an eigenvalue problem where e^{Γ} is the eigenvalue of the transfer matrix \mathbf{T} ; hence, combining the transfer-matrix method with Bloch wave theory generates an eigenvalue problem that can be solved for the propagation constants [32].

Bloch wave theory was developed under the lens of solid-state physics to describe electrons propagating through crystalline solids, but the theory holds for any type of wave propagating through any kind of array of periodic discontinuities. For example, Mead [33] showed how the free harmonic motion of infinite beams on equally-spaced supports obeys Bloch wave theory (see Figure 17). He generated dispersion plots relating the propagation constant to the driving frequency and clearly identified stop-bands and pass-bands. Notice how just like for the electron travelling through a periodic lattice, each section of the beam between adjacent supports has an identical vibrational mode only they are modulated in amplitude by an exponentially decaying term containing the attenuation constant. Three years later, Mead [34] would then go on to rework his previous findings into more general expressions encompassing

other kinds of periodic systems; he even touched on wave propagation in two-dimensional periodic systems in which waves propagate across the system at a characteristic angle.

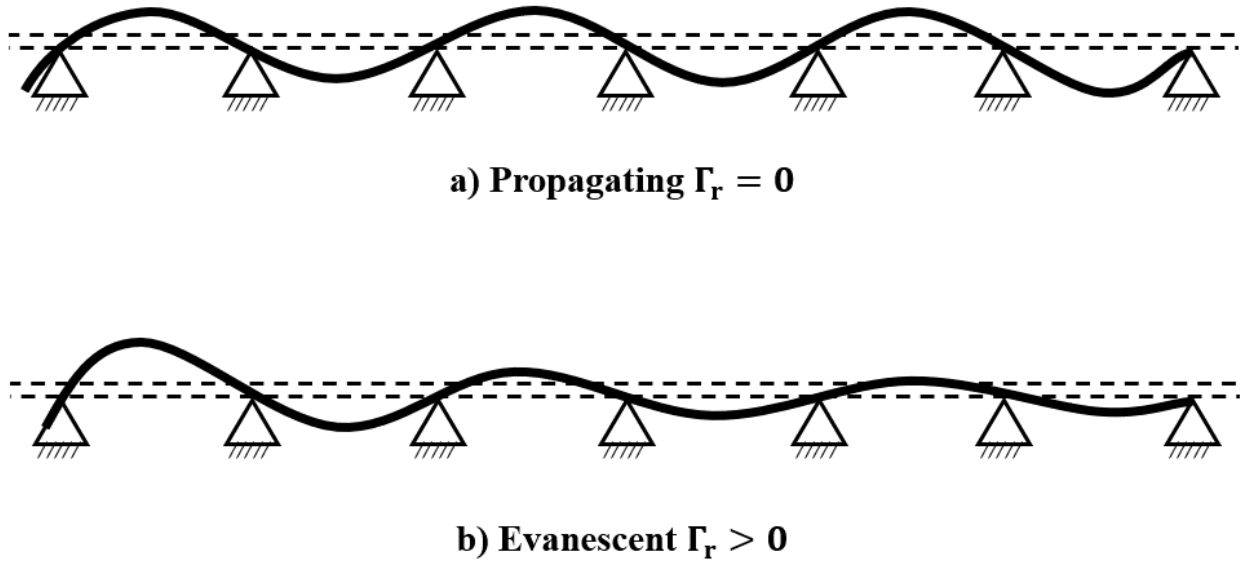


Figure 17. Example Schematic of Propagating and Evanescent Bloch Waves of a Beam on Periodically-Spaced Supports

Bloch wave theory can also be applied to a duct lined with a periodic arrangement of Helmholtz resonators (see Figure 18). Bradley [35] was the first to show that an infinite array of periodically arranged quarter-wavelength tubes lining a duct wall generates Bloch waves and exhibits Bragg reflection, and from there, Sugimoto and Horioka [36] showed that a duct lined with an infinite array of Helmholtz resonators exhibits the same phenomena. Wang and Mak [16] showed that the transfer matrix method can be used in conjunction with Bloch wave theory (as shown in Equation (15)) to describe such a system. By applying this technique, they were able to investigate how the number of resonators modified the attenuation, ranging from one cell up to an infinite case. Their analysis will be omitted here since their techniques will be shown in great detail throughout the subsequent analytical modelling sections of this thesis. One of the most important findings in their work was that careful selection of the periodic distance can result in generating Bragg reflection at frequencies below the resonant frequency of the Helmholtz resonator. This phenomenon is highly relevant to the aerospace industry, since the low-frequency attenuation of turbofan engine noise is essentially limited by the volume of the Helmholtz resonator; since the thickness limitations on liners are becoming more stringent,

designing liners with a periodic spacing of resonators would be beneficial in generating low-frequency absorption currently unattainable with limited-thickness traditional liners.

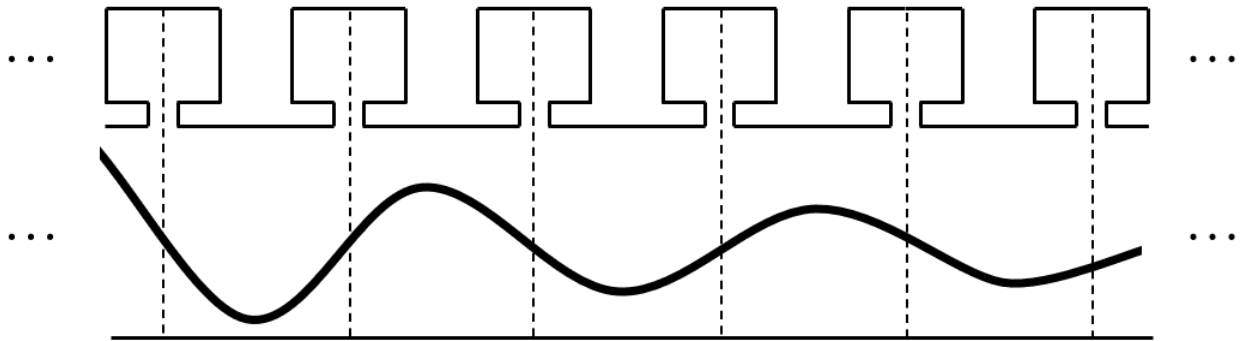


Figure 18. Example Schematic of the Decaying Plane Wave Envelope of an Evanescent Bloch Wave Propagating through a Duct Lined with a Periodic Array of Helmholtz Resonators

Not only can the periodic distance of the resonators be altered to achieve increased transmission loss across a wider range of frequencies, but another way to take advantage of metamaterial physics is to connect the cavities of the resonators together via coupling tubes (see Figure 19). Connecting the Helmholtz resonators together allows for waves to propagate through the chain of resonator cavities, thus adding another degree of freedom to the system. The path along this new degree of freedom essentially becomes another array of periodically spaced discontinuities which can be optimized using metamaterial physics principles. Having another degree of freedom to work with allows for more possibilities to manipulate the characteristics of the system and thus achieve transmission loss over a greater frequency range.

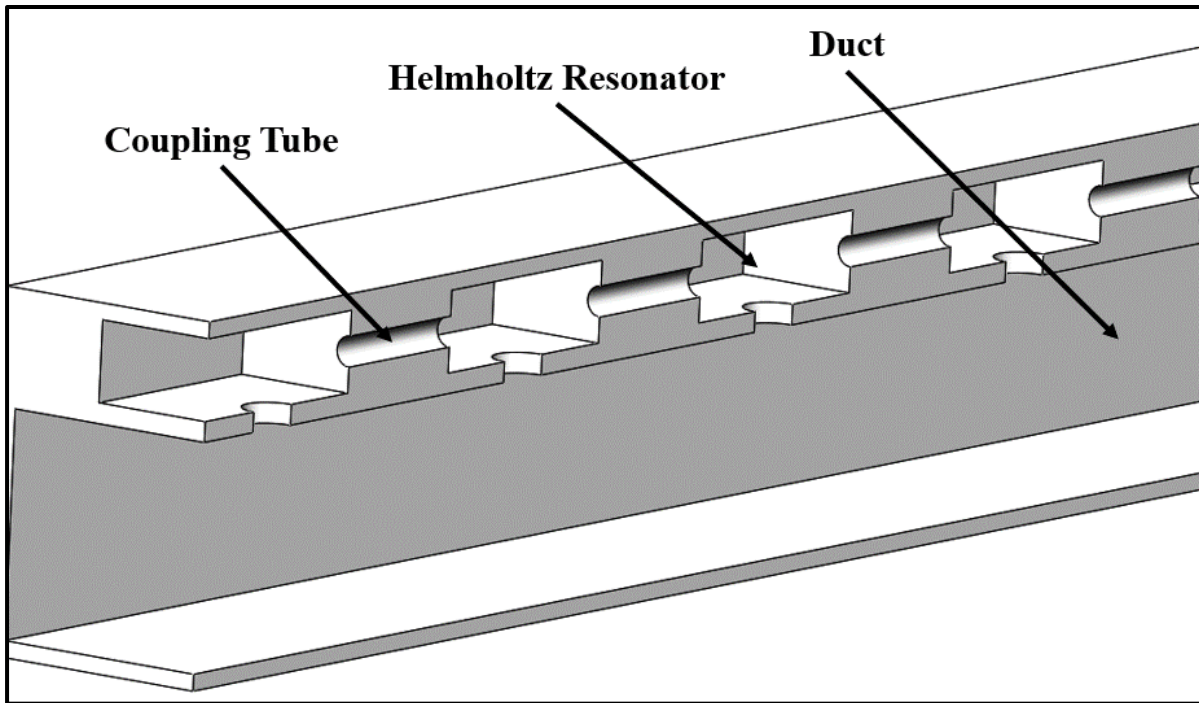


Figure 19. Section View of an Array of Connected, Periodically-Spaced Helmholtz Resonators

In addition to the attenuation from the Helmholtz resonators and from Bragg reflection, this system also achieves attenuation via the interaction of the traveling Bloch waves in the two waveguides when they interface at the necks of the resonators. Consider a simpler example illustrated in Figure 20 that works on the same principle. If the two waveguides are different mediums, then they will have different wave speeds c_1 and c_2 . At some points along the acoustically transparent sheet, the two waves are going to be in phase, and at other points, they are going to be out of phase. That means that the waves will interfere constructively at some points and destructively at others. For some frequencies the phase difference between the two interacting waves will destructively interfere enough to attenuate a significant amount of sound.

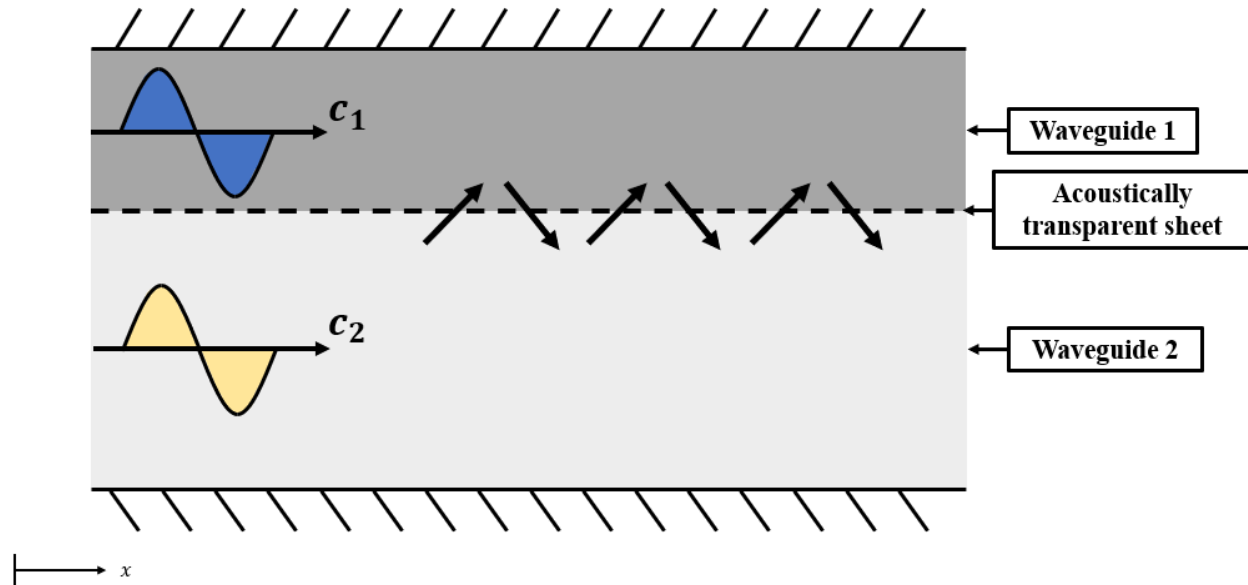


Figure 20. Schematic of Two Inhomogeneous Waveguides with Different Wave Speeds Coupled by an Acoustically Transparent Sheet

Rather than using two different mediums to create the difference in wave speed, an acoustic delay line can be created instead. Fuller [37] developed an acoustic delay line attenuator that consisted of an annular waveguide containing interstitial orifice plates. The annular waveguide surrounded the main circular duct with one interface at the upstream end and one interface at the downstream end. Some of the energy in the main duct would enter the alternate waveguide through the upstream interface, and because of the orifice plates, the wave would travel slower than the wave in the main duct and be out of phase by the time the wave reached the downstream interface. By using the right amount of orifice plates, the phase delay could be controlled such that destructive interference could be achieved at the desired frequencies.

The connected Helmholtz resonator array works the same way. In this case, the alternate waveguide is the resonator cavity chain (see Figure 21). The resonator cavity chain is coupled to the main duct by the necks of the Helmholtz resonators which is analogous to the acoustically transparent sheet from Figure 20. The two waveguides have different wave speeds because the waveguide created by the resonator cavity chain has an area that is frequently changing thus slowing the wave down in a way that is similar to Fuller's acoustic delay line of orifice plates [37]; hence, along the interface of the two paths (i.e., the necks), the two waves are going to be in

phase at some points, and at other points, they are going to be out of phase. For some frequencies the phase difference between the two interacting waves will destructively interfere enough to attenuate a significant amount of sound. At other frequencies that do not result in destructive interference, attenuation will be achieved by other methods like Helmholtz resonance and Bragg reflection. Combining all three concepts together (Helmholtz resonance, Bragg reflection, and the destructive interference between the waveguide and the duct), sound attenuation can be achieved across a wide frequency range as will be shown in this thesis.

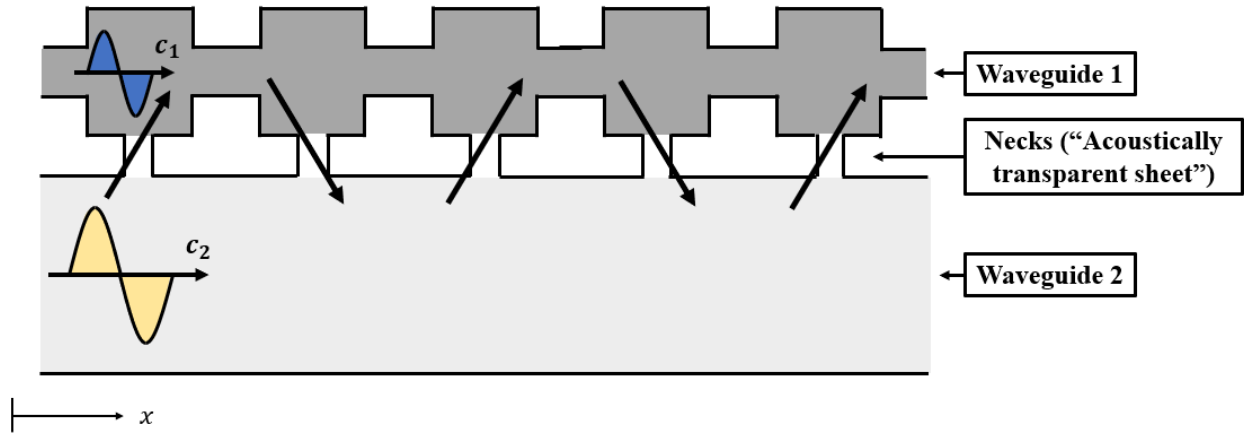


Figure 21. Schematic of the Energy Transfer Between the Waves of the Duct and the Chain of Resonator Cavities

The normalized acoustic impedance of a liner is a measure of how well the liner will absorb sound, and is given by

$$Z = \frac{p}{\rho c(\mathbf{u} \cdot \mathbf{n})} = R + jX \quad (16)$$

where Z is the impedance of the liner at a point of interest normalized by the characteristic impedance of air (i.e., ρc), p is the acoustic pressure at that point, ρ and c are the density and speed of sound of air respectively, \mathbf{u} and \mathbf{n} are the acoustic particle velocity vector and unit normal vector into the liner respectively, and R and X are the real and imaginary components of the impedance referred to as the acoustic resistance and reactance respectively [11]. Because the waves traveling through the coupled-resonator waveguide are going to be in phase with the waves traveling through the main duct at some points along the axis of the interface, and at other points, they are going to be out of phase, that means that the waves will interfere constructively at some points and destructively at others; constructive interference will result in an increased

pressure at that location while destructive interference will result in decreased pressure. If the pressure then varies along the acoustically transparent sheet, then the impedance will vary as well because impedance is proportional to the pressure (as shown in Equation (16)); hence, this new design shifts the focus from the conventional, local-reacting liner to an extended-reacting, connected-HR liner with spatially varying acoustic impedance (see Figure 22). Note that extended-reacting liners are not traditionally characterized by impedance since impedance is formally defined as a local-reacting quantity but will be done so herein for comparison purposes [11].

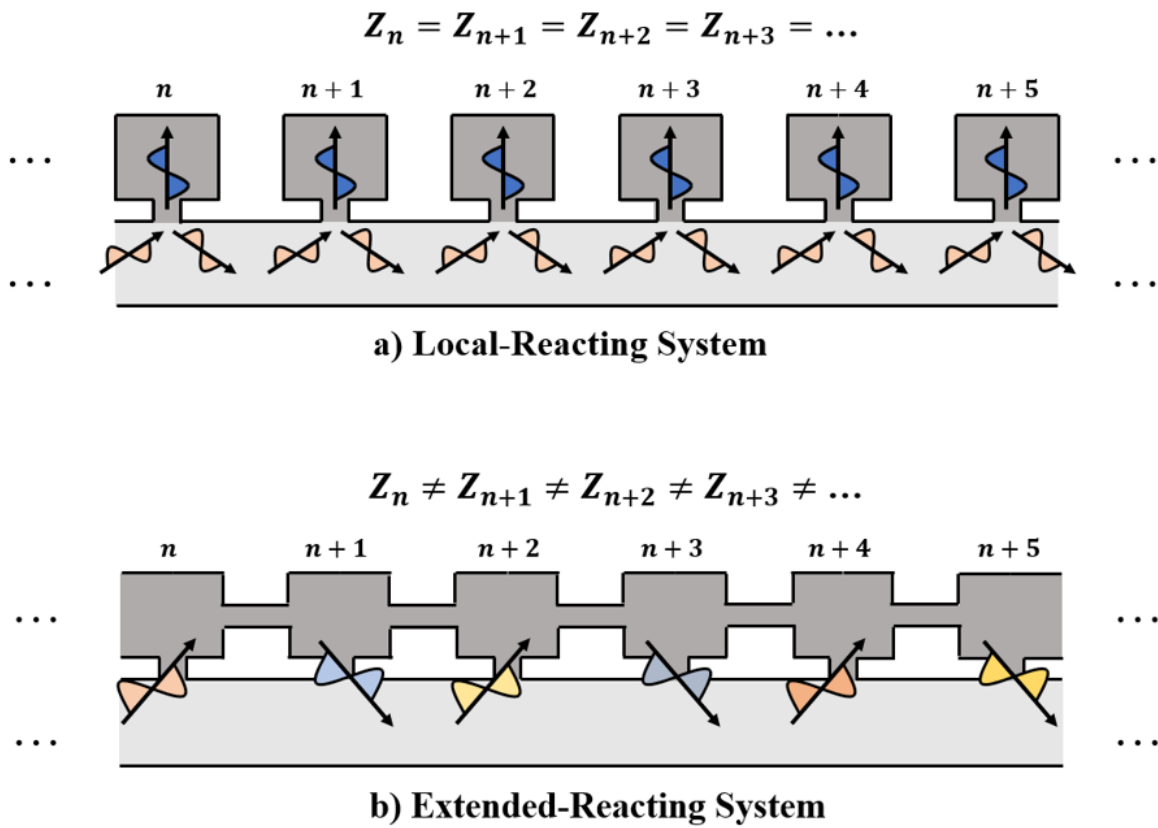


Figure 22. Schematic of a) Unconnected HRs Acting as a Local-Reacting System b) Connected HRs Acting as an Extended-Reacting System

The mathematical formulation for this connected system will again rely on the combination of the transfer-matrix method and Bloch wave theory. The steps taken to arrive at the final expressions are based on the work of Pachebat and Kergomard [15] who derived an expression for the transmission coefficient of a system of inhomogeneous parallel waveguides

coupled by perforations. Their analysis will be omitted here since their techniques will be shown in great detail throughout the subsequent analytical modelling sections of this work.

1.4. Introduction to acoustic metamaterials

Acoustic metamaterials is a relatively new field of study; only in more recent decades has the field of acoustics caught on to the advantages that metamaterial technology possesses. An acoustic metamaterial (AMM) is a system where sound waves propagate through periodically arranged acoustic impedance discontinuities located in a matrix [38]. Just like with crystalline solids, acoustic metamaterials used for noise absorption usually employ locally resonant devices arranged in a periodic lattice. While acoustic impedance discontinuities certainly modify the propagation of acoustic waves in a medium, *periodically* arranging these discontinuities can induce Bloch waves that exhibit Bragg reflection. Like in crystal lattices, these acoustic metamaterial systems behave like a band-stop filter such that alternating bands of acoustic energy propagation and energy attenuation occur. Just like in quantum physics, these alternating bands are known as pass-bands and stop-bands and can be visualized using dispersion curves. In the case of stop-bands, the energy is blocked due to either the local resonances, or the destructive interference between the incident waves and the waves that were reflected from the periodic discontinuities. By creating stop bands of attenuation via periodically spaced discontinuities, metamaterials offer advantages not possible with traditional absorptive materials.

AMM as it is known today can be broken up into two major categories: phononic crystals and sonic crystals. Phononic crystals feature periodically-arranged elastic, solid media while sonic crystals feature alternating periodic media in which at least one material is a fluid or gas. One of the earliest works in phononic crystals was with a composite of lead spheres coated with silicone rubber embedded in a hard epoxy matrix (see Figure 23) that resulted in low frequency bands in which sound transmission through the structure was minimized [39]. Local resonances were induced by the lead spheres within the elastic silicone rubber shells. For the first local resonant mode, the lead sphere was found to move with a maximum displacement inside the rubber, and for the second resonant mode, the displacement of the rubber was maximized while the displacement of the lead was minimized. Hirsekorn [40] presented similar findings using simulation tools to predict the response of silicone rubber coated hollow steel cylinders in an epoxy matrix. Fuller and Saux [38] sought to improve the low-frequency sound absorbing

performance of poro-elastic foams by embedding a periodic arrangement of multiple small masses into a poro-elastic matrix material. Slagle [41] combined this concept with the inclusion of interstitial microperforated panels as well as an active control method that adjusts the dynamics of the embedded masses.

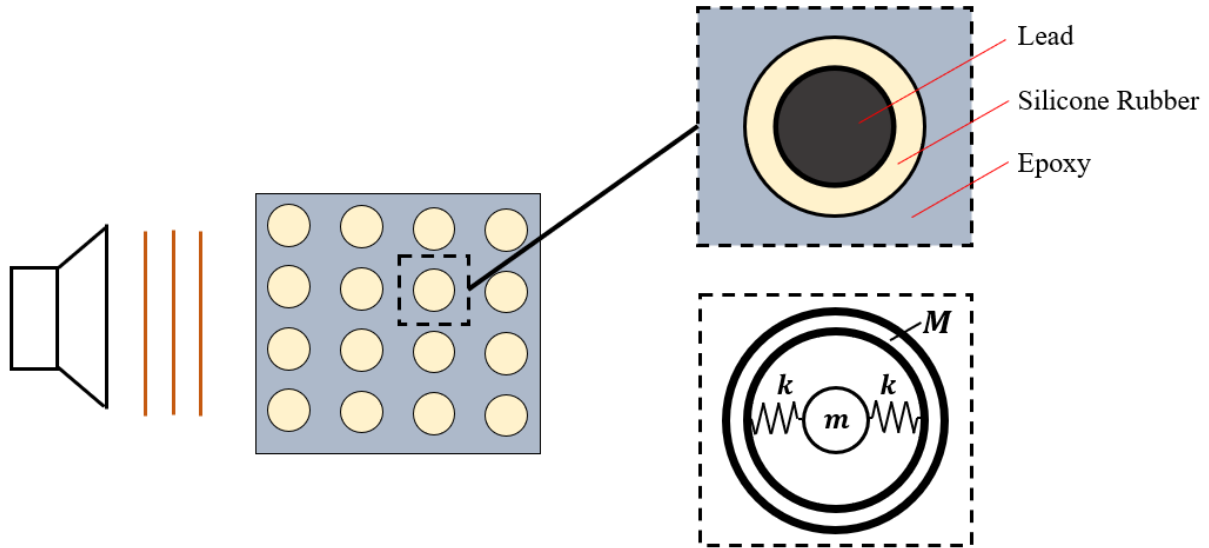


Figure 23. Sketch of Phononic Crystals Concept Proposed by Liu (not to scale) [39] and the Equivalent Mass-Spring System

One of the earliest works in sonic crystals was on a periodic array of rigid cylinders in air (see Figure 24a) [42]. The cylinders were oriented with a specific periodic distribution so as to refract the incident sound waves similar to refractive devices used in optics. They speculated that this metamaterial concept could be used to create an acoustic lens that refracts sound towards a focal point much like an optical lens. Hu et al. [43] analyzed a modified concept based on the same idea but featured split tubes instead of solid cylinders (see Figure 24b). The split tubes act as Helmholtz resonators where the hollow cylinder acts as the air cavity and the slit acts as the neck. Comparing acoustic lens configurations between the split-tube cylinders and solid cylinders, they found that the split-tube configuration yielded a higher intensity at the focal point of the lens. A dispersion plot was generated by imposing Bloch periodic boundary conditions on their finite difference simulations. Two stop bands were found, one resulting from Bragg reflection and another from the Helmholtz resonators. Torrent et al. [44] performed similar work using wooden rods arranged in a circular-shaped cluster, and later, Torrent and Sánchez-Dehesa [45] proposed a square-shaped cluster with the radii of the cylinders varying in the direction perpendicular to the lens axis.

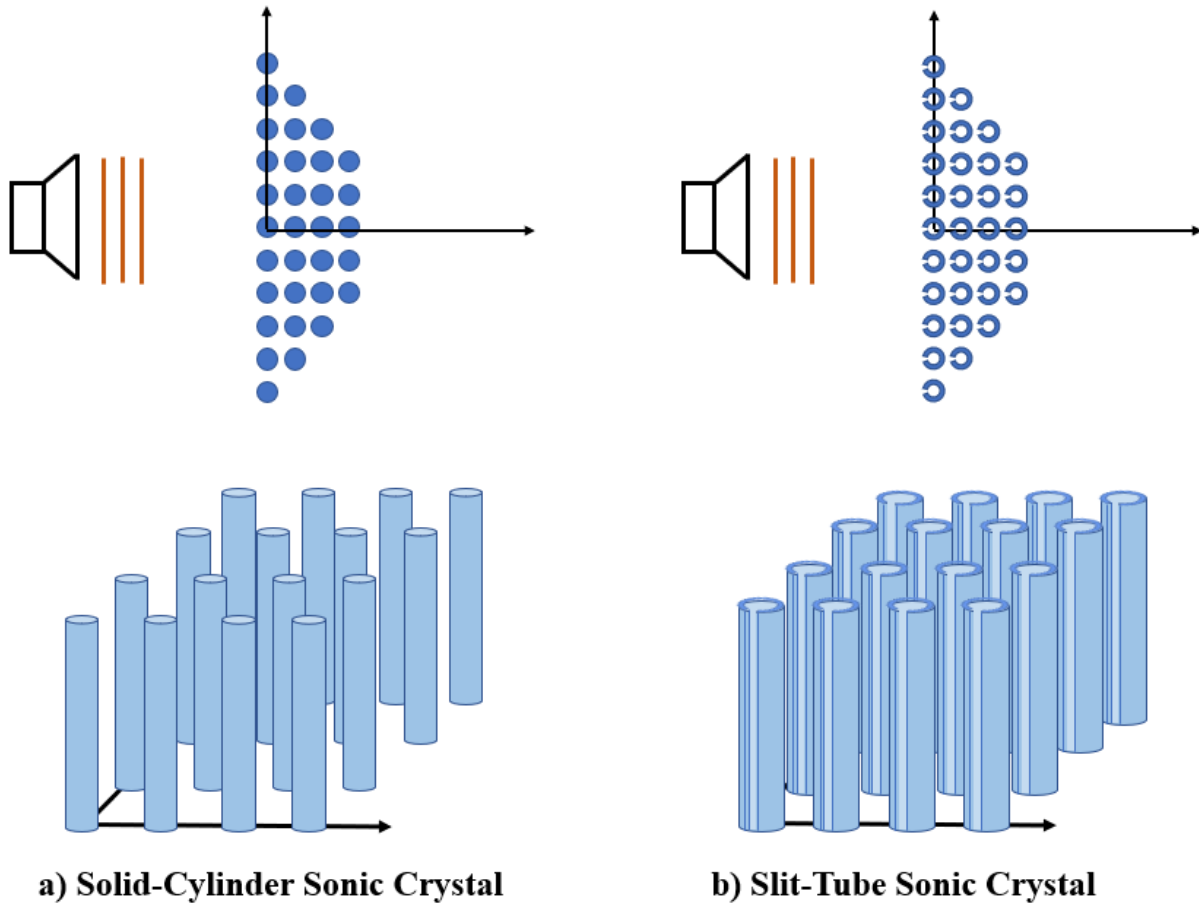


Figure 24. Sketch of the Top View and Isometric View of a) Solid-Cylinder Sonic Crystal and b) Slit-Tube Sonic Crystal

Fang et al. [46] used Bloch wave theory to calculate the performance of an array of Helmholtz resonators lining an aluminum duct immersed in water. The predicted ultrasonic frequency attenuation was verified with experimental results. Yang et al. [47] paved the way for membrane-type metamaterials. Their design featured locally resonant circular elastic membranes fixed to the inner walls of a tube. Sound transmission occurred at the resonant frequencies of the membranes, but the sound transmission was canceled between the two because of the superposition of the modes in that region. Masses were added to the center of the membrane to tune its vibrational modes. Baz et al. [48] would later extend this idea by creating an array of active membranes using piezoelectric materials.

Cummer and Schurig [49] first predicted via numerical simulations that an acoustic cloak is possible in two-dimensional space using metamaterial technology. An acoustic cloak is essentially a shell placed around an object that prevents the object from scattering incident sound

waves. An observer standing on the other side of the cloaked object would essentially hear the sound as if the object was not there. Chen and Chan [50] demonstrated that acoustic cloaking is in fact possible to be achieved in three-dimensional space as well. Cummer et al. [51] would also go on to verify these findings in three-dimensional space using an alternate mathematical approach. Farhat et al. [52] were the first to realize such a device experimentally. They constructed a metamaterial acoustic cloak by machining 100 total sectors out of an approximately 1-1/2-in. I.D. x 4-in. O.D. solid metal ring, and experimentally demonstrated that their design decreased backscattering of surface waves off a rigid cylinder in a low-viscosity and finite-density fluid. Their numerical simulations indicated that the forward scattering of the surface waves would also diminish, however they were unable to verify these predictions experimentally due to the limitations of their experimental setup. Popa et al. [53] would also go on to build an acoustic cloak using periodic layers of stacked perforated plastic plates.

AMM may provide a better option for noise cancellation in certain aerospace applications. These structures allow for sound wave manipulation that is not possible in more traditional structures, and thus the opportunity for quieter aircraft engines.

1.5. Objectives

With the advent of high-powered computational software capable of numerical modeling of complex systems, an increasing reliance on its technology has emerged. While a powerful tool, without a foundational understanding of the underlying physics of these complex systems, the creation of novel design solutions becomes more of a guess-and-check process rather than a conscious and intentional manipulation of parameters. The main focus of this research is therefore on the physics behind the acoustic metamaterial liner configurations presented herein. For this work, numerical modelling is only really used to verify the analytical modelling. With that in mind, the overall objectives, are then to study the mechanics of AMM liner configurations through analytical modeling, to verify the accuracy of the analytical modeling through reliable numerical modeling, to validate the predicted results through experimental testing, and to explore how to implement this technology in aircraft engines inlets.

The experimental testing is performed in a grazing incidence impedance tube at the Center for Aerospace Acoustics within the National Institute of Aerospace (NIA). The main

acoustic performance metric of interest is the transmission loss across the duct. The transmission loss quantifies the amount of acoustic energy that is attenuated by the material. The formula for the transmission loss in dB is given by

$$TL = 20 \log_{10} \left| \frac{P_{in}^+}{P_{out}^+} \right| \quad (17)$$

where P_{in}^+ and P_{out}^+ are the pressure coefficients of the forward traveling wave at the inlet and outlet of a duct lined with a liner sample (see Figure 25) [12].

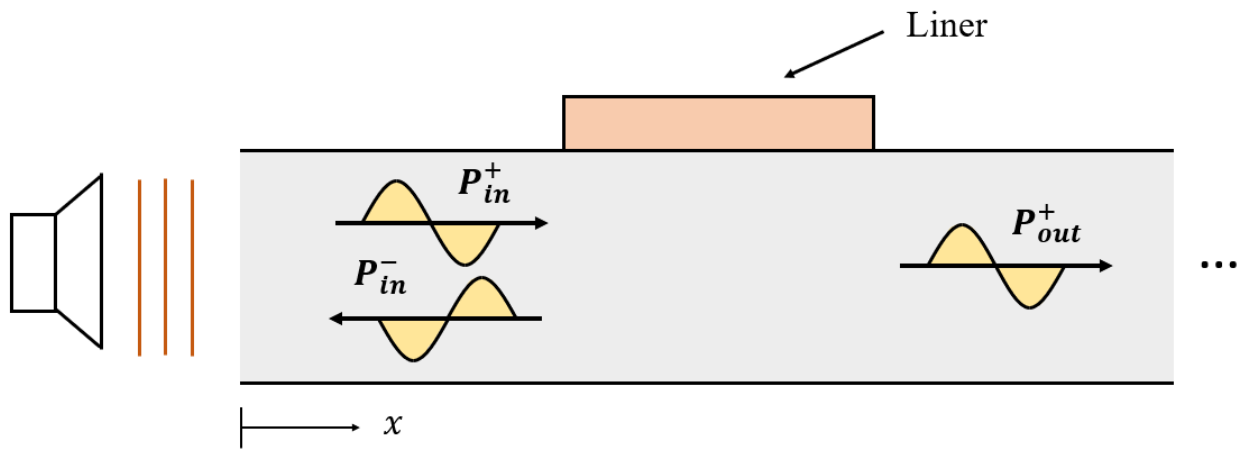


Figure 25. Schematic of Incident, Reflected, and Transmitted Waves in a Duct with a Liner Sample

Using AMM principles, the transmission loss can be increased at specific frequencies of interest that are unattainable with conventional liner technology. The AMM liner will be designed by connecting Helmholtz resonators together along their cavities with coupling tubes. A parameter study of this AMM liner design is performed by analyzing the effects of the resonator and coupling tube geometry as well as the number of resonators. The ultimate effort of this thesis is to uncover the physics behind this AMM design and suggest improved practical aircraft inlet liner designs.

1.6. Outline

Chapter 1 introduces the traditional approaches to aircraft engine acoustic attenuation along with a basic overview of acoustic metamaterials and the underlying physics of metamaterials. A spatially varying impedance liner concept consisting of connected Helmholtz resonator cavities is presented and the objectives of this research are listed.

Chapter 2 investigates the detailed analytical and numerical modeling of an array of Helmholtz resonators within the perspective of AMM. The transfer matrix method and Bloch wave theory are introduced and implemented on the geometry to find the transmission loss and propagation constants across a finite and infinite system. The analytical results are compared with the numerical results in order to verify the accuracy of the analytical modeling approach.

Chapter 3 investigates the detailed analytical and numerical modeling of an array of connected Helmholtz resonator cavities using transfer matrix method and Bloch wave theory. The propagation constants and transmission loss of the system are determined for both a finite and infinite system. A parameter study is conducted to identify how varying the components of the system varies the transmission loss characteristics. The analytical results are compared with the numerical results in order to verify the accuracy of the analytical modeling approach.

Chapter 4 provides the results of the experimental testing and validation. Both an unconnected array of Helmholtz resonators and a connected array of Helmholtz resonators are tested on the in-house impedance tube and the transmission loss across each system are determined experimentally. The results are compared with the results of the analytical modeling in order to validate the predicted trends.

Chapter 5 provides the major conclusions of the research work and offers insight on potential future work.

2. ARRAY OF HELMHOLTZ RESONATORS

This chapter describes the analytical and numerical modeling of a periodic array of Helmholtz resonators developed and studied as part of this thesis. The analytical modeling of sound propagation through a duct lined with periodically spaced Helmholtz resonators is presented for both a finite system and an infinite system. A numerical model using Actran is constructed, and the theoretical and numerical results are compared. The goal of the analytical study is to learn how the spacing of the resonators impacts the results of the transmission loss with hopes of achieving greater transmission loss across wider ranges of frequencies with a particular focus on attenuating lower frequencies.

For this analysis, the system will be under time harmonic excitation at the upstream end of the duct. Only frequencies below the first duct mode will be considered, meaning only plane waves will exist in the duct. In a rigid-walled rectangular waveguide, only plane waves will propagate if the frequency is given by

$$f < \frac{c}{2a} \quad (18)$$

where c is the speed of sound and a is the maximum dimension of the cross-section of the duct [12]. As such, the analysis will assume lumped parameters. Neither damping nor flow will be included, and the duct walls will be considered perfectly rigid. In the finite model, the ends of the duct will be considered anechoic, meaning that no sound will reflect off those surfaces.

2.1. Analytical modeling of an infinite array of Helmholtz resonators

The purpose of developing this analytical model is to learn how the spacing of the resonators affects the stop band behavior of the system. This model will use a transfer matrix approach [14] and Bloch wave theory [31] to determine the transmission loss of an infinite duct loaded with an infinite number of periodically-spaced Helmholtz resonators (see Figure 26).

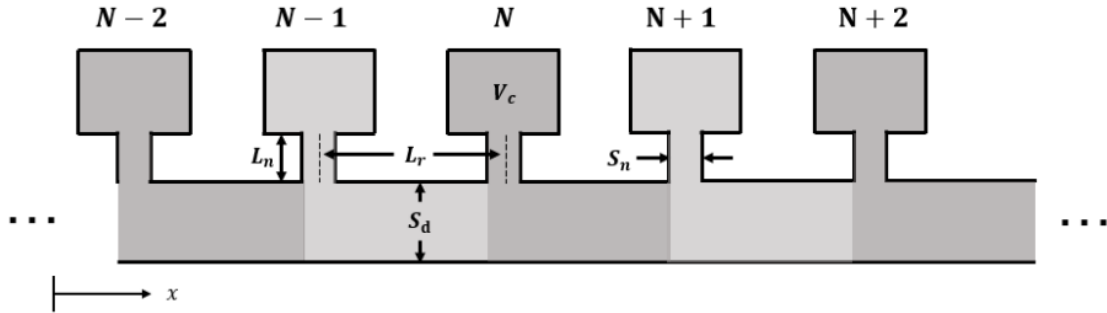


Figure 26: Infinite Array of Helmholtz Resonators Schematic

In this type of analysis, the first step is to specify a unit cell. For periodic systems, the unit cell is the geometry that repeats across the entire domain at the same spacing. In this system of unconnected Helmholtz resonators, a single unit cell consists of a portion of the duct treated with a Helmholtz resonator followed by an untreated portion of the duct between resonators. This unit cell definition is illustrated in Figure 26 where each unit cell is highlighted in alternate shades of gray. Because the unit cell repeats without interruption, the periodic lattice is now defined, and now a transfer matrix across the unit cell needs to be found.

A single transfer matrix across this unit cell is not immediately obvious, so the unit cell will need to be split into two subsections; the transfer matrix across the unit cell for this system will then be the product of two transfer matrices, one for each subsection. The first subsection transfer matrix will be for the portion of the duct that is treated with the Helmholtz resonator (see Figure 27), and the second subsection transfer matrix will be for the portion of the duct that is untreated between resonators (see Figure 29).

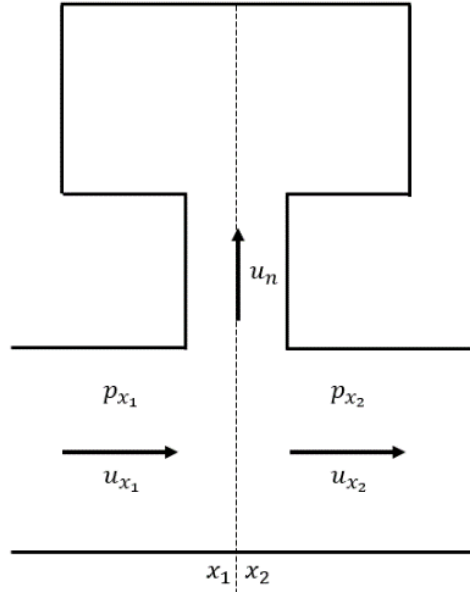


Figure 27. First Subsection of the Unit Cell used to Write the Transfer Matrix Across a Portion of the Duct Treated with a Resonator

The transfer matrix across the first subsection of the unit cell is for a portion of the duct that is treated with a resonator. This transfer matrix is found by identifying the state variable relationship on either side of the resonator x_1 and x_2 [14]. Because lumped parameters are assumed, a simplifying assumption is made that the impedance along the duct changes abruptly at the midline of the resonator, rather than gradually. Because of continuity of pressure and volume velocity at the x_1, x_2 interface, the following boundary conditions can be written:

$$\begin{aligned}
 p_{x_1} &= p_{x_2} = p_n \\
 u_{x_1} &= u_{x_2} + u_n \\
 \frac{p_n}{u_n} &= Z_r
 \end{aligned} \tag{19}$$

where p is the acoustic pressure in the duct, u is the acoustic volume velocity in the duct, Z_r is the acoustic impedance of the Helmholtz resonator. In lumped parameter analysis, a Helmholtz resonator can be treated as a mass attached to a spring where the mass represents the neck and the spring represents the cavity (see Figure 28) [12]. The impedance of such a system is given by

$$Z_r = j \frac{\omega \rho (L_n + \Delta L_n)}{S_n} - j \frac{\rho c^2}{\omega V_c} \tag{20}$$

where ω is the angular frequency, ρ is the air density, L_n is the neck length, ΔL_n is the end correction for the neck, c is the speed of sound in air, S_n is the cross-sectional area of the resonator neck, and V_c is the volume of the cavity [12].

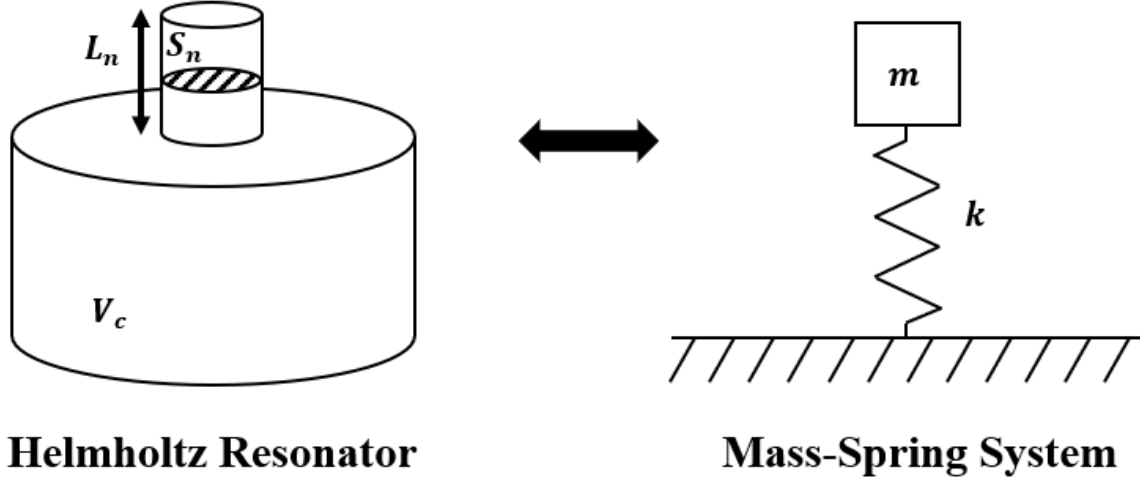


Figure 28. Schematic of a Helmholtz Resonator Represented as a Mass-Spring System

Rearranging the relationships in Equation (19) into transfer matrix form gives

$$\begin{bmatrix} p_{x_2} \\ u_{x_2} \end{bmatrix} = \mathbf{T}_r \begin{bmatrix} p_{x_1} \\ u_{x_1} \end{bmatrix} = \begin{bmatrix} 1 & 0 \\ -1/Z_r & 1 \end{bmatrix} \begin{bmatrix} p_{x_1} \\ u_{x_1} \end{bmatrix} \quad (21)$$

where \mathbf{T}_r is the transfer matrix of the portion of the unit cell where the duct is lined with a Helmholtz resonator. Note that henceforth, capital bold letters such as \mathbf{T}_r will refer to 2nd-order matrices. The next transfer matrix required for the complete description of a unit cell is the transfer matrix relating the point just downstream of the resonator to the point just upstream of the next resonator (see Figure 29).

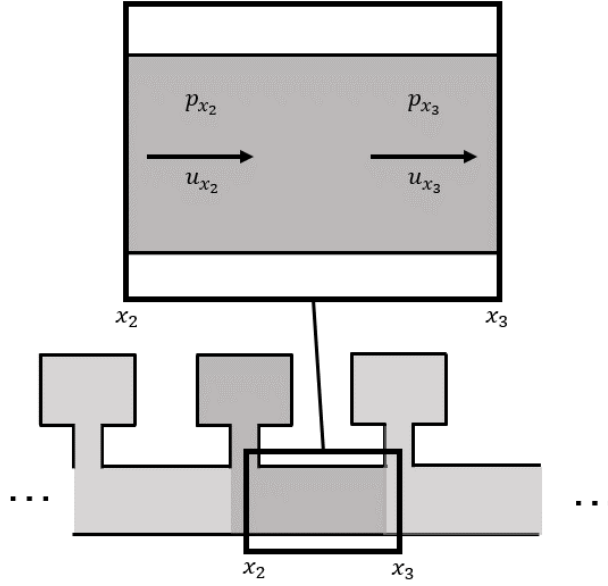


Figure 29. Second Subsection of the Unit Cell used to Write the Transfer Matrix Across the Duct Between Resonators

The transfer matrix across a portion of the duct between resonators is classical [15] and is given by

$$\begin{bmatrix} p_{x_3} \\ u_{x_3} \end{bmatrix} = \mathbf{T}_d \begin{bmatrix} p_{x_2} \\ u_{x_2} \end{bmatrix} = \begin{bmatrix} \cos(kL_r) & -jZ_d \sin(kL_r) \\ -j \frac{\sin(kL_r)}{Z_d} & \cos(kL_r) \end{bmatrix} \begin{bmatrix} p_{x_2} \\ u_{x_2} \end{bmatrix} \quad (22)$$

where k is the acoustic wavenumber, L_r is the distance between resonators, and Z_d is the acoustic impedance of the duct given by

$$Z_d = \frac{\rho c}{S_d} \quad (23)$$

where S_d is the cross-sectional area of the duct [12].

The transfer matrix for the unit cell of a duct loaded with a periodic array of Helmholtz resonators as defined in Figure 26 is thus the product of these two transfer matrices which can be written as

$$\begin{bmatrix} p_{n+1} \\ u_{n+1} \end{bmatrix} = \mathbf{T}_d \mathbf{T}_r \begin{bmatrix} p_n \\ u_n \end{bmatrix} = \mathbf{T}_{cell} \begin{bmatrix} p_n \\ u_n \end{bmatrix} \quad (24)$$

where \mathbf{T}_{cell} is the unit cell transfer matrix, and n and $n + 1$ represent the arbitrary beginning and end x -locations of the unit cell respectively. Now that the transfer matrix for the unit cell is known, the next step is to use this transfer matrix to describe a system of infinite cells.

Recall that according to Bloch wave theory [31], a dynamic periodic system can be described in terms of a single periodic function:

$$f(x + L) = e^{\Gamma} f(x) \quad (25)$$

where Γ is known as the propagation constant. Using this form, Equation (24) can be rewritten as

$$\begin{bmatrix} p_{n+1} \\ u_{n+1} \end{bmatrix} = e^{\Gamma} \begin{bmatrix} p_n \\ u_n \end{bmatrix} \quad (26)$$

The propagation constant can be solved by recognizing that Equations (24) and (26) together form the classical eigenvalue problem, $\mathbf{A}\mathbf{v} = \lambda\mathbf{v}$, as follows:

$$\mathbf{T}_{cell} \begin{bmatrix} v_1 \\ v_2 \end{bmatrix} = e^{\Gamma} \begin{bmatrix} v_1 \\ v_2 \end{bmatrix} \quad (27)$$

where e^{Γ} is the eigenvalue λ of the unit cell transfer matrix, and $\mathbf{v} = \begin{bmatrix} v_1 \\ v_2 \end{bmatrix}$ is the eigenvector of the unit cell transfer matrix [16]. The eigenvector \mathbf{v} represents the linear combination of pressure and velocity states throughout the duct, while the eigenvalue e^{Γ} contains the propagation constant Γ that describes the changes in phase and amplitude between cells. Together, they describe the vibrational modes of the lattice operating in a Bloch state [31]. Since this matrix is 2nd-order, there will be two eigenvectors, two corresponding eigenvalues, and thus two propagation constants describing two Bloch waves. For this system, these two propagation constants turn out to be equal in magnitude but opposite in sign. Recall from a previous section that the sign of the propagation constant determines the direction that the Bloch wave is traveling. This result means that the two Bloch waves generated by this system are identical but propagate in opposite directions. Based on the coordinate system specified in Figure 26, a negative propagation constant corresponds to a forward-traveling Bloch wave whereas a positive propagation constant corresponds to a backward-traveling Bloch wave. Since the propagation

constant carries all the information that relates the phase and amplitude changes between cells, they are all that are needed to describe the infinite system. Since the propagation constants come from the eigenvalues, the next step is to find the eigenvalues of the unit cell transfer matrix \mathbf{T}_{cell} .

To find the eigenvalues, the eigenequation $\mathbf{T}_{cell}\mathbf{v} = \lambda\mathbf{v}$ first needs to be rearranged into

$$(\mathbf{T}_{cell} - \lambda\mathbf{I})\mathbf{v} = \mathbf{0} \quad (28)$$

where $\mathbf{I} = \begin{bmatrix} 1 & 0 \\ 0 & 1 \end{bmatrix}$ is the 2nd-order identity matrix and $\mathbf{0} = \begin{bmatrix} 0 \\ 0 \end{bmatrix}$ [16]. The eigenvalues are the solution to the dispersion equation [15] given by

$$\det(\mathbf{T}_{cell} - \lambda\mathbf{I}) = 0 \quad (29)$$

To make this make this calculation simpler, let

$$\begin{aligned} \mathbf{T}_{cell} &= \mathbf{T}_d\mathbf{T}_r \\ \mathbf{T}_d &= \begin{bmatrix} A & B \\ C & A \end{bmatrix} \end{aligned} \quad (30)$$

where $A = \cos(kL_r)$, $B = -jZ_d \sin(kL_r)$, $C = -j \sin(kL_r)/Z_d$ as shown before. The eigenvalues are thus

$$\lambda_{1,2} = \frac{2AZ_r - B \pm \sqrt{4BCZ_r^2 - 4ABZ_r + B^2}}{2Z_r} \quad (31)$$

The propagation constants are then simply

$$\Gamma_{1,2} = \ln(\lambda_{1,2}) \quad (32)$$

These propagation constants can now be studied in the form of a dispersion plot (see Figure 30) to understand the stop-band behavior of the system. Recall from a previous section that dispersion plots, when used in vibrations and acoustics, are a way to visualize the relationship between the propagation constant Γ and frequency f [34]. The resonator size and spacing was selected such that distinct stop-band behavior could be predicted and eventually validated experimentally.

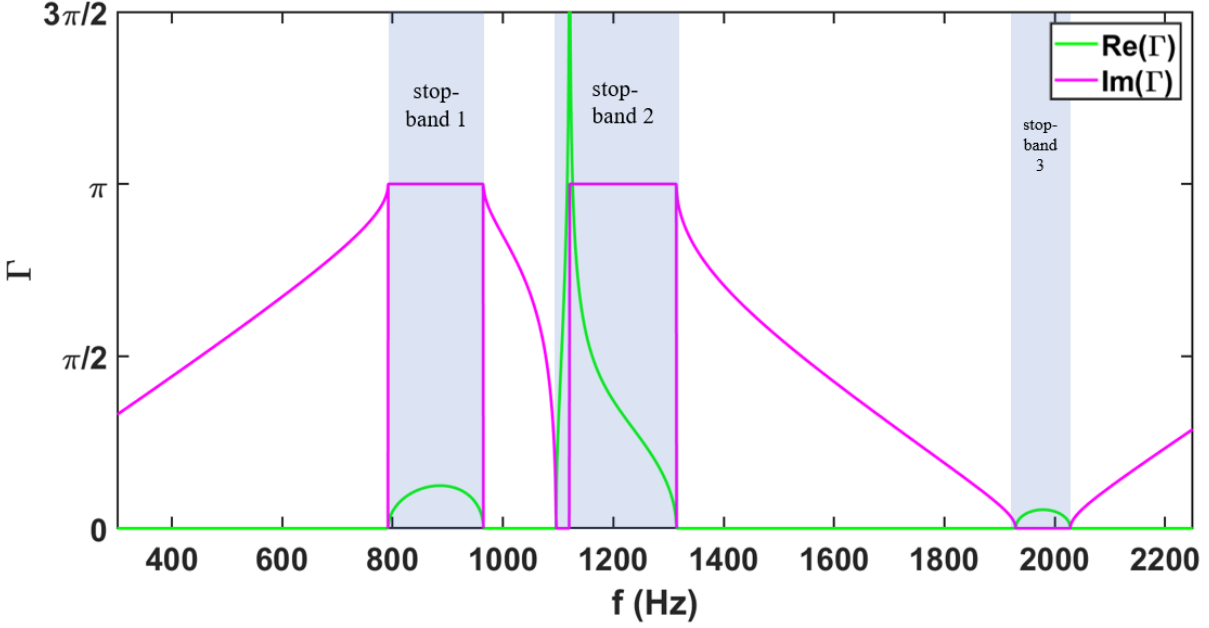


Figure 30. Dispersion Plot for Infinite Array of Helmholtz Resonators

$$L_r = 7 \text{ in}, L_n = 0.25 \text{ in}, \Delta L_n = 0.67 \text{ in}, S_n = 1.77 \text{ in}^2, S_d = 9 \text{ in}^2, V_c = 7 \text{ in}^3$$

Because the two propagation constants have the same magnitude but with opposite signs for opposite directions of propagation, only the positive propagation constants are shown in the plot to avoid redundancy. Notice that for the frequency bands highlighted in blue, the phase constant (i.e., the imaginary component of the propagation constant) is 0 or π ; recall from a previous section that a forward-traveling Bloch wavefunction is given by

$$\Psi_{Bloch} = e^{-\Gamma} u(x) = e^{-(\Gamma_r + i\Gamma_i)} u(x) \quad (33)$$

where $u(x) = u(x + L_r)$ is a periodic function describing the identical motion occurring in each individual cell, which is modulated by the exponentially-decaying plane wave envelope across the cells $e^{-\Gamma}$. If the phase constant Γ_i is 0 or a multiple of π , the $e^{-i\Gamma_i}$ term becomes unity meaning there is no phase change from cell to cell, and the Bloch wave simply does not propagate. The attenuation constant Γ_r is non-zero in these blue highlighted regions, which indicates that the sound gets attenuated from cell to cell. These frequency bands highlighted in blue are thus stop-bands of the system.

These stop-bands arise physically because of the Helmholtz resonance and Bragg reflection within the duct. According to the formula for the resonant frequency of a Helmholtz resonator [12],

$$f_{HR} = \frac{c}{2\pi} \sqrt{\frac{S_n}{V_c(L_n + \Delta L_n)}} \quad (34)$$

the resonant frequency for this geometry should be 1120 Hz, which is in the range of stop-band 2 on the dispersion plot. Recall from a previous section that Bragg reflection [23] occurs when the periodic discontinuities of a lattice are spaced a multiple of a half of a wavelength such that

$$f_{Bragg} = m \frac{c}{2L_r}, (m = 1, 2, \dots) \quad (35)$$

Given that the resonators are periodically spaced at a distance $L_r = 7 \text{ in}$, the stop-bands should thus occur at 960 Hz and 1930 Hz which fall just within the stop-band ranges in the dispersion plot (see Figure 31).

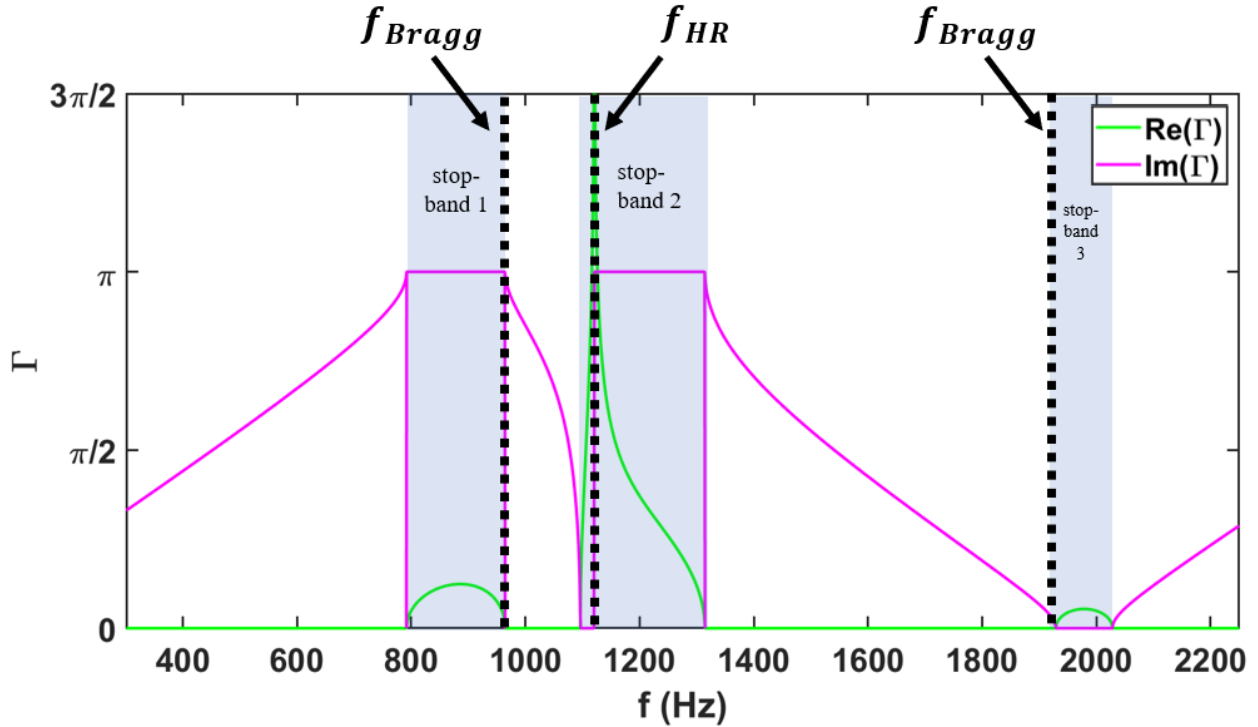


Figure 31. Dispersion Plot for Infinite Array of Helmholtz Resonators with Bragg and HR Frequencies Shown

Notice that the Bragg reflection frequency in this case is lower than the resonant frequency of the Helmholtz resonator. This observation highlights the advantages of altering the resonator spacing – that frequencies lower than the resonant frequency of the Helmholtz resonator can be attenuated via Bragg reflection. As the attenuation of lower frequencies is paramount in aerospace applications, this idea of increasing the spacing between resonators proves to be quite useful. Understanding these physics principles helps to more intelligently manipulate the geometry of the system to achieve the desired stop-band characteristics for the application. The results of a parameter study will later be discussed to verify and explore these stop-band physics principles. Now that an infinite model has been developed, the next step is to develop a more practical, finite model.

2.2. Analytical modeling of a finite array of Helmholtz resonators

The purpose of this analytical study is to understand how an array of Helmholtz resonators affects the transmission loss in a finite (and hence more practical) system (see Figure 32). Introducing this parameter into the analytical model can thus be used to more accurately reflect aerospace applications in which limited space is available like in the aircraft engine inlet.

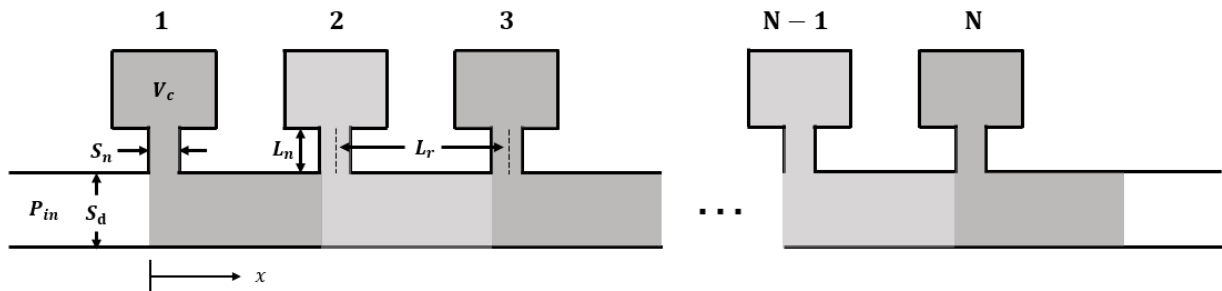


Figure 32. Finite Array of Helmholtz Resonators

Now that the transfer matrix across a single cell is written (as seen in the previous section), a relationship between the beginning and end states of a finite array of N resonators can be expressed. Since the cells are all identical, the transfer matrix across an entire duct loaded with N resonators can be written as

$$\begin{bmatrix} p_N \\ u_N \end{bmatrix} = \mathbf{T}_{cell}^N \begin{bmatrix} p_1 \\ u_1 \end{bmatrix} \quad (36)$$

While this transfer matrix exponentiation method is viable, this method becomes less practical for large N . Rather than having to perform matrix multiplication N times to obtain the result, a more accurate and less computationally expensive method is to diagonalize the matrix. A diagonal matrix raised to a power simply raises the scalar terms along the diagonal to that power, which is a much simpler calculation than repetitive matrix multiplication. A matrix can be diagonalized by writing it in the form

$$\mathbf{A} = \mathbf{V}\mathbf{D}\mathbf{V}^{-1} = \mathbf{V} \begin{bmatrix} \lambda_1 & 0 \\ 0 & \lambda_2 \end{bmatrix} \mathbf{V}^{-1} \quad (37)$$

where \mathbf{V} is the matrix of eigenvectors of \mathbf{A} and \mathbf{D} is a matrix of the corresponding eigenvalues of \mathbf{A} arranged along the diagonal. Instead of exponentiating the original matrix, the terms along the diagonalized matrix can be exponentiated instead thereby reaching the same result with less computational difficulty:

$$\mathbf{A}^N = \mathbf{V}\mathbf{D}^N\mathbf{V}^{-1} = \mathbf{V} \begin{bmatrix} \lambda_1^N & 0 \\ 0 & \lambda_2^N \end{bmatrix} \mathbf{V}^{-1} \quad (38)$$

Because of the implementation of Bloch wave theory for the development of the infinite model, the eigenvalues have already been determined. The eigenvalues and eigenvectors in the finite array are no different, seeing as though the unit cell has not changed. The eigenvalues and eigenvectors for a unit cell can be used for eigendecomposition in the following way:

$$\begin{bmatrix} p_N \\ u_N \end{bmatrix} = \mathbf{V}\mathbf{D}^N\mathbf{V}^{-1} \begin{bmatrix} p_1 \\ u_1 \end{bmatrix} \quad (39)$$

where \mathbf{V} is the matrix of eigenvectors for the unit cell that correspond to the eigenvalues along the diagonal of \mathbf{D} . The eigenvalues were solved in the previous section, now the eigenvectors must be found. If we let $\mathbf{T}_0 = (\mathbf{T}_{cell} - \lambda\mathbf{I})$, then Equation (28) becomes

$$\begin{aligned} \mathbf{T}_0 \mathbf{v} &= \mathbf{0} \\ \mathbf{T}_0 &= \begin{bmatrix} A_0 & B_0 \\ C_0 & D_0 \end{bmatrix} \end{aligned} \quad (40)$$

and because $\det(\mathbf{T}_0) = 0$ as shown in the previous section, $A_0D_0 = B_0C_0$. Thus, the eigenvectors can be written in the following general form:

$$\begin{aligned} \mathbf{v} &= a_0 \begin{bmatrix} v_0 \\ -1 \end{bmatrix} \\ v_0 &= \frac{B_0}{A_0} = \frac{D_0}{C_0} \end{aligned} \quad (41)$$

where a_0 is just an arbitrary constant scalar multiplier. The eigenvector matrix \mathbf{V} can now be formed:

$$\mathbf{V} = \begin{bmatrix} v_0^{(1)} & v_0^{(2)} \\ -1 & -1 \end{bmatrix} \quad (42)$$

where the two $v_0^{(1,2)}$ correspond to the two eigenvalues $\lambda_{1,2}$. The eigendecomposition of the system is then given as

$$\begin{bmatrix} p_N \\ u_N \end{bmatrix} = \begin{bmatrix} v_0^{(1)} & v_0^{(2)} \\ -1 & -1 \end{bmatrix} \begin{bmatrix} \lambda_1^N & 0 \\ 0 & \lambda_2^N \end{bmatrix} \begin{bmatrix} v_0^{(1)} & v_0^{(2)} \\ -1 & -1 \end{bmatrix}^{-1} \begin{bmatrix} p_1 \\ u_1 \end{bmatrix} \quad (43)$$

Recall from Equation (32) that the propagation constants are related to the eigenvalues by $\Gamma_{1,2} = \ln(\lambda_{1,2})$. Since the propagation constants are equal in magnitude and opposite in sign (i.e., $\Gamma_1 = -\Gamma_2$), the numbering of the propagation constants is arbitrary, so to simplify, let $\lambda_1 = e^\Gamma$ and $\lambda_2 = e^{-\Gamma}$. Equation (43) can thus be rewritten as

$$\begin{bmatrix} p_N \\ u_N \end{bmatrix} = \begin{bmatrix} v_0^{(1)} & v_0^{(2)} \\ -1 & -1 \end{bmatrix} \begin{bmatrix} e^{N\Gamma} & 0 \\ 0 & e^{-N\Gamma} \end{bmatrix} \begin{bmatrix} v_0^{(1)} & v_0^{(2)} \\ -1 & -1 \end{bmatrix}^{-1} \begin{bmatrix} p_1 \\ u_1 \end{bmatrix} \quad (44)$$

which reduces to

$$\begin{bmatrix} p_N \\ u_N \end{bmatrix} = \frac{1}{v_0^{(1)} - v_0^{(2)}} \begin{bmatrix} e^{N\Gamma} v_0^{(1)} - e^{-N\Gamma} v_0^{(2)} & v_0^{(1)} v_0^{(2)} (e^{N\Gamma} - e^{-N\Gamma}) \\ e^{-N\Gamma} - e^{N\Gamma} & e^{-N\Gamma} v_0^{(1)} - e^{N\Gamma} v_0^{(2)} \end{bmatrix} \begin{bmatrix} p_1 \\ u_1 \end{bmatrix} \quad (45)$$

At this stage, the system is completely defined except for what occurs at the first cell and the last cell. In other words, expressions for p_1 , u_1 , p_N , and u_N are needed. The inlet of the system contains a forward traveling and backward traveling plane wave with plane wave coefficients C_{in}^+ , C_{in}^- . The outlet is treated as anechoic meaning there only exists a forward traveling wave with plane wave coefficient C_{out}^+ and no reflected waves. With these boundary conditions, Equation (45) can be written as

$$\begin{bmatrix} C_{out}^+ \\ C_{out}^- \\ Z_d \end{bmatrix} = \frac{1}{v_0^{(1)} - v_0^{(2)}} \begin{bmatrix} e^{N\Gamma} v_0^{(1)} - e^{-N\Gamma} v_0^{(2)} & v_0^{(1)} v_0^{(2)} (e^{N\Gamma} - e^{-N\Gamma}) \\ e^{-N\Gamma} - e^{N\Gamma} & e^{-N\Gamma} v_0^{(1)} - e^{N\Gamma} v_0^{(2)} \end{bmatrix} \begin{bmatrix} C_{in}^+ + C_{in}^- \\ C_{in}^+ - C_{in}^- \\ Z_d \end{bmatrix} \quad (46)$$

Keeping in mind that $C_{in}^+ + C_{in}^- = P_{in}$ where P_{in} is a known pressure input into the duct, there are now three equations and three unknowns, and the system can be solved. The three unknowns are solved to be

$$\begin{aligned} C_{in}^+ &= \frac{P_{in}}{2} \left(\frac{v_0^{(1)} v_0^{(2)} (e^{2N\Gamma} - 1) + Z_d (v_0^{(1)} + v_0^{(2)}) (e^{2N\Gamma} + 1) + Z_d^2 (1 - e^{2N\Gamma})}{v_0^{(1)} v_0^{(2)} (e^{2N\Gamma} - 1) + Z_d v_0^{(2)} e^{2N\Gamma} - Z_d v_0^{(1)}} \right) \\ C_{in}^- &= \frac{P_{in}}{2} \left(\frac{(e^{2N\Gamma} - 1)(v_0^{(1)} + Z_d)(v_0^{(2)} + Z_d)}{v_0^{(1)} v_0^{(2)} (e^{2N\Gamma} - 1) + Z_d v_0^{(2)} e^{2N\Gamma} - Z_d v_0^{(1)}} \right) \\ C_{out}^+ &= - \frac{P_{in} Z_d e^{2N\Gamma} (v_0^{(1)} - v_0^{(2)})}{v_0^{(1)} v_0^{(2)} (e^{2N\Gamma} - 1) + Z_d v_0^{(2)} e^{2N\Gamma} - Z_d v_0^{(1)}} \end{aligned} \quad (47)$$

The ratio of incident wave over the transmitted wave is thus

$$\frac{C_{in}^+}{C_{out}^+} = \cosh(N\Gamma) + \frac{\sinh(N\Gamma) (Z_d^2 - v_0^{(1)} v_0^{(2)})}{Z_d (v_0^{(1)} - v_0^{(2)})} \quad (48)$$

The transmission loss for a finite array of Helmholtz resonators $TL = 20 \log_{10} |C_{in}^+ / C_{out}^+|$ can then be written as

$$TL = 20 \log_{10} \left| \cosh(N\Gamma) + \frac{\sinh(N\Gamma) (Z_d^2 - v_0^{(1)} v_0^{(2)})}{Z_d (v_0^{(1)} - v_0^{(2)})} \right| \quad (49)$$

The transmission loss for an array of four Helmholtz resonators with the same geometry and spacing as the infinite array is plotted in Figure 33.

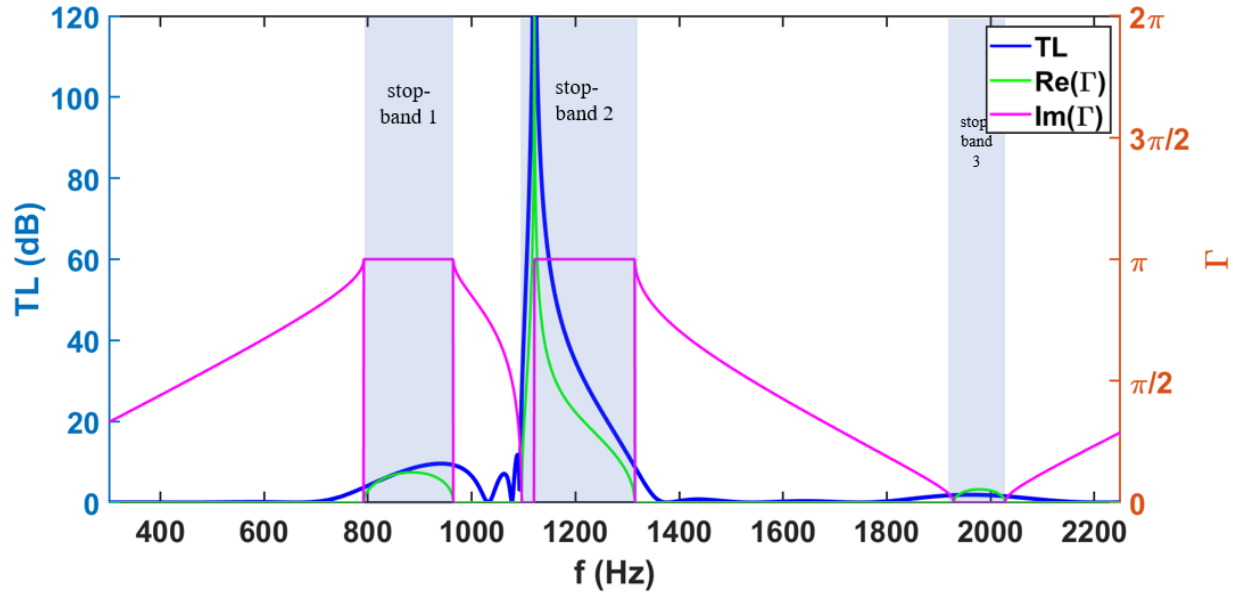


Figure 33. Transmission Loss Plot for Finite Array of Helmholtz Resonators

$$N = 4, P_{in} = 94 \text{ dB}, L_r = 7 \text{ in}, L_n = 0.25 \text{ in}, \Delta L_n = 0.67 \text{ in}, S_n = 1.77 \text{ in}^2, S_d = 9 \text{ in}^2, V_c = 7 \text{ in}^3$$

The results indicate that the transmission loss formula given in Equation (49) is accurate since the transmission loss peaks seem to line up with the stop-bands predicted from the propagation constants. This result will later be compared to the results from a numerical computation in Actran to verify that the transmission loss is in fact accurate.

Now that the transmission loss can be determined across a finite set of Helmholtz resonators, it is interesting to consider what happens as the number of resonators N increases. The transmission loss normalized by the number of resonators or TL/N can be plotted across a higher range of N and trends can be observed (see Figure 34).

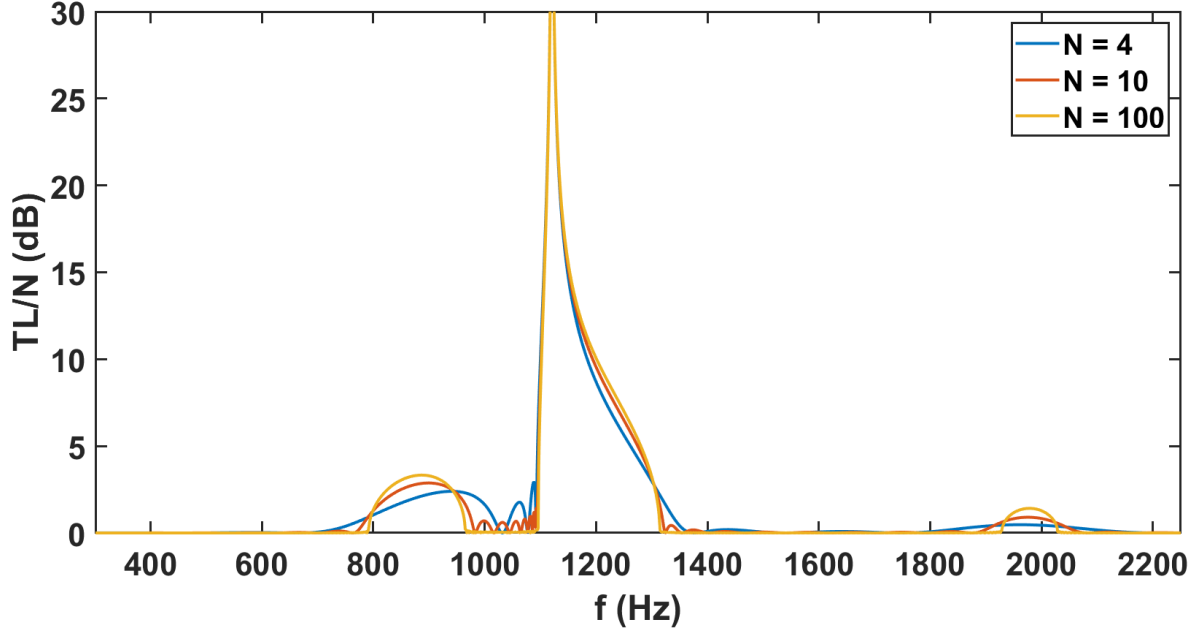


Figure 34. The Effect of Number of Resonators N on normalized transmission loss TL/N

Inferring from this plot, since the normalized transmission loss plot shape remains similar for each case, then the overall transmission loss would increase as the number of resonators increases. The similarity of the curves indicates that the number of resonators does not significantly alter the frequencies attenuated. This conclusion makes sense given that the transmission loss peaks seem to line up with the location of the stop-bands that had been determined for an infinite system. This realization suggests that as the number of resonators increases, the transmission loss plot should line up closer and closer to those attenuation constant curve from the dispersion plot.

Wang et al. [16] showed that the normalized transmission loss does in fact converge to the same shape as the attenuation constant in the dispersion plot. To show that this is true, an alternate formulation is required. By writing the transfer matrix of a cell between the pressure coefficients of the forward and backward traveling waves in the duct instead of pressure and volume velocity, the normalized transmission loss of an infinite number of resonators can be found. Writing the transfer matrix in terms of the pressure coefficients would yield a new representation

$$\begin{bmatrix} C_{n+1}^+ \\ C_{n+1}^- \end{bmatrix} = \hat{T}_{cell} \begin{bmatrix} C_n^+ \\ C_n^- \end{bmatrix} \quad (50)$$

and finding the eigenvalues and eigenvectors using a similar process as before, one could express the pressure coefficients as the combination of positive and negative traveling Bloch waves such that

$$\begin{bmatrix} C_n^+ \\ C_n^- \end{bmatrix} = a_n \mathbf{v}_1 + b_n \mathbf{v}_2 = a_n \begin{bmatrix} v_1^+ \\ v_1^- \end{bmatrix} + b_n \begin{bmatrix} v_2^+ \\ v_2^- \end{bmatrix} \quad (51)$$

where now, based on the way the state variables are defined, the combination of eigenvector components $a_n v_1^+ + b_n v_2^+$ represent a linear combination of forward traveling waves, and $a_n v_1^- + b_n v_2^-$ represent a linear combination of backward traveling waves. Expressing the states of the pressure coefficients in this way, the pressure coefficients of the n^{th} resonator can be expressed in the following fashion:

$$\begin{aligned} \begin{bmatrix} C_n^+ \\ C_n^- \end{bmatrix} &= \mathbf{T}_{cell} \begin{bmatrix} C_{n-1}^+ \\ C_{n-1}^- \end{bmatrix} = \mathbf{T}_{cell}^2 \begin{bmatrix} C_{n-2}^+ \\ C_{n-2}^- \end{bmatrix} = \dots = \mathbf{T}_{cell}^{n-1} \begin{bmatrix} C_1^+ \\ C_2^- \end{bmatrix} \\ &= a_1 \mathbf{T}_{cell}^{n-1} \mathbf{v}_1 + b_1 \mathbf{T}_{cell}^{n-1} \mathbf{v}_2 = a_1 \lambda_1^{n-1} \mathbf{v}_1 + b_1 \lambda_2^{n-1} \mathbf{v}_2 \end{aligned} \quad (52)$$

where $a_n = a_1 \lambda_1^{n-1}$ and $b_n = b_1 \lambda_2^{n-1}$. Therefore, the beginning and end boundary conditions can be written as

$$\begin{aligned} a_1 \lambda_1^{-1} v_1^+ + b_1 \lambda_2^{-1} v_2^+ + a_1 \lambda_1^{-1} v_1^- + b_1 \lambda_2^{-1} v_2^- &= P_0 \\ a_1 \lambda_1^{N-1} v_1^- + b_1 \lambda_2^{N-1} v_2^- &= 0 \end{aligned} \quad (53)$$

and the normalized transmission loss can be expressed as

$$\frac{TL}{N} = \frac{20}{N} \log_{10} \left| \frac{a_1 \lambda_1^{-1} v_1^+ + b_1 \lambda_2^{-1} v_2^+}{a_1 \lambda_1^{N-1} v_1^- + b_1 \lambda_2^{N-1} v_2^-} \right| \quad (54)$$

Recall that because $\lambda_1 = e^\Gamma$ and $\lambda_2 = e^{-\Gamma}$, then $\lambda_1 = \frac{1}{\lambda_2}$, so one of the eigenvalues will always be $|\lambda| < 1$ when $N \rightarrow \infty$. Therefore, if $\lambda_1 < 1$ for a particular frequency, then the $a_1 \lambda_1^{N-1} v_1^-$ term in Equation (53) will approaches 0, so $b_1 = 0$. Conversely, if $\lambda_2 < 1$ for a particular frequency, the $b_1 \lambda_2^{N-1} v_2^-$ term in Equation (53) will approaches 0, so $a_1 = 0$. As a result, Equation (54) approaches

$$\lim_{N \rightarrow \infty} \frac{TL}{N} = -20 \log_{10} \left| \min |\lambda_{1,2}| \right| \quad (55)$$

where $\min |\lambda_{1,2}|$ represents whichever eigenvalue has a smaller magnitude at each frequency.

Or equivalently

$$\lim_{N \rightarrow \infty} \frac{TL}{N} = 20 \log_{10} \left| \max |\lambda_{1,2}| \right| \quad (56)$$

where $\max |\lambda_{1,2}|$ represents whichever eigenvalue has a larger magnitude at each frequency. This form will be used later when examining the connected resonator system. Plotting the result of this equation for the system in question yields the expected result (see Figure 35).

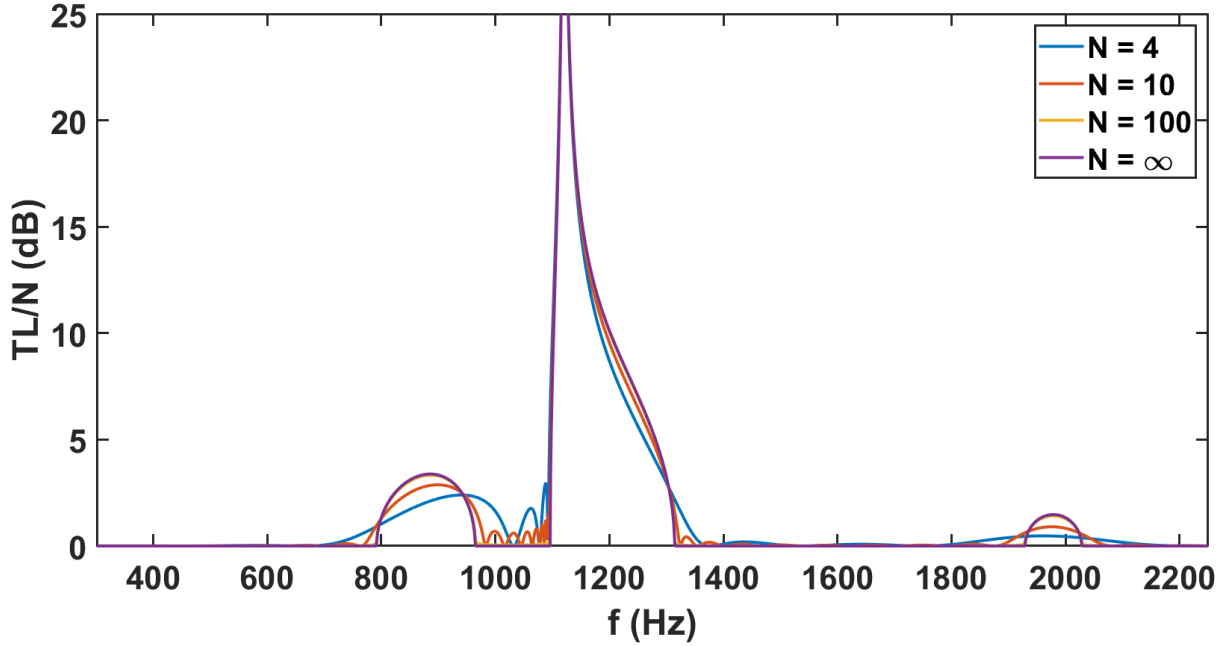


Figure 35. Normalized transmission loss TL/N as $N \rightarrow \infty$

Clearly from this figure, the equation Wang [16] gives for $\lim_{N \rightarrow \infty} TL/N$ is accurate. As $N \rightarrow \infty$, the normalized transmission loss converges to $20 \log_{10} \left| \max |\lambda_{1,2}| \right|$.

2.3. Numerical modeling array of Helmholtz resonators

The purpose of the numerical modeling is solely to verify the accuracy of the analytical modeling. The numerical modeling tool of choice was Actran. Actran is a program capable of modelling complex acoustic phenomena such as sound propagation, transmission, and absorption via the finite element method [54].

To begin the numerical modeling process, a mesh of the system needed to be defined. Actran allows the user to either create a mesh using tools within the program, define a mesh using a reference to external mesh files, or define the mesh explicitly in terms of all nodal

coordinates and element connectivities [55]. To determine the most practical meshing approach for the applications of this research, the complexity of the geometry of the system needed to be taken into consideration. A CAD model of the fluid domain of the system was created in SolidWorks (see Figure 36) with the same dimensions as the analytical models in the previous sections. The geometry was selected such that the system could eventually be tested on the grazing incidence impedance tube at the Center for Aerospace Acoustics (as will be shown in a future section). Generally speaking, the shape of a Helmholtz resonator cavity is arbitrary because only the total volume of the cavity plays a role in the resonators performance when lumped parameters are assumed [12]; however, the cavities were chosen to be rectangular because the connected array that is investigated in a future section is easier to model mathematically when the cross-section of the cavity remains constant along the axis of the duct.

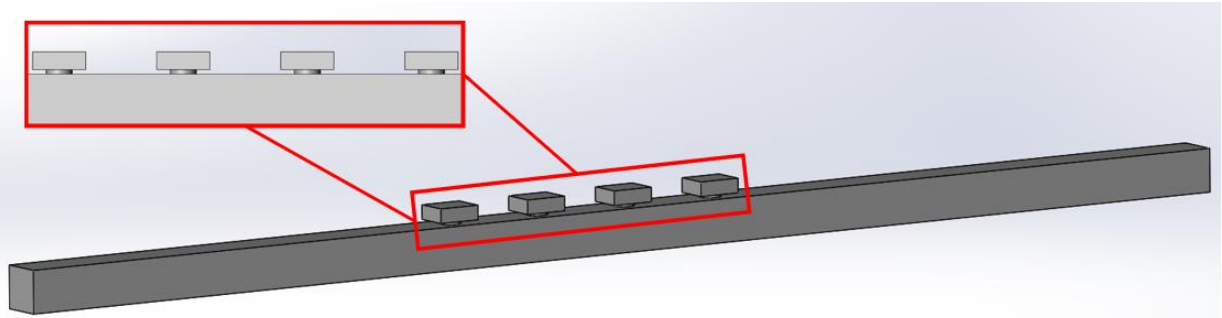


Figure 36. CAD Model of the Fluid Domain of the Grazing Impedance Tube Lined with Four Helmholtz Resonators

Given that the geometry is not particularly complex, it is a good candidate for a structured mesh [56]. In general, basic meshes can be grouped into two main types: structured and unstructured (see Figure 37) [56]. Structured meshes feature a more orderly arrangement of elements which makes the system easier to solve; unstructured meshes, on the other hand, do not have element spacing constraints and are thus better at conforming to complex geometries [57].

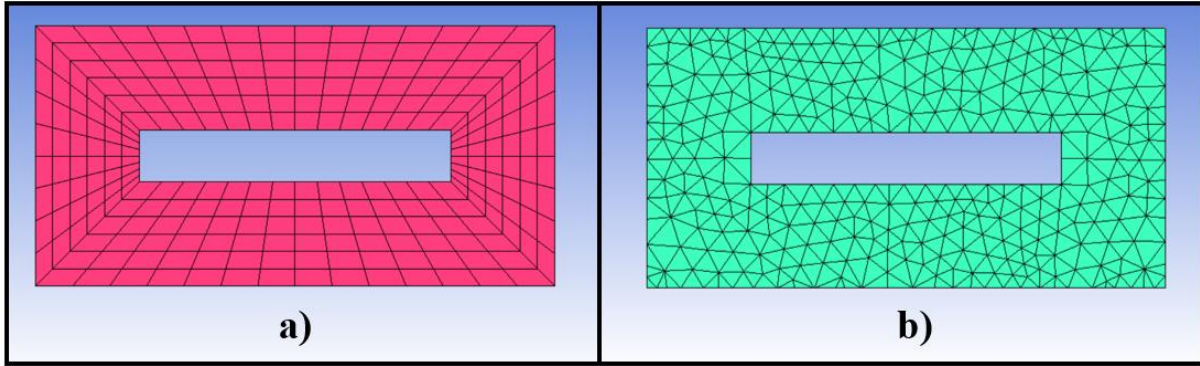


Figure 37. Different Types of Meshes: a) Structured mesh and b) Unstructured mesh

A specific type of structured mesh called a multi-block structured mesh (see Figure 38) proved to be useful for this research. This type of mesh is effective when different mesh patterns are required for different portions of the domain; for example, making the mesh finer in areas where high precision is necessary while leaving the mesh coarser in less critical areas [58]. This mesh is created by splitting up the domain into smaller subdomains called “blocks,” illustrated by the different shadings in Figure 38, each having their own mesh pattern that together form the complete mesh [58].

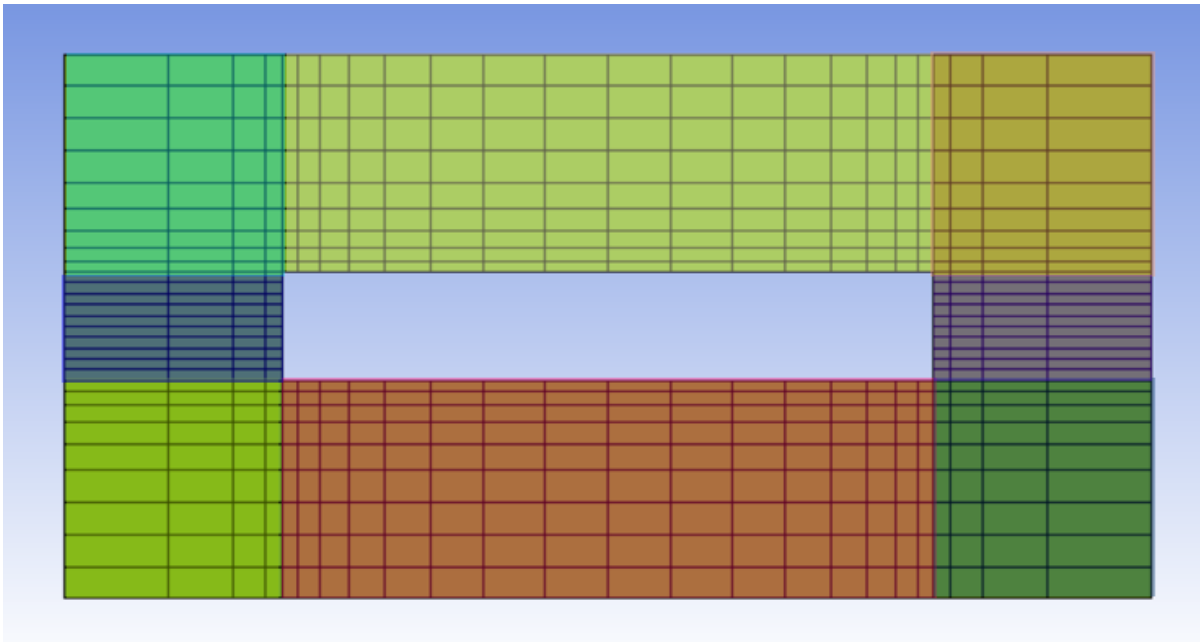


Figure 38. Example Schematic of a Multi-Block Structured Mesh with Eight Different Blocks Each Highlighted in a Different Color

For the array of Helmholtz resonators system, the block topology (see Figure 39) was chosen as follows: a block for an untreated portion of the duct, a block for the neck of a resonator,

a block for the cavity of the resonator, a block for a treated portion of the duct (directly under the resonator), and so on for all of the other resonators in the array as well as the termination. Notice how each block has a slightly different mesh pattern. That way, the mesh can be made finer near the neck and coarser in the untreated duct. A finer mesh is desired in and around the necks since the sound field is more complex in these regions [59]. A minimum of six elements per wavelength was maintained throughout the entire domain as a rule of thumb [60].

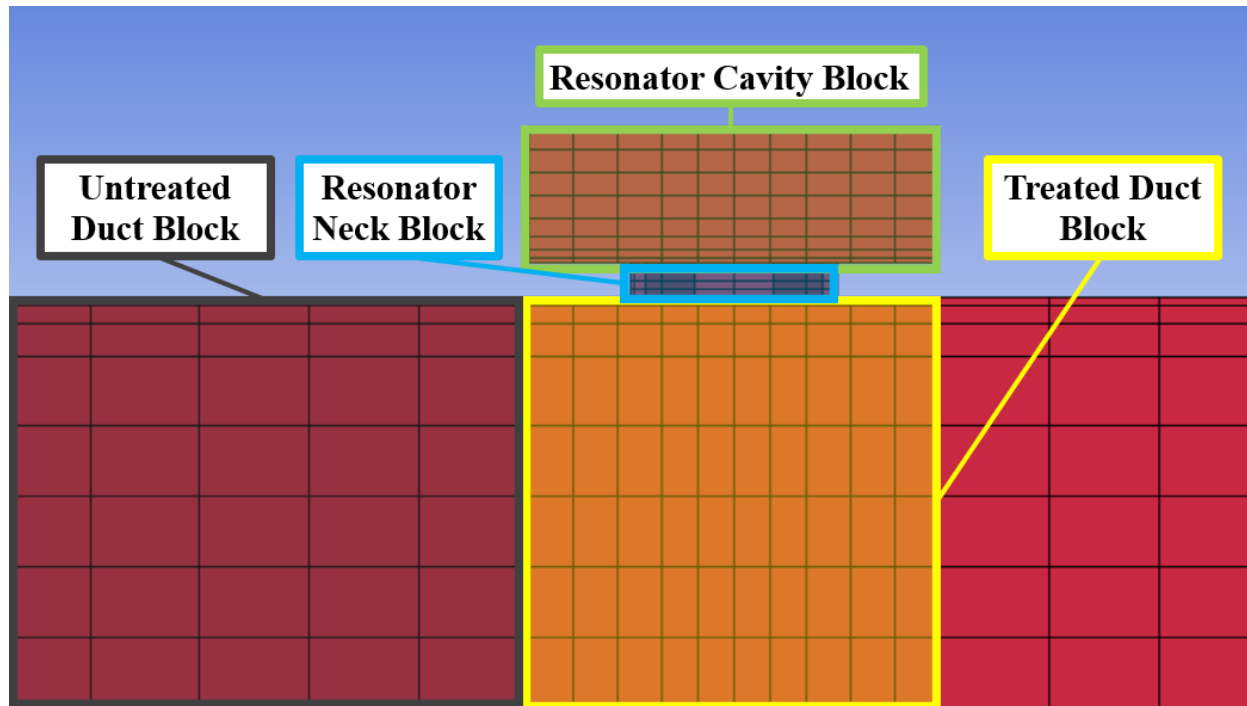


Figure 39. Block Topology for a Unit Cell of the Helmholtz Resonator Array

Ansys ICEM CFD is a meshing software which has an intuitive multi-block meshing interface as well as an ability to output the mesh into the “Actran” file format [61]. Hence, this program was selected to generate the mesh (shown in Figure 40), and the mesh data was then outputted from ICEM CFD and imported into Actran. The surface highlighted in blue was specified to be the inlet, and the parallel surface on the opposite end of the duct was specified to be the outlet; that way, boundary conditions could be applied to these surfaces in Actran.

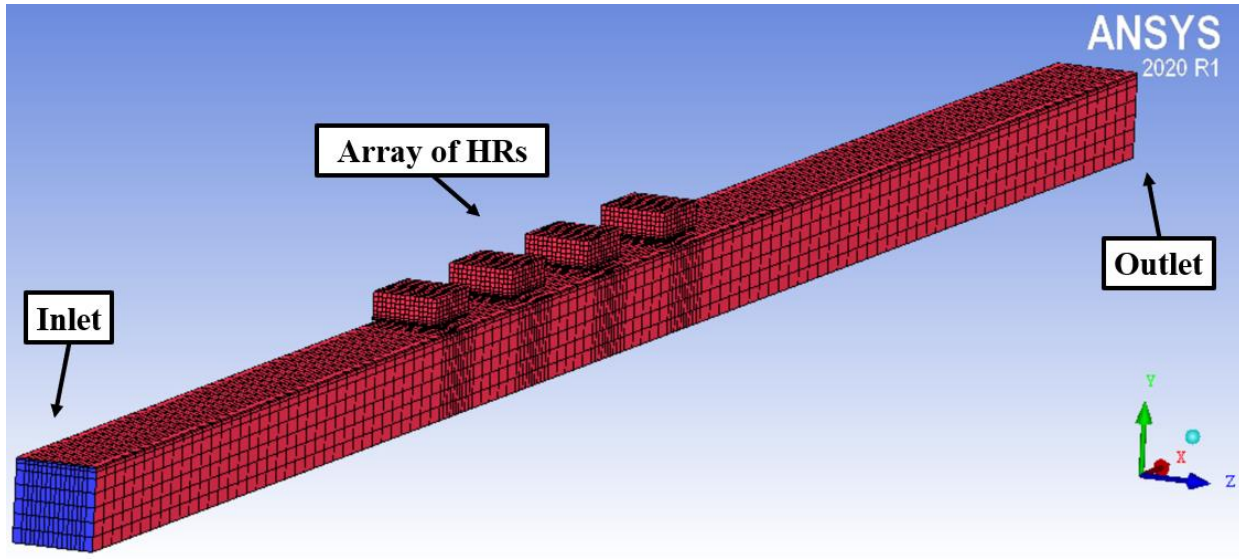


Figure 40. Mesh of Grazing Impedance Tube Lined with Four Helmholtz Resonators

Actran's direct frequency response computation procedure was selected for this analysis. The direct frequency response computation procedure calculates the response of an acoustic system to a specific excitation according to the following formula:

$$(\mathbf{K} + i\omega\mathbf{C} - \omega^2\mathbf{M})\mathbf{x}(\omega) = \mathbf{F}(\omega) \quad (57)$$

where \mathbf{K} , \mathbf{C} , \mathbf{M} are the stiffness, damping, and mass matrices across the entire domain, $\mathbf{x}(\omega)$ is the response vector for each frequency, and $\mathbf{F}(\omega)$ is the force vector for each frequency [62].

A 1 Pa pressure input was applied at the inlet surface. Both the input surface and output surfaces were specified as anechoic to prevent reflections. The transmission loss for this numerical model is plotted in Figure 41. Two color maps of the acoustic pressure along the duct (in dB) are shown in Figure 42 and Figure 43 for the two stop-band frequencies of interest: the first Bragg reflection frequency and the Helmholtz resonant frequency.

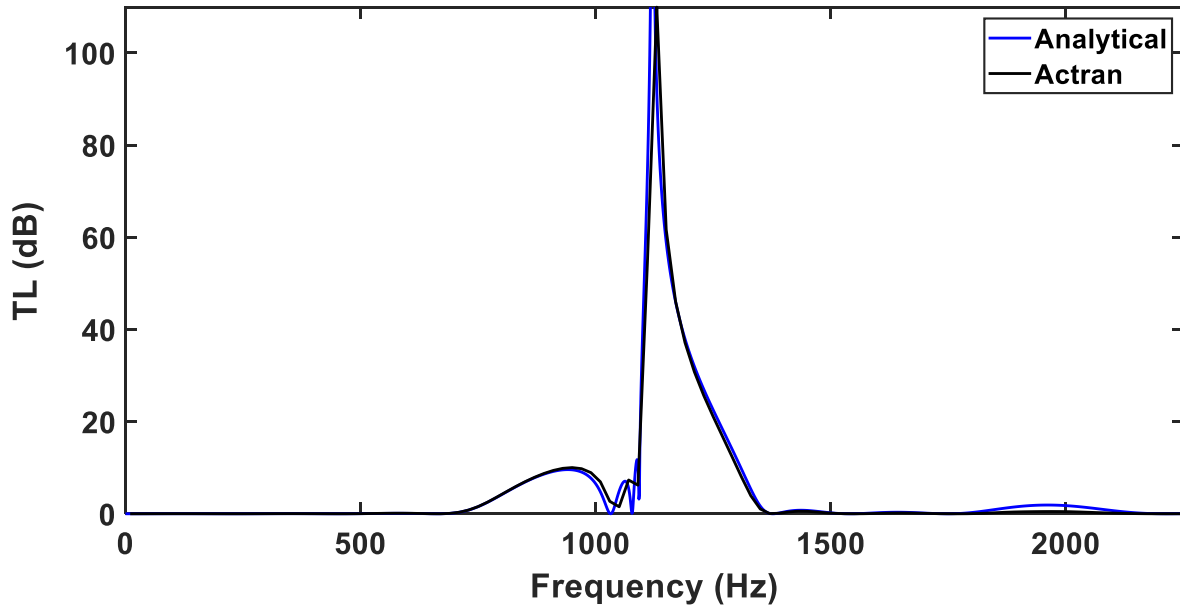


Figure 41. Numerical Solution for Transmission Loss Across Impedance Tube Lined with Four Helmholtz Resonators

$$N = 4, P_{in} = 94 \text{ dB}, L_r = 7 \text{ in}, L_n = 0.25 \text{ in}, S_n = 1.77 \text{ in}^2, S_d = 9 \text{ in}^2, V_c = 7 \text{ in}^3$$

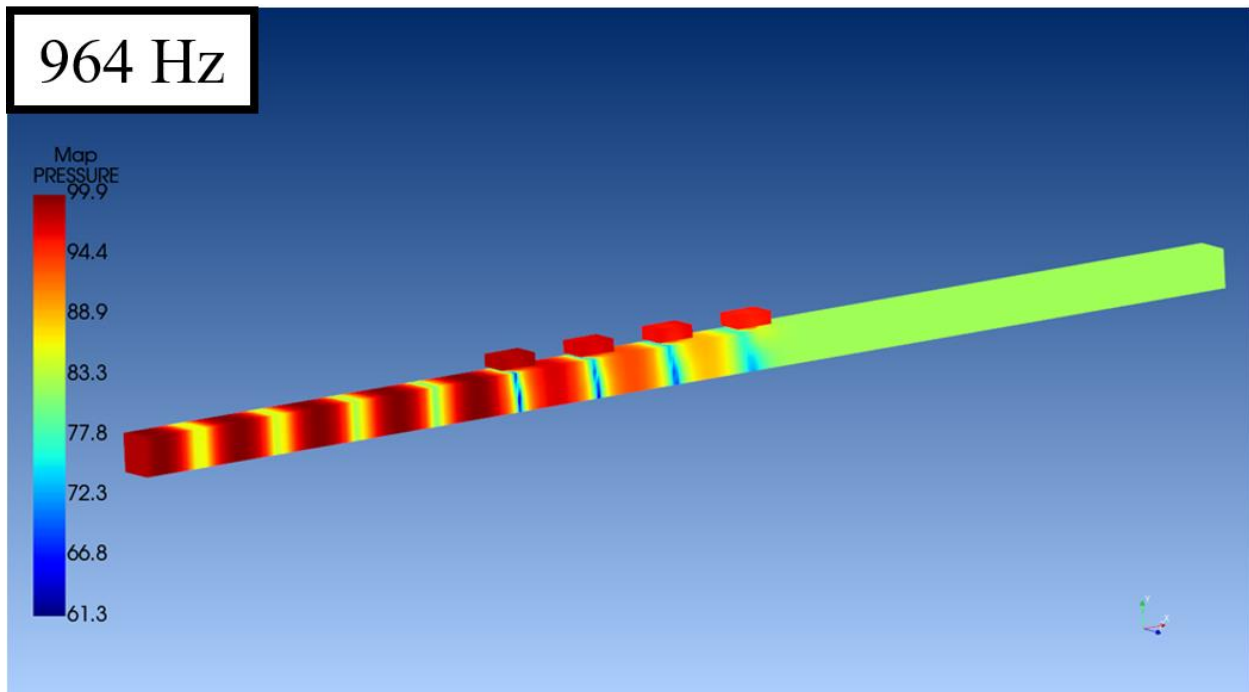


Figure 42. Color Map of Acoustic Pressure in dB for the Impedance Tube Lined with Four Helmholtz Resonators at the First Bragg Reflection Frequency

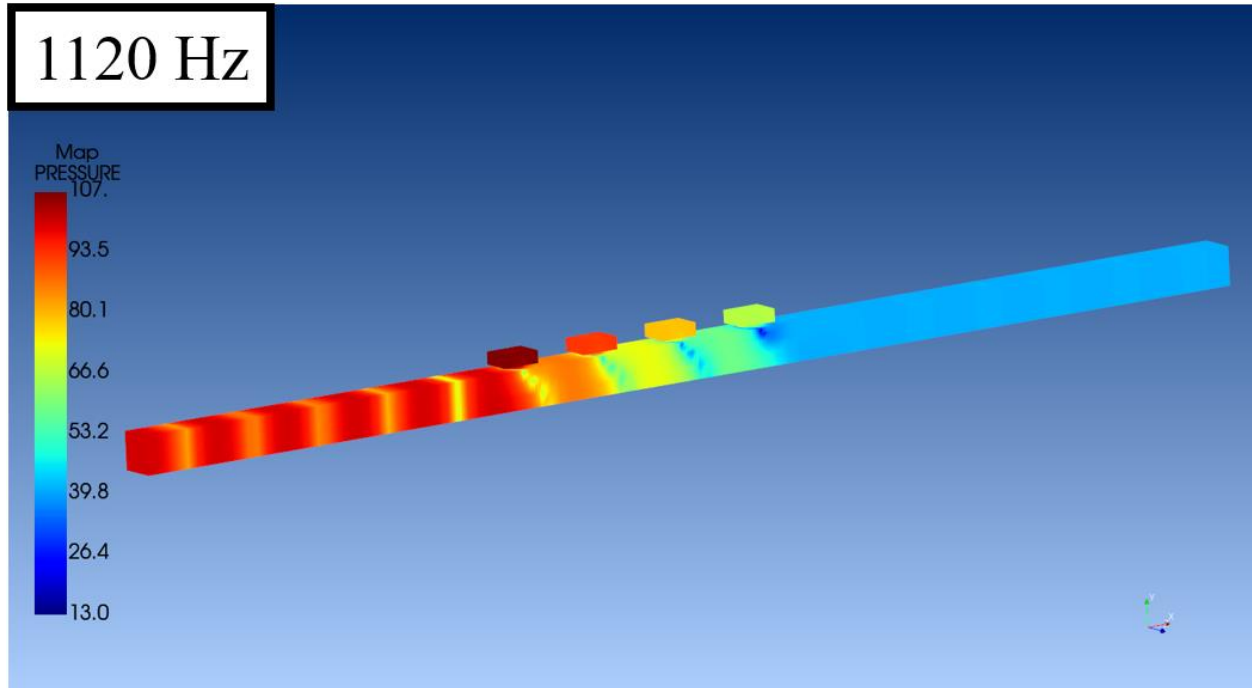


Figure 43. Color Map of Acoustic Pressure in dB for the Impedance Tube Lined with Four Helmholtz Resonators at the Helmholtz resonant Frequency

According to Figure 41 the numerical solution lines up almost exactly with the analytical solution. Note that even though technically the transmission loss of a Helmholtz resonator at its resonant frequency without damping is essentially infinite, both the analytical solution and the numerical solution must approximate finite values at the peak. Between the two models, the finite value approximations at the Helmholtz resonant frequency differ considerably in magnitude (i.e., the analytical solution predicts 218 dB at the peak while the numerical solution predicts 110 dB). As such, the data surrounding these peak frequencies will misalign slightly (by a maximum of about 4 dB). Elsewhere, the numerical and the analytical solutions align to within 2 dB. Because the analytical solution closely matches the numerical solution, the analytical solution is thus considered to be an accurate model. In a later section, the experimental results of this geometry on the impedance tube will be shown to further validate these findings.

This system is considered a local-reacting system and thus has an identical acoustic impedance value at the axial location of each resonator [11]. Recall that the normalized acoustic impedance of a liner is a measure of how well the liner will absorb sound, and is given by

$$Z = \frac{p}{\rho c(\mathbf{u} \cdot \mathbf{n})} = R + jX \quad (58)$$

where Z is the impedance of the liner at a point of interest normalized by the characteristic impedance of air (i.e., ρc), p is the acoustic pressure at that point, ρ and c are the density and speed of sound of air respectively, \mathbf{u} and \mathbf{n} are the acoustic particle velocity vector and unit normal vector into the liner respectively, and R and X are the real and imaginary components of the impedance referred to as the acoustic resistance and reactance respectively [11]. Actran was used to verify that the acoustic impedance was in fact the same at each axial location containing a resonator (see Figure 44 and Figure 45 for the impedance at the Bragg reflection frequency and Helmholtz resonant frequency respectively).

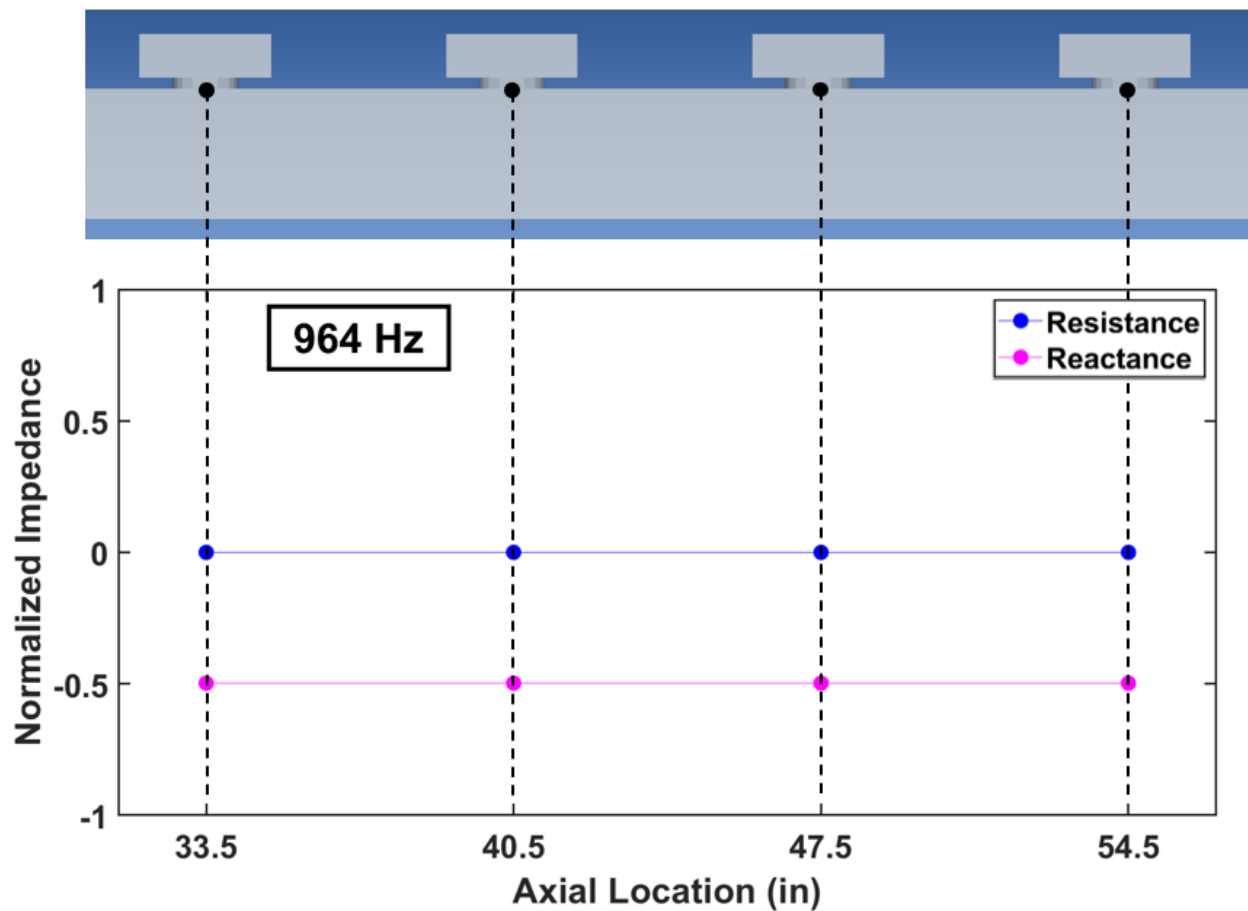


Figure 44. Normalized Acoustic Impedance for Helmholtz Resonator Array Solved Using Actran – First Bragg Reflection Frequency

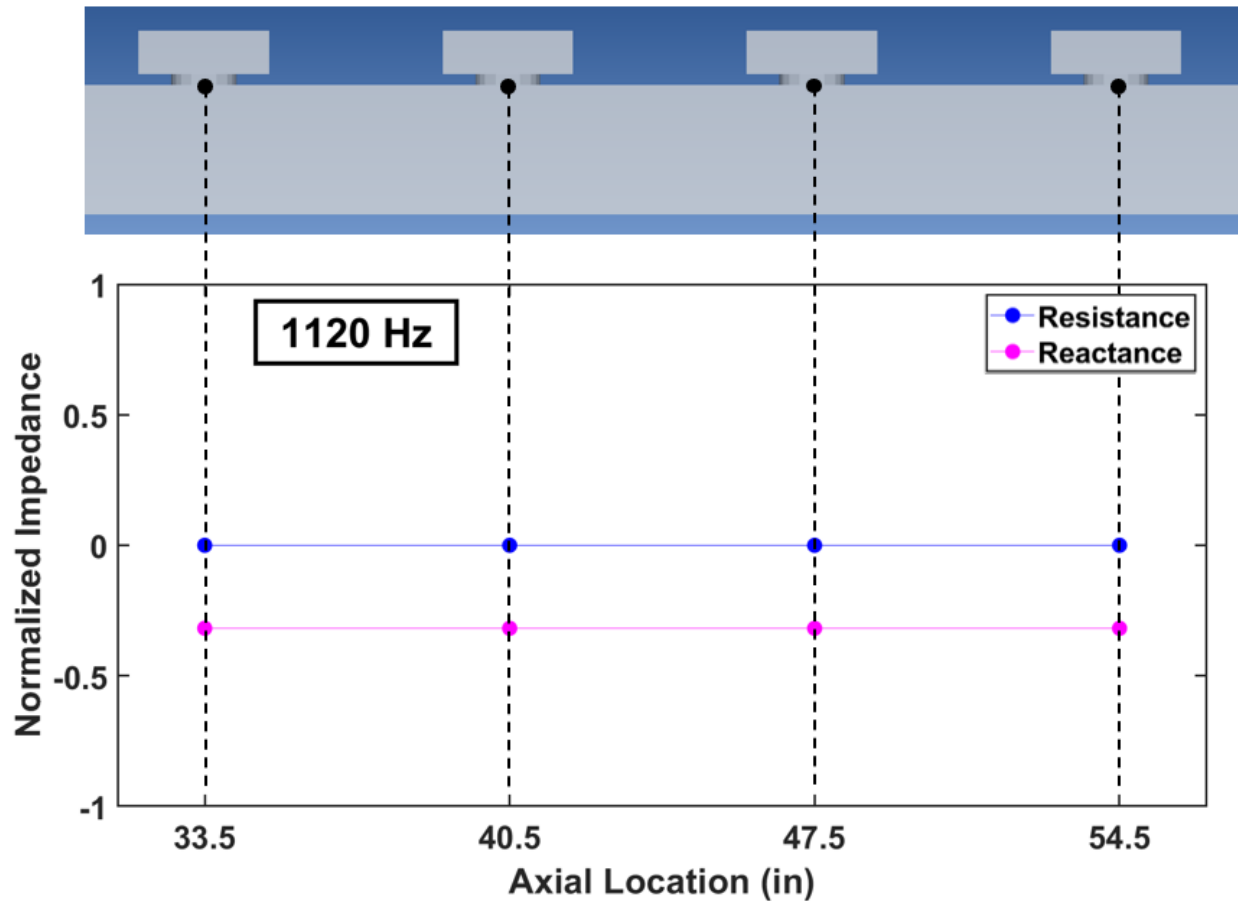


Figure 45. Normalized Acoustic Impedance for Helmholtz Resonator Array Solved Using Actran – Helmholtz Resonant Frequency

Since the impedance was found to be identical at each axial location containing a resonator, the system can in fact be classified as a local-reacting system. This same procedure will later be performed on the connected array of Helmholtz resonators which is shown to be an extended-reacting system. Recall that an extended-reacting system allows for sound to travel through the body of the liner, meaning the liner will have a spatially-varying impedance [11]. The two systems will then be compared based on their impedance plots in order to unveil the underlying physics governing their performance.

2.4. Conclusions

The similarity between the analytical and numerical solutions verifies that a duct lined with periodically-spaced Helmholtz resonators can accurately be modeled using the transfer-matrix method in conjunction with Bloch wave theory. The results show that stop-bands from Bragg reflection can be induced by specifically tuning the spacing of the resonators to a multiple

of a half-wavelength of the incoming sound waves and that the frequencies of those stop-bands are not altered by the number of resonators. As the number of resonators approaches infinity, the normalized transmission loss converges to the shape of the attenuation constant. This periodic-spacing phenomenon shows promise for the aerospace industry since tuning the resonator spacing distance in liners can lead to additional transmission loss stop-bands across a wider frequency range. Careful resonator spacing can even increase transmission loss at frequencies lower than the Helmholtz resonant frequency as illustrated in the previous results of this section.

3. CONNECTED HELMHOLTZ RESONATORS

This chapter describes the analytical and numerical modeling of an array of connected Helmholtz resonators developed as part of this thesis. The theoretical modeling of sound propagation through a duct lined with periodically-spaced, Helmholtz resonators connected at their cavities by coupling tubes is presented. A numerical model using Actran is constructed, and the results are presented. A parameter study of the system is conducted, and conclusions are discussed.

The goal of this connected Helmholtz resonator AMM design is to achieve greater transmission loss across a wider range of frequencies than is attainable by traditional honeycomb liners. The system attenuates a wider range of frequencies by combining the concepts of the unconnected periodic Helmholtz resonator array explained in the previous section with a spatially-varying impedance concept. Coupling the cavities of the resonators together with tubes (referred to hereafter as “coupling tubes”) allows for another path for the sound waves to travel (see Figure 46). Unlike the main duct, this alternate path has a periodically-varying cross-section because the coupling tubes are smaller in diameter than the cross-section of the resonator cavities. As the sound travels along this chain of resonator cavities and coupling tubes, the sound wave gets slowed down by the changing cross-section. Because the duct and this alternate waveguide are connected by the necks of the periodically-spaced resonators, the two waves interact with one another (see Figure 47). Since the wave traveling through the alternate waveguide is slower than the wave traveling through the duct, the two will have a phase delay. At some points along the interface of the two waveguides, the waves will be in phase causing the pressure to be maximized and other points the waves will be out of phase causing the pressure to be minimized. Recall that the impedance of the liner is directly proportional to the pressure; hence, since the pressure varies along the interface, so will the impedance. The system is thus a global-reacting system rather than a local reacting system because waves are permitted to travel axially through the system and a spatially-varying impedance is observed. At some frequencies, more destructive interference will occur than constructive interference thus resulting in a higher transmission loss at those frequencies. Since the coupling tubes are small in diameter compared to the cross-section of the cavity of the resonator, the resonators will still resonate locally but with a broadening of the resonant frequency. By having the resonators spaced periodically as

before, Bragg reflection will still occur. By incorporating the local resonance concept, Bragg reflection, and the destructive interference between the waves traveling through the alternate waveguide and the duct, the connected array of Helmholtz resonators will achieve a high transmission loss across a broad range of frequencies.

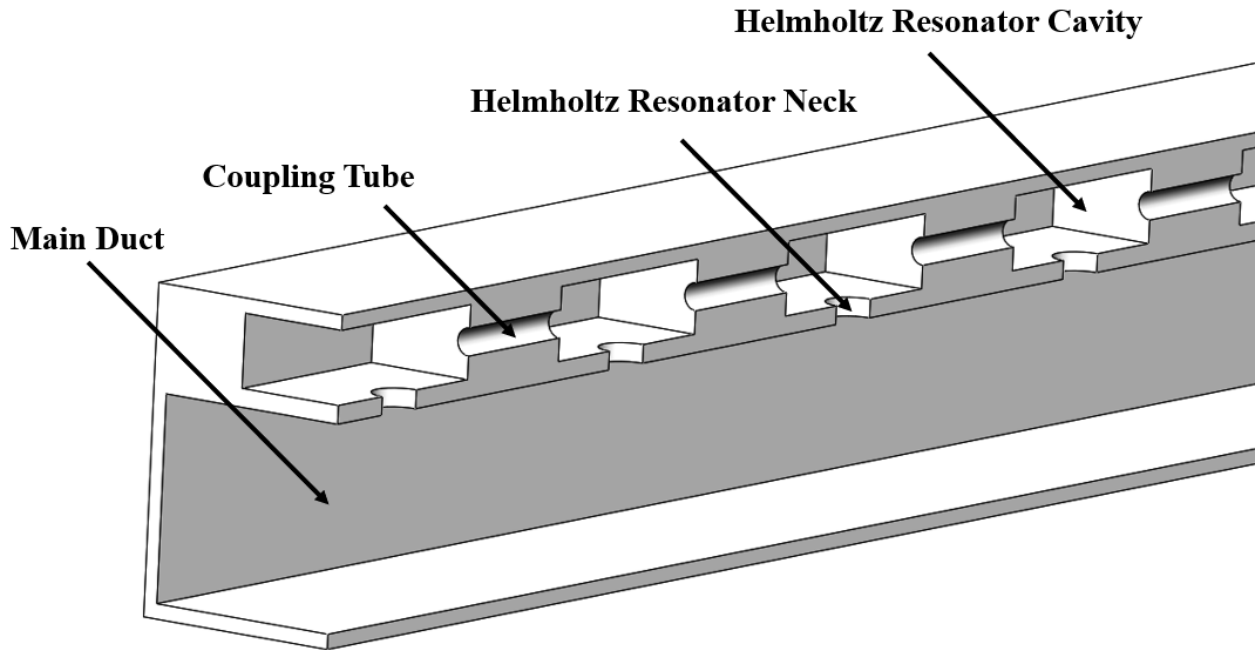


Figure 46. Schematic of the Connected Array of Helmholtz Resonator Concept

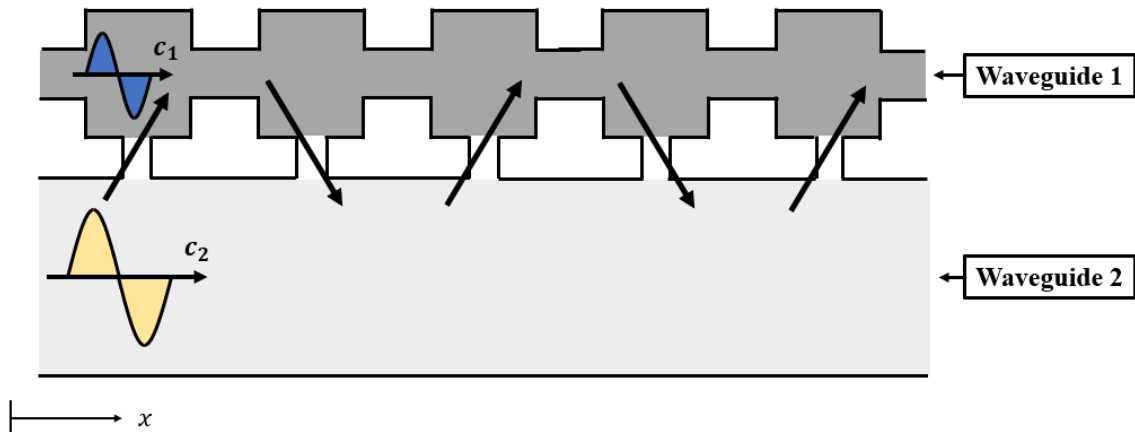


Figure 47. Schematic of the Energy Transfer Between the Two Waveguides Caused by the Interaction of the Two Travelling Waves at the Necks

Adding coupling tubes between the resonator cavities creates another degree of freedom in the system. Since the connected resonators are still arranged in a periodic fashion, Bloch

wave theory can still be applied. Now that there are two waveguides, there will be four Bloch waves: a forward and backward traveling wave in the main duct and likewise in the chain of coupled resonators. Dispersion plots will be generated to examine the propagation constants of these waves. The dispersion plots will reveal the stop-band behavior of this system as well as the frequency bands in which all the Bloch waves are simultaneously propagating. High transmission loss will result for frequencies in which all four Bloch waves experience a stop-band or when all four Bloch waves are propagating but interfere destructively (as will be discussed later in more detail).

For this analysis, the system will be under time harmonic excitation at the upstream end of the duct. Only frequencies below the first duct mode will be considered, meaning only plane waves will exist in the duct. Recall that in a rigid-walled rectangular waveguide, only plane waves will propagate if the frequency is given by

$$f < \frac{c}{2a} \quad (59)$$

where c is the speed of sound and a is the maximum dimension of the cross-section of the duct [12]. As such, the analysis will assume lumped parameters. Neither damping nor flow will be included, and the duct walls will be considered perfectly rigid. In the finite model, the ends of the duct will be considered anechoic, meaning that no sound will reflect off those surfaces. The mathematical processes herein will follow similar processes used by Pachebat and Kergomard [15] who found the dispersion relation and transmission coefficient of homogeneous and inhomogeneous lattices of parallel waveguides coupled by perforations such as perforated tube mufflers.

3.1. Analytical modeling of an infinite array of connected Helmholtz resonators

The purpose of this analytical study is to determine how connecting the cavities of the Helmholtz resonators together (and thus creating an acoustic metamaterial system with increased degrees of freedom) affects the stop-band behavior of the system. The parameters of this system are defined in Figure 48. The system will again be modeled by using the transfer-matrix method in conjunction with Bloch wave theory to find the propagation constants of the Bloch waves.

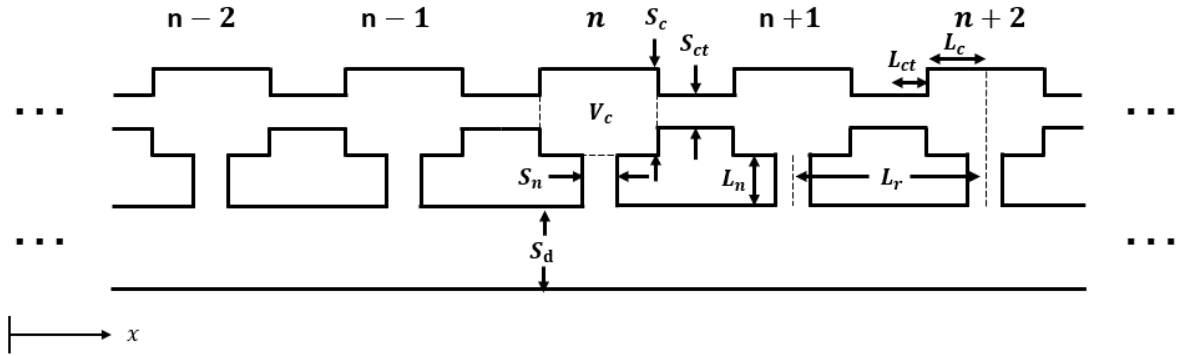


Figure 48. Infinite Array of Connected Helmholtz Resonators Schematic

The same symbolic nomenclature is used as the unconnected array of Helmholtz resonators study from the previous section, with the addition of four new symbols: S_c is the uniform cross-sectional area of the resonator cavity, S_{ct} is the uniform cross-sectional area of the coupling tube, L_{ct} is the half length of the coupling tube, and L_c is half length of the resonator in the axial direction specified on the schematic by x .

The first step is to identify a unit cell. In this case, there are actually two different useful definitions of a unit cell that will both be used during different parts of this analysis to derive the propagation constants and transmission loss. The first form is a symmetric cell and the second is an asymmetric cell (see Figure 49). The top half of the symmetric unit cell consists of three parts; from upstream to downstream, half of a coupling tube, a resonator, and half of the next adjacent coupling tube. The bottom half of the symmetric cell consists of a portion of the duct that is of the same length as the top half. Finally, the top half and bottom half of the symmetric cell are united by the neck of the resonator located in the center of the cell. The asymmetric cell consists of the same components but in a different order; the top half of the asymmetric cell from upstream to downstream consists of half of a resonator cavity, a coupling tube, and half of the next resonator cavity in that order, while the bottom half of the asymmetric cell consists of a portion of the duct that is of the same length as the top half. Finally, the top half and bottom half of the asymmetric cell are united by the neck of the upstream resonator but not the neck of the downstream resonator.

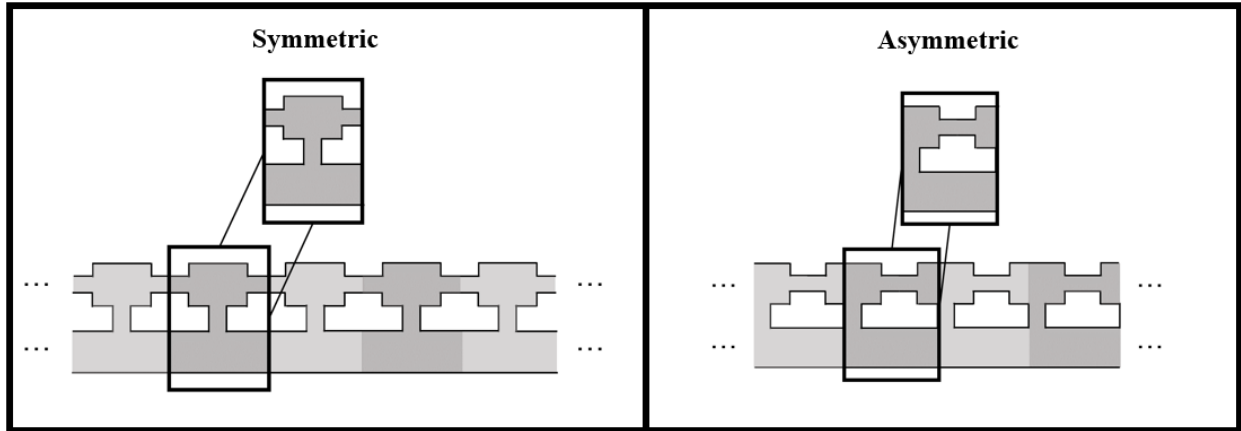


Figure 49. Symmetric and Asymmetric Cell for Infinite Array of Connected Resonators

The transfer matrices for both types of cells will be derived simultaneously. The transfer matrices will be 4th-order this time since now the continuity of pressure and volume velocity must be considered in both the main duct and across the coupled resonator cavity waveguide. Recall from the unconnected resonator analytical study that to get the transfer matrix across a unit cell requires splitting the unit cell into subsections, finding the transfer matrices across each subsection, and then multiplying the transfer matrices of the subsections together to arrive at the total transfer matrix across the unit cell. Both unit cells have the same subsections but in a different order (see Figure 50). Notice from Figure 50 that by finding three particular transfer matrices, \mathbb{T}_{ct} , \mathbb{T}_c , and \mathbb{T}_n , both the symmetric and asymmetric unit cells can be fully defined in terms of those three transfer matrices. \mathbb{T}_{ct} represents the transfer matrix across half of a coupling tube as well as the portion of the main duct directly below it; \mathbb{T}_c represents the transfer matrix across half of a resonator cavity as well as the portion of the main duct directly below it; and \mathbb{T}_n represents the transfer matrix across the portion of the resonator cavity and the main duct that are united by the neck of the resonator. The next step is to find these three transfer matrices.

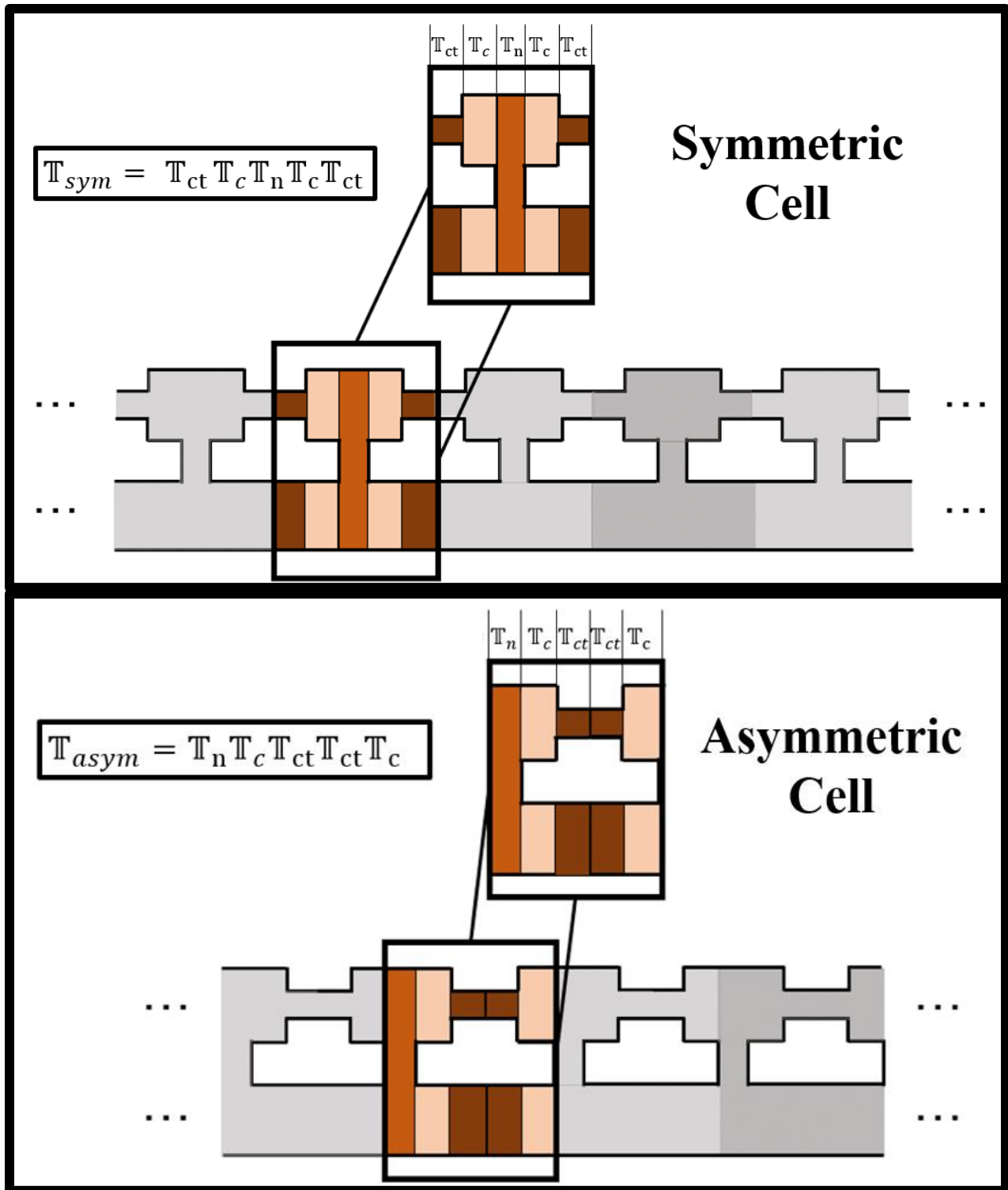


Figure 50. Symmetric and Asymmetric Cells with Subsections Highlighted

Beginning with the transfer matrix across half of a coupling tube, this system can be treated as two unconnected waveguides with different uniform cross-sections as shown in Figure 51. Since both waveguides have uniform cross-section, the classical 2nd-order transfer matrix for

a uniform cross-section waveguide can be applied (which was used previously for the derivation of the unconnected resonator array) and arranged into a 4th-order transfer matrix to describe both guides at the same time [15]. The transfer matrix for this portion of the unit cell can be written as follows.

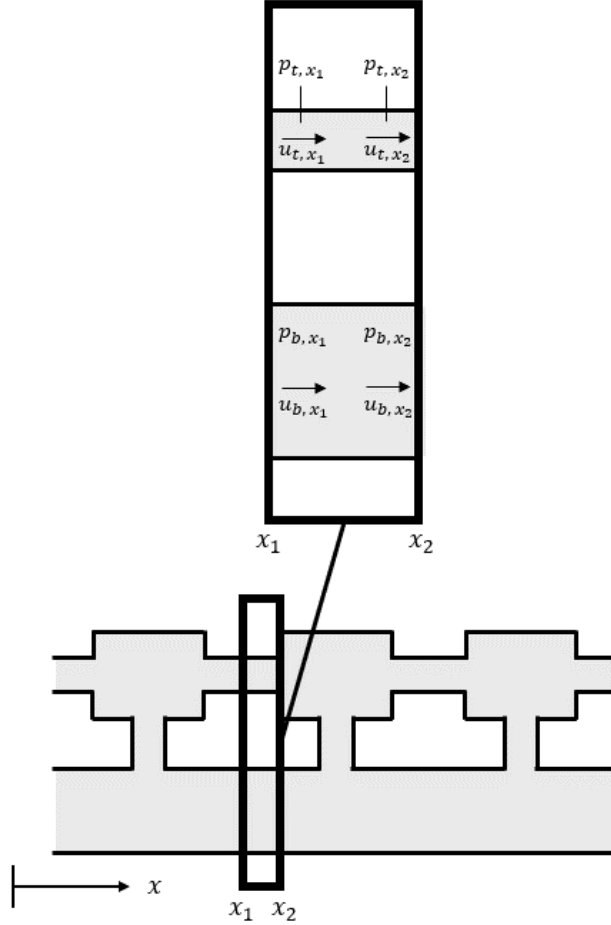


Figure 51. First subsection of unit cell used to write the \mathbb{T}_{ct} transfer matrix

$$\begin{bmatrix} p_{t, x_2} \\ u_{t, x_2} \\ p_{b, x_2} \\ u_{b, x_2} \end{bmatrix} = \mathbb{T}_{ct} \begin{bmatrix} p_{t, x_1} \\ u_{t, x_1} \\ p_{b, x_1} \\ u_{b, x_1} \end{bmatrix} = \begin{bmatrix} \mathbf{T}_{1ct} & \mathbf{0} \\ \mathbf{0} & \mathbf{T}_{2ct} \end{bmatrix} \begin{bmatrix} p_{t, x_1} \\ u_{t, x_1} \\ p_{b, x_1} \\ u_{b, x_1} \end{bmatrix} \quad (60)$$

$$\mathbf{T}_{1ct} = \begin{bmatrix} \cos(k(L_{ct} + \Delta L_{ct})) & -jZ_{ct} \sin(k(L_{ct} + \Delta L_{ct})) \\ -j \frac{\sin(k(L_{ct} + \Delta L_{ct}))}{Z_{ct}} & \cos(k(L_{ct} + \Delta L_{ct})) \end{bmatrix} \quad (61)$$

$$\mathbf{T}_{2ct} = \begin{bmatrix} \cos(kL_{ct}) & -jZ_d \sin(kL_{ct}) \\ -j \frac{\sin(kL_{ct})}{Z_d} & \cos(kL_{ct}) \end{bmatrix} \quad (62)$$

where x_1 and x_2 refer to the upstream and downstream locations of the state variables, the subscript t refers to the states in the upper portion of the system (i.e., the resonator cavity chain), the subscript b refers to the lower portion of the system (i.e., the duct), \mathbb{T}_{ct} is the 4th-order transfer matrix for this subsection and can be thought of as a block matrix containing 2nd order submatrices \mathbf{T}_{1t} and \mathbf{T}_{2t} as well as the 2nd order $\mathbf{0}$ submatrix. From henceforth, symbols stylized in double-struck font as \mathbb{T} will represent 4th-order matrices, and symbols that are in bold font as \mathbf{T}_{1t} and \mathbf{T}_{2t} will represent 2nd-order matrices. Notice that the block matrix \mathbb{T}_{ct} is block diagonal, meaning that the submatrices \mathbf{T}_{1ct} and \mathbf{T}_{2ct} occur along the diagonal while the $\mathbf{0}$ submatrix occurs off the diagonal. This realization will make the later calculation of the eigenvalues easier. In Figure 51, L_{ct} is the half-length of the connecting tube, and $Z_{ct} = \rho c/S_{ct}$ is the impedance of the coupling tube. Like the neck of a Helmholtz resonator, a correction factor ΔL_{ct} can be applied to the length of the coupling tube to account for the small volume of air in the cavity adjacent to the coupling tube that moves with the air in the coupling tube and adds extra “length” [12].

The next subsection transfer matrix is for the distance across half of the resonator cavity (see Figure 52). This is because the resonator cavity has a different impedance than the coupling tube since the cavity has a different cross-sectional area. Only half of the cavity is considered in this transfer matrix because the impedance then changes again at the x location where the neck meets the cavity. For the sake of simplicity, the impedance change resulting from the neck is assumed to occur instantaneously at the midpoint of the cavity; therefore, in this subsection described by the transfer matrix \mathbb{T}_c , no energy transfer between the top and bottom waveguides occurs, but in the next subsection described by the transfer matrix \mathbb{T}_n , all of the energy transfer between the top and bottom waveguide will occur. This simplifying assumption allows for this section described by \mathbb{T}_c to again be represented as two separate ducts with different uniform cross-sections; the next transfer matrix \mathbb{T}_n will then occur at the midpoint of the resonator and will account for the energy transfer between the top and bottom waveguides of the system all at once. The transfer matrix across the length of half of a cavity is given by

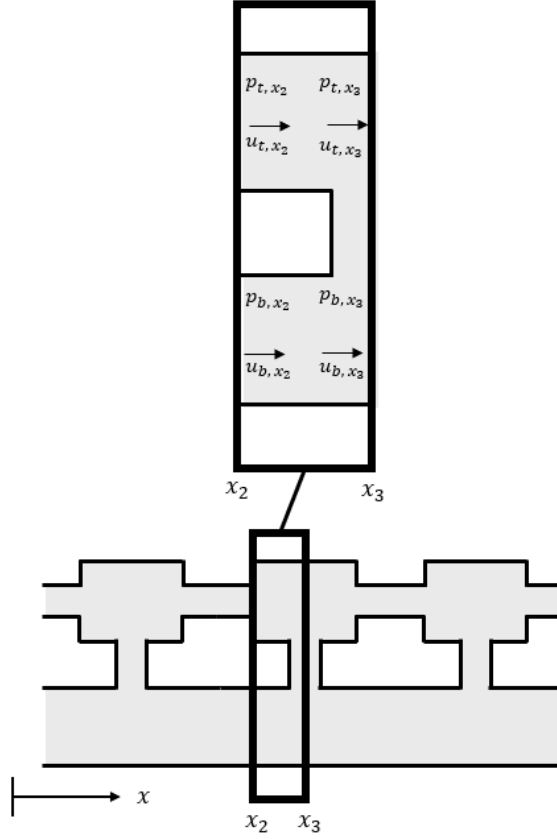


Figure 52. Second subsection of unit cell used to write the \mathbb{T}_c transfer matrix

$$\begin{bmatrix} p_{t,x_3} \\ u_{t,x_3} \\ p_{b,x_3} \\ u_{b,x_3} \end{bmatrix} = \mathbb{T}_c \begin{bmatrix} p_{t,x_2} \\ u_{t,x_2} \\ p_{b,x_2} \\ u_{b,x_2} \end{bmatrix} = \begin{bmatrix} \mathbf{T}_{1c} & \mathbf{0} \\ \mathbf{0} & \mathbf{T}_{2c} \end{bmatrix} \begin{bmatrix} p_{t,x_2} \\ u_{t,x_2} \\ p_{b,x_2} \\ u_{b,x_2} \end{bmatrix} \quad (63)$$

$$\mathbf{T}_{1c} = \begin{bmatrix} \cos(kL_c) & -jZ_c \sin(kL_c) \\ -j \frac{\sin(kL_c)}{Z_c} & \cos(kL_c) \end{bmatrix} \quad (64)$$

$$\mathbf{T}_{2c} = \begin{bmatrix} \cos(kL_c) & -jZ_d \sin(kL_c) \\ -j \frac{\sin(kL_c)}{Z_d} & \cos(kL_c) \end{bmatrix} \quad (65)$$

where L_c is the half-length of the resonator cavity and $Z_c = \rho c/S_c$ is the impedance in the cavity. Because this transfer matrix is for uniform cross-sections only, the resonators need to be rectangular rather than cylindrical because otherwise, the cross-sectional area would change across the radial dimension. Note that this matrix is again block diagonal. Also note that there is no transfer matrix at the interface of the coupling tube and the resonator cavity because that

system can be thought of as an expansion chamber; at the interface of an expansion chamber, the pressures and volume velocities on either side of the interface are equal and can thus be represented by the identity matrix.

The final subsection transfer matrix needed to define a unit cell accounts for the impedance change at the center of the cavity where it is assumed that all energy transfer between the top and bottom waveguides occurs (see Figure 53). Because of continuity of pressure and volume velocity at the interface, the following equations can be written

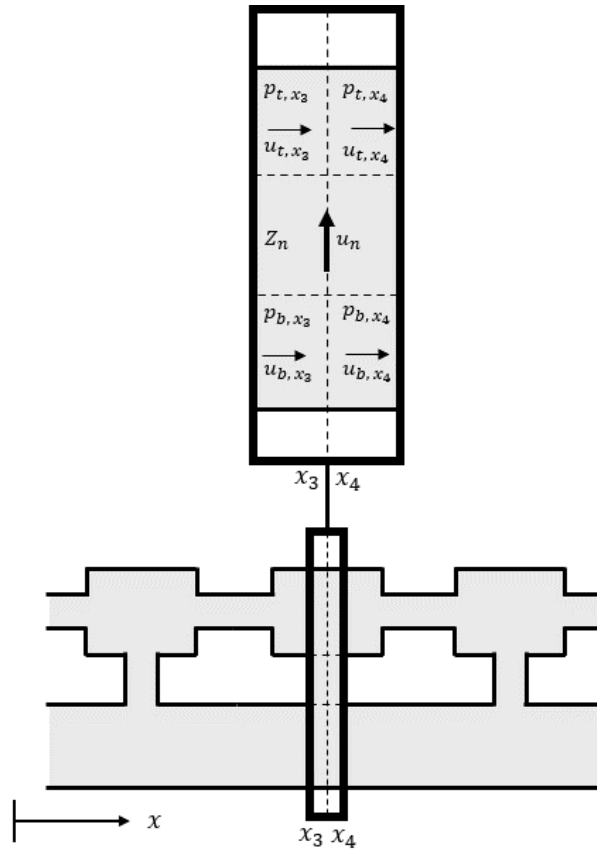


Figure 53. Third subsection of unit cell used to write the \mathbb{T}_n transfer matrix

$$\begin{aligned}
 p_{t,x_3} &= p_{t,x_4} \\
 p_{b,x_3} &= p_{b,x_4} \\
 u_{t,x_4} &= u_{t,x_3} + u_n \\
 u_{b,x_4} &= u_{b,x_3} - u_n \\
 Z_n &= \frac{p_{b,x_3} - p_{t,x_3}}{u_n}
 \end{aligned} \tag{66}$$

where u_n is the volume velocity in the neck with direction assumed to be upwards, and Z_n is the impedance of the neck. Because the present analysis only considers plane waves, the neck of the Helmholtz resonator can be treated as a mass of air which can be taken to be $Z_n = j\omega\rho(L_n + \Delta L_n)/S_n$ [12]. In this case, x_3 and x_4 are taken to be the x locations directly to the left and directly to the right of the boundary respectively. The above equations can then be rearranged into the following transfer matrix

$$\begin{aligned}
\begin{bmatrix} p_{t,x_4} \\ u_{t,x_4} \\ p_{b,x_4} \\ u_{b,x_4} \end{bmatrix} &= \mathbb{T}_n \begin{bmatrix} p_{t,x_3} \\ u_{t,x_3} \\ p_{b,x_3} \\ u_{b,x_3} \end{bmatrix} = \begin{bmatrix} 1 & 0 & 0 & 0 \\ -\frac{1}{Z_n} & 1 & \frac{1}{Z_n} & 0 \\ 0 & 0 & 1 & 0 \\ \frac{1}{Z_n} & 0 & -\frac{1}{Z_n} & 1 \end{bmatrix} \begin{bmatrix} p_{t,x_3} \\ u_{t,x_3} \\ p_{b,x_3} \\ u_{b,x_3} \end{bmatrix} \\
&= \begin{bmatrix} I - N & N \\ N & I - N \end{bmatrix} \begin{bmatrix} p_{t,x_3} \\ u_{t,x_3} \\ p_{b,x_3} \\ u_{b,x_3} \end{bmatrix} \\
N &= \begin{bmatrix} 0 & 0 \\ \frac{1}{Z_n} & 0 \end{bmatrix}, I = \begin{bmatrix} 1 & 0 \\ 0 & 1 \end{bmatrix}
\end{aligned} \tag{67}$$

Now that all of the necessary transfer matrices needed to make up a unit cell have been defined, the transfer matrix across an entire unit cell can be written as the product of a combination of these transfer matrices. For the symmetric and the asymmetric unit cell, the total transfer matrix can be expressed as

$$\mathbb{T}_{sym} = \mathbb{T}_{ct} \mathbb{T}_c \mathbb{T}_n \mathbb{T}_c \mathbb{T}_{ct} \tag{68}$$

$$\mathbb{T}_{asym} = \mathbb{T}_n \mathbb{T}_c \mathbb{T}_{ct} \mathbb{T}_{ct} \mathbb{T}_c \tag{69}$$

As was done for the unconnected resonator array in the previous section, the eigenvalues and eigenvectors of the cell transfer matrix now need to be determined next to find the propagation constants (and eventually the transmission loss). Either the symmetric or the asymmetric unit cell can be used to find the eigenvalues and eigenvectors, but the asymmetric unit cell is much easier to work with mathematically when solving the eigenequation. When finding the transmission loss, however (see next section), the symmetric unit cell becomes much

easier to work with mathematically. For now, the asymmetric unit cell will be used to derive the eigenvalues and eigenvectors. In order to derive the eigenvalues and eigenvectors, the following eigenequation must be solved:

$$(\mathbb{T}_{asym} - \lambda \mathbb{I}) \mathbb{v}_{asym} = \mathbb{0} \quad (70)$$

where λ are the eigenvalues, \mathbb{I} is the 4th-order identity matrix, \mathbb{v}_{asym} are the 4x1 eigenvectors of the asymmetric unit cell and $\mathbb{0}$ is a 4x1 matrix of 0's. Here, the asymmetrical unit cell \mathbb{T}_{asym} is chosen because it simplifies the problem considerably. Because \mathbb{T}_c and \mathbb{T}_{ct} are block diagonal, and the product of block diagonal matrices is also a block diagonal matrix, then the asymmetric transfer matrix can be rewritten as $\mathbb{T}_{asym} = \mathbb{T}_n \mathbb{T}_g$ where $\mathbb{T}_g = \mathbb{T}_c \mathbb{T}_{ct} \mathbb{T}_{ct} \mathbb{T}_c$. Because \mathbb{T}_g is block diagonal, the 4th-order eigenvalue problem can be rewritten in a much simpler block matrix form:

$$\begin{bmatrix} (\mathbf{I} - \mathbf{N})\mathbf{T}_{g1} - \lambda & \mathbf{N}\mathbf{T}_{g2} \\ \mathbf{N}\mathbf{T}_{g1} & (\mathbf{I} - \mathbf{N})\mathbf{T}_{g2} - \lambda \end{bmatrix} \begin{bmatrix} \mathbf{v}_{asym1} \\ \mathbf{v}_{asym2} \end{bmatrix} = \begin{bmatrix} \mathbf{0} \\ \mathbf{0} \end{bmatrix} \quad (71)$$

where $\mathbb{T}_g = \begin{bmatrix} \mathbf{T}_{g1} & \mathbf{0} \\ \mathbf{0} & \mathbf{T}_{g2} \end{bmatrix}$ and $\mathbb{v}_{asym} = \begin{bmatrix} \mathbf{v}_{asym1} \\ \mathbf{v}_{asym2} \end{bmatrix}$.

Subtracting row 2 from row 1 in Equation (71) gives

$$((\mathbf{I} - 2\mathbf{N})\mathbf{T}_{g1} - \lambda \mathbf{I}) \mathbf{v}_{asym1} = ((\mathbf{I} - 2\mathbf{N})\mathbf{T}_{g2} - \lambda \mathbf{I}) \mathbf{v}_{asym2} \quad (72)$$

Adding these two rows together gives

$$(\mathbf{T}_{g1} - \lambda \mathbf{I}) \mathbf{v}_{asym1} = -(\mathbf{T}_{g2} - \lambda \mathbf{I}) \mathbf{v}_{asym2} = \mathbf{v}_0 \quad (73)$$

Rearranging \mathbf{v}_0 in Equation (73) and substituting into Equation (72) gives

$$((\mathbf{I} - 2\mathbf{N})\mathbf{T}_{g1} - \lambda \mathbf{I})(\mathbf{T}_{g1} - \lambda \mathbf{I})^{-1} \mathbf{v}_0 = -((\mathbf{I} - 2\mathbf{N})\mathbf{T}_{g2} - \lambda \mathbf{I})(\mathbf{T}_{g2} - \lambda \mathbf{I})^{-1} \mathbf{v}_0 \quad (74)$$

Substituting $\mathbf{K} = (\mathbf{I} - 2\mathbf{N})$ and recognizing that $\mathbf{K}\mathbf{T} - \lambda \mathbf{I} = \mathbf{K}(\mathbf{T} - \lambda \mathbf{I}) + \lambda(\mathbf{K} - \mathbf{I})$, Equation (74) can be further simplified to

$$\left(2\mathbf{K} + \lambda(\mathbf{K} - \mathbf{I}) \left((\mathbf{T}_{g1} - \lambda \mathbf{I})^{-1} + (\mathbf{T}_{g2} - \lambda \mathbf{I})^{-1} \right) \right) \mathbf{v}_0 = \mathbf{0} \quad (75)$$

If $\mathbf{T}_{g1} = \begin{bmatrix} A_1 & B_1 \\ C_1 & D_1 \end{bmatrix}$ and $\mathbf{T}_{g2} = \begin{bmatrix} A_2 & B_2 \\ C_2 & D_2 \end{bmatrix}$ where $A_{1,2}$, $B_{1,2}$, $C_{1,2}$, and $D_{1,2}$ where all defined previously, then Equation (75) simplifies to

$$\begin{aligned} \mathbf{T}_0 \mathbf{v}_0 &= \mathbf{0} \\ \mathbf{T}_0 &= \begin{bmatrix} 2 & 0 \\ C_0 & D_0 \end{bmatrix} \\ C_0 &= -\frac{4}{Z_n} - \frac{2\lambda}{Z_n} \left(\frac{D_1 - \lambda}{\lambda^2 - (A_1 + D_1)\lambda + \det(\mathbf{T}_{g1})} + \frac{D_2 - \lambda}{\lambda^2 - (A_2 + D_2)\lambda + \det(\mathbf{T}_{g2})} \right) \\ D_0 &= 2 + \frac{2\lambda}{Z_n} \left(\frac{B_1}{\lambda^2 - (A_1 + D_1)\lambda + \det(\mathbf{T}_{g1})} + \frac{B_2}{\lambda^2 - (A_2 + D_2)\lambda + \det(\mathbf{T}_{g2})} \right) \end{aligned} \quad (76)$$

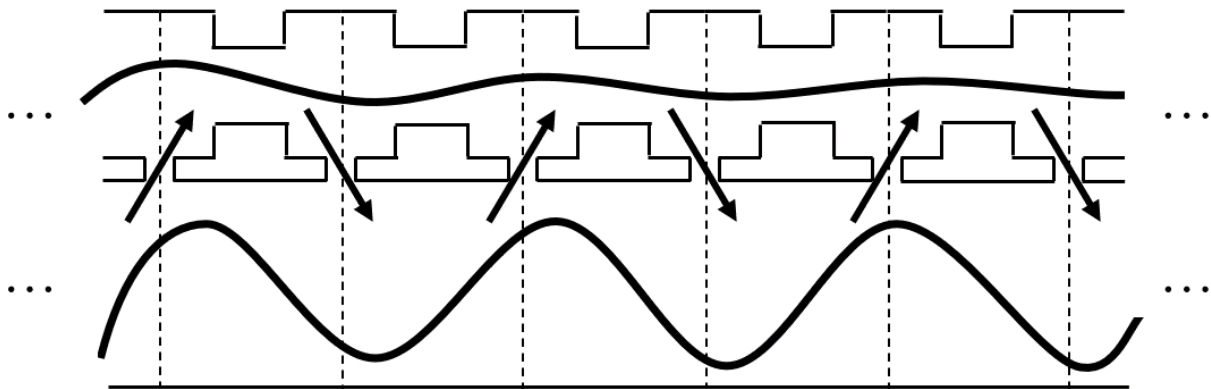
This 2nd-order matrix equation above is equivalent to the 4th-order matrix in Equation (70) [15]. Setting $\det(\mathbf{T}_0) = 0$ will thus give the dispersion equation and allow for the calculation of the eigenvalues of the unit cell. Because of the 0 in the first row, second column of \mathbf{T}_0 , $\det(\mathbf{T}_0) = 0$ simplifies to $D_0 = 0$. If \mathbf{T}_{g1} is calculated, one finds that $A_1 = D_1$ and that $\det(\mathbf{T}_{g1}) = 1$. Similarly, $A_2 = D_2$ and $\det(\mathbf{T}_{g2}) = 1$ [15]. With these simplifications in mind and recalling that the eigenvalues can be rewritten in terms of the propagation constants Γ via $\lambda = e^\Gamma$, the dispersion equation $\det(\mathbf{T}_0) = 0$ can be written as follows

$$2 + \frac{B_1}{Z_n(\cosh(\Gamma) - A_1)} + \frac{B_2}{Z_n(\cosh(\Gamma) - A_2)} = 0 \quad (77)$$

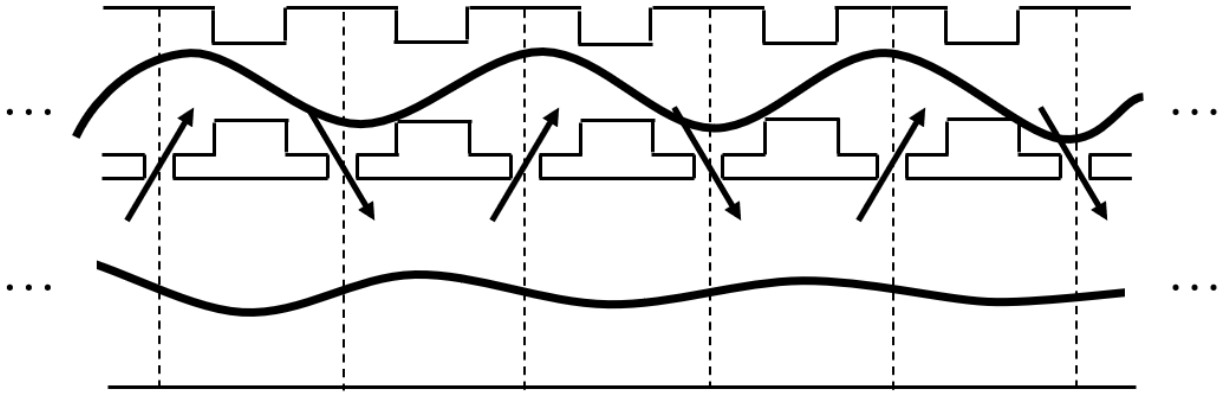
This dispersion equation has four solutions for Γ that come in pairs, one pair for the forward and backward traveling Bloch waves through the main duct and one for the forward and backward traveling Bloch waves through the coupled resonator cavity waveguide. As such, one pair of solutions feature complex-valued propagation constants with the same magnitude but opposite signs, while the other pair of solutions feature a different set of complex-valued propagation constants with the same magnitude but opposite signs. The real component is again referred to as the attenuation constant, and recall that it is a measure of the attenuation across the cells resulting from the Bloch wave. The imaginary component is again referred to as the phase constant, and recall that it is a measure of the phase difference across the cells resulting from the propagation of a Bloch wave.

For this system, there are again two different kinds of stop-bands that are possible: a stop-band from the resonant frequency of the Helmholtz resonator and a stop-band from Bragg reflection (which again arises when the periodic distance between two cells is a multiple of a half-wavelength of the incoming waves). For any given frequency, four possible scenarios can occur:

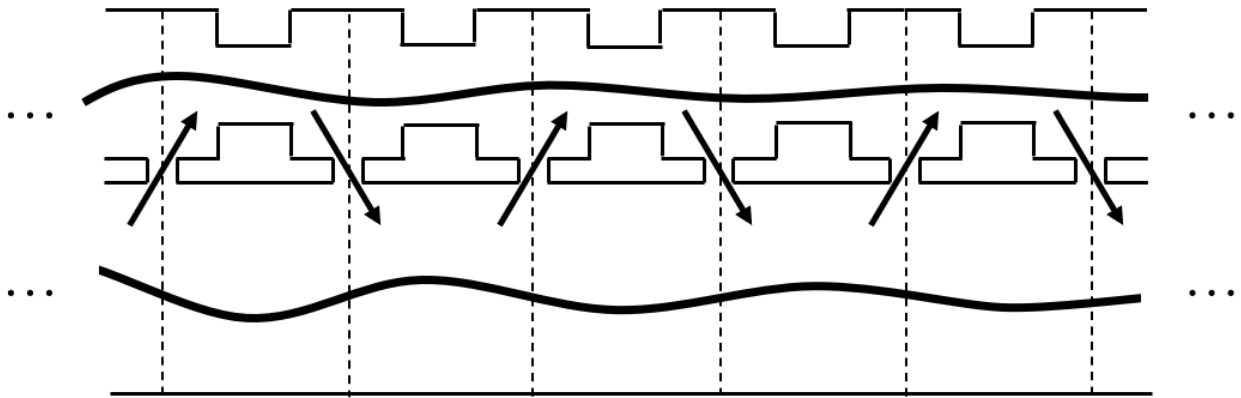
- 1) a propagating Bloch wave in the duct and an evanescent Bloch wave in the alternate waveguide (see Figure 54a)
- 2) an evanescent Bloch wave in the duct and a propagating Bloch wave in the alternate waveguide (see Figure 54b)
- 3) an evanescent Bloch wave in the duct and an evanescent Bloch wave in the alternate waveguide (see Figure 54c)
- 4) a propagating Bloch wave in the duct and a propagating Bloch wave in the alternate waveguide (see Figure 54d)



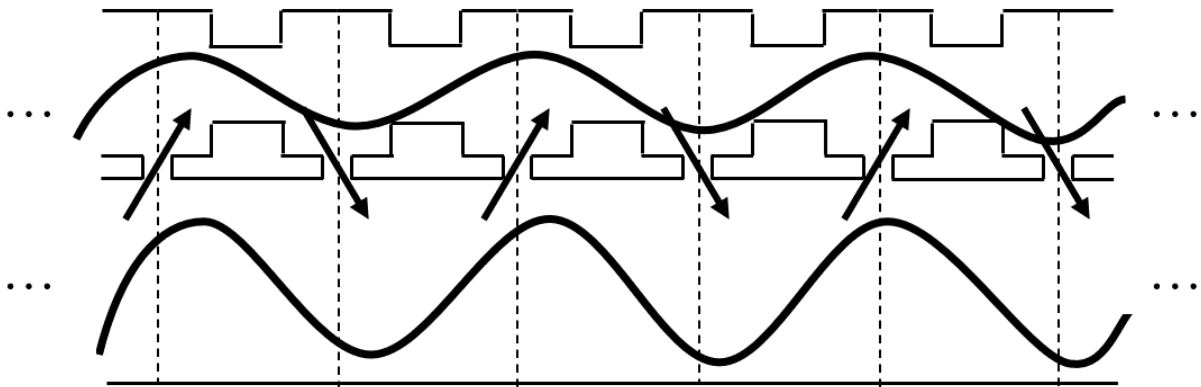
a) Propagating in Duct, Evanescent in Alternate Waveguide



b) Evanescent in Duct, Propagating in Alternate Waveguide



c) Evanescent in Duct, Evanescent in Alternate Waveguide



d) Propagating in Duct, Propagating in Alternate Waveguide

Figure 54. Possible Scenarios for the Two Forward-Travelling Bloch Waves for any Given Frequency

Because this system has two forward traveling Bloch waves instead of one, to prevent sound transmission to the end of the duct they both need to be evanescent or both need to be propagating. From Figure 54, if only one is evanescent, then sound can simply travel through the other path and reach the end of the duct. On the other hand, if both are evanescent, then the Bloch wave becomes attenuated in both paths, so no sound will reach the end of the duct. In the case of two propagating Bloch waves, the two waves have the opportunity to destructively interfere as they interact at the location of the necks. This case is only possible because of the array of connected resonator cavities, and thus would not be possible in the unconnected resonator array studied in the previous sections. This system thus has an advantage in that it creates an additional method by which sound attenuation can occur in addition to Helmholtz resonance and Bragg reflection.

To best visualize the behavior of these two forward-traveling Bloch waves at different frequencies, it is again helpful to formulate a dispersion plot for this system using Equation (77) (see Figure 55). Again, for better readability, the following dispersion plot only shows the positive components of the propagation constants corresponding to the backward traveling Bloch waves since the negative components are just a mirror image.

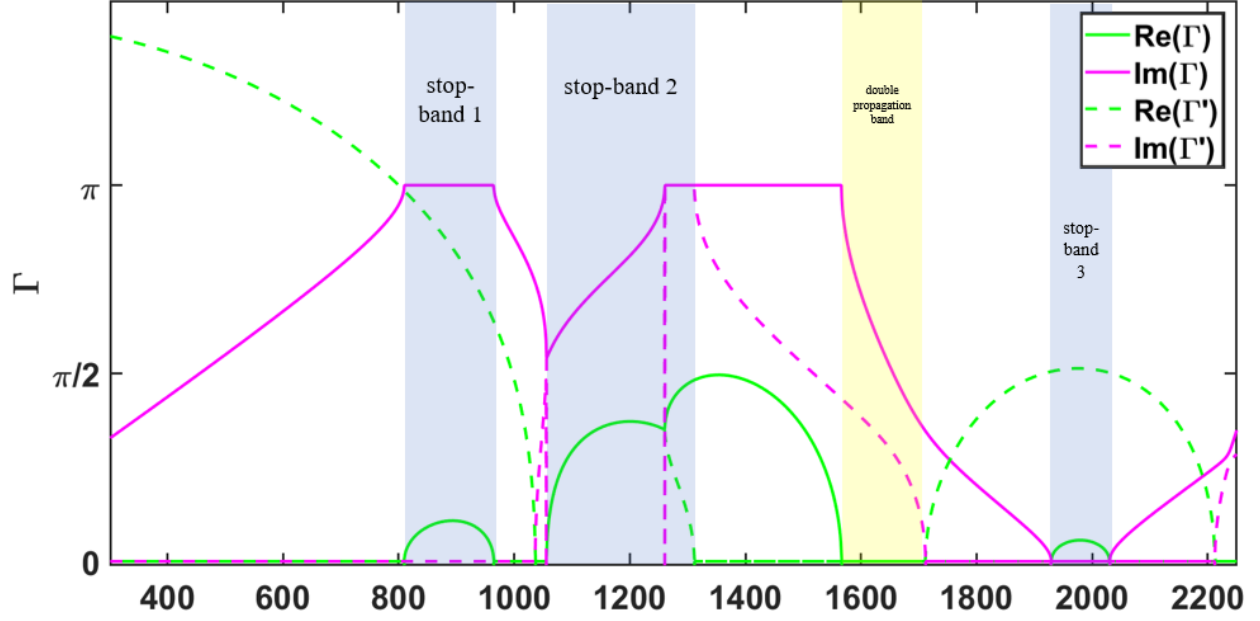


Figure 55. Dispersion Plot for Infinite Array of Connected Helmholtz Resonators

$$L_r = 7 \text{ in}, L_n = 0.25 \text{ in}, \Delta L_n = 0.49 \text{ in}, S_n = 1.77 \text{ in}^2, S_d = 9 \text{ in}^2, V_c = 7 \text{ in}^3, S_{ct} = 0.11 \text{ in}^2, S_c = 2.34 \text{ in}^2, L_{ct} = 2 \text{ in}, \Delta L_{ct} = 0.03 \text{ in}, L_c = 1.5 \text{ in}$$

Now that there are two different Bloch waves traveling in the same direction, the location of the stop-bands will not necessarily be the same for each. Even if one Bloch wave is experiencing a stop-band, energy transmission can still occur through the other waveguide not experiencing a stop-band (again, see Figure 54). Therefore, absolute stop-bands for the system arise when *both* Bloch waves experience a stop-band simultaneously. In these absolute stop-bands, the effectiveness is limited by the attenuation constant with the smaller value; if the one attenuation constant is lower than the other, then that means that one Bloch wave gets attenuated less than the other. The Bloch wave that gets attenuated less is the one that is going to allow for more transmission through the system and hence limit the sound attenuation.

Recall from a previous section that a forward-traveling Bloch wavefunction is given by

$$\Psi_{Bloch} = e^{-\Gamma} u(x) = e^{-(\Gamma_r + i\Gamma_i)} u(x) \quad (78)$$

where $u(x) = u(x + L_r)$ is a periodic function describing the identical motion occurring in each individual cell, which is modulated by the exponentially-decaying plane wave envelope across the cells $e^{-\Gamma}$. If the phase constant Γ_i is 0 or a multiple of π , the $e^{-i\Gamma_i}$ term becomes unity

meaning there is no phase change from cell to cell, and the Bloch wave simply does not propagate. If the attenuation constant Γ_r is non-zero, then that indicates that the sound gets attenuated from cell to cell. From looking at this dispersion plot, one can identify where the absolute stop-bands will occur (highlighted in blue). With this particular system geometry, the first stop band is 810-960 Hz, the next is 1050-1310 Hz, and the last is 1930-2030 Hz. In the first stop band, both attenuation constants are non-zero and both phase constants are either 0 or π , so this translates to two Bloch waves that are not propagating. In the second stop band, both Bloch waves are propagating since the phase constant is between 0 and π but their attenuation constants are both non-zero (in fact, they are overlapping on the plot, meaning they are identical) which indicates the propagating Bloch waves get attenuated. In the third stop band, both Bloch waves are not propagating because the phase constants are 0 for both and the attenuation constants are non-zero.

The dispersion plot also reveals areas where both Bloch waves are propagating simultaneously. In this “double propagation band” (specifically 1570-1710 Hz for this geometry), the attenuation constants are both 0 while both propagation constants are between 0 and π , meaning that the two Bloch wave propagate without decaying. It will be shown in the next section that though this area is not a stop-band, the transmission loss in that band will increase for finite lattices, an advantage that the connected resonator system has over the unconnected system.

The mathematical determination of the stop-band behavior described above can also be verified in a physical way. According to the formula for the resonant frequency of a Helmholtz resonator $c/2\pi \sqrt{S_n/V_c(L_n + \Delta L_n)}$ [12], the resonant frequency for this geometry should be 1250 Hz, which is in the range of stop-band 2 on the dispersion plot. Bragg reflection is known to occur when the periodic discontinuities of a lattice are a multiple of a half of a wavelength, and given that the resonator spacing $L_r = 7 \text{ in}$, one finds that the stop-bands occur around those frequencies (960 Hz and 1930 Hz). Because the Bragg stop-bands of the Γ curves appear to align more closely with the unconnected resonator case (refer back to Figure 30), one can infer that Γ is the propagation constant for the waves traveling through the duct and Γ' is the propagation constant for waves traveling through the coupled resonators.

The double propagation band is only possible because of the fact that the resonators are connected together at the cavities and is thus dependent on the geometry of the coupling tube. Understanding these physics principles helps to more intelligently manipulate the geometry of the system to achieve the desired stop-band characteristics for future applications. The results of a parameter study will later be discussed to verify these stop-band physics principles and explore the double propagation band in more detail. The next step is to examine a finite array of connected Helmholtz resonators.

3.2 Analytical modeling of a finite array of connected Helmholtz resonators

The purpose of the analytical study of a finite array of periodically-spaced Helmholtz resonators with coupled cavities (see Figure 56) is to understand how connecting the cavities of the Helmholtz resonators together affects the transmission loss of a finite (and hence more practical) system. Notice how in Figure 56, the first and the N^{th} resonators both have half of a “coupling tube” on both sides despite there not being another two resonators to connect to. The reason for this is to maintain the definition of the symmetric unit cell (refer back to Figure 49). In practical applications, it may be more desirable to remove the half coupling tubes to fit more resonators; however, in doing so, the approach discussed so far and immediately following will only be relevant for the number cells that geometrically match the unit cell (i.e. $N - 2$). That being said, eliminating the half of a coupling tube from these resonators can be done, they just require their own separate transfer matrices and thus increase the mathematical complexity (as will be shown later). By removing the half coupling tubes from the ends, the transmission loss plot would also shift slightly from what is predicted by the dispersion plot, albeit not by much since the coupling tubes can be assumed to be smaller than the cavities of the resonator. Therefore, in the interest of analytical continuity, the system illustrated in Figure 56 will be explored first, and then a solution for the case without the half coupling tubes at the ends will be explored afterwards. The same assumptions from the infinite case will be applied with an additional assumption that the half coupling tubes at the opposite ends of the entire finite system are rigidly terminated.

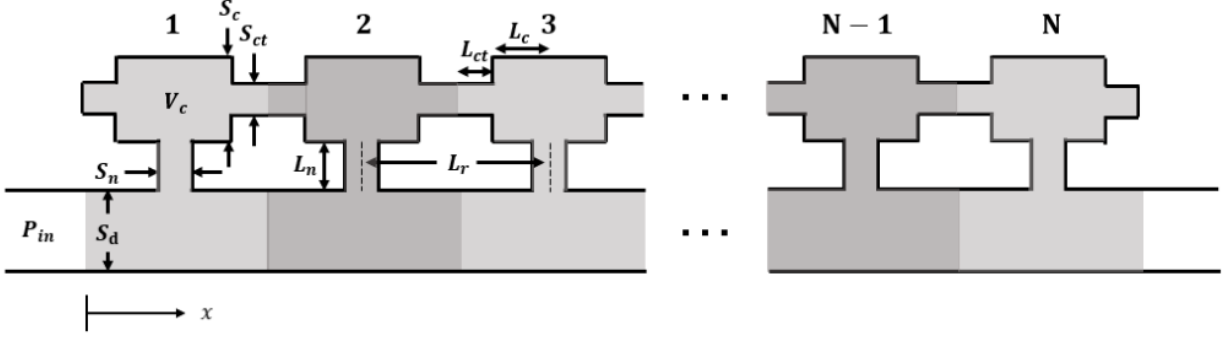


Figure 56. Finite Array of Connected Helmholtz Resonators Schematic

Recall from the section on the unconnected array of Helmholtz resonators that the beginning and end states of the system in question can be related by the cell transfer matrices as follows

$$\begin{bmatrix} p_{t,N} \\ u_{t,N} \\ p_{b,N} \\ u_{b,N} \end{bmatrix} = \mathbb{T}_{cell}^N \begin{bmatrix} p_{t,1} \\ u_{t,1} \\ p_{b,1} \\ u_{b,1} \end{bmatrix} \quad (79)$$

where \mathbb{T}_{cell} can be chosen to either be \mathbb{T}_{sym} or \mathbb{T}_{asym} , and the subscripts 1 and N represent the state variables at the beginning of the 1st cell and the end of the N^{th} cell respectively. Also recall that in order to simplify the mathematical complexity associated with the multiplication of N matrices, one can perform eigendecomposition of the transfer matrix to reveal a much simpler form mathematically:

$$\begin{bmatrix} p_{t,N} \\ u_{t,N} \\ p_{b,N} \\ u_{b,N} \end{bmatrix} = \mathbb{V} \mathbb{D}^N \mathbb{V}^{-1} \begin{bmatrix} p_{t,1} \\ u_{t,1} \\ p_{b,1} \\ u_{b,1} \end{bmatrix} \quad (80)$$

$$\mathbb{V} = [\mathbb{V}_{cell}^{(1)} \quad \mathbb{V}_{cell}^{(2)} \quad \mathbb{V}_{cell}^{(3)} \quad \mathbb{V}_{cell}^{(4)}],$$

$$\mathbb{D} = \begin{bmatrix} \lambda^{(1)} & 0 & 0 & 0 \\ 0 & \lambda^{(2)} & 0 & 0 \\ 0 & 0 & \lambda^{(3)} & 0 \\ 0 & 0 & 0 & \lambda^{(4)} \end{bmatrix} = \begin{bmatrix} e^{\Gamma} & 0 & 0 & 0 \\ 0 & e^{-\Gamma} & 0 & 0 \\ 0 & 0 & e^{\Gamma'} & 0 \\ 0 & 0 & 0 & e^{-\Gamma'} \end{bmatrix}$$

where \mathbb{V} is the 4th-order matrix of the unit cell's 4th-order eigenvectors $\mathbb{V}_{cell}^{(i)}$ that correspond to the unit cell's eigenvalues $\lambda^{(i)}$ in the diagonal eigenvalue matrix \mathbb{D} where $i = 1, 2, 3, 4$. \mathbb{V} can be composed of either the eigenvectors for the symmetric cell \mathbb{V}_{sym} or the eigenvectors of the asymmetric cell \mathbb{V}_{asym} , while the eigenvalues remain the same regardless of whether the unit cell

is defined in the symmetric way or the asymmetric way. The eigenvectors represent the linear combination of pressure and volume velocity states throughout the whole system. Each eigenvalue pair, as explained in the previous section, represents a pair of forward and backward traveling Bloch waves given by $(\Gamma, -\Gamma)$ and $(\Gamma', -\Gamma')$ that dictates how waves propagate through the lattice.

The eigenvectors for an asymmetric cell are found by recognizing from Equation (73) that if \mathbf{v}_0 can be found, then the eigenvector submatrices \mathbf{v}_{asym1} and \mathbf{v}_{asym2} can be found and form the complete 4th-order eigenvector expression \mathbb{v}_{asym} . \mathbf{v}_0 is found using Equation (76) and remembering that $\det(\mathbf{T}_0) = 0$ and thus $D_0 = 0$. Rewriting Equation (76) with these simplifications in mind, the general form of \mathbf{v}_0 can be determined:

$$\begin{aligned} \begin{bmatrix} 2 & 0 \\ C_0 & 0 \end{bmatrix} \mathbf{v}_0 &= \mathbf{0} \\ \mathbf{v}_0 &= a_0 \begin{bmatrix} \mathbf{0} \\ -\mathbf{1} \end{bmatrix} \end{aligned} \quad (81)$$

where a_0 is just an arbitrary constant scalar multiplier. Rearranging Equation (73), substituting in this new form of \mathbf{v}_0 , and recalling that $A_1 = D_1$, $\det(\mathbf{T}_{g1}) = 1$, $A_2 = D_2$, and $\det(\mathbf{T}_{g2}) = 1$ gives

$$\begin{aligned} \mathbf{v}_{asym1} &= \frac{a_0}{\lambda^2 - 2A_1\lambda + 1} \begin{bmatrix} B_1 \\ \lambda - A_1 \end{bmatrix} \\ \mathbf{v}_{asym2} &= -\frac{a_0}{\lambda^2 - 2A_2\lambda + 1} \begin{bmatrix} B_2 \\ \lambda - A_2 \end{bmatrix} \end{aligned} \quad (82)$$

where λ is a solution to the dispersion equation given by Equation (77), and \mathbf{v}_{asym1} and \mathbf{v}_{asym2} form the 4th-order eigenvector for an asymmetric cell $\mathbb{v}_{asym} = a_0 \begin{bmatrix} \mathbf{v}_{asym1} \\ \mathbf{v}_{asym2} \end{bmatrix}$.

The eigenvectors for a symmetric cell can be formed from the eigenvectors of the asymmetric cell in the following way.

$$\begin{aligned} \mathbf{v}_{sym1} &= \mathbf{T}_{L1} \mathbf{v}_{asym1} \\ \mathbf{v}_{sym2} &= \mathbf{T}_{L2} \mathbf{v}_{asym2} \end{aligned} \quad (83)$$

where $\mathbf{T}_{L1,2} = \begin{bmatrix} A_{L1,2} & B_{L1,2} \\ C_{L1,2} & D_{L1,2} \end{bmatrix}$ are the submatrices of the 4th-order transfer matrix $\mathbb{T}_L = \mathbb{T}_{ct}\mathbb{T}_c = \begin{bmatrix} \mathbf{T}_{L1} & \mathbf{0} \\ \mathbf{0} & \mathbf{T}_{L2} \end{bmatrix}$. \mathbb{T}_L represents the transfer matrix of the portion of the symmetric cell that is directly to the left of the neck (i.e., half of a coupling tube and half of a resonator cavity). Similarly, $\mathbb{T}_R = \mathbb{T}_c\mathbb{T}_{ct} = \begin{bmatrix} \mathbf{T}_{R1} & \mathbf{0} \\ \mathbf{0} & \mathbf{T}_{R2} \end{bmatrix}$ represents the transfer matrix of the portion of the symmetric cell that is directly to the right of the neck (i.e., half of a resonator and half of a coupling tube). Together, $\mathbf{T}_{g1} = \mathbf{T}_{L1}\mathbf{T}_{R1}$ and $\mathbf{T}_{g2} = \mathbf{T}_{L2}\mathbf{T}_{R2}$. Notice that $\begin{bmatrix} A_{L1,2} & B_{L1,2} \\ C_{L1,2} & D_{L1,2} \end{bmatrix} = \begin{bmatrix} D_{R1,2} & B_{R1,2} \\ C_{R1,2} & A_{R1,2} \end{bmatrix}$ and $\det(\mathbf{T}_{L1,2}) = \det(\mathbf{T}_{R1,2}) = 1$. This also means that $A_{1,2} = D_{1,2} = A_{L1,2}D_{L1,2} + B_{L1,2}C_{L1,2}$; $B_{1,2} = 2B_{L1,2}D_{L1,2}$; $C_{1,2} = 2C_{L1,2}A_{L1,2}$. With all of these relationships in mind, \mathbf{v}_{sym1} and \mathbf{v}_{sym2} from Equation (83) then simplify to

$$\begin{aligned} \mathbf{v}_{sym1} &= \frac{a_0}{\lambda^2 - 2A_1\lambda + 1} \begin{bmatrix} B_{R1}(1 + \lambda) \\ -A_{R1}(1 - \lambda) \end{bmatrix} \\ \mathbf{v}_{sym2} &= -\frac{a_0}{\lambda^2 - 2A_2\lambda + 1} \begin{bmatrix} B_{R2}(1 + \lambda) \\ -A_{R2}(1 - \lambda) \end{bmatrix} \end{aligned} \quad (84)$$

The eigenvectors for the symmetric cell will be used to form the eigenvector matrix \mathbb{V} from Equation (80) rather than the eigenvectors for the asymmetric cell because they make Equation (80) easier to evaluate. \mathbb{V} is therefore given by

$$\begin{aligned} \mathbb{V} &= a_0 \begin{bmatrix} z_1 & z_1 & z_1' & z_1' \\ h_1 & -h_1 & h_1' & -h_1' \\ -z_2 & -z_2 & -z_2' & -z_2' \\ -h_2 & h_2 & -h_2' & h_2' \end{bmatrix} \begin{bmatrix} e^{-\Gamma/2} & 0 & 0 & 0 \\ 0 & e^{\Gamma/2} & 0 & 0 \\ 0 & 0 & e^{-\Gamma'/2} & 0 \\ 0 & 0 & 0 & e^{\Gamma'/2} \end{bmatrix} \\ z_{1,2} &= \frac{B_{R1,2} \cosh(\Gamma/2)}{\cosh(\Gamma) - A_{1,2}}, & z'_{1,2} &= \frac{B_{R1,2} \cosh(\Gamma'/2)}{\cosh(\Gamma') - A_{1,2}} \\ h_{1,2} &= \frac{A_{R1,2} \sinh(\Gamma/2)}{\cosh(\Gamma) - A_{1,2}}, & h'_{1,2} &= \frac{A_{R1,2} \sinh(\Gamma'/2)}{\cosh(\Gamma') - A_{1,2}} \end{aligned} \quad (85)$$

At this stage, the system is completely defined except for what occurs at the boundaries. The inlet of the system contains a forward traveling and backward traveling plane wave with plane wave coefficients C_{in}^+ , C_{in}^- , and the outlet is treated as anechoic meaning only a forward traveling wave with plane wave coefficient C_{out}^+ exists with no reflected waves. The volume

velocity in the cavity resonator waveguide is equal to zero at the hard-walled beginning and end of the guide. With these boundary conditions, Equation (80) can be written as

$$\begin{bmatrix} p_{t,N} \\ 0 \\ C_{out}^+ \\ C_{out}^- \\ \frac{C_{out}^+}{Z_d} \end{bmatrix} = \begin{bmatrix} z_1 & z_1 & z_1' & z_1' \\ h_1 & -h_1 & h_1' & -h_1' \\ -z_2 & -z_2 & -z_2' & -z_2' \\ -h_2 & h_2 & -h_2' & h_2' \end{bmatrix} \begin{bmatrix} e^{N\Gamma} & 0 & 0 & 0 \\ 0 & e^{-N\Gamma} & 0 & 0 \\ 0 & 0 & e^{N\Gamma'} & 0 \\ 0 & 0 & 0 & e^{-N\Gamma'} \end{bmatrix} \begin{bmatrix} z_1 & z_1 & z_1' & z_1' \\ h_1 & -h_1 & h_1' & -h_1' \\ -z_2 & -z_2 & -z_2' & -z_2' \\ -h_2 & h_2 & -h_2' & h_2' \end{bmatrix}^{-1} \begin{bmatrix} p_{t,1} \\ 0 \\ C_{in}^+ + C_{in}^- \\ \frac{C_{in}^+}{Z_d} - \frac{C_{in}^-}{Z_d} \end{bmatrix} \quad (86)$$

Keeping in mind that $C_{in}^+ + C_{in}^- = P_{in}$ where P_{in} is a known pressure input into the duct, there are now 5 equations and 5 unknowns, and the system can be solved; however, it will be shown that converting this diagonalized transfer matrix into an impedance matrix form greatly reduces the mathematical complexity of the problem [15]. In the impedance matrix form, the two 0's in the two state vectors in the above equation will be moved to one side, thus completely eliminating two equations and reducing the 4th-order system to a 2nd-order system. To convert to an impedance matrix, the transfer matrix must first be rearranged into the following form:

$$\begin{bmatrix} \mathbf{P}_N \\ \mathbf{U}_N \end{bmatrix} = \begin{bmatrix} \mathbf{A} & \mathbf{B} \\ \mathbf{C} & \mathbf{D} \end{bmatrix} \begin{bmatrix} \mathbf{P}_1 \\ \mathbf{U}_1 \end{bmatrix} \quad (87)$$

where $\mathbf{P}_N = \begin{bmatrix} p_{t,N} \\ p_{b,N} \end{bmatrix}$, $\mathbf{U}_N = \begin{bmatrix} u_{t,N} \\ u_{b,N} \end{bmatrix}$, $\mathbf{P}_1 = \begin{bmatrix} p_{t,1} \\ p_{b,1} \end{bmatrix}$, $\mathbf{U}_1 = \begin{bmatrix} u_{t,1} \\ u_{b,1} \end{bmatrix}$, and $\begin{bmatrix} \mathbf{A} & \mathbf{B} \\ \mathbf{C} & \mathbf{D} \end{bmatrix}$ are 2nd-order submatrices that will be found to make the above equation true. Once in this form, the impedance matrix is a simple rearrangement as follows

$$\begin{bmatrix} \mathbf{P}_1 \\ \mathbf{P}_N \end{bmatrix} = \begin{bmatrix} \mathbf{A}\mathbf{C}^{-1} & \mathbf{B} - \mathbf{A}\mathbf{C}^{-1}\mathbf{D} \\ \mathbf{C}^{-1} & -\mathbf{C}^{-1}\mathbf{D} \end{bmatrix} \begin{bmatrix} \mathbf{U}_1 \\ \mathbf{U}_N \end{bmatrix} \quad (88)$$

To obtain $\begin{bmatrix} \mathbf{A} & \mathbf{B} \\ \mathbf{C} & \mathbf{D} \end{bmatrix}$, one simply has to swap the 2nd and 3rd rows and the 2nd and 3rd columns of the eigenvector matrix \mathbb{V} and eigenvalue matrix \mathbb{D} and then rewrite the equation as shown below

$$\begin{bmatrix} p_{t,N} \\ p_{b,N} \\ u_{t,N} \\ u_{b,N} \end{bmatrix} = \tilde{\mathbb{V}} \tilde{\mathbb{D}}^N \tilde{\mathbb{V}}^{-1} \begin{bmatrix} p_{t,1} \\ p_{b,1} \\ u_{t,1} \\ u_{b,1} \end{bmatrix} \quad (89)$$

$$\tilde{\mathbb{V}} = a_0 \begin{bmatrix} z_1 & z_1' & z_1 & z_1' \\ -z_2 & -z_2' & -z_2 & -z_2' \\ h_1 & h_1' & -h_1 & -h_1' \\ -h_2 & -h_2' & h_2 & h_2' \end{bmatrix} \begin{bmatrix} e^{-\Gamma/2} & 0 & 0 & 0 \\ 0 & e^{-\Gamma'/2} & 0 & 0 \\ 0 & 0 & e^{\Gamma/2} & 0 \\ 0 & 0 & 0 & e^{\Gamma'/2} \end{bmatrix}$$

$$\tilde{\mathbb{D}} = \begin{bmatrix} e^\Gamma & 0 & 0 & 0 \\ 0 & e^{\Gamma'} & 0 & 0 \\ 0 & 0 & e^{-\Gamma} & 0 \\ 0 & 0 & 0 & e^{-\Gamma'} \end{bmatrix}$$

Using the more convenient block notation, $\tilde{\mathbb{V}}$ simplifies to

$$\tilde{\mathbb{V}} = \begin{bmatrix} \mathbf{Z} & \mathbf{0} \\ \mathbf{0} & \mathbf{H} \end{bmatrix} \begin{bmatrix} \mathbf{I} & \mathbf{I} \\ \mathbf{I} & -\mathbf{I} \end{bmatrix} \tilde{\mathbb{D}}^{-\frac{1}{2}} \quad (90)$$

$$\mathbf{Z} = \begin{bmatrix} z_1 & z_1' \\ -z_2 & -z_2' \end{bmatrix}, \quad \mathbf{H} = \begin{bmatrix} h_1 & h_1' \\ -h_2 & -h_2' \end{bmatrix}$$

which means the transfer matrix can thus be written as

$$\begin{bmatrix} p_{t,N} \\ p_{b,N} \\ u_{t,N} \\ u_{b,N} \end{bmatrix} = \begin{bmatrix} \mathbf{Z} & \mathbf{0} \\ \mathbf{0} & \mathbf{H} \end{bmatrix} \begin{bmatrix} \mathbf{C}_N & \mathbf{S}_N \\ \mathbf{S}_N & \mathbf{C}_N \end{bmatrix} \begin{bmatrix} \mathbf{Z} & \mathbf{0} \\ \mathbf{0} & \mathbf{H} \end{bmatrix}^{-1} \begin{bmatrix} p_{t,1} \\ p_{b,1} \\ u_{t,1} \\ u_{b,1} \end{bmatrix} \quad (91)$$

$$\mathbf{C}_N = \begin{bmatrix} \cosh(N\Gamma) & 0 \\ 0 & \cosh(N\Gamma') \end{bmatrix}, \quad \mathbf{S}_N = \begin{bmatrix} \sinh(N\Gamma) & 0 \\ 0 & \sinh(N\Gamma') \end{bmatrix}$$

Now, the impedance matrix can be formed according to the process shown in Equation (88). The impedance matrix is thus

$$\begin{bmatrix} p_{t,1} \\ p_{b,1} \\ p_{t,N} \\ p_{b,N} \end{bmatrix} = \begin{bmatrix} \mathbf{Z} & \mathbf{0} \\ \mathbf{0} & \mathbf{Z} \end{bmatrix} \begin{bmatrix} \mathbf{C}_N \mathbf{S}_N & -\mathbf{S}_N^{-1} \\ \mathbf{S}_N^{-1} & -\mathbf{S}_N^{-1} \mathbf{C}_N \end{bmatrix} \begin{bmatrix} \mathbf{H} & \mathbf{0} \\ \mathbf{0} & \mathbf{H} \end{bmatrix}^{-1} \begin{bmatrix} u_{t,1} \\ u_{b,1} \\ u_{t,N} \\ u_{b,N} \end{bmatrix} \quad (92)$$

where the identity $(\mathbf{S}_N - \mathbf{C}_N \mathbf{S}_N^{-1} \mathbf{C}_N) = -\mathbf{S}_N^{-1}$ is used. Recalling the boundary condition $u_{t,1} = u_{t,N} = 0$, this 4th-order impedance matrix reduces down to a 2nd-order impedance matrix which is much easier to solve:

$$\begin{bmatrix} p_{b,1} \\ p_{b,N} \end{bmatrix} = \begin{bmatrix} Z_A & -Z_B \\ Z_B & -Z_A \end{bmatrix} \begin{bmatrix} u_{b,1} \\ u_{b,N} \end{bmatrix} \quad (93)$$

$$Z_A = \hat{Z} \coth(N\Gamma) - \hat{Z}' \coth(N\Gamma'), \quad Z_B = \hat{Z} / \sinh(N\Gamma) - \hat{Z}' / \sinh(N\Gamma')$$

$$\hat{Z} = z_2 h_1' / \det(\mathbf{H}), \quad \hat{Z}' = z_2' h_1 / \det(\mathbf{H})$$

Remembering the boundary conditions specified previously, this equation becomes

$$\begin{bmatrix} C_{in}^+ + C_{in}^- \\ C_{out}^+ \end{bmatrix} = \begin{bmatrix} Z_A & -Z_B \\ Z_B & -Z_A \end{bmatrix} \begin{bmatrix} C_{in}^+/Z_d - C_{in}^-/Z_d \\ C_{out}^+/Z_d \end{bmatrix} \quad (94)$$

Keeping in mind that $C_{in}^+ + C_{in}^- = P_{in}$ where P_{in} is a known pressure input into the duct, there are now three equations and three unknowns, and the system can be solved. The three unknowns are solved to be

$$\begin{aligned} C_{in}^+ &= \frac{P_{in}(Z_A + Z_d - Z_B)(Z_A + Z_d + Z_B)}{2(Z_d Z_A + Z_A^2 - Z_B^2)} \\ C_{in}^- &= -\frac{P_{in}(Z_d^2 - Z_A^2 + Z_B^2)}{2(Z_d Z_A + Z_A^2 - Z_B^2)} \\ C_{out}^+ &= \frac{P_{in} Z_d Z_B}{Z_d Z_A + Z_A^2 - Z_B^2} \end{aligned} \quad (95)$$

the transmission loss $TL = 20 \log_{10} |C_{in}^+/C_{out}^+|$ can be found directly from the 2nd-order impedance matrix given in Equation (93) and written as follows

$$TL = 20 \log_{10} \left| \frac{(Z_A + Z_d - Z_B)(Z_A + Z_d + Z_B)}{2Z_B Z_d} \right| \quad (96)$$

With this much more convenient equation, there is no need to solve systems of equations which greatly cuts down on computation time. Instead, TL can be calculated directly with only a few parameters. Not only that, but this formula can also handle higher N as compared to the other formulation previously presented. The previous formulation encounter matrix singularity issues as $N \rightarrow \infty$, but this direct TL formula does not. Because the computation time for computing the transmission loss is greatly reduced and the number of resonators N of the system can be increased without matrix singularity issues, this formulation of the transmission loss will prove to be very useful for parameter studies of this system (as will be shown in the next section). The transmission loss is shown in Figure 57.

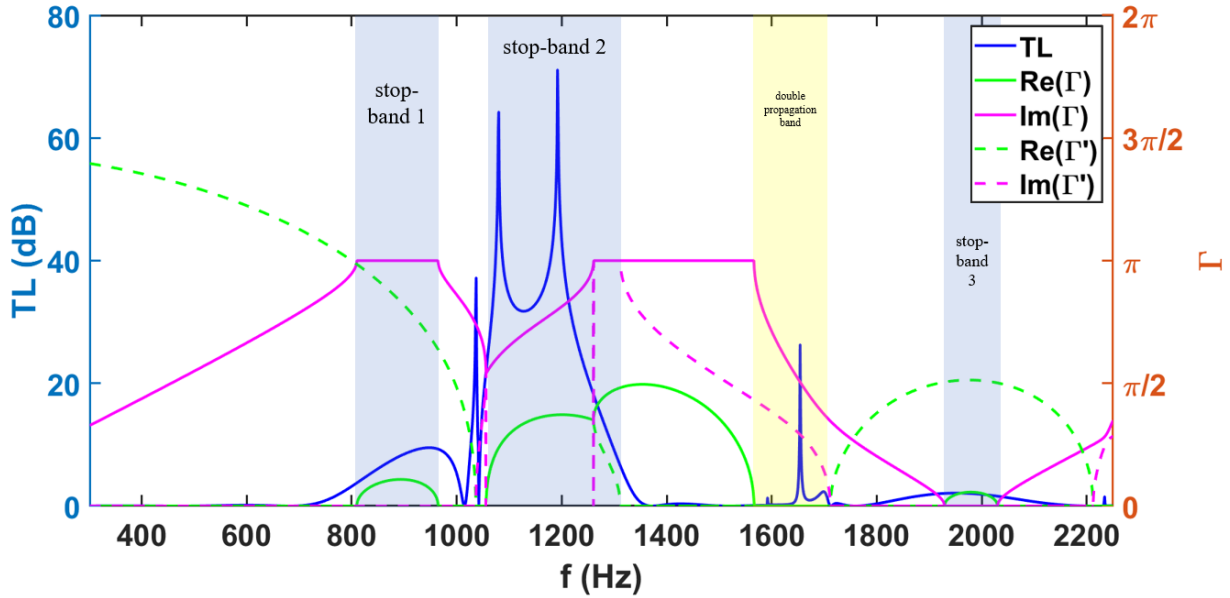


Figure 57. Transmission Loss Plot for Finite Array of Connected Helmholtz Resonators

$$N = 4, P_{in} = 94 \text{ dB}, L_r = 7 \text{ in}, L_n = 0.25 \text{ in}, \Delta L_n = 0.49 \text{ in}, S_n = 1.77 \text{ in}^2, S_d = 9 \text{ in}^2, V_c = 7 \text{ in}^3, S_{ct} = 0.11 \text{ in}^2, S_c = 2.34 \text{ in}^2, L_{ct} = 2 \text{ in}, \Delta L_{ct} = 0.03 \text{ in}, L_c = 1.5 \text{ in}$$

The results indicate that the transmission loss formula given in Equation (96) is accurate insofar as the transmission loss peaks seem to line up with the absolute stop-bands predicted from the infinite connected resonator propagation constants. In addition, the transmission loss peaks in the double-propagation band as well indicating that the two Bloch waves propagating in the same direction interfere destructively. This finding will be discussed in more detail later. This transmission loss plot will also later be compared to the results from a numerical computation in Actran to verify the accuracy. Before comparing the transmission loss plots of the connected and unconnected resonator arrays, the effect of not including the “half coupling tube” on the ends of the finite system will first be investigated (see Figure 58). As will be shown, the transmission loss plot does change slightly if the beginning and end resonators are not unit cells. In this instance, the math does not simplify quite as nicely.

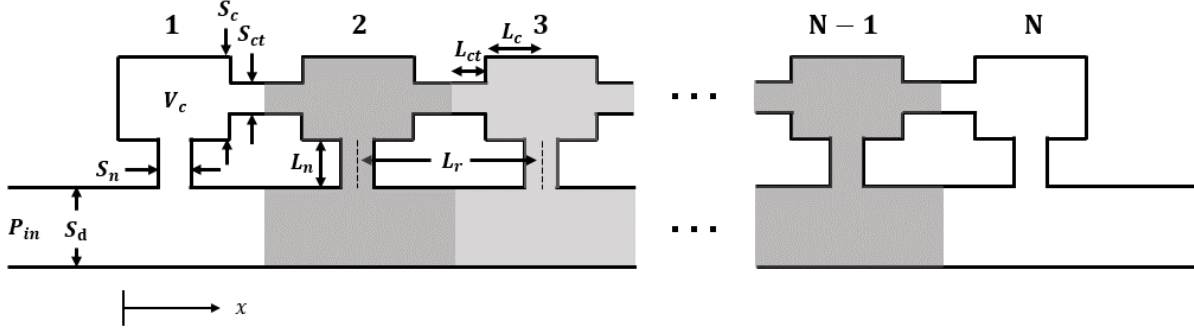


Figure 58. Finite Array of Connected Helmholtz Resonators with Non-Cellular Ends

The eigenvalues and eigenvectors remain the same since the unit cell is still defined in the same way, however, since the beginning and end resonators are not unit cells, the eigenvalue matrix will be raised to $N - 2$ rather than N , and there are two additional transfer matrices that need to be added for the first and last resonators. Following the same logic as before, this system can be expressed as

$$\begin{bmatrix} p_{t,end} \\ u_{t,end} \\ p_{b,end} \\ u_{b,end} \end{bmatrix} = \mathbb{T}_{end} \mathbb{V} \mathbb{D}^{N-2} \mathbb{V}^{-1} \mathbb{T}_{beg} \begin{bmatrix} p_{t,beg} \\ u_{t,beg} \\ p_{b,beg} \\ u_{b,beg} \end{bmatrix}$$

$$\mathbb{T}_{end} = \mathbb{T}_c \mathbb{T}_n \mathbb{T}_c \mathbb{T}_{ct} = \begin{bmatrix} \mathbf{T}_{end1} & \mathbf{0} \\ \mathbf{0} & \mathbf{T}_{end2} \end{bmatrix} = \begin{bmatrix} A_{end1} & B_{end1} & 0 & 0 \\ C_{end1} & D_{end1} & 0 & 0 \\ 0 & 0 & A_{end2} & B_{end2} \\ 0 & 0 & C_{end2} & D_{end2} \end{bmatrix} \quad (97)$$

$$\mathbb{T}_{beg} = \mathbb{T}_{ct} \mathbb{T}_c \mathbb{T}_n \mathbb{T}_c = \begin{bmatrix} \mathbf{T}_{beg1} & \mathbf{0} \\ \mathbf{0} & \mathbf{T}_{beg2} \end{bmatrix} = \begin{bmatrix} A_{beg1} & B_{beg1} & 0 & 0 \\ C_{beg1} & D_{beg1} & 0 & 0 \\ 0 & 0 & A_{beg2} & B_{beg2} \\ 0 & 0 & C_{beg2} & D_{beg2} \end{bmatrix}$$

Rearranging the 2nd and 3rd columns and 2nd and 3rd rows results in

$$\begin{bmatrix} p_{t,end} \\ p_{b,end} \\ u_{t,end} \\ u_{b,end} \end{bmatrix} = \tilde{\mathbb{T}}_{end} \begin{bmatrix} \mathbf{Z} & \mathbf{0} \\ \mathbf{0} & \mathbf{H} \end{bmatrix} \begin{bmatrix} \mathbf{C}_{N-2} & \mathbf{S}_{N-2} \\ \mathbf{S}_{N-2} & \mathbf{C}_{N-2} \end{bmatrix} \begin{bmatrix} \mathbf{Z} & \mathbf{0} \\ \mathbf{0} & \mathbf{H} \end{bmatrix}^{-1} \tilde{\mathbb{T}}_{beg} \begin{bmatrix} p_{t,beg} \\ p_{b,beg} \\ u_{t,beg} \\ u_{b,beg} \end{bmatrix}$$

$$\mathbf{C}_{N-2} = \begin{bmatrix} \cosh((N-2)\Gamma) & 0 \\ 0 & \cosh((N-2)\Gamma') \end{bmatrix}, \quad \mathbf{S}_{N-2} = \begin{bmatrix} \sinh((N-2)\Gamma) & 0 \\ 0 & \sinh((N-2)\Gamma') \end{bmatrix} \quad (98)$$

$$\tilde{\mathbb{T}}_{end} = \begin{bmatrix} \mathbf{A}_{end} & \mathbf{B}_{end} \\ \mathbf{C}_{end} & \mathbf{D}_{end} \end{bmatrix} = \begin{bmatrix} A_{end1} & 0 & B_{end1} & 0 \\ 0 & A_{end2} & 0 & B_{end2} \\ C_{end1} & 0 & D_{end1} & 0 \\ 0 & C_{end2} & 0 & D_{end2} \end{bmatrix}$$

$$\tilde{\mathbb{T}}_{beg} = \begin{bmatrix} \mathbf{A}_{beg} & \mathbf{B}_{beg} \\ \mathbf{C}_{beg} & \mathbf{D}_{beg} \end{bmatrix} = \begin{bmatrix} A_{beg1} & 0 & B_{beg1} & 0 \\ 0 & A_{beg2} & 0 & B_{beg2} \\ C_{beg1} & 0 & D_{beg1} & 0 \\ 0 & C_{beg2} & 0 & D_{beg2} \end{bmatrix}$$

This formulation does not reduce to a simple expression. Hence the best course of action for finding the transmission loss of this system for small N is to find the impedance matrix using the same methods as before but numerically instead of symbolically. Finding the impedance matrix numerically and solving for $TL = 20 \log_{10} |C_{in}^+ / C_{out}^+|$ results in the “Non-Cellular Ends” curve shown in Figure 59.

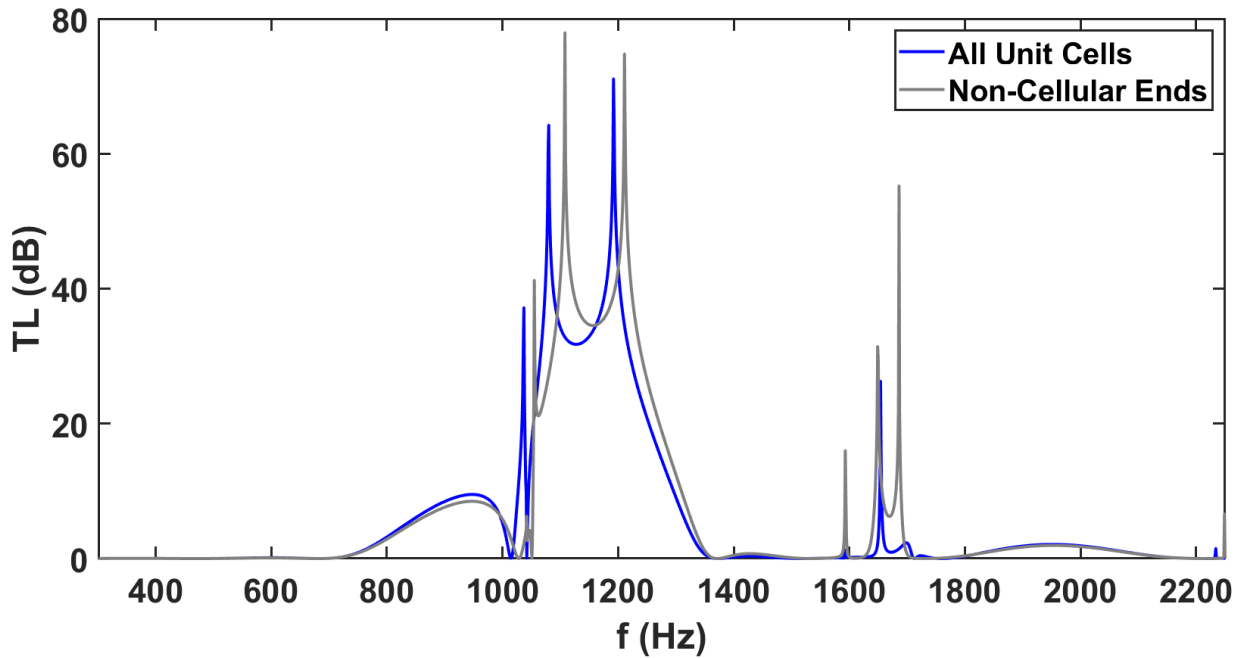


Figure 59. Comparison Between All Unit Cells and Non-Cellular Ends Systems

Based on the plot of the transmission loss of the two systems, the system with non-cellular ends (i.e., the system that does not include the half coupling tubes on the ends) does not change the results significantly. The same relative shape is observed, with peaks slightly shifted. As such, the two systems can generally be considered approximately equal. This approximation becomes even more true as the number of resonators increases since the ends then have less impact on the entire system; however, if the transmission loss is still desired for the system with non-cellular ends at higher N , the impedance matrix cannot be found numerically without singularity issues.

The best course of action in this case is to use a different representation that while slower computationally, does not run into singularity issues.

Recall from the derivation of the $\lim_{N \rightarrow \infty} TL/N$, that the N^{th} cell can be expressed as the linear combination of its eigenvectors:

$$\begin{bmatrix} p_{t,n} \\ u_{t,n} \\ p_{b,n} \\ u_{b,n} \end{bmatrix} = a_n \mathbb{V}_1 + b_n \mathbb{V}_2 + c_n \mathbb{V}_3 + d_n \mathbb{V}_4 \quad (99)$$

where a_n, b_n, c_n, d_n are complex constants for the N^{th} cell. All of the cells in the duct can thus be expressed as

$$\begin{aligned} \begin{bmatrix} p_{t,n} \\ u_{t,n} \\ p_{b,n} \\ u_{b,n} \end{bmatrix} &= \mathbb{T}_{cell} \begin{bmatrix} p_{t,n-1} \\ u_{t,n-1} \\ p_{b,n-1} \\ u_{b,n-1} \end{bmatrix} = \mathbb{T}_{cell}^2 \begin{bmatrix} p_{t,n-2} \\ u_{t,n-2} \\ p_{b,n-2} \\ u_{b,n-2} \end{bmatrix} = \dots = \mathbb{T}_{cell}^{n-1} \begin{bmatrix} p_{t,1} \\ u_{t,1} \\ p_{b,1} \\ u_{b,1} \end{bmatrix} \\ &= a_1 \mathbb{T}_{cell}^{n-1} \mathbb{V}_1 + b_1 \mathbb{T}_{cell}^{n-1} \mathbb{V}_2 + c_1 \mathbb{T}_{cell}^{n-1} \mathbb{V}_3 + d_1 \mathbb{T}_{cell}^{n-1} \mathbb{V}_4 \\ &= a_1 \lambda_1^{n-1} \mathbb{V}_1 + b_1 \lambda_2^{n-1} \mathbb{V}_2 + c_1 \lambda_3^{n-1} \mathbb{V}_3 + d_1 \lambda_4^{n-1} \mathbb{V}_4 \end{aligned}$$

where a_1, b_1, c_1, d_1 are complex constants for the 1st cell. The beginning state variables can then be related to the 1st cell via a transfer matrix as follows

$$\begin{bmatrix} p_{t,1} \\ u_{t,1} \\ p_{b,1} \\ u_{b,1} \end{bmatrix} = \mathbb{T}_{res_1} \begin{bmatrix} p_{t,beg} \\ u_{t,beg} \\ p_{b,beg} \\ u_{b,beg} \end{bmatrix} = \mathbb{T}_{ct} \mathbb{T}_c \mathbb{T}_n \mathbb{T}_c \begin{bmatrix} p_{t,beg} \\ u_{t,beg} \\ p_{b,beg} \\ u_{b,beg} \end{bmatrix} \quad (100)$$

where \mathbb{T}_{res_1} is the transfer matrix of the first resonator (which is not a unit cell). The above equation can then be rearranged such that

$$\begin{bmatrix} p_{t,beg} \\ u_{t,beg} \\ p_{b,beg} \\ u_{b,beg} \end{bmatrix} = \mathbb{T}_c^{-1} \mathbb{T}_n^{-1} \mathbb{T}_c^{-1} \mathbb{T}_{ct}^{-1} \begin{bmatrix} p_{t,1} \\ u_{t,1} \\ p_{b,1} \\ u_{b,1} \end{bmatrix} = \mathbb{T}_c^{-1} \mathbb{T}_n^{-1} \mathbb{T}_c^{-1} \mathbb{T}_{ct}^{-1} (a_1 \lambda_1 \mathbb{V}_1 + b_1 \lambda_2 \mathbb{V}_2 + c_1 \lambda_3 \mathbb{V}_3 + d_1 \lambda_4 \mathbb{V}_4) \quad (101)$$

and the end state variables can be written as

$$\begin{aligned}
\begin{bmatrix} p_{t,end} \\ u_{t,end} \\ p_{b,end} \\ u_{b,end} \end{bmatrix} &= \mathbb{T}_{resN} \begin{bmatrix} p_{t,n} \\ u_{t,n} \\ p_{b,n} \\ u_{b,n} \end{bmatrix} = \mathbb{T}_c \mathbb{T}_n \mathbb{T}_c \mathbb{T}_{ct} \begin{bmatrix} p_{t,n} \\ u_{t,n} \\ p_{b,n} \\ u_{b,n} \end{bmatrix} \\
&= \mathbb{T}_c \mathbb{T}_n \mathbb{T}_c \mathbb{T}_{ct} (a_1 \lambda_1^{n-1} \mathbf{v}_1 + b_1 \lambda_2^{n-1} \mathbf{v}_2 + c_1 \lambda_3^{n-1} \mathbf{v}_3 + d_1 \lambda_4^{n-1} \mathbf{v}_4)
\end{aligned} \tag{102}$$

where \mathbb{T}_{resN} is the transfer matrix of the last resonator (which is not a unit cell). Recalling the boundary conditions from before, this system of equations can be solved numerically for $TL = 20 \log_{10} |C_{in}^+ / C_{out}^+|$ at a much higher N .

Seeing that the analytical modeling for the finite connected resonator system has now been fully developed, the connected and unconnected resonator systems can now be compared (see Figure 60). The arrangement with non-cellular ends (i.e., no half coupling tube on the ends of the finite array) is shown in the plot to represent the connected resonator system. Ultimately, this is the case that will be used throughout the rest of the thesis to represent the connected resonator array. The reason it will be used is again because it is more space efficient to not have to include the half coupling tubes on the ends of the finite system. Since space is so limited in aircraft turbofan engine inlets, this case will thus be more relevant.

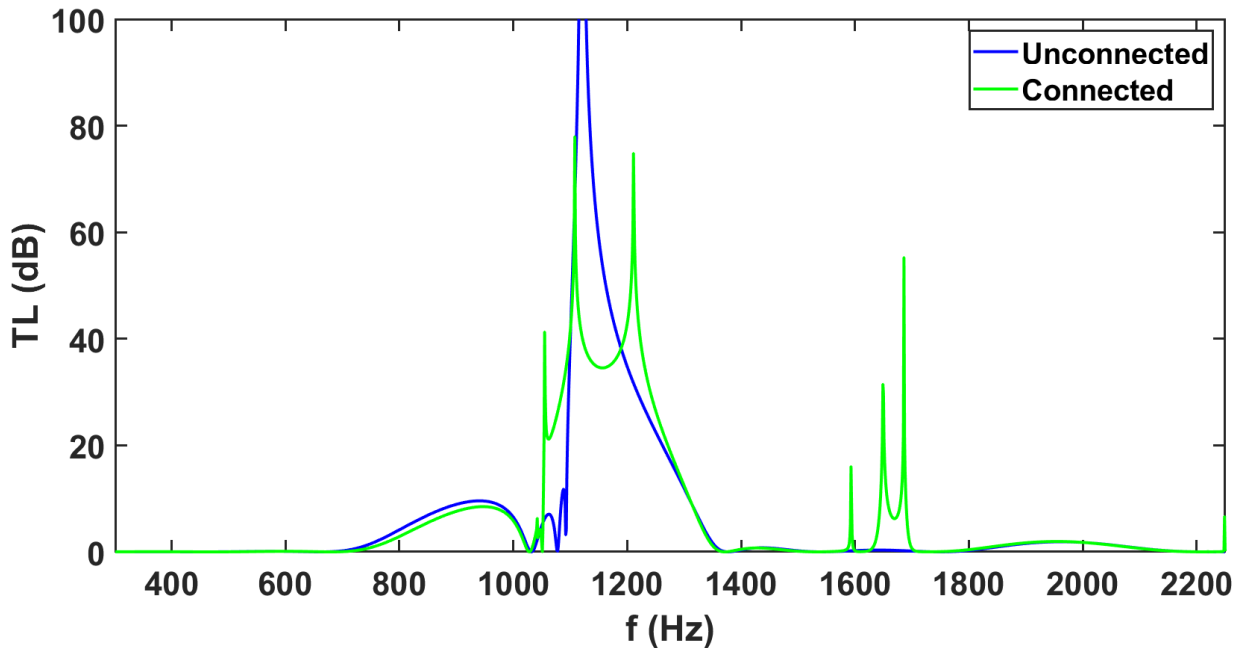


Figure 60. Connected and Unconnected Resonator Systems Comparison

$$\begin{aligned}
N = 4, P_{in} = 94 \text{ dB}, L_r = 7 \text{ in}, L_n = 0.25 \text{ in}, S_n = 1.77 \text{ in}^2, S_d = 9 \text{ in}^2, V_c = 7 \text{ in}^3, S_{ct} = 0.11 \text{ in}^2, S_c = 2.34 \text{ in}^2, L_{ct} \\
= 2 \text{ in}, \Delta L_{ct} = 0.03 \text{ in}, L_c = 1.5 \text{ in}, \Delta L_n (\text{connected}) = 0.49 \text{ in}, \Delta L_n (\text{unconnected}) = 0.67 \text{ in}
\end{aligned}$$

The transmission loss plots are similar for the most part, but with key differences. The Bragg-type peaks at 960 and 1930 Hz remain unchanged because the spacing of the resonators is the same in both systems. The transmission loss peak due to the resonant frequency of the Helmholtz resonator at 1120 Hz is no longer as strong for the connected resonators case because some energy is now getting transferred through the connected cavities; in turn however, the peak widens. The new set of peaks between 1590-1700 Hz were not evident in the unconnected system, meaning these peaks result from connecting the resonator cavities together. Recall from the infinite connected resonator study that this frequency range makes up the double propagation band. The transmission loss peaks in this range are therefore the result of the interaction of the two traveling Bloch waves, one in the duct and one through the connected resonators. Based on all of these observations, connecting the resonators offers clear advantages over the unconnected resonator case. More specific conclusions will be drawn in the parameter study to come. First, however, this model needs to be verified against a numerical Actran model.

3.3. Numerical modeling of an array of connected Helmholtz resonators

The purpose of the numerical modeling is solely to verify the accuracy of the analytical modeling. Again, the numerical modeling tool of choice was Actran.

To begin the numerical modeling process, a mesh of the system needed to be defined. A CAD model of the fluid domain of the system was created in SolidWorks (see Figure 61) with the same dimensions as the analytical model for the connected resonator array. The geometry was selected such that the system could eventually be tested on the grazing incidence impedance tube at the Center for Aerospace Acoustics (as will be shown in a future section).

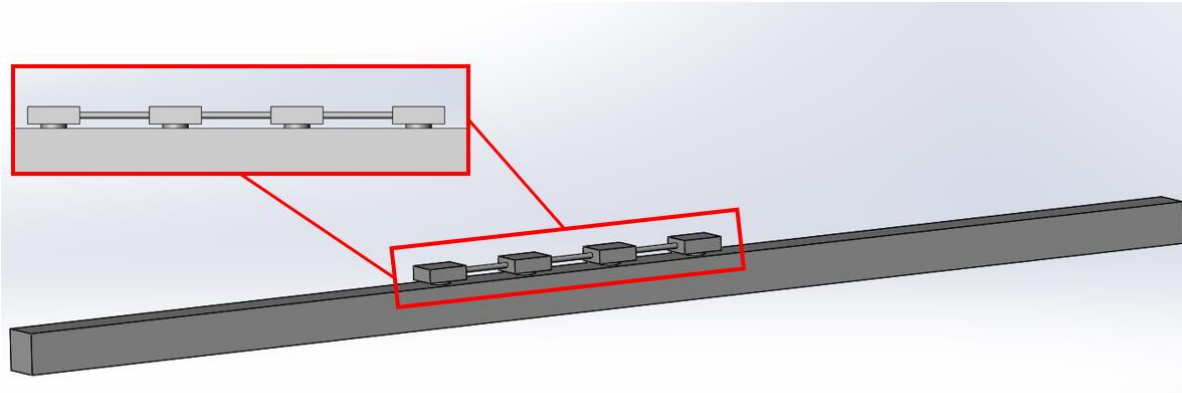


Figure 61. CAD Model of Grazing Impedance Tube Lined with Four Connected Helmholtz Resonators

$$N = 4, P_{in} = 94 \text{ dB}, L_r = 7 \text{ in}, L_n = 0.25 \text{ in}, S_n = 1.77 \text{ in}^2, S_d = 9 \text{ in}^2, V_c = 7 \text{ in}^3, S_{ct} = 0.11 \text{ in}^2, S_c = 2.34 \text{ in}^2, L_{ct} = 2 \text{ in}, L_c = 1.5 \text{ in}$$

For the array of coupled Helmholtz resonators, the block topology (see Figure 62) was chosen as follows: a block for an untreated portion of the duct, a block for a coupling tube, a block for the neck of a resonator, a block for the cavity of the resonator, a block for a treated portion of the duct (directly under the resonator), and so on for all of the other resonators, coupling tubes, and duct segments in the array.

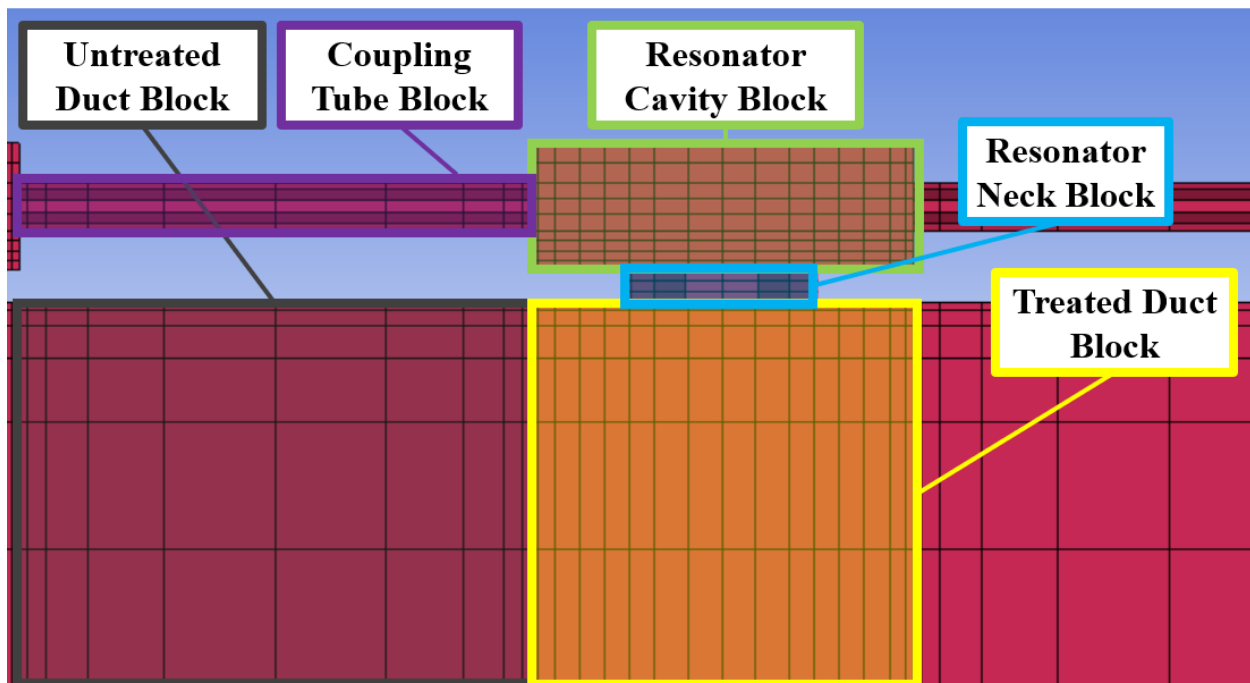


Figure 62. Block Topology for Part of the Coupled Helmholtz Resonator Array

Ansys ICEM CFD was again used to generate the mesh (shown in Figure 63 and Figure 64), and the mesh data was then outputted from ICEM CFD and read into Actran.

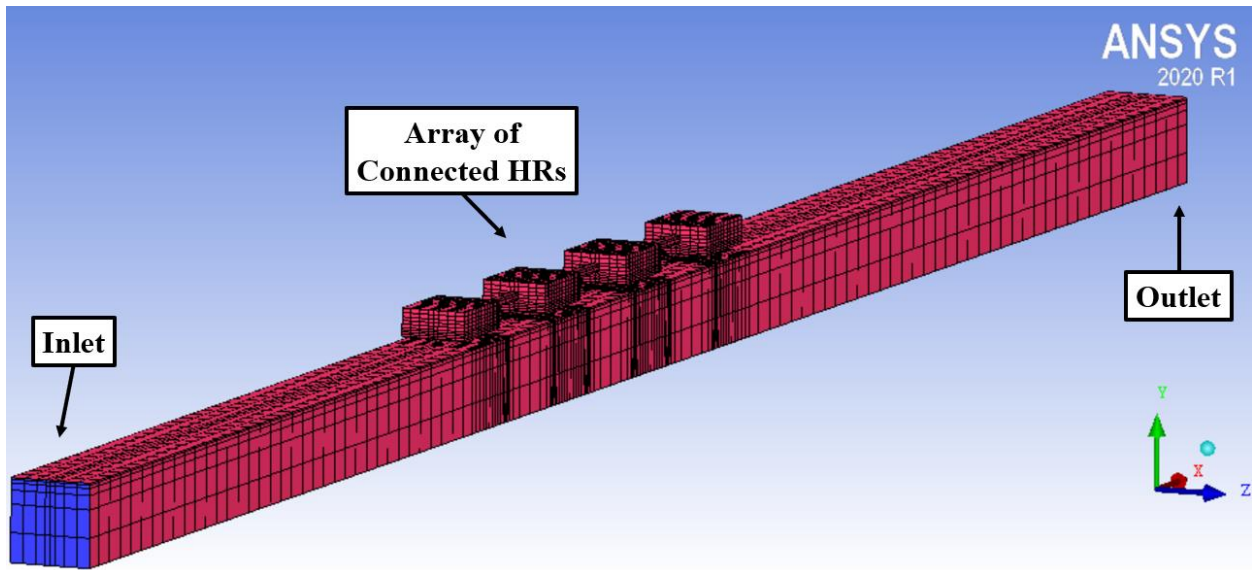


Figure 63. Mesh of Grazing Impedance Tube Lined with Four Connected Helmholtz Resonators – Isometric View

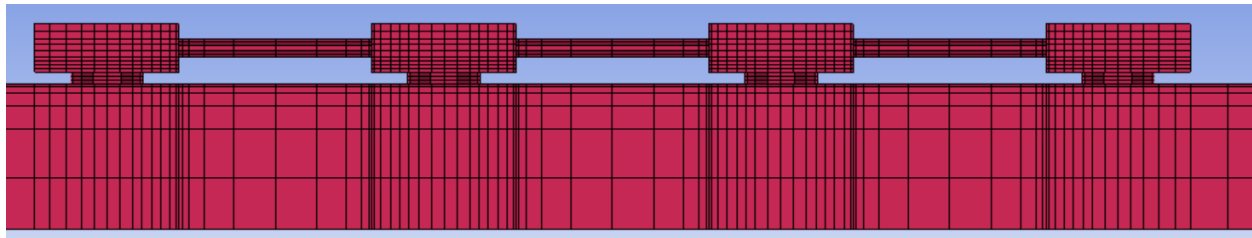


Figure 64. Mesh of Grazing Impedance Tube Lined with Four Connected Helmholtz Resonators – Side View

The transmission loss for this numerical model is shown in Figure 65. Three color maps of the acoustic pressure along the duct (in dB) were generated: Figure 66 for the first Bragg reflection frequency, Figure 67 for the Helmholtz resonant frequency, and Figure 68 for the first peak of the double-propagation band.

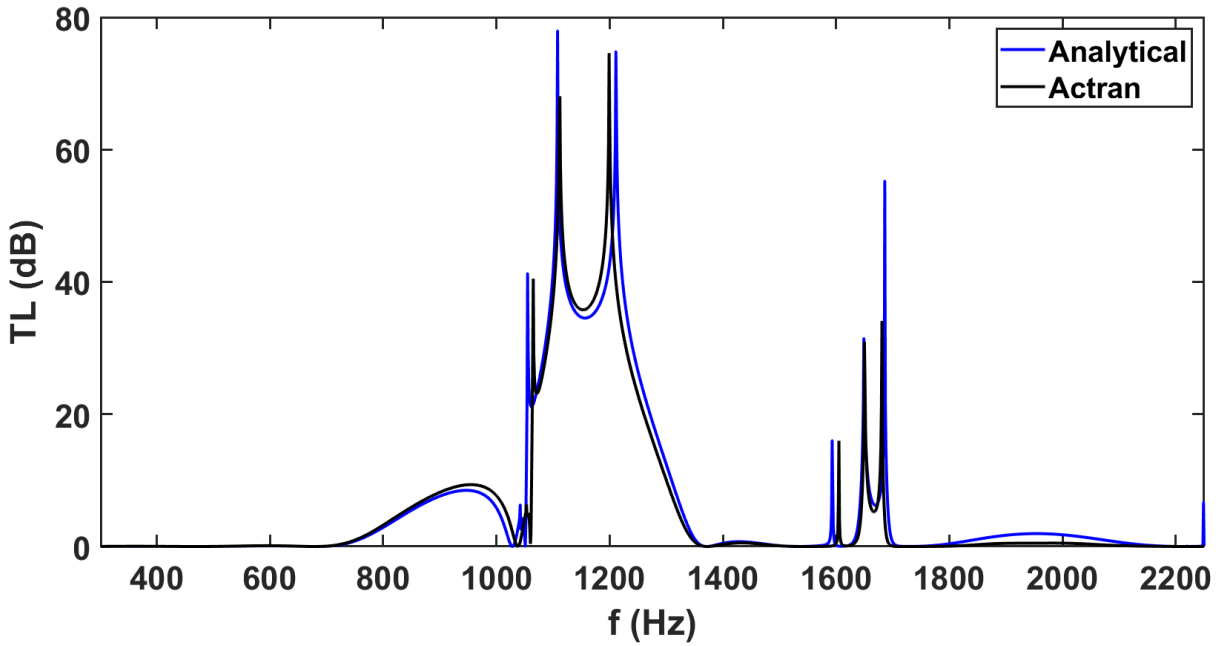


Figure 65. Numerical Solution for Transmission Loss Across Impedance Tube Lined with Four Connected Helmholtz Resonators

$N = 4, P_{in} = 94 \text{ dB}, L_r = 7 \text{ in}, L_n = 0.25 \text{ in}, \Delta L_n = 0.49 \text{ in}, S_n = 1.77 \text{ in}^2, S_d = 9 \text{ in}^2, V_c = 7 \text{ in}^3, S_{ct} = 0.11 \text{ in}^2, S_c = 2.34 \text{ in}^2, L_{ct} = 2 \text{ in}, \Delta L_{ct} = 0.03 \text{ in}, L_c = 1.5 \text{ in}$

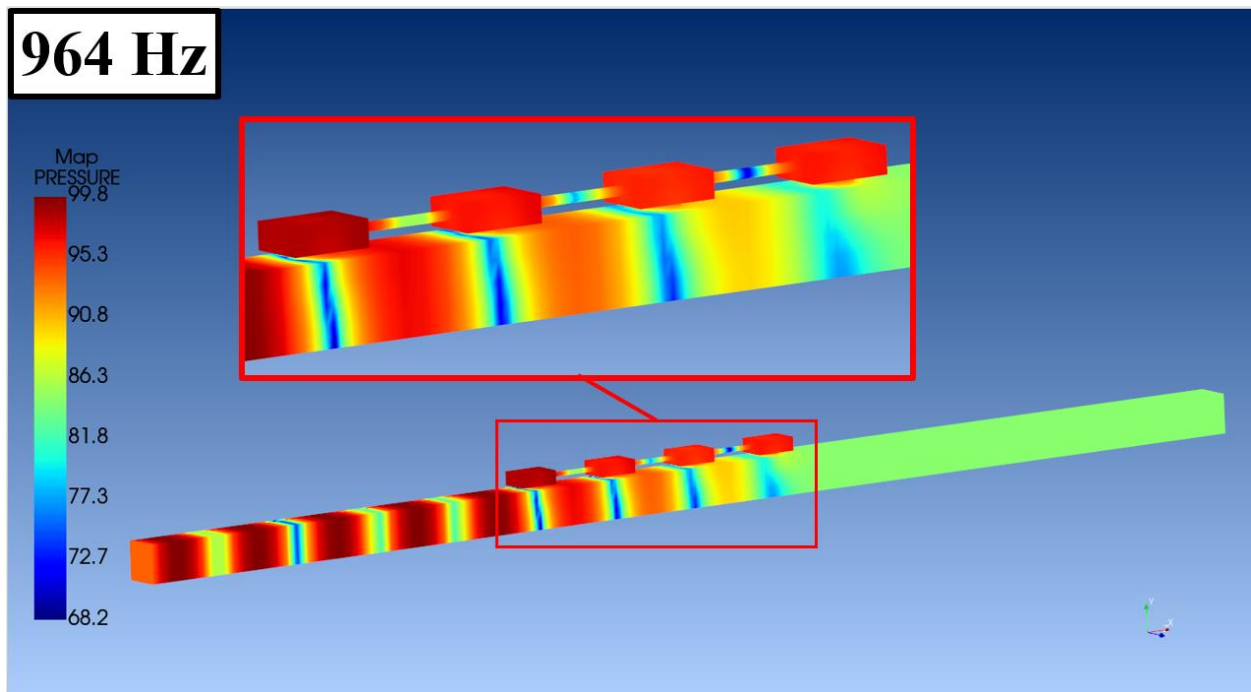


Figure 66. Color Map of Acoustic Pressure in dB for the Impedance Tube Lined with Four Connected Helmholtz Resonators at First Bragg Reflection Frequency

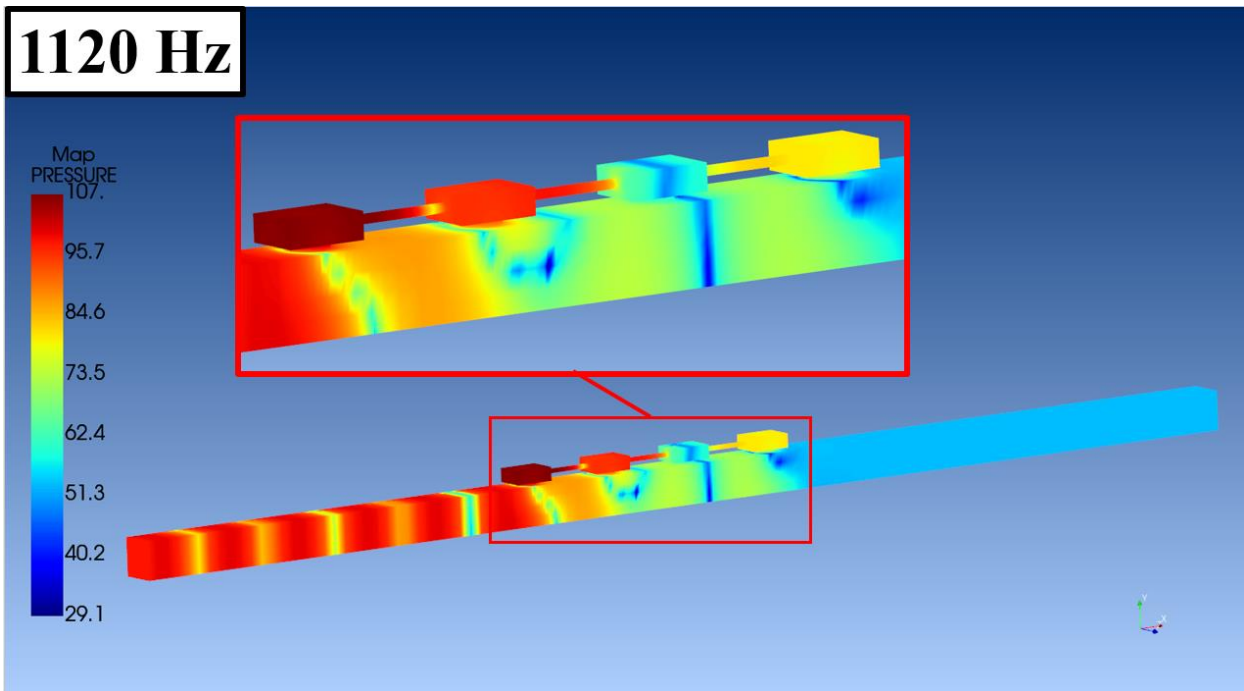


Figure 67. Color Map of Acoustic Pressure in dB for the Impedance Tube Lined with Four Connected Helmholtz Resonators at Second Stop-Band Frequency

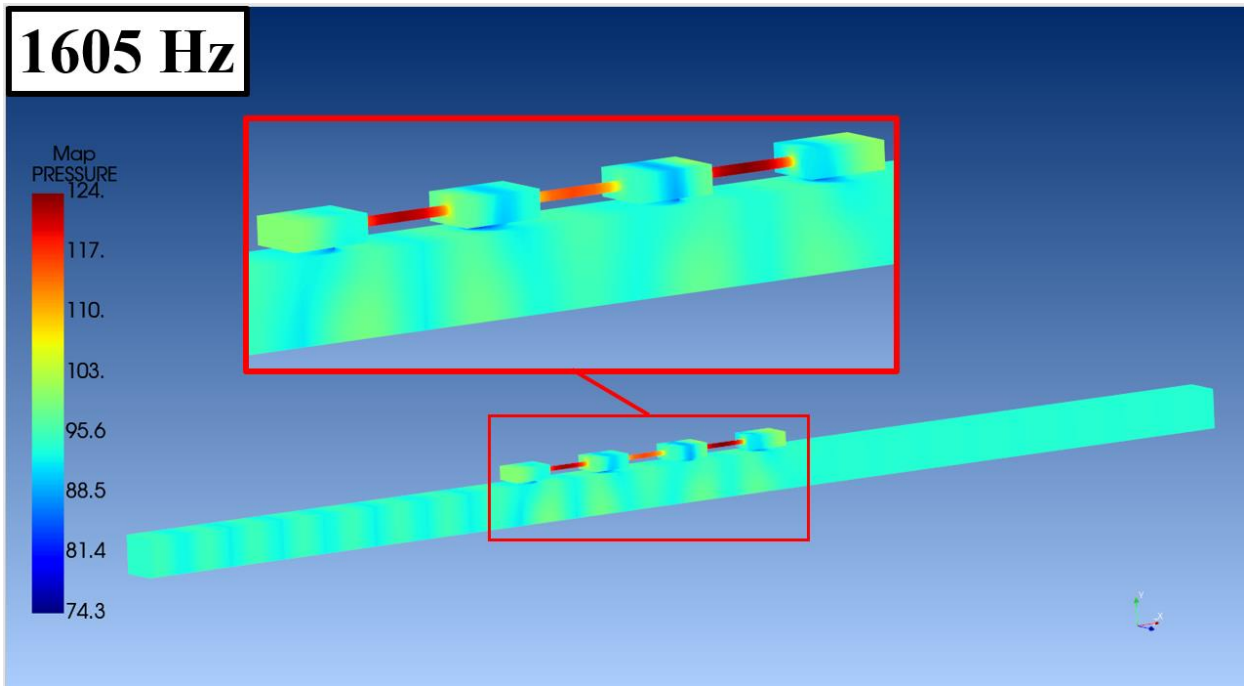


Figure 68. Color Map of Acoustic Pressure in dB for the Impedance Tube Lined with Four Connected Helmholtz Resonators at First Peak Frequency in Double-Propagation Band

According to Figure 65 the numerical solution lines up almost exactly with the analytical solution for the connected array of Helmholtz resonators without the half coupling tubes on the

ends. The analytical solution is thus assumed to be considered an accurate formulation. Note that there is a slight difference in the two curves which is most likely due to a small error in the end corrections applied to the necks and the coupling tubes, but the difference between the curves is small enough to be considered relatively insignificant. In a later section, the experimental results of this geometry on the impedance tube will be shown to further validate these findings.

This system is considered an extended-reacting system and thus has a varying acoustic impedance value along the liner [11]. Actran was used to verify that the acoustic impedance varied at each axial location containing a resonator (see Figure 69 and Figure 70 for the impedance at the first two stop-band frequencies and Figure 71 for the impedance at the first peak of the double-propagation band).

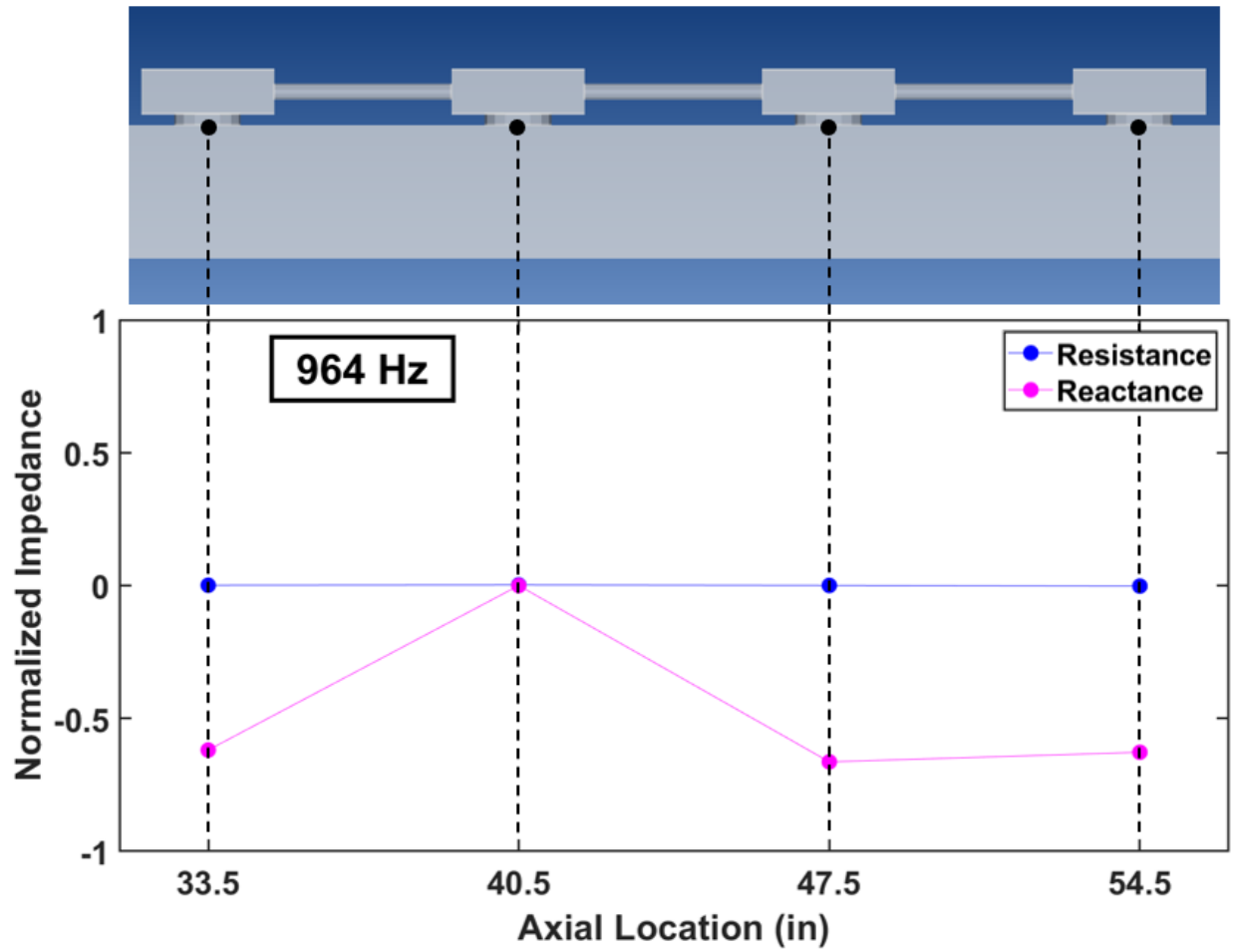


Figure 69. Normalized Acoustic Impedance for Connected Helmholtz Resonator Array Solved Using Actran - First Bragg Reflection Frequency

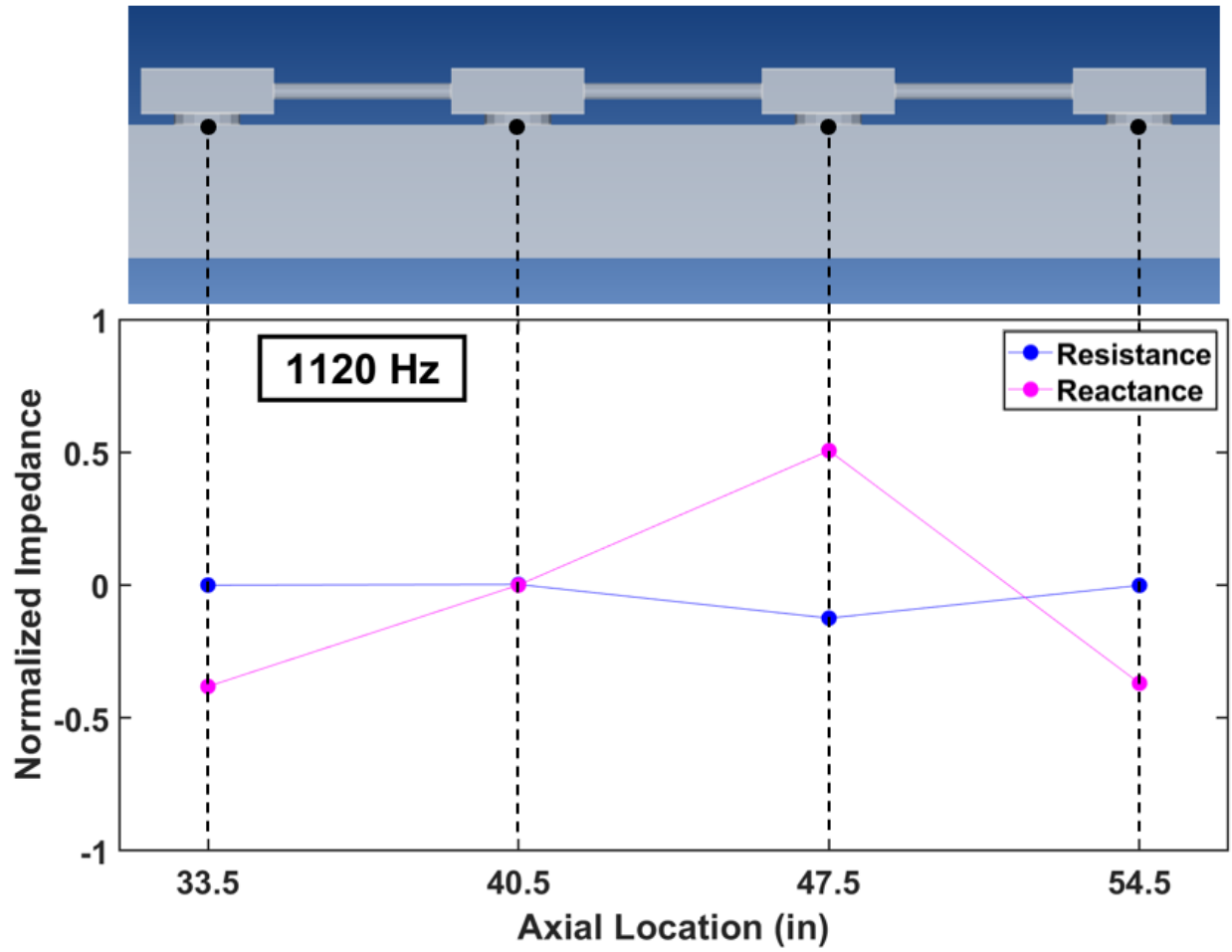


Figure 70. Normalized Acoustic Impedance for Connected Helmholtz Resonator Array Solved Using Actran – Helmholtz Resonant Frequency

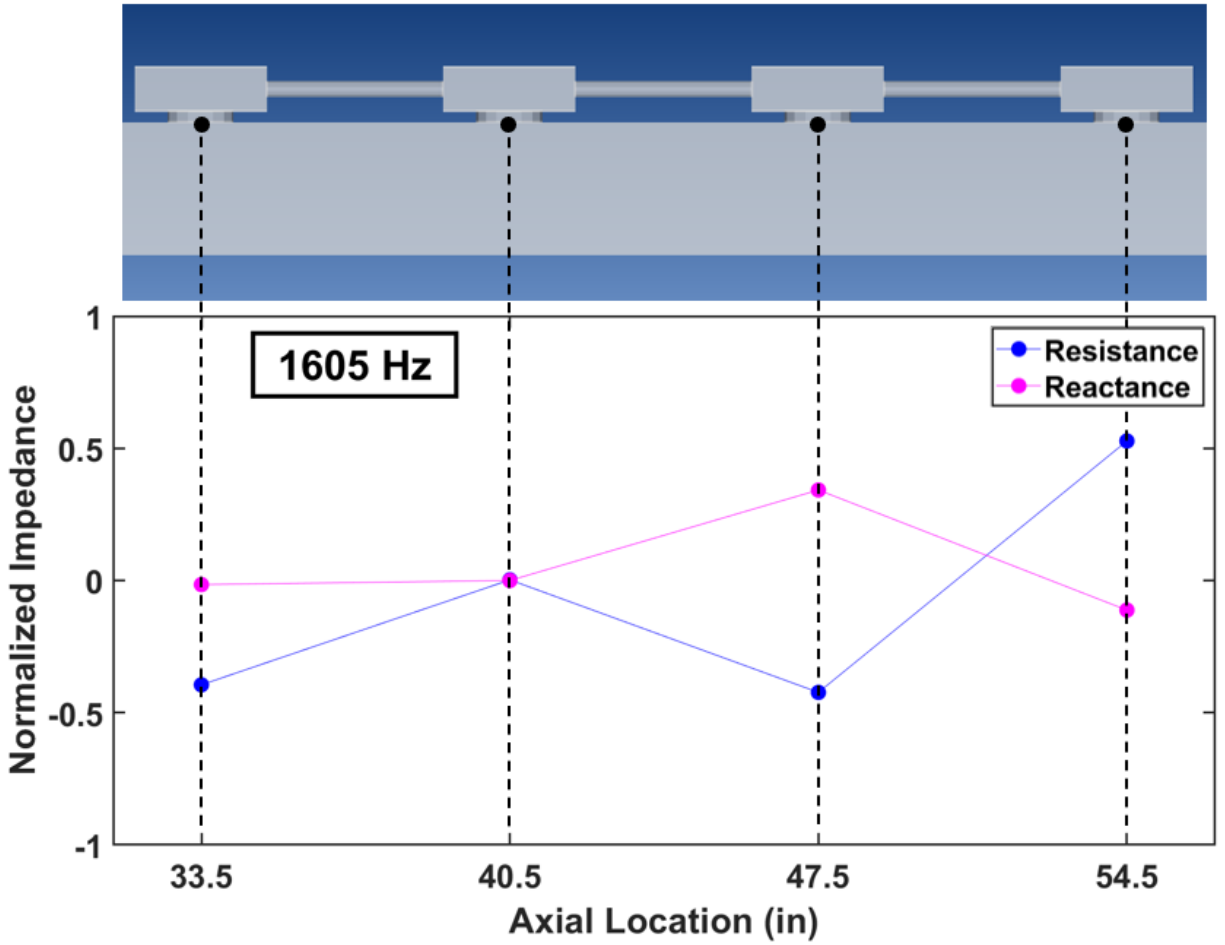


Figure 71. Normalized Acoustic Impedance for Connected Helmholtz Resonator Array Solved Using Actran - First Peak Frequency in Double-Propagation Band

3.4. Parameter studies of an array of connected Helmholtz resonators

Now that the modeling has been sufficiently developed, the parameters can be explored to better understand their impact on the transmission loss using the analytical model for the array of connected Helmholtz resonators (without half coupling tubes on the ends of the first and last resonators). The effect of various parameters have already been alluded to previously in this paper, but now those claims will be verified. Table 1 lists the various parameters and how they have been modified.

Table 1. Connected Helmholtz Resonator Parameter Values to be Evaluated in Inches

Neck Length L_n (in.)	0.125	0.25	0.375	0.5	0.625	x	x	x
Neck Diameter D_n (in.)	1.0	1.25	1.5	1.75	2.0	x	x	x
Cavity Height H_c (in.)	0.5	1.0	1.5	2.0	2.5	x	x	x
Coupling Tube Length $2L_{ct}$ (in.)	2.75	3.0	3.25	3.5	3.75	4.0	4.25	4.5
Resonator Spacing L_r (in.)	6.0	7.0	8.0	9.0	10.0	11.0	x	x
Coupling Tube Diameter D_{ct} (in.)	0.125	0.375	0.625	0.875	x	x	x	x
Number of Resonators N	4	10	100	∞	x	x	x	x

The original parameters used in the analytical modeling of the previous section will be considered the baseline and are shown in bold font in the table for reference. The transmission loss plot for this baseline case is repeated here in Figure 72 for clarity. Notice how the bands of interest are highlighted, and the Helmholtz resonant frequency f_{HR} and Bragg reflection frequencies f_{Bragg} are identified. The stop bands resulting from Bragg reflection are highlighted in blue, the stop band from the Helmholtz resonant frequency are highlighted in red, and the double propagation bands are highlighted in green. Recall that the double propagation bands contain the frequencies in which both forward traveling Bloch waves are propagating which leads to destructive interference and hence increased transmission loss.

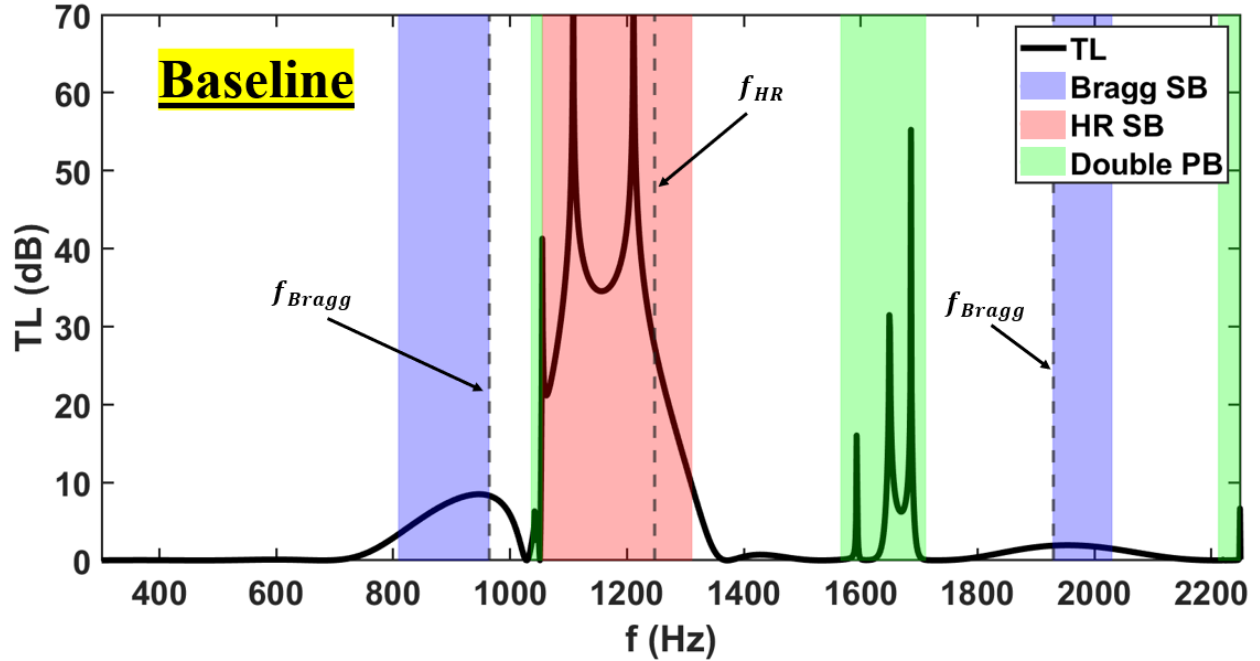


Figure 72. Baseline Case used for Parameter Study – Finite Array of Connected Helmholtz Resonators with Non-Cellular Ends

For each parameter change, the baseline parameters will be fixed, so as to only examine the modification of one parameter at a time. Conducting a parameter study in this way will allow for a better understanding of how each individual parameter affects the transmission loss of the system. The locations of the Bragg reflection stop bands, Helmholtz resonance stop-band, and double propagation bands will also be identified on each plot to help explain the resulting transmission loss. The results presented next are from the analytical model of the finite array of connected Helmholtz resonators with non-cellular ends (half coupling tubes not included on the ends of the first and last resonators of the system, repeated here in Figure 73 for clarity).

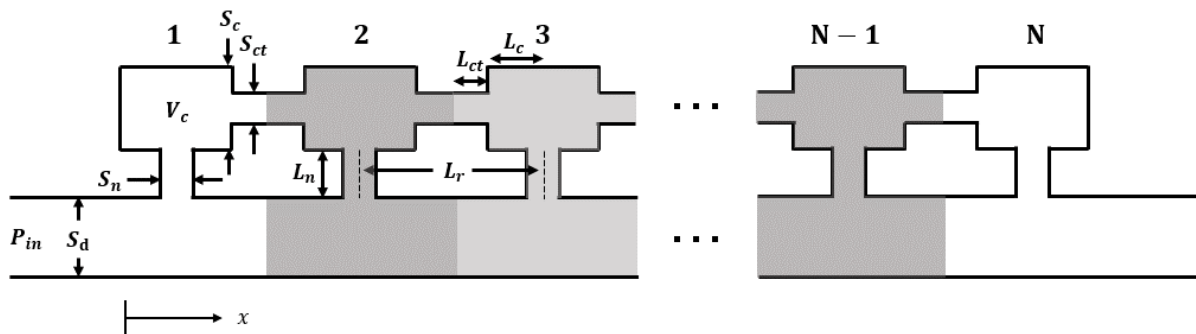


Figure 73. Finite Array of Connected Helmholtz Resonators with Non-Cellular Ends

3.4.1. Change in neck length

The first parameter of this study is the neck length. The effect of neck length on the transmission loss is plotted in the figures below from the lowest to highest values given in Table 1. The first value of the neck length is 0.125 in., and the results are plotted in Figure 74.

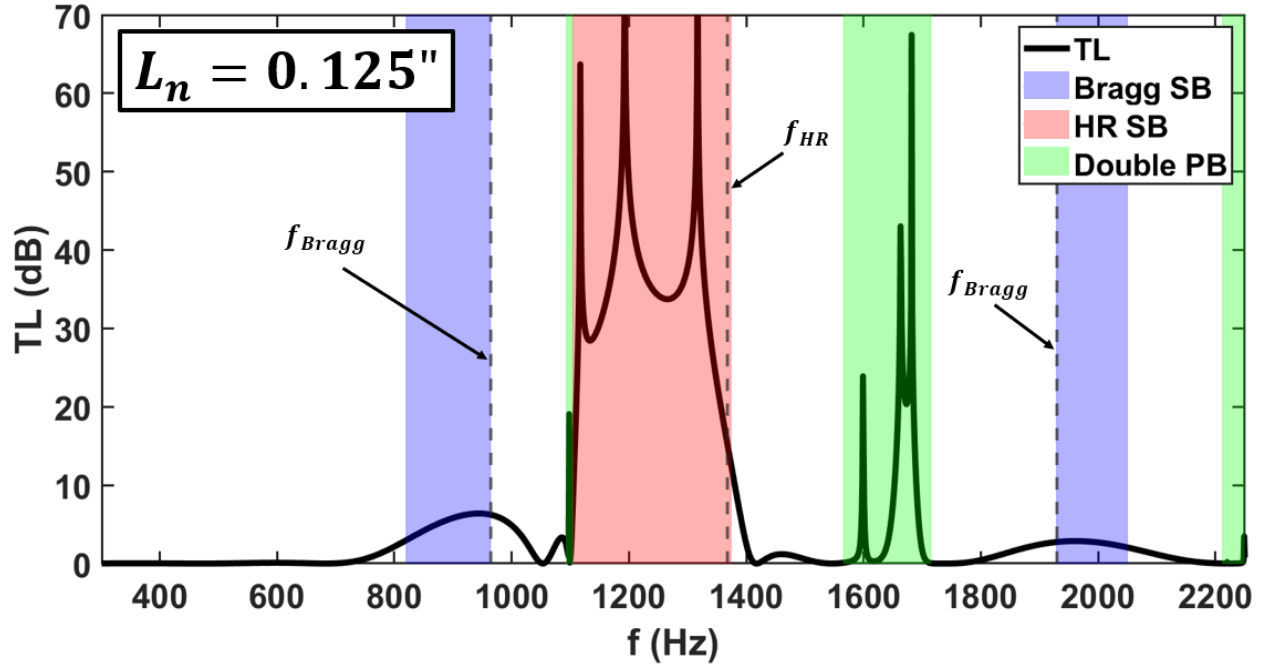


Figure 74. Neck Length = 0.125 in.

When the neck length is 0.125 in., the transmission loss plot shape, the locations of the stop bands, and the location of the double propagation band are all relatively similar to the baseline. The large peaks in the Helmholtz resonance stop band have shifted slightly farther to the right than the baseline. According to the formula for the Helmholtz resonant frequency,

$$f_{HR} = \frac{c}{2\pi} \sqrt{\frac{S_n}{V_c(L_n + \Delta L_n)}} \quad (103)$$

the Helmholtz resonant frequency should be ~1368 Hz which is ~120 Hz higher than the baseline. Because the Helmholtz resonant frequency has shifted to the right, the fact that the Helmholtz resonance stop band has also shifted to the right is logical.

Despite the Helmholtz resonant frequency shifting to the right, the Bragg reflection frequencies have not moved. Recall that the Bragg reflection frequencies occur when the resonator spacing is a multiple of a half of a wavelength, or

$$f_{Bragg} = m \frac{c}{2L_r}, (m = 1, 2, \dots) \quad (104)$$

Because the Bragg reflection frequencies are determined by the spacing of the resonators, then they should remain constant in this study since the resonator spacing is held constant. In this case and for all the cases that follow in this neck length study, the Bragg frequencies are 964 Hz and 1929 Hz. Since there are multiple Bragg frequencies, the “first Bragg frequency” will refer to the lower of the two, while the “second Bragg frequency” will refer to the higher and likewise with the Bragg stop bands. The Bragg stop bands align closely with the Bragg frequencies. The transmission loss within these stop bands, however, has changed slightly. Within the first Bragg stop band (~820-970 Hz), the transmission loss has decreased slightly from the baseline while the second Bragg-type stop band (~1930-2050 Hz) has seen an increase in transmission loss. Because the Helmholtz resonance stopband has moved to the right while the second Bragg stop band has simultaneously seen an increase in transmission loss, then this result indicates that as the Helmholtz resonance stop band approaches a Bragg stop band, the effects of the two phenomena combine: local resonance and Bragg reflection are both occurring at similar frequencies causing a large reflection of energy back towards the inlet and hence, large transmission loss in the Bragg stop band. On the other hand, as the Helmholtz resonance stop band moves farther away from the Bragg stop band (as is the case with the first Bragg stop band), this combination phenomenon does not occur and less energy gets reflected, so the transmission loss decreases.

The double propagation band has not changed in location or width compared to the baseline (1565-1710 Hz); however, the transmission loss peaks inside the double propagation band have increased. This result occurs because as the neck length decreases, the coupled-cavity waveguide and the duct become closer together and thus more interaction between the waves traveling through each path can occur. The more the waves can interact, the greater the potential for destructive interference and thus higher transmission loss. Alternatively, the longer the neck length is, the larger the distance between the two paths becomes, and the less likely the waves

will interact, leading to less destructive interference and less transmission loss. The next value of the neck length is 0.25 in. (recall that this is the baseline case), and the results are plotted in Figure 75.

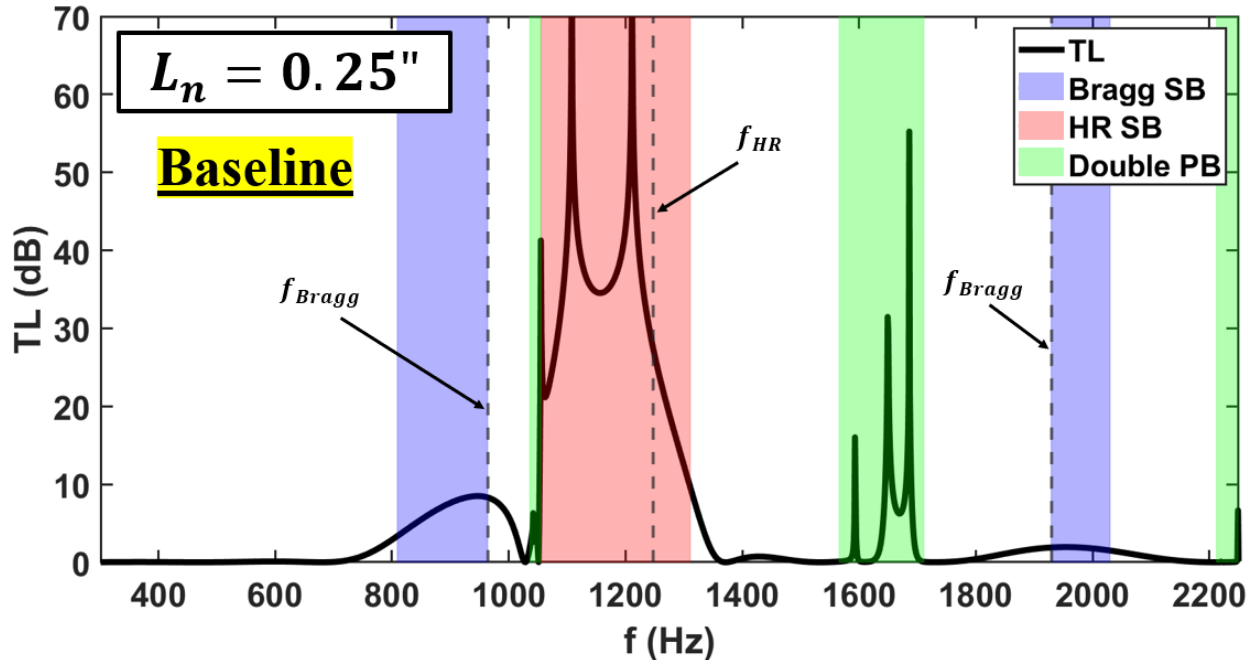


Figure 75. Neck Length = 0.25 in.

Since the neck length is longer than the previous case, according to the formula for the Helmholtz resonant frequency (Equation 103), the resonant frequency decreases. As such, the Helmholtz stop band shifts to the left. The Bragg frequencies remain in the same place because the resonator spacing is held constant; however, the first Bragg stop band (810-960 Hz) has seen an increase in transmission loss compared to the previous case, and the second Bragg stop band (~1930-2030 Hz) has seen a decrease in transmission loss. The reason the transmission loss has shifted in these regions is the same reason as in the previous case, only this time, the Helmholtz resonance stop band has moved closer to the first Bragg stop band and farther from the second: the local resonances and the Bragg reflection occur at frequencies that are closer together and hence the effects from each phenomenon get combined to produce larger energy reflection and thus increased transmission loss in the first Bragg stop band.

The double propagation band is exactly the same as the previous case, except the transmission loss peaks within the band have decreased. This result occurs because the longer the neck length is, the larger the distance between the two paths become, and the less the waves

will interact, leading to less destructive interference and less transmission loss. The next value of the neck length is 0.375 in., and the results are plotted in Figure 76.

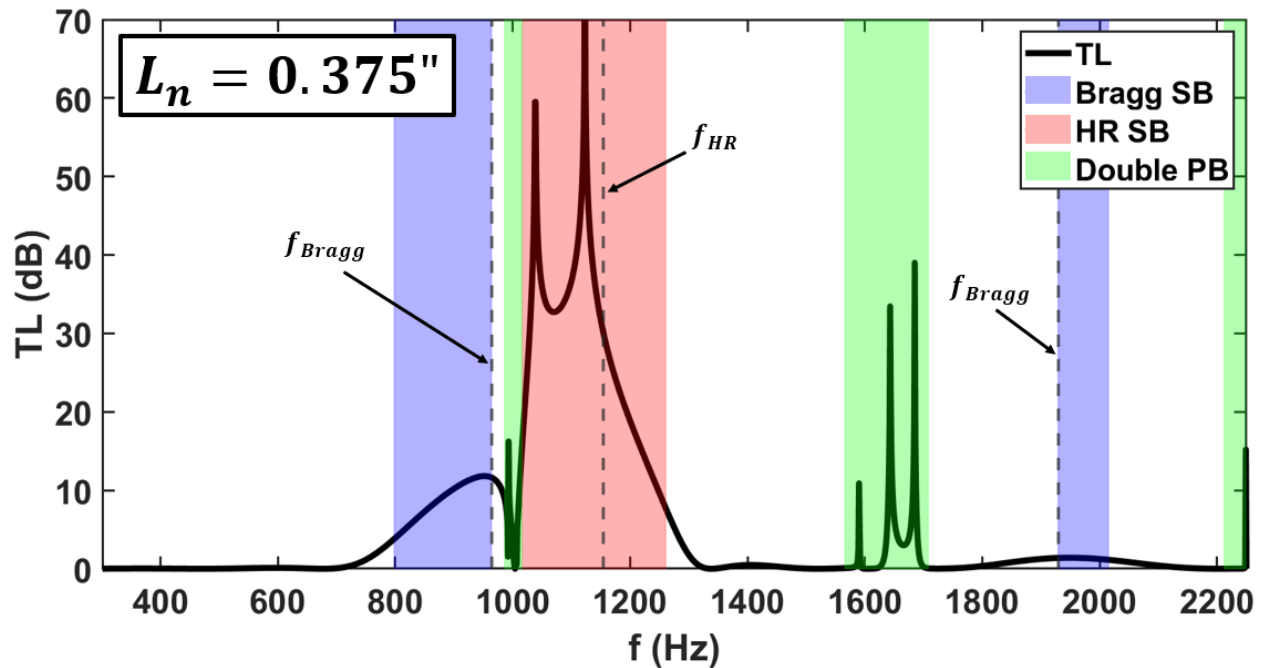


Figure 76. Neck Length = 0.375 in.

Again, an increase in the neck length causes the Helmholtz resonant frequency to decrease and the Helmholtz stop band to shift to the left. As the Helmholtz stop band approaches the first Bragg stop band, the transmission loss within the first Bragg stop band increases, while the transmission loss inside the second Bragg stop band decreases. The effects of local resonance and Bragg reflection occur at frequencies that are close in value and hence, the two phenomena combine to reflect large amounts of energy which increases the transmission loss in the first Bragg stop band. The transmission loss peaks in the double propagation band decrease in magnitude because as the neck length gets longer, the waves traveling through the coupled-cavity waveguide and the duct do not interact as much meaning that less destructive interference occurs. The next value of the neck length is 0.5 in., and the results are plotted in Figure 77.

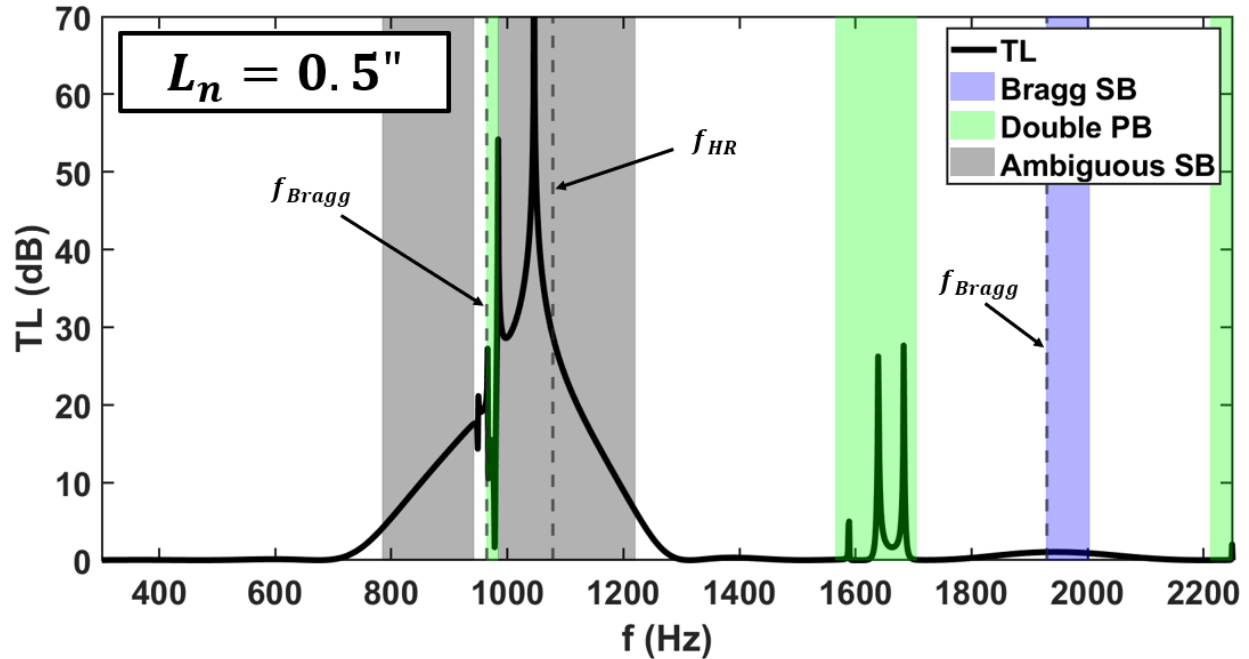


Figure 77. Neck Length = 0.5 in.

The neck length is now longer than the previous case, meaning that the Helmholtz resonant frequency is lower. The Helmholtz resonant frequency and the Bragg reflection frequency are now even closer together than in previous cases. In fact, they are now so close together, that the transmission loss peaks from these individual phenomena have lumped together into one curve. Also, it is unclear which stop band is which in this region. In previous cases, the leftmost stopband was always the Bragg stop band, but in this case, the Bragg frequency occurs outside of the leftmost stop band. The Helmholtz resonant frequency occurs outside of the leftmost stop band as well, making the physical origins of this stop band ambiguous. The ambiguity in the stop bands in this region is a result of all three physical phenomena occurring simultaneously (i.e., Bragg reflection, Helmholtz resonance, and a thin double propagation band in between, all occurring within frequencies quite close together). Because all three phenomena are occurring at similar frequencies, the precise locations of these stop bands are thus expected to shift slightly (from where they would normally be situated if they were occurring independently of the other three) due to these combined effects. The last value of the neck length is 0.625 in., and the results are plotted in Figure 78.

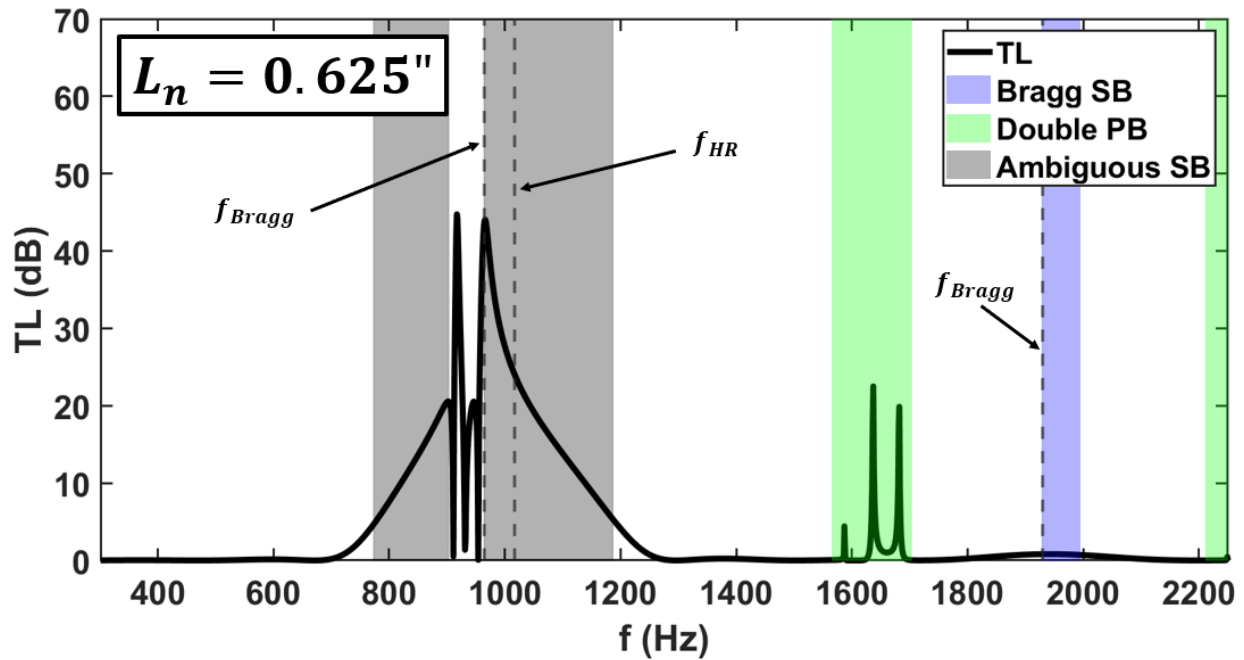


Figure 78. Neck Length = 0.625 in.

The neck is now longer than the previous cases, and the Helmholtz resonant frequency has again shifted further to the left. The effects of the Helmholtz resonance and Bragg reflection are both occurring at close to the same frequency, and hence their effects are being combined. Like in the previous case, the combination of these effects leads to one lumped peak in the transmission loss but ambiguity in the physical origins of the stop bands. The transmission loss peaks in the double propagation band (1565-1710 Hz) have further decreased in value because as the necks get longer, the waves traveling through the coupled-cavity waveguide and the duct interfere less. All of these transmission loss curves are overlaid in Figure 79 for reference.

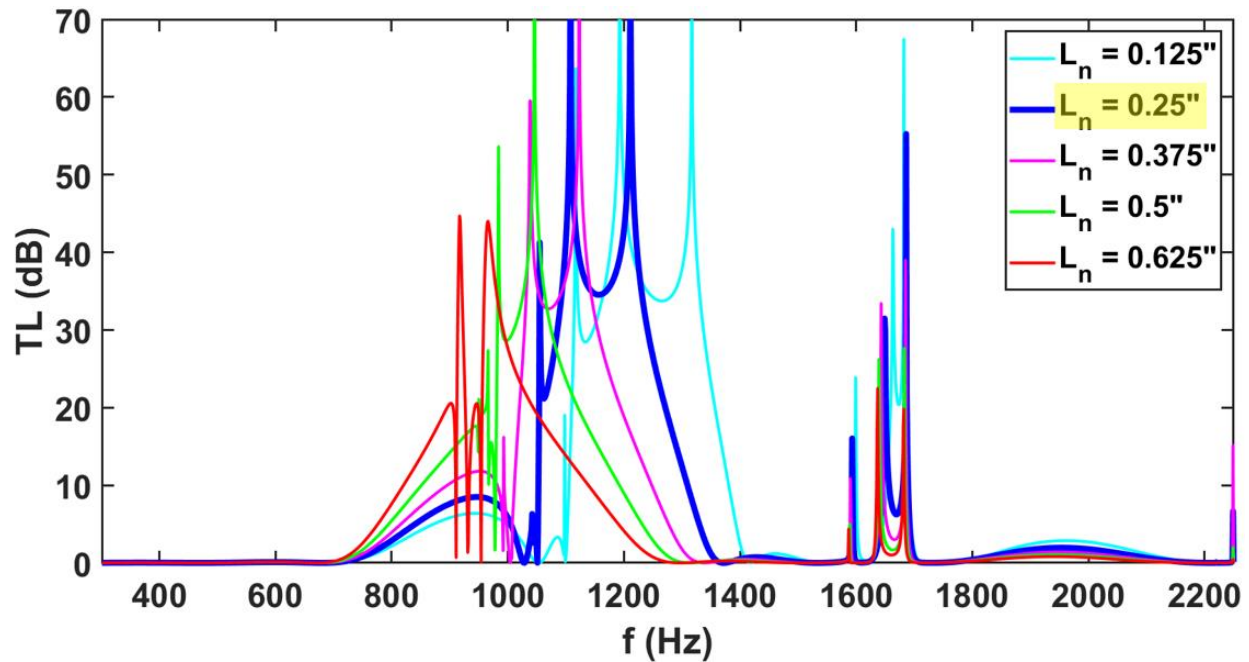


Figure 79. Effect of Neck Length on Transmission Loss – All Plots Combined

In summary, as the neck length increases, the Helmholtz resonant frequency decreases, while the Bragg frequencies and the location of the double propagation band remain constant. As the Helmholtz resonant frequency gets closer to the first Bragg frequency with increasing neck length, the effects of the two phenomena combine together into one lumped transmission loss curve while the magnitude of the transmission loss near the second Bragg frequency decreases. The peaks in the double propagation band decrease with increasing neck length because as the neck gets longer, the spacing between the coupled-cavity waveguide and the main duct increases, which limits the interaction of the waves traveling through each path. If the waves interact less, then there is less opportunity for destructive interference and hence transmission loss.

3.4.2. Change in neck diameter

The next parameter of this study is the neck diameter. The effect of neck diameter on the transmission loss is plotted in the figures below from the lowest to highest values given in Table 1. The first value of the neck diameter is 1.0 in., and the results are plotted in Figure 80.

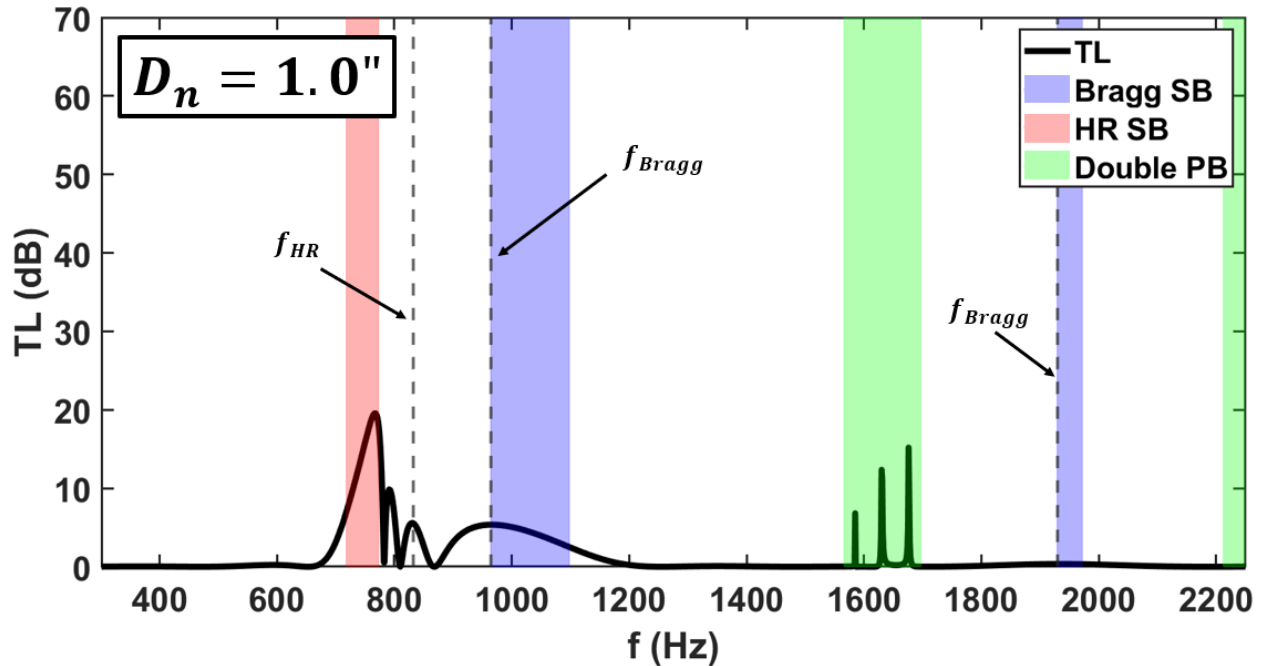


Figure 80. Neck Diameter = 1.0 in.

When the neck diameter is 1.0 in., the transmission loss plot looks quite different from the baseline case. According to the Helmholtz resonant frequency formula,

$$f_{HR} = \frac{c}{2\pi} \sqrt{\frac{S_n}{V_c(L_n + \Delta L_n)}} \quad (105)$$

the Helmholtz resonant frequency is 832 Hz, which is 415 Hz lower than the baseline. As such, the Helmholtz resonance stop band has shifted to the left on the plot along with the transmission loss peak within the band. Note that the Helmholtz resonant frequency is actually outside of the Helmholtz resonance stop band. Slight discrepancies like this are to be expected since the addition of coupling tubes to the cavities is going to change the Helmholtz resonant frequency to a different value than that of a classical Helmholtz resonator without coupling tubes; therefore, the classical Helmholtz resonant frequency formula given in Equation (105) should be treated more so as an approximation of the resonant frequency, while the Helmholtz resonance stop band should be considered a more accurate frequency range in which resonance occurs. Nonetheless, both will be plotted for comparison purposes.

Despite the Helmholtz resonant frequency shifting to the right, the Bragg reflection frequencies have not moved. Recall that the Bragg reflection frequencies occur when the resonator spacing is a multiple of a half of a wavelength, or

$$f_{Bragg} = m \frac{c}{2L_r}, (m = 1, 2, \dots) \quad (106)$$

Because the Bragg reflection frequencies are determined by the spacing of the resonators, then they should remain constant in this study since the resonator spacing is held constant. In this case and for all the cases that follow in this neck diameter study, the Bragg frequencies are 964 Hz and 1929 Hz. Since there are multiple Bragg frequencies, the “first Bragg frequency” will again refer to the lower of the two, while the “second Bragg frequency” will again refer to the higher and likewise with the Bragg reflection stop bands. The Bragg stop bands align closely with the Bragg frequencies. The transmission loss in the second Bragg stop band, however, has decreased from the baseline case. Recall from the discussions on the neck length that as the Helmholtz resonant frequency comes closer to a Bragg frequency, the effects of local resonances combine with Bragg reflection and the transmission loss increases, whereas when the Helmholtz resonant frequency moves farther from the Bragg frequency, this combination effect lessens and the transmission loss decreases.

The peaks in the double propagation band are small compared to the baseline case. The larger the neck diameter, the more energy can traverse through the necks and into the coupling tubes, whereas the smaller the neck diameter, the less energy can traverse through the necks. The more energy present in the coupling tubes in this band means more opportunity for destructive interference with the energy in the main duct; hence, since neck diameter in this case is smaller than the neck diameter of the baseline case, less energy is going through the coupled-cavity waveguide, meaning less destructive interference and thus less transmission loss. The next value of the neck diameter is 1.25 in., and the results are plotted in Figure 81.

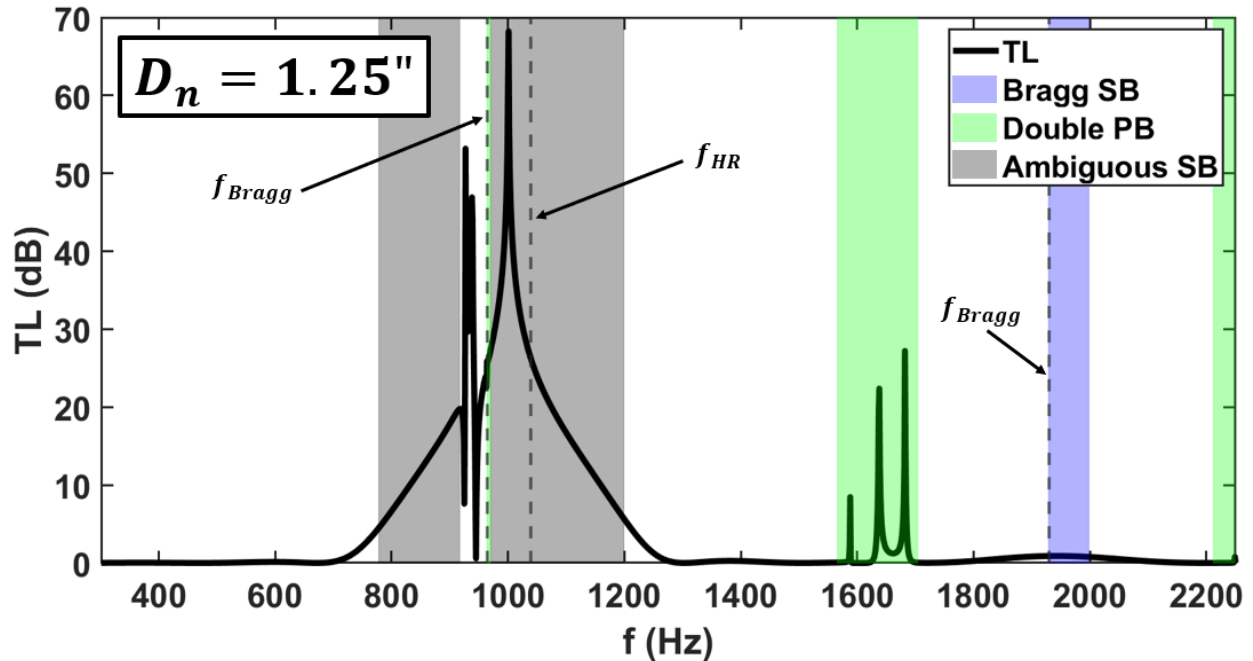


Figure 81. Neck Diameter = 1.25 in.

Since the neck diameter is larger in this case than the previous case, the Helmholtz resonant frequency will shift to a higher frequency. According to the Helmholtz resonant frequency formula given in Equation (105), the Helmholtz resonant frequency is 1040 Hz which is higher than the previous case by 208 Hz. At this neck diameter, the Helmholtz resonant frequency and first Bragg frequency (964 Hz) are close together. As a result, the transmission loss curves resulting from these two phenomena merge into one curve. It is unclear which stop band is which in this region. In previous cases, the leftmost stopband was always the Bragg stop band, but in this case, the Bragg frequency occurs outside of the leftmost stop band. The Helmholtz resonant frequency occurs outside of the leftmost stop band as well, making the physical origins of this stop band ambiguous. The ambiguity in the stop bands in this region is a result of all three physical phenomena occurring simultaneously (i.e., Bragg reflection, Helmholtz resonance, and a thin double propagation band between the two all occurring at frequencies quite close together). Because all three phenomena are occurring at similar frequencies, the precise locations of these stop bands are thus expected to shift slightly (from where they would normally be situated if they were occurring independently of the other three) due to these combined effects.

The peaks in the double propagation band are larger than the previous case. The larger the neck diameter, the more energy can traverse through the necks and into the coupling tubes, and hence, more energy present in the coupling tubes means more opportunity for destructive interference with the energy in the main duct. The transmission loss peaks increase in this region as a result. The next value of the neck diameter is 1.5 in. (which is the baseline case), and the results are plotted in Figure 82.

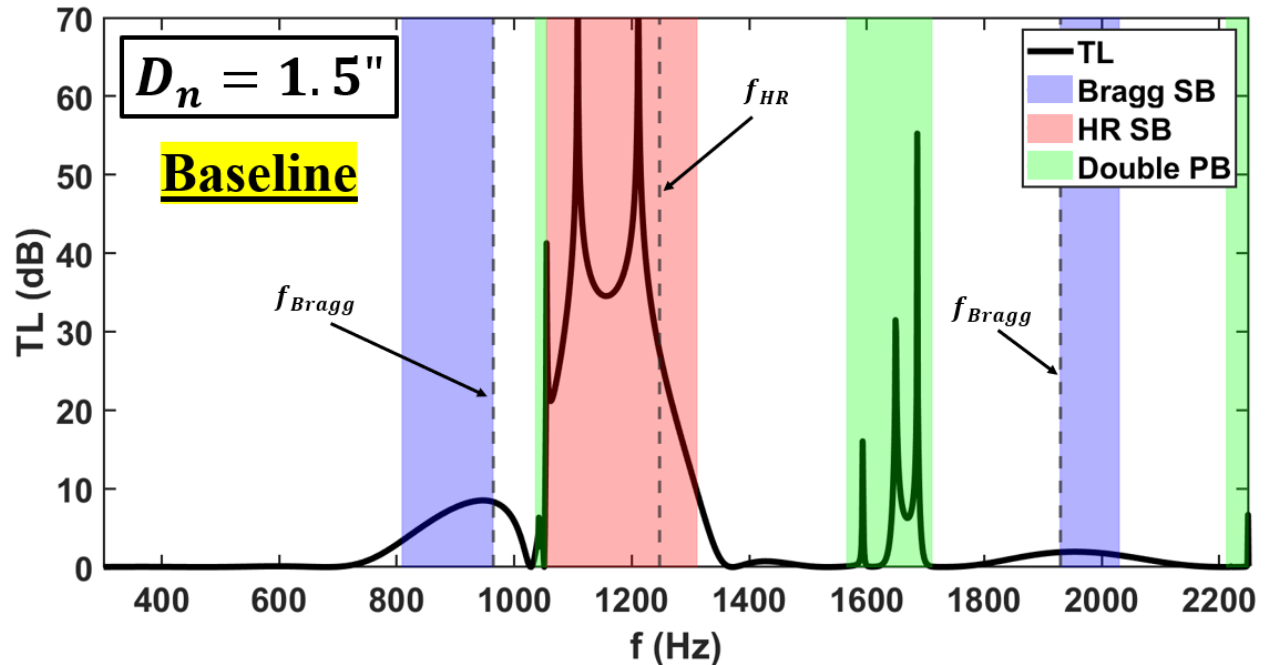


Figure 82. Neck Diameter = 1.5 in.

The Helmholtz resonant frequency again increases as the neck diameter increases. Now that the Helmholtz resonance frequency is farther away from the first Bragg frequency, the effects of the two are no longer merged together. As a result, the physical origins of the stop bands are no longer ambiguous. The transmission loss has also increased slightly in the second Bragg stop band because as the Helmholtz resonant peak approaches a stop band, the combined effects of local resonance and Bragg reflection increases the transmission loss in that region. The peaks in the double propagation band have also increased because with a larger neck diameter, more energy can traverse the neck and travel down the coupling tubes. The more the waves travel down the coupling tubes, the more opportunity for destructive interference and hence increased transmission loss. The next value of the neck diameter is 1.75 in., and the results are plotted in Figure 83.

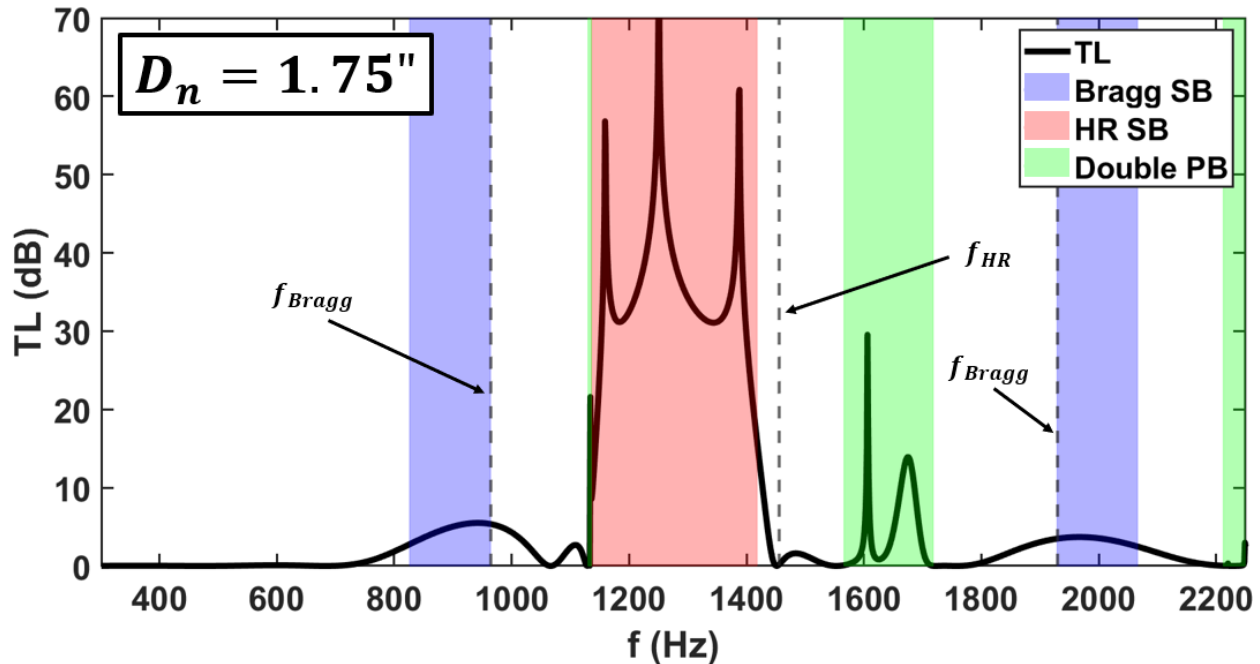


Figure 83. Neck Diameter = 1.75 in.

Now that the neck diameter is 1.75 in., the Helmholtz resonant frequency has shifted further to the right. The transmission loss in the first Bragg stop band has decreased slightly from the previous case while the transmission loss in the second Bragg stop band has increased slightly. This observation is a result of local resonance occurring at a frequency that is closer to the second frequency in which Bragg reflection occurs rather than the first, so the transmission loss will increase in that region due to these combined effects (as discussed previously). In the double propagation band, however, the shape of the transmission loss has shifted. This result occurs because as the Helmholtz resonant frequency approaches the frequencies where double propagation occurs, the vertical oscillatory motion of the air from the Helmholtz resonators and the Bloch wave propagation through the coupled-resonator waveguide conflict. In other words, rather than the two phenomena reinforcing each other like Helmholtz resonance combined with Bragg reflection, when Helmholtz resonance is combined with double propagation, the two phenomena physically oppose each other. Hence the transmission loss shape in the double propagation band is modified from the previous case now that the Helmholtz stop band is closer to it. The last value of the neck diameter is 2.0 in., and the results are plotted in Figure 84.

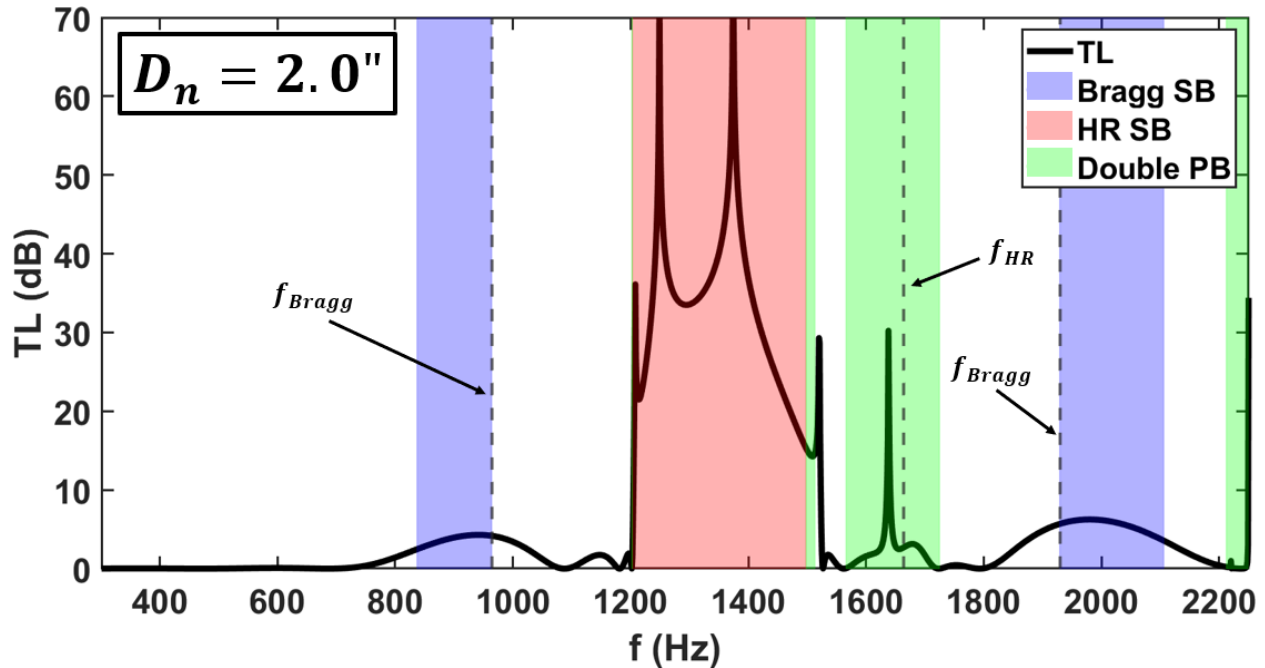


Figure 84. Neck Diameter = 2.0 in.

Now that the neck diameter is 2.0 in., the Helmholtz resonant frequency has increased; however, the Helmholtz stop band has only shifted slightly. As a result, the Helmholtz resonant frequency occurs well outside the Helmholtz stop band. Like in the previous case, the vertical oscillatory motion of the air from the Helmholtz resonator and the Bloch wave propagation through the coupled-resonator waveguide physically oppose each other; hence, they cannot coexist at similar frequencies. Because of the coupling tubes, the system is not an array of purely classical Helmholtz resonators, so the fact that the classical Helmholtz resonant frequency occurs outside the Helmholtz resonant band is possible. The coupling tubes simply alter the resonant behavior of the system. All of these transmission loss curves are overlaid in Figure 85 for reference.

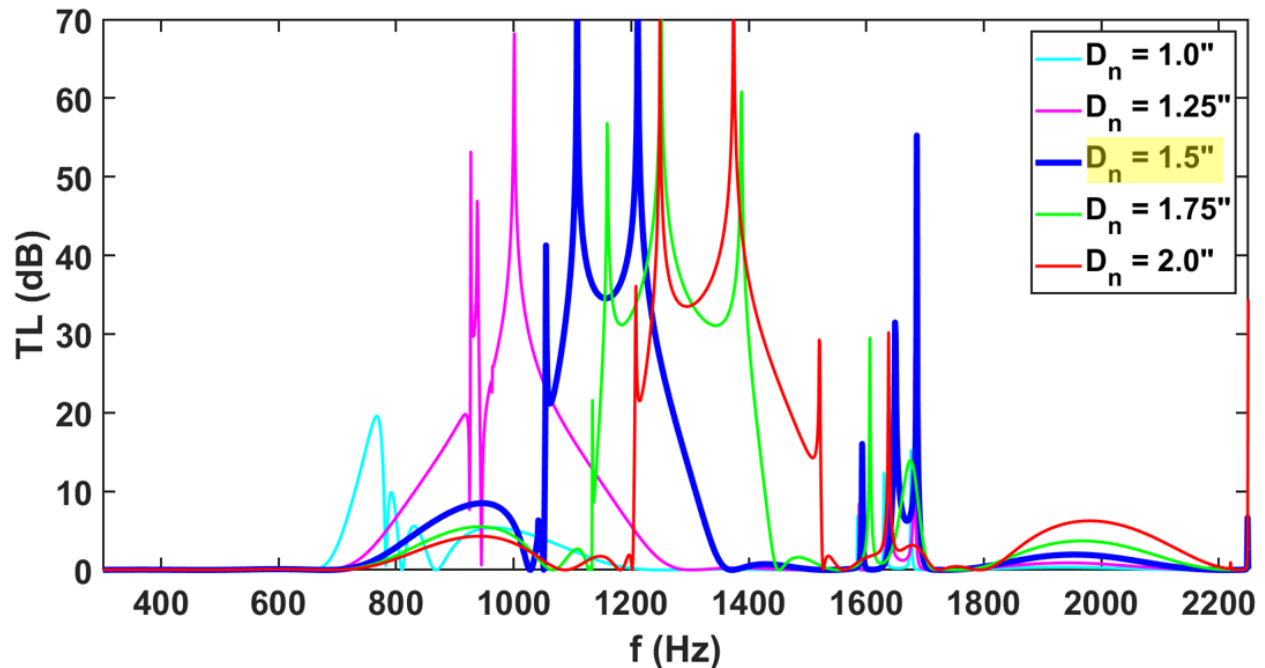


Figure 85. Effect of Neck Diameter on Transmission Loss – All Plots Combined

In summary, as the neck diameter increases, the Helmholtz resonant frequency increases, while the Bragg frequencies and the location of the double propagation band remain constant. As the Helmholtz resonant frequency gets closer to the first Bragg frequency with increasing neck diameter, the effects of the two phenomena combine together into one lumped transmission loss curve. The peaks in the double propagation band increase with increasing neck diameter because as the neck gets wider, more energy is permitted through the neck and into the coupled-resonator waveguide; if more energy goes through the waveguide, then there is more opportunity for destructive interference with the waves in the main duct and hence increased transmission loss. As the Helmholtz stop band gets closer to the double propagation band, however, the two phenomena interfere with one another, and less waves propagate through the coupled-resonator waveguide leading to less destructive interference and less transmission loss in that band. The Helmholtz stop band is modified by the forces from the coupling tubes, so the classical Helmholtz resonant frequency can certainly occur outside the Helmholtz stop band.

3.4.3. Change in cavity height

The next parameter of this study is the cavity height. The reason that cavity height was modified as a parameter instead of cavity volume is that the dimension upon which the volume is changed now matters. Because the resonators are connected via a coupling tube, modifying the

cavity height does not change the coupling tube length, whereas modifying the cavity length along the axis of the duct does modify the coupling tube length. The effect of cavity height on the transmission loss is plotted in the figures below from the lowest to highest values given in Table 1. The first value of the cavity height is 0.5 in., and the results are plotted in Figure 86.

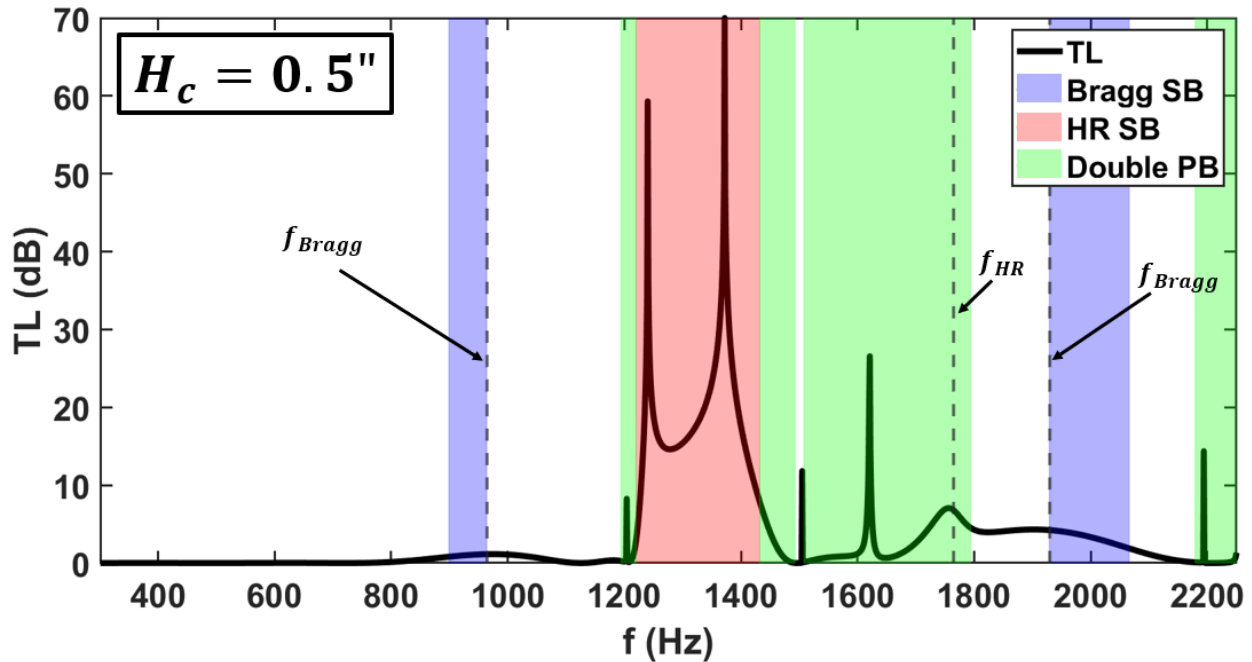


Figure 86. Cavity Height = 0.5 in.

Because the cavity height is 0.5 in., and thus the Helmholtz resonant frequency is much higher than the baseline case. Recall from the previous section on neck diameter that the Helmholtz stop band and the double propagation band cannot coexist because of the conflicting motion of the air in the coupled-resonator waveguide. As such, the transmission loss in the double propagation band is limited. Note, however, that the width of the double propagation band has increased in comparison to the baseline case. This occurs because as the cavity height decreases, the height becomes closer to the diameter of the coupling tubes (in this case, the height of the cavity is 0.5 in., and the coupling tube diameter is 0.375 in.). As the cavity height approaches the coupling tube diameter, the “cavity” becomes less of a resonator and instead becomes more of a uniform cross-section waveguide. Hence, double propagation can occur in a wider frequency range because the nature of the couple resonators is more akin to a uniform cross-section waveguide. The next value of the cavity height is 1.0 in. (which is the baseline), and the results are plotted in Figure 87.

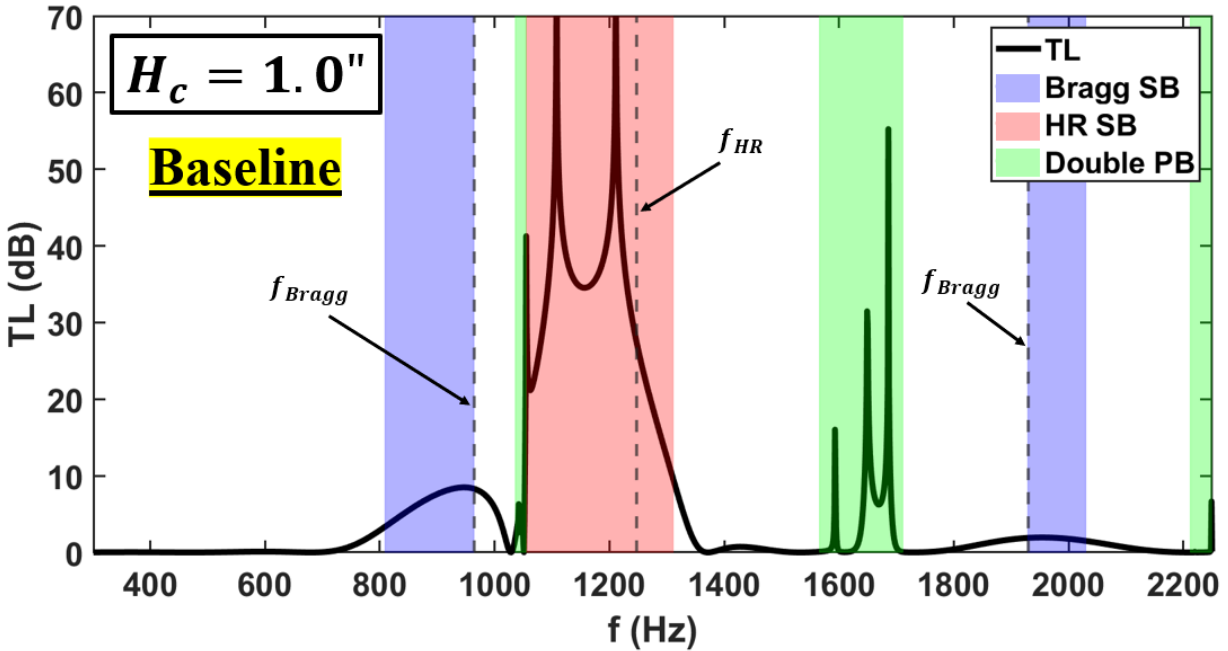


Figure 87. Cavity Height = 1.0 in.

This case has a cavity height of 1.0 in., and thus the resonant frequency is lower. As discussed in previous sections, as the resonant frequency decreases, the Helmholtz stop band also shifts to lower frequencies. The closer the Helmholtz stop band is to a Bragg stop band, the more that the physical phenomena will reinforce each other; hence, the transmission loss increases in the Bragg stop band. The next value of the cavity height is 1.5 in., and the results are plotted in Figure 88.

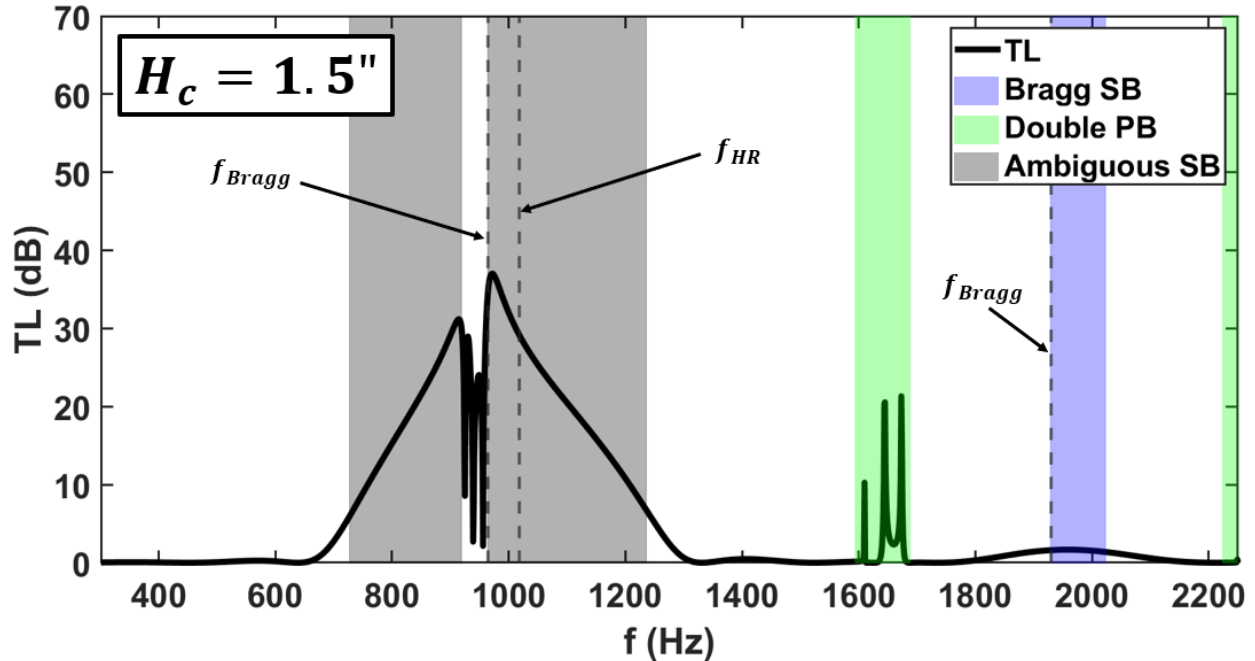


Figure 88. Cavity Height = 1.5 in.

The cavity height is now 1.5 in., and as a result, the Helmholtz resonant frequency decreases. Like cases previously discussed, the Helmholtz resonant frequency is close to the Bragg frequency, and thus, the transmission loss resulting from the two phenomena merge into one large lobe. The physical origins of the stop bands near this lobe are ambiguous since either one could be due to the Helmholtz resonant frequency or from the Bragg frequency. The width of the double propagation band has also decreased because as the height of the cavity gets larger, the effect of the coupling tubes become less significant. The system becomes less like a uniform waveguide, and more like classical Helmholtz resonators. The next value of the cavity height is 2.0 in., and the results are plotted in Figure 89.

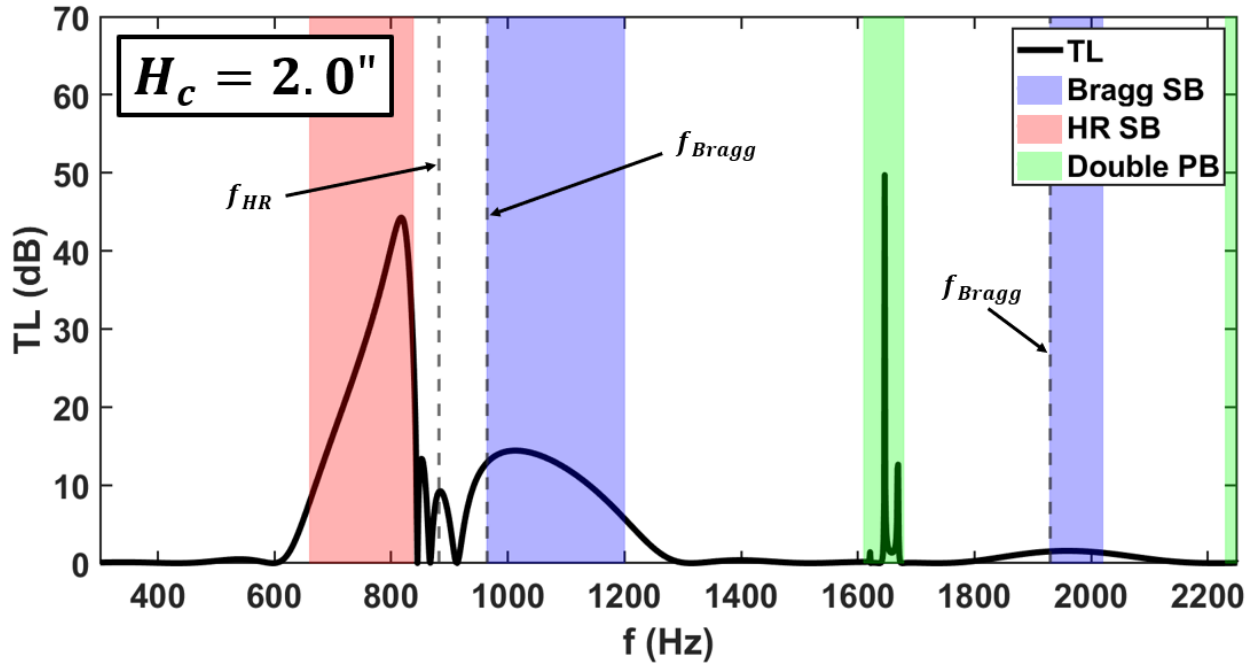


Figure 89. Cavity Height = 2.0 in.

The cavity height is now 2.0 in., so the Helmholtz resonant frequency is lower than the previous cases. The Helmholtz resonant frequency is now so low that the Helmholtz stop band is on the other side of the first Bragg stop band. The double propagation band has decreased in width because the greater the height of the cavities in relation to the diameter of the coupling tubes, the more the system approaches an array of classical Helmholtz resonators and less energy propagates through the relatively small diameter coupling tubes. The last value of the cavity height is 2.5 in., and the results are plotted in Figure 90.

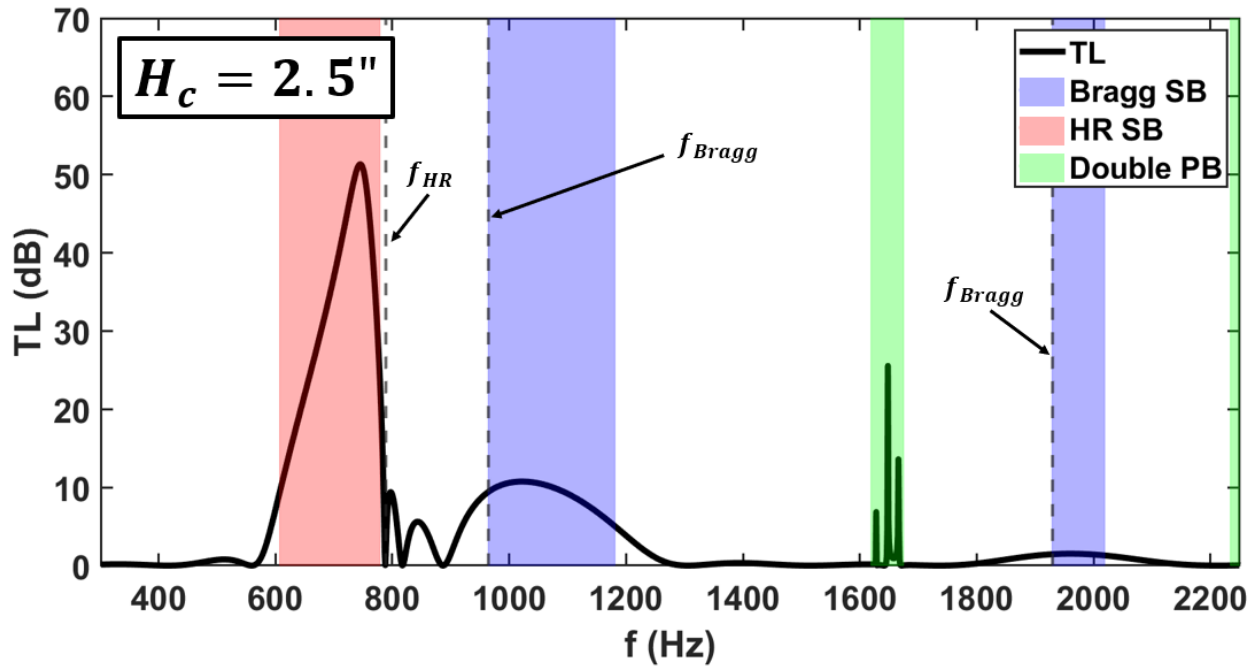


Figure 90. Cavity Height = 2.5 in.

The cavity height in this case is 2.5 in., so the Helmholtz resonant frequency is lower than the preceding cases. The width of the double propagation band is narrower than the preceding cases as well. The height of the cavity is so large in comparison to the diameter of the coupling tubes, that the system behaves more like classical Helmholtz resonators rather than a second waveguide. All of these transmission loss curves are overlaid in Figure 91 for reference.

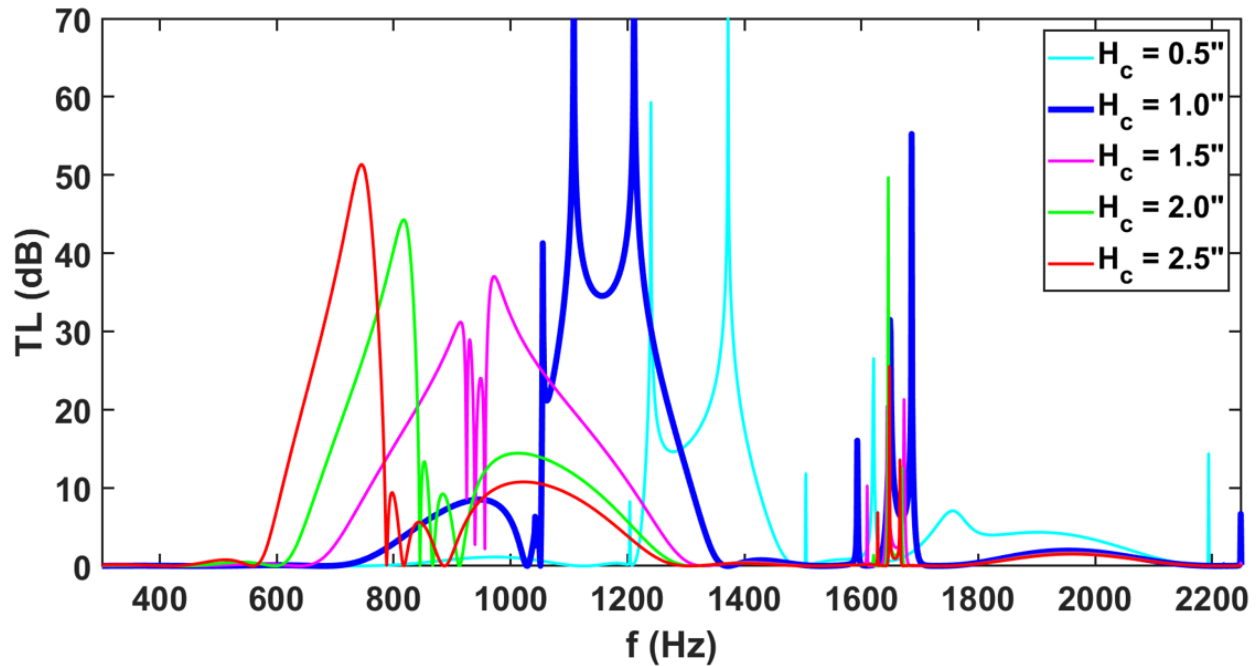


Figure 91. Effect of Cavity Height on Transmission Loss – All Plots Combined

In summary, as the cavity height increases, the Helmholtz resonant frequency decreases, while the Bragg frequencies remain constant. As the Helmholtz resonant frequency gets closer to the first Bragg frequency with increasing cavity height, the effects of the two phenomena combine together into one lumped transmission loss curve. The width of the double propagation band decreases with increasing cavity height because as the cavities get taller in comparison to the diameter of the coupling tubes, the system more closely approximates an array of classical Helmholtz resonators rather than a waveguide of uniform cross section. In other words, as the cavity height increases in comparison to the coupling tubes, less energy gets transferred into the coupling tubes and there is less opportunity for destructive interference between the waves in the coupled-resonator waveguide and the main duct (i.e., less transmission loss). As the Helmholtz stop band gets closer to the double propagation band, however, the two phenomena interfere with one another, and less waves propagate through the coupled-resonator waveguide leading to less destructive interference and less transmission loss in that band.

3.4.4. Change in length of coupling tubes

The next parameter of this study is the length of the coupling tube. The effect of the coupling tube length on the transmission loss is plotted in the figures below from the lowest to highest values given in Table 1. Recall that half a coupling tube is represented by the variable L_{ct} , so the full coupling tube length investigated in this study is given by $2L_{ct}$. To modify the coupling tube length, the length of the resonator cavities must change, but the height and overall volume of the cavities are held constant by modifying the width of the cavities in the span-wise direction.

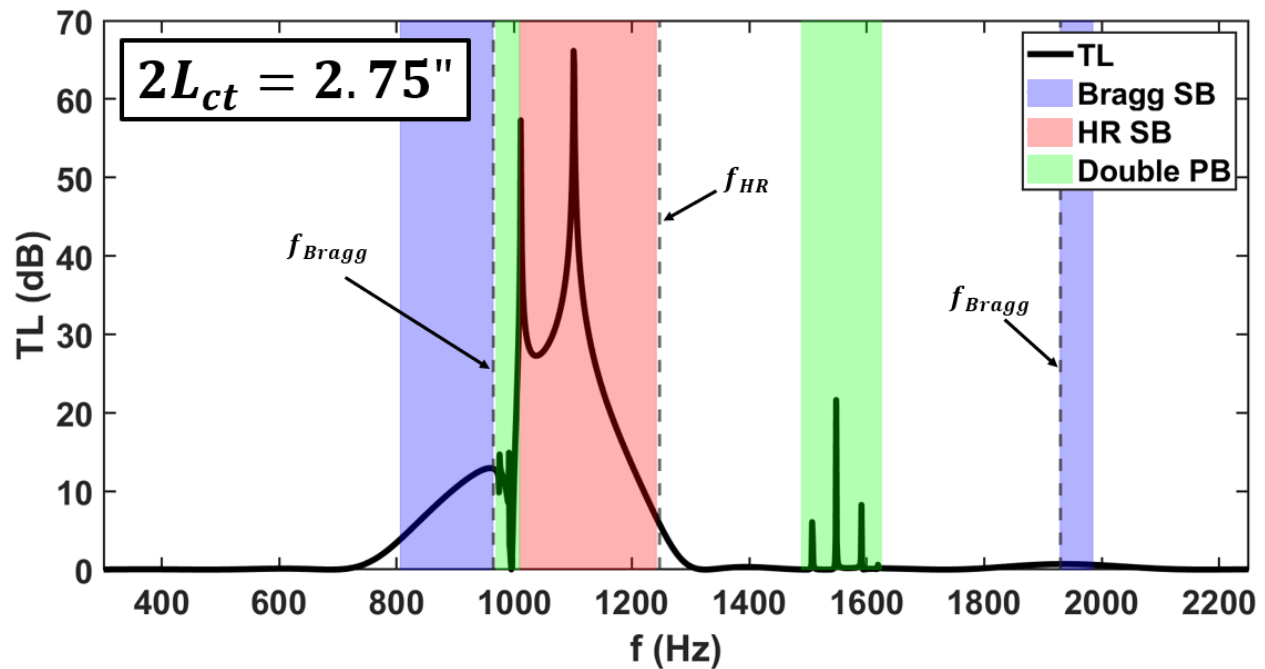


Figure 92. Coupling Tube Length = 2.75 in.

For all of these cases, the coupling tube is the only parameter that is modified. Since the resonant frequency for a classical Helmholtz resonator and the Bragg reflection frequency do not depend on this variable (see Equation (105) and (106) respectively), their values will not change for any of these cases; however, recall from the explorations of the preceding parameters that because of the addition of coupling tubes, the Helmholtz stop band more accurately describes this system rather than the classical Helmholtz resonant frequency. As such, the Helmholtz stop band will move slightly while the classical Helmholtz resonant frequency will not because of the influence of the coupling tubes. In this case, the results look similar to the baseline case (where

the coupling tubes are 4.0 in.); however, the transmission loss peaks in the double propagation band are lower in magnitude. This result occurs because as the coupling tubes get shorter the length of the cavities has to increase in order to maintain the same resonator spacing (but height and total volume are kept constant by varying the width of the cavities). As such, the system approaches an array of classical Helmholtz resonators and becomes less like a waveguide. The next value of the coupling tube length is 3.0 in., and the results are plotted in Figure 93.

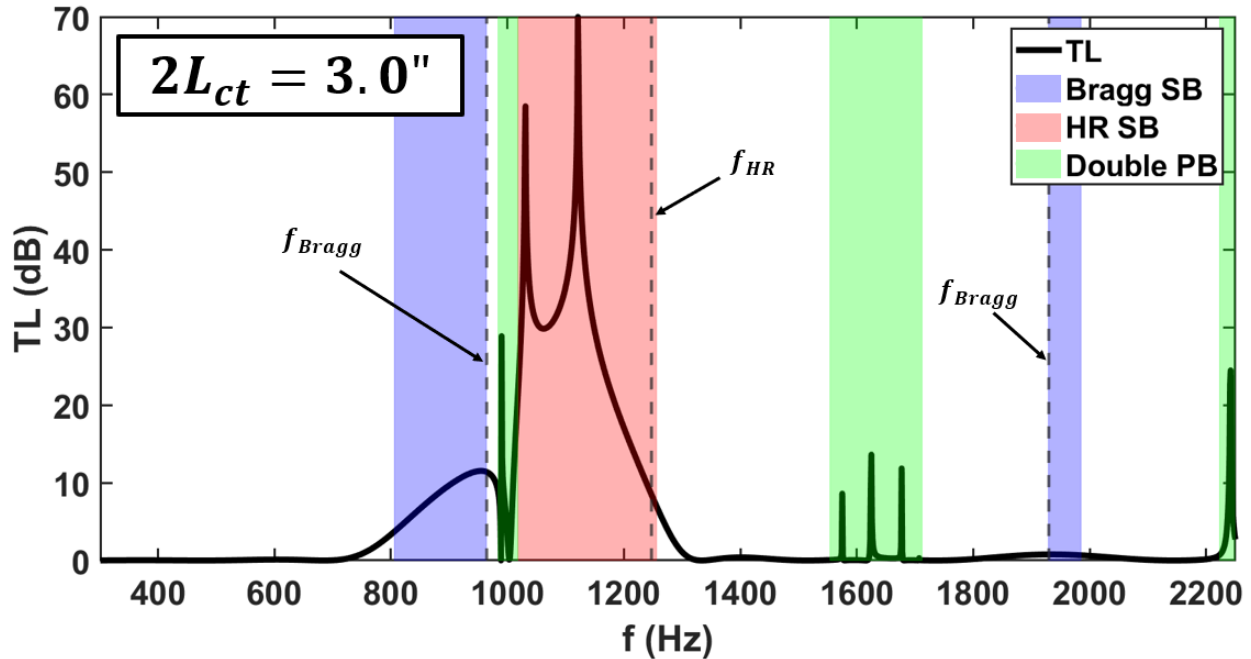


Figure 93. Coupling Tube Length = 3.0 in.

Recall that the waves traveling through the coupled-resonator waveguide will travel at a different speed than the waves in the main duct because the changing cross-sectional area in the coupled-resonator waveguide slows the waves down. When the waves of two different speeds arrive at the interface (the necks of the Helmholtz resonators), they will either be in phase or out of phase causing interference; thus, when the length of the coupling tube increases, the phase difference between the waves traveling in the coupled-resonator waveguide and the main duct will change. Because the phase difference changes, different frequencies will now experience destructive interference. As a result, the double propagation band will shift when the length of the coupling tube changes as it does here. Because the Helmholtz resonance is affected by the coupling tubes, the Helmholtz stop band also shifts slightly. The next value of the coupling tube length is 3.25 in., and the results are plotted in Figure 94.

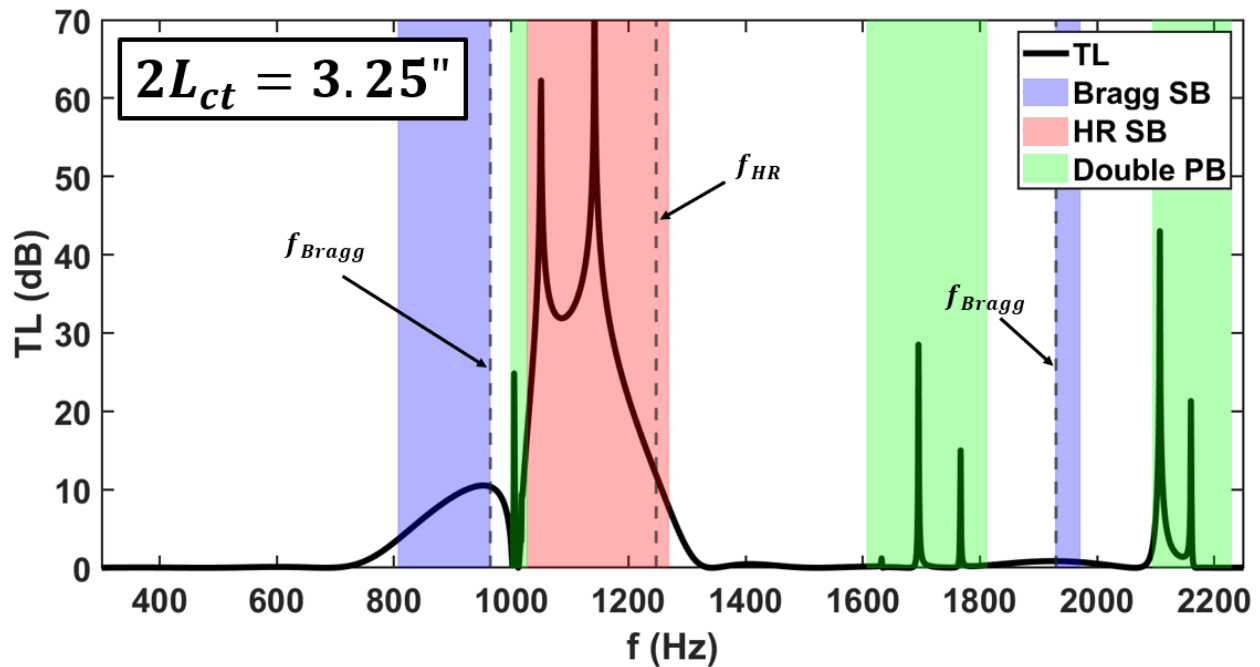


Figure 94. Coupling Tube Length = 3.25 in.

For this case, the coupling tube has increased to 3.25 in. As a result, the phase difference between the waves traveling in the coupled-resonator waveguide and the main duct will change again, and because the phase difference changes, different frequencies will now experience destructive interference; hence, the double propagation band again shifts. A new double propagation band has also appeared on the right side of the second Bragg stop band. These frequencies are also experiencing destructive interference at this coupling tube length. Also, as the coupling tube gets longer, the resonators get narrower in length. As a result, the system acts more like a waveguide and less like classical Helmholtz resonators. The coupling tubes thus become more responsible for attenuation than the cavities, and thus more transmission loss occurs in the double propagation band than in previous cases. The next value of the coupling tube length is 3.5 in., and the results are plotted in Figure 95.

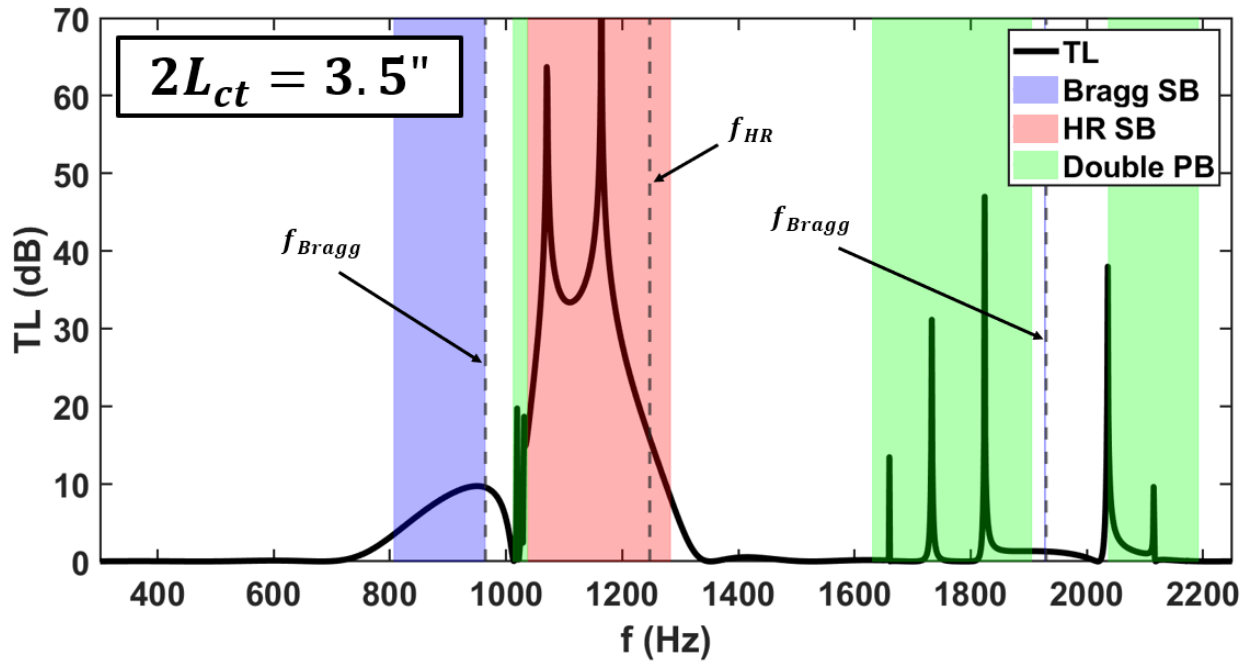


Figure 95. Coupling Tube Length = 3.5 in.

The coupling tube length is now 3.5 in. For the same reasons as before, the increase in coupling tube length has again shifted the frequencies that experience destructive interference. Now, the transmission loss in the two double propagation bands has increased again because the system becomes more like a waveguide and less like classical Helmholtz resonators, so now more energy is attenuated via the interaction of the two traveling waves. The next value of the coupling tube length is 3.75 in., and the results are plotted in Figure 96.

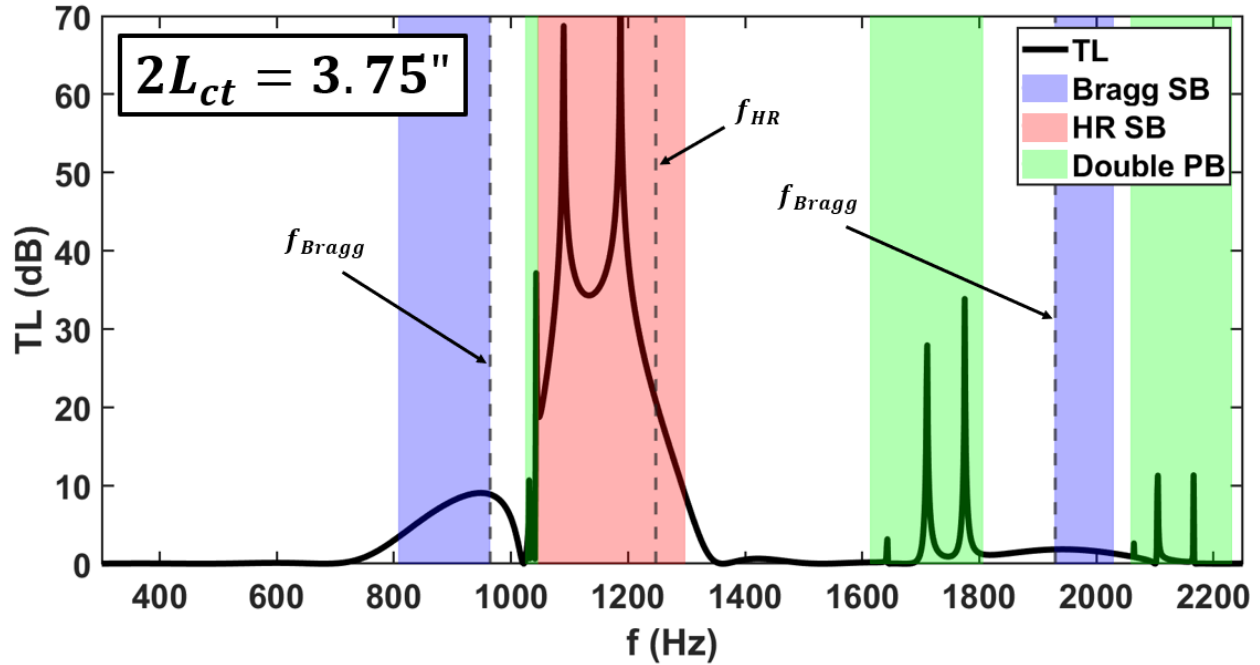


Figure 96. Coupling Tube Length = 3.75 in.

Because the coupling tube has changed, the double propagation band frequencies have shifted again. This pattern will continue throughout the rest of the cases (see below). All of these transmission loss curves are overlaid in Figure 100 for reference.

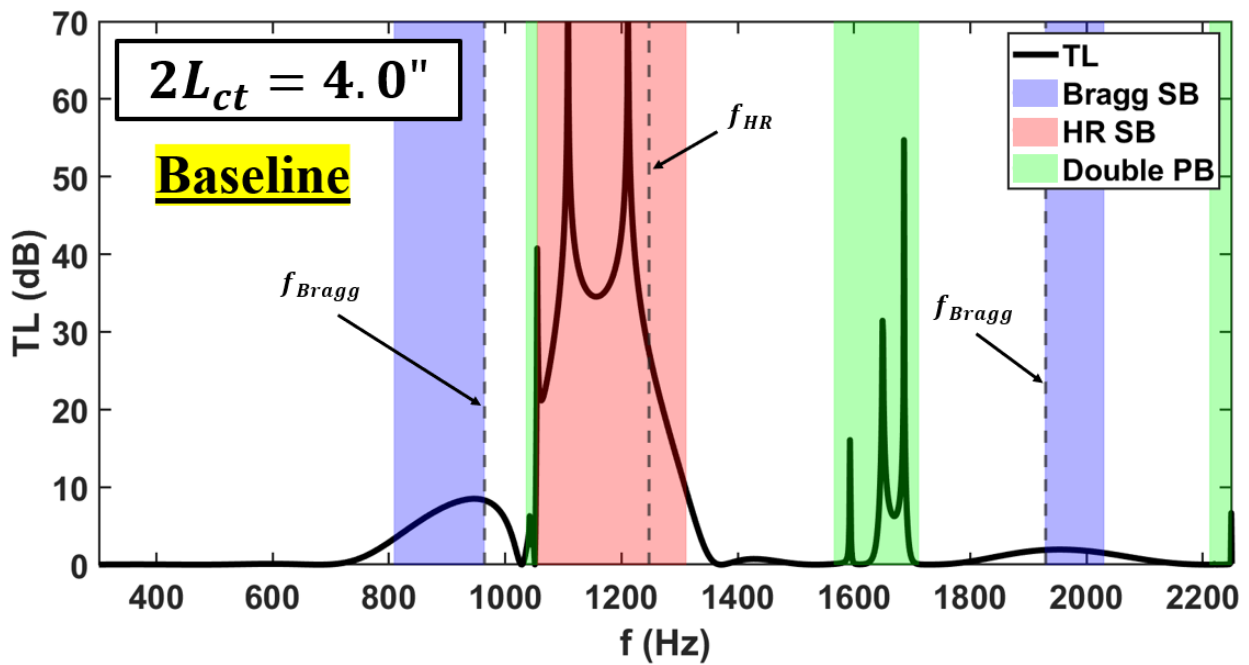


Figure 97. Coupling Tube Length = 4.0 in.

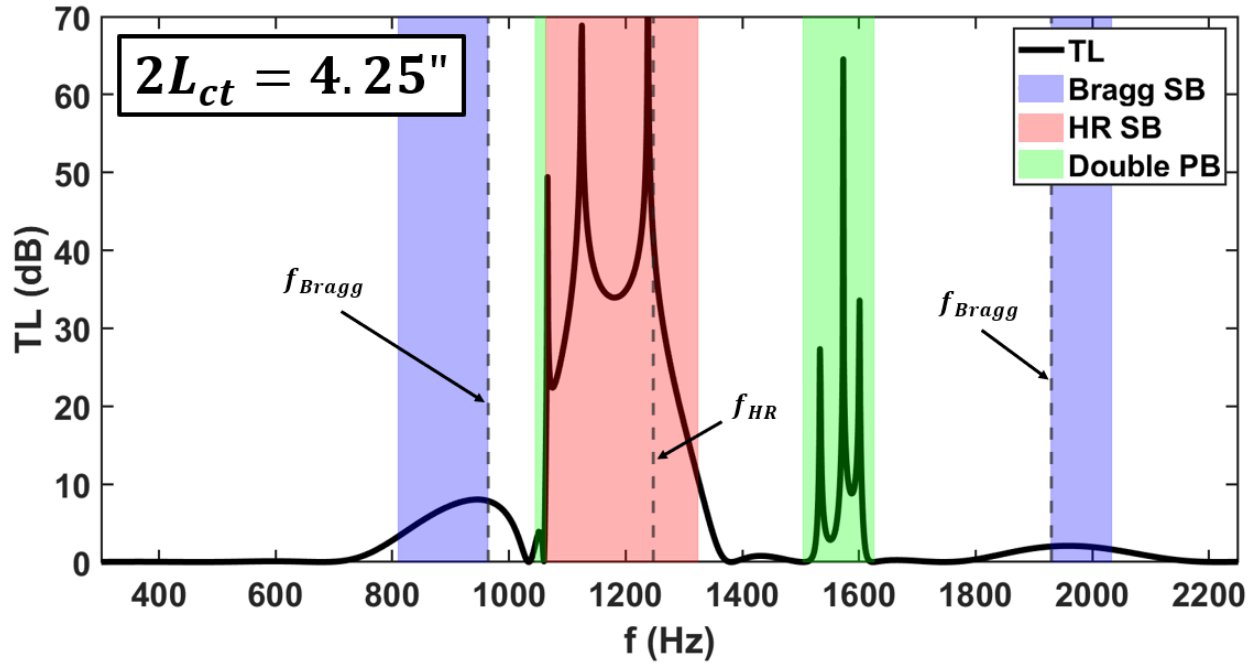


Figure 98. Coupling Tube Length = 4.25 in.

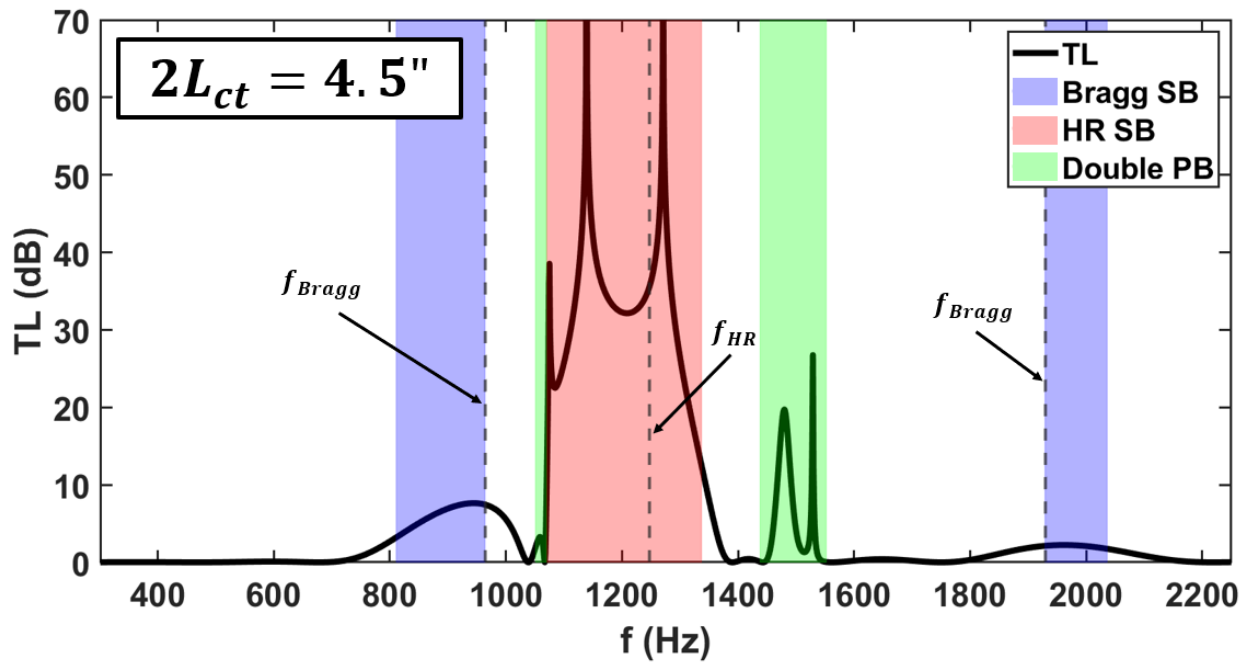


Figure 99. Coupling Tube Length = 4.5 in.

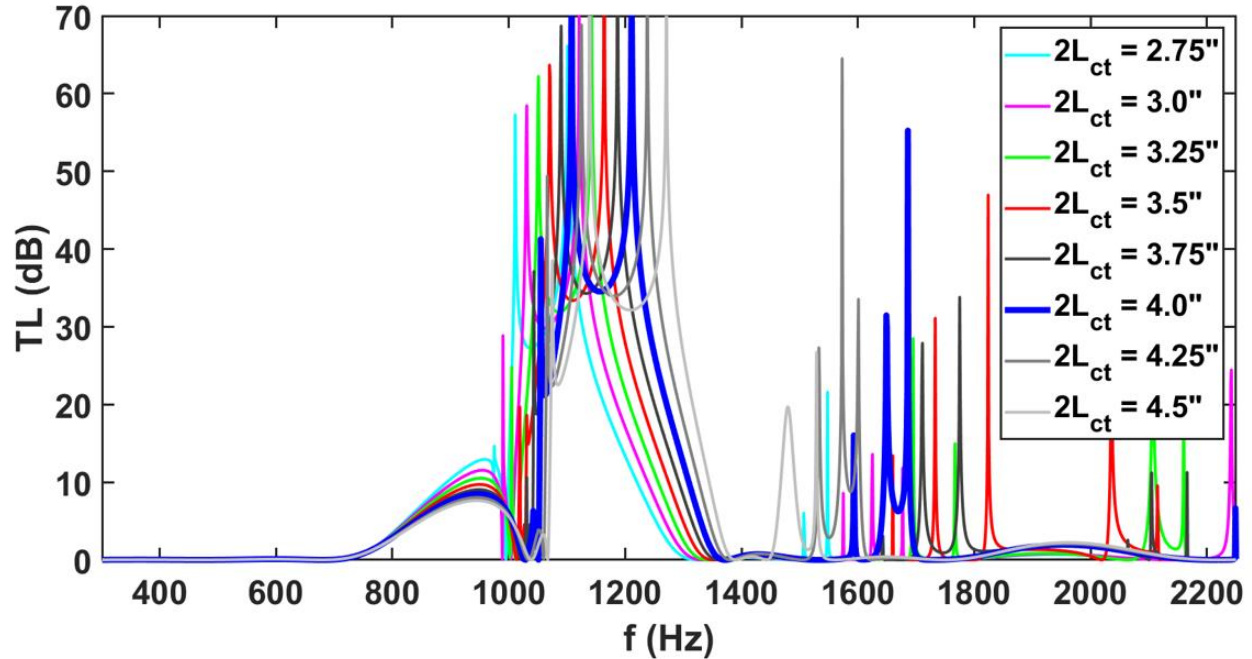


Figure 100. Effect of Coupling Tube Length on Transmission Loss – All Plots Combined

In summary, for different lengths of the coupling tube, the waves traveling through the coupled-resonator waveguide will be out of phase with the waves traveling through the main duct upon reaching the interface (i.e., the necks) for different frequencies; hence, destructive interference will occur at different frequencies and the locations of the double propagation bands will shift. Because the Helmholtz resonators are influenced by the coupling tubes, the Helmholtz stop bands will also shift slightly.

3.4.5. Change in spacing between the resonators

The next parameter of this study is the spacing between the resonators. The effect of the resonator spacing on the transmission loss is plotted in the figures below from the lowest to highest values given in Table 1. As the resonator spacing increased, the coupling tube length, resonator cavity height, and resonator cavity volume were held constant; therefore, the cavity length in the axial direction had to change to maintain the coupling tube length, and the cavity width in the span-wise direction had to change to maintain the cavity height and volume. The first value is 6.0 in., and the results are plotted in Figure 101.

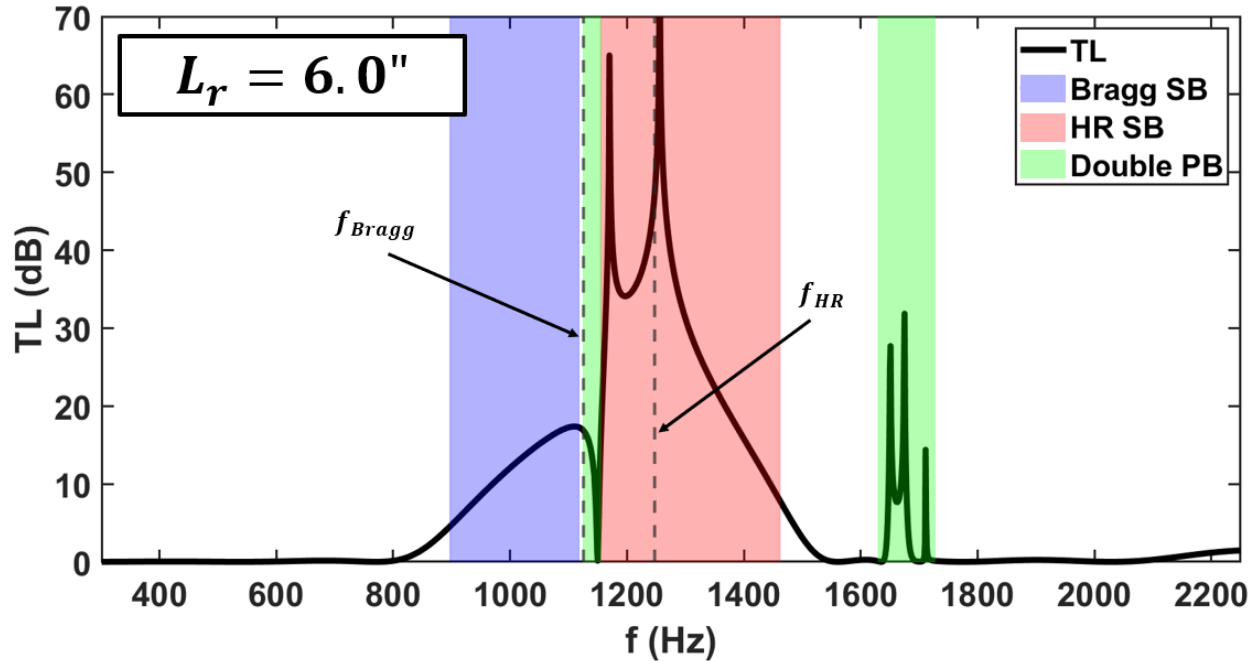


Figure 101. Resonator Spacing = 6.0 in.

At a resonator spacing of 6.0 in. (1.0 in. lower than the baseline), the Bragg frequencies shift to the right. Recall that Bragg reflection occurs when the spacing between the resonators is a multiple of a half of a wavelength; hence, by altering the resonator spacing, the frequencies at which Bragg reflection occurs will change. The second Bragg frequency is now 2250 Hz which occurs above the first cut-on mode (1,0,0) of the duct and is thus ignored. Because the Bragg stop band has shifted closer to the Helmholtz resonant stop band, the transmission loss within both of the band begin to lump together into one curve as was seen in previous investigations of the other parameters. The next resonator spacing value is 7.0 in. (which is the baseline), and the results are plotted in Figure 102.

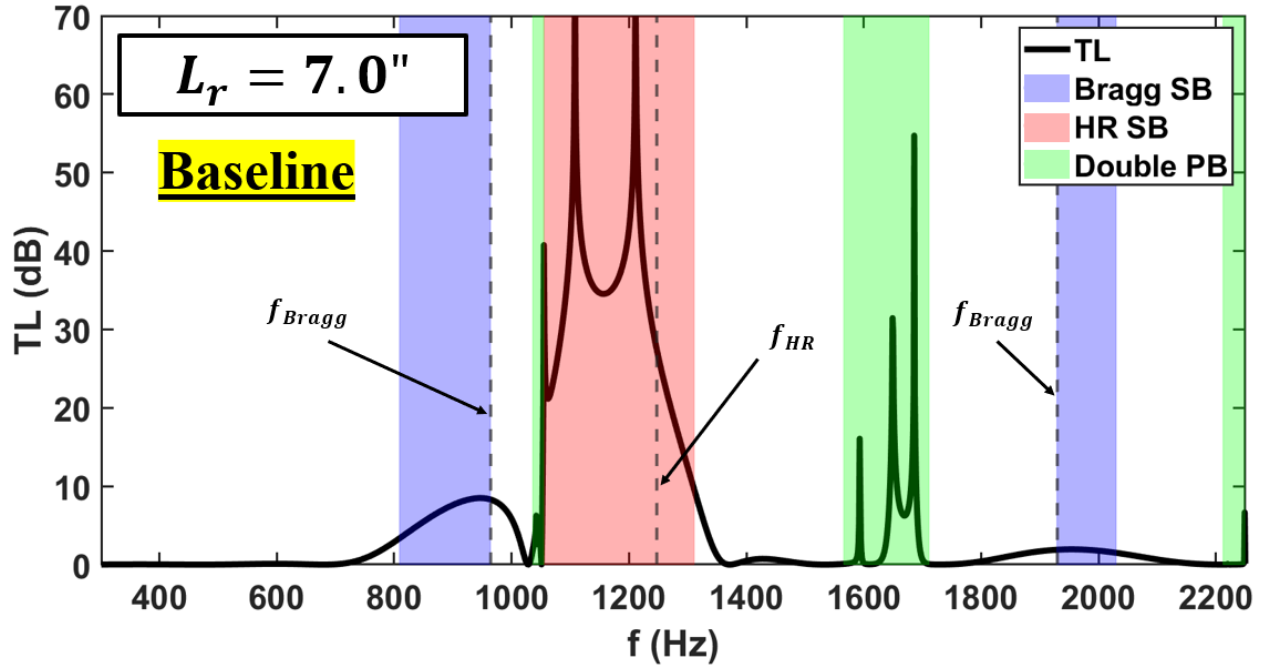


Figure 102. Resonator Spacing = 7.0 in.

The resonator spacing is now 7.0 in. By increasing the resonator spacing, the Bragg frequencies have shifted to the left. The next value for the resonator spacing is 8.0 in., and is shown in Figure 103.

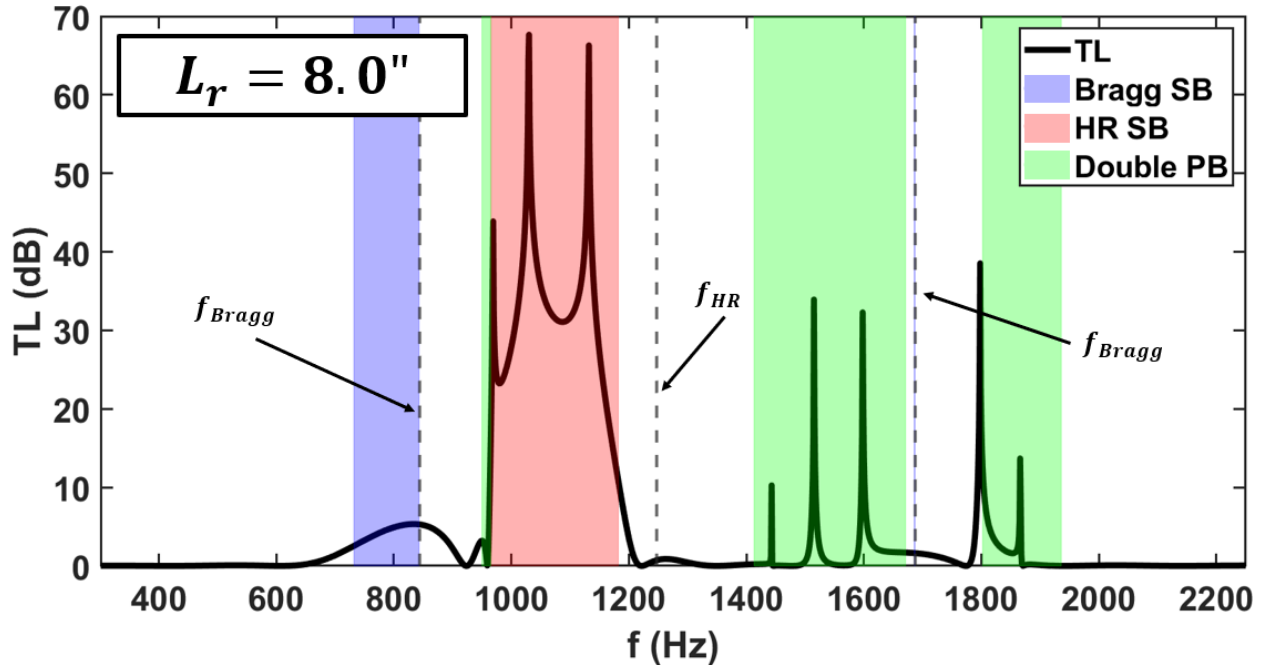


Figure 103. Resonator Spacing = 8.0 in.

The resonator spacing is now 8.0 in. Because the resonator spacing has increased from the previous case, the Bragg frequencies decreased. Recall that since the other parameters must remain constant, when the resonator spacing is increased, the cavity length is increased to maintain the coupling tube length of 4.0 in. As a result, the width must decrease in order to maintain the same cavity volume and height for each case. Because the length of the cavity increases and the width of the cavity decreases (while the height stays the same), the cavities become longer and thinner making them more like waveguides and less like resonators. This observation is the same as the observation made in the previous section regarding the coupling tube length, but this time, however, instead of the coupling tube length increasing, the length of the cavities is increasing. Before, when the coupling tube length increased, the waves spent a longer duration of travel through the coupling tube compared to the resonator cavity, whereas in this case, the waves spend a longer duration traveling through the resonator cavity compared to the coupling tube. When the coupling tube length was changed, the frequencies of the double propagation band would change as a result of this, and thus, the same phenomena occurs when manipulating the resonator spacing (and the cavity length by extension). The next value for the resonator spacing is 9.0 in., and is shown in Figure 104.

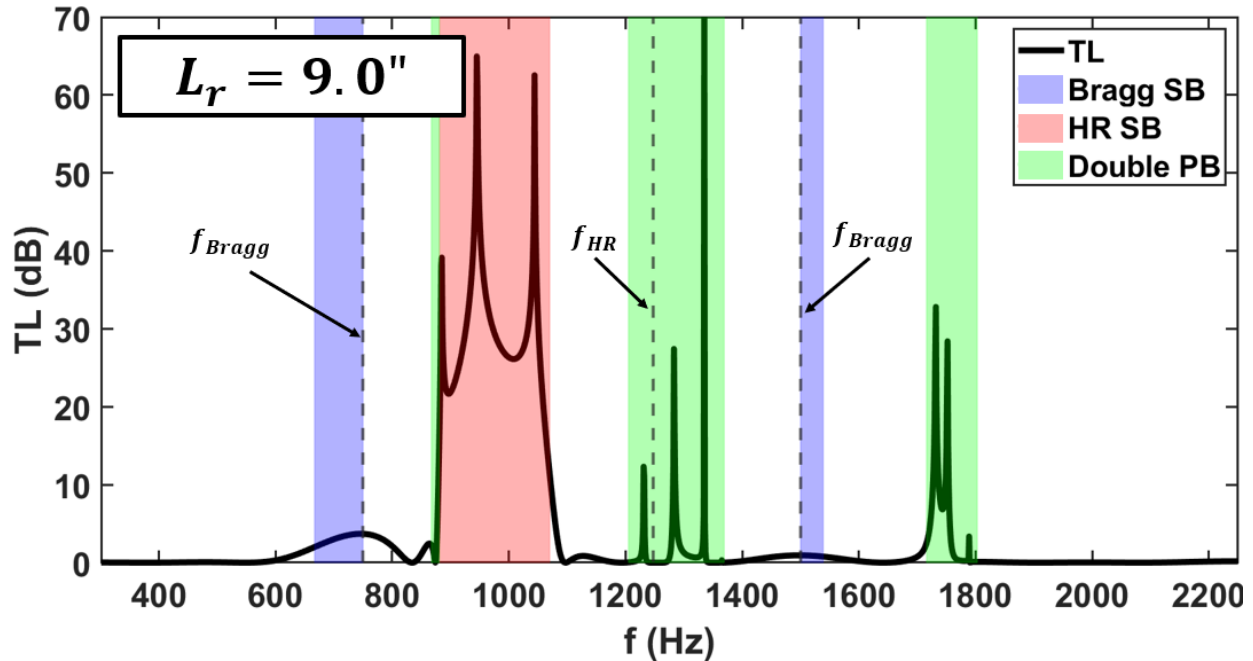


Figure 104. Resonator Spacing = 9.0 in.

In this case, the resonator spacing is 9.0 in. Again, because the resonator spacing changes while the coupling tube length is held constant, the length and width of the cavity must change to maintain the volume of cavity. The cavity gets longer and thinner making the cavity more of a waveguide rather than a resonator. As the cavity length increases, the waves spend a longer duration in the cavity as opposed to the coupling tubes which changes the wave speed through the resonator-cavity waveguide which means different frequencies will now experience destructive interference. The double propagation bands shift as a result. The greater the resonator spacing, the lower the Bragg frequencies, so the Bragg stop bands shift further to the left. The Helmholtz band also shifts to the left because the resonators are affected by the motion of air in the coupling tubes and hence do not resonate at the classical Helmholtz resonant frequency f_{HR} . The last two cases demonstrate the same phenomena (see Figure 105 and Figure 106). All of these transmission loss curves are overlaid in Figure 107 for reference.

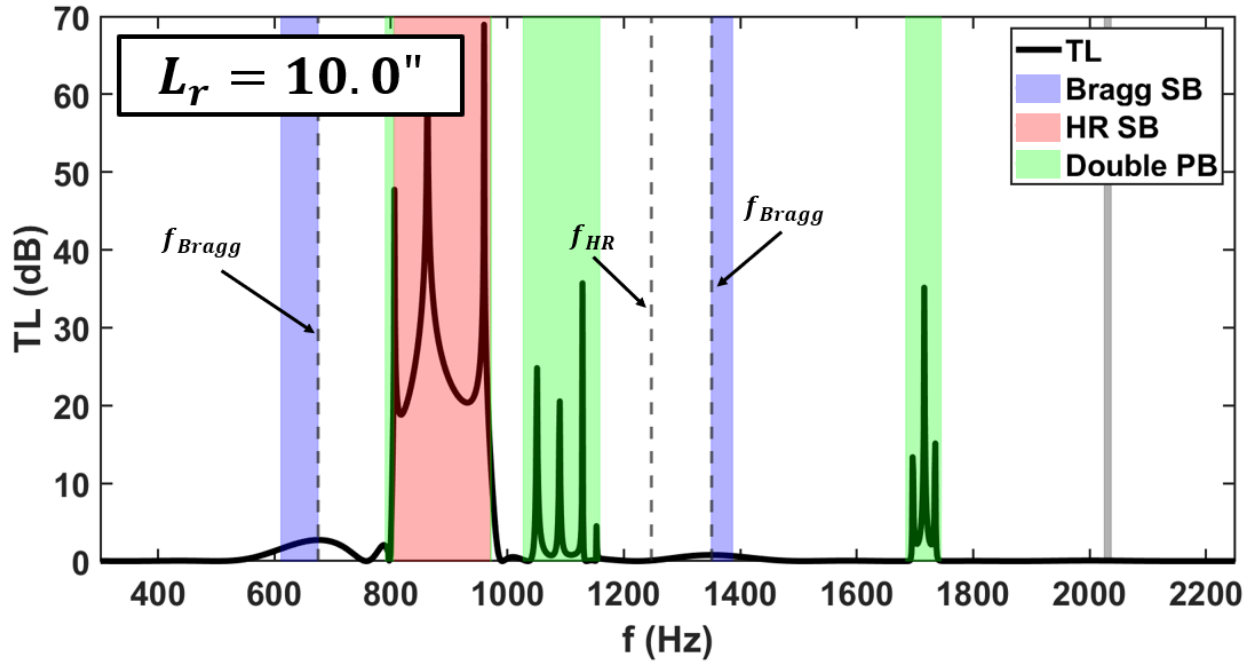


Figure 105. Resonator Spacing = 10.0 in.

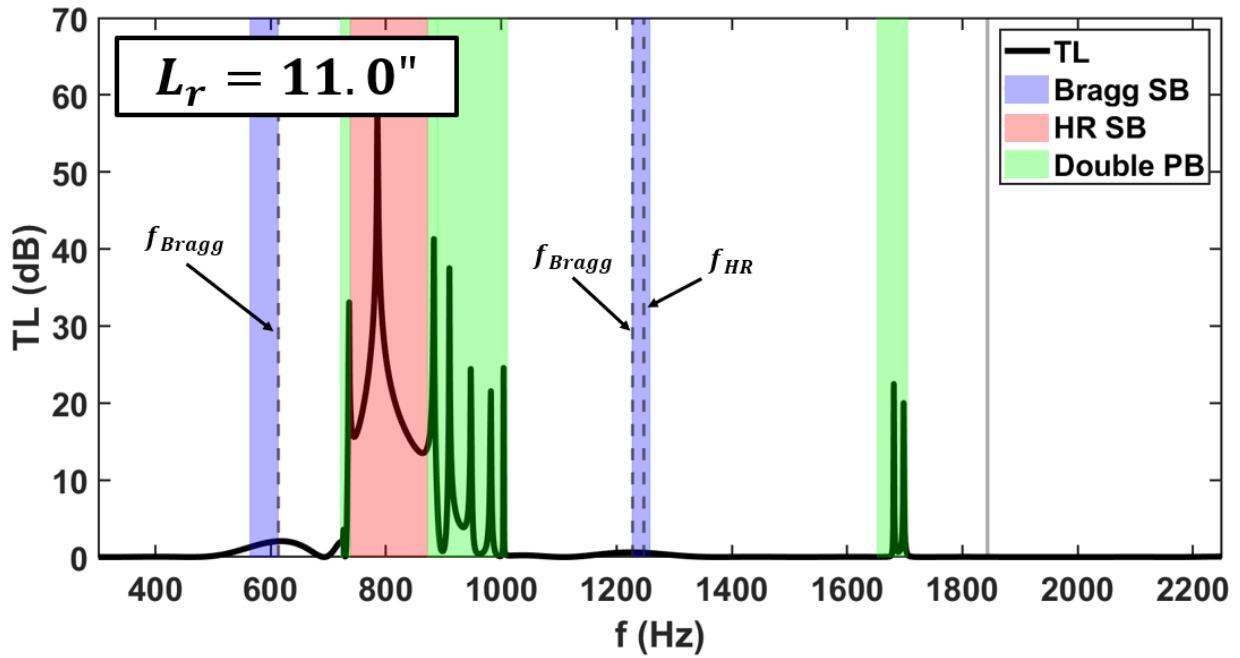


Figure 106. Resonator Spacing = 11.0 in.

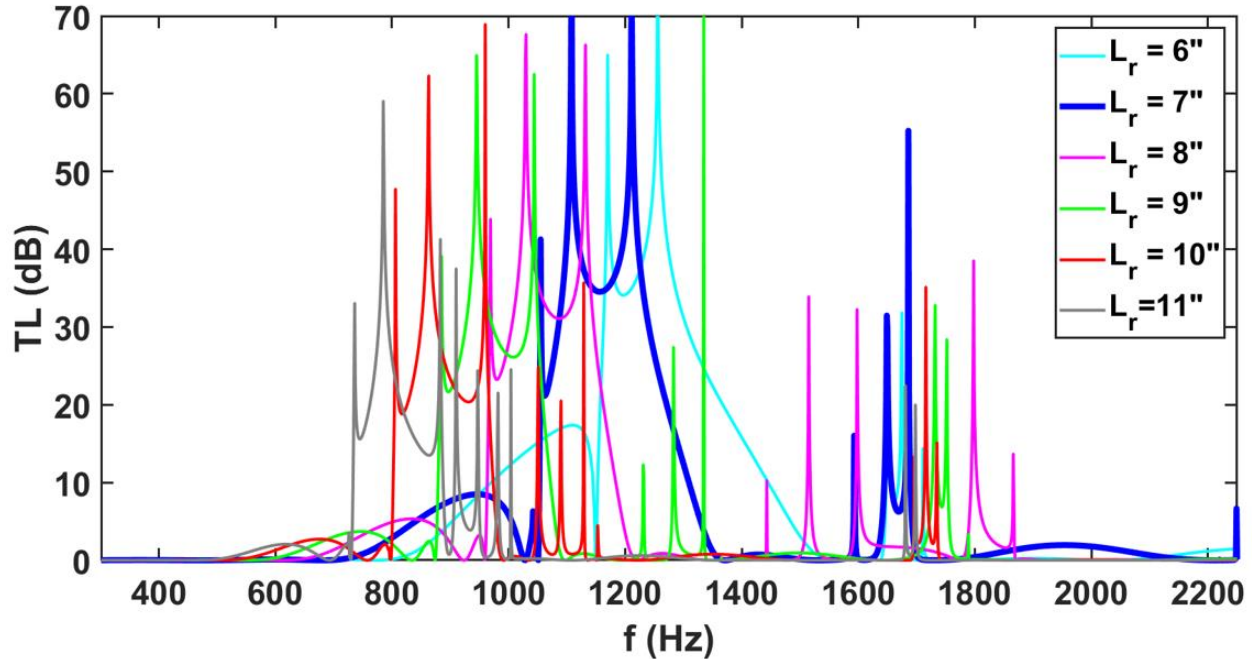


Figure 107. Effect of Resonator Spacing on Transmission Loss – All Plots Combined

In summary, when the resonator spacing increases, Bragg reflection occurs at lower frequencies, so the Bragg stop bands shift to the left. Because the coupling tube length is held constant, when the resonator spacing is increased, the length of the cavities must also increase, and the width of the cavities must decrease in order to maintain the volume and height of the resonators. When the resonators become longer and thinner, they act more like waveguides rather than resonators; hence, the waves traveling through the coupled-resonator cavities spend a longer duration in the “resonators” which have a larger cross-sectional area than the coupling tubes. As a result of these changes, the waves that destructively interfere with the waves in the main duct at the interface (i.e., the necks) will be of a different frequency range than the baseline case. As such, the double propagation bands will shift. The Helmholtz stop band will also shift from what is predicted from the classical Helmholtz resonant frequency since the inclusion of coupling tubes will affect the resonant properties of the cavity.

3.4.6. Change in diameter of the coupling tubes

The next parameter of this study is the diameter of the coupling tube. The effect of the coupling tube diameter on the transmission loss is plotted in the figures below from the lowest to highest values given in Table 1. The first case for the coupling tube diameter is 0.125 in., and the transmission loss plot is given in Figure 108.

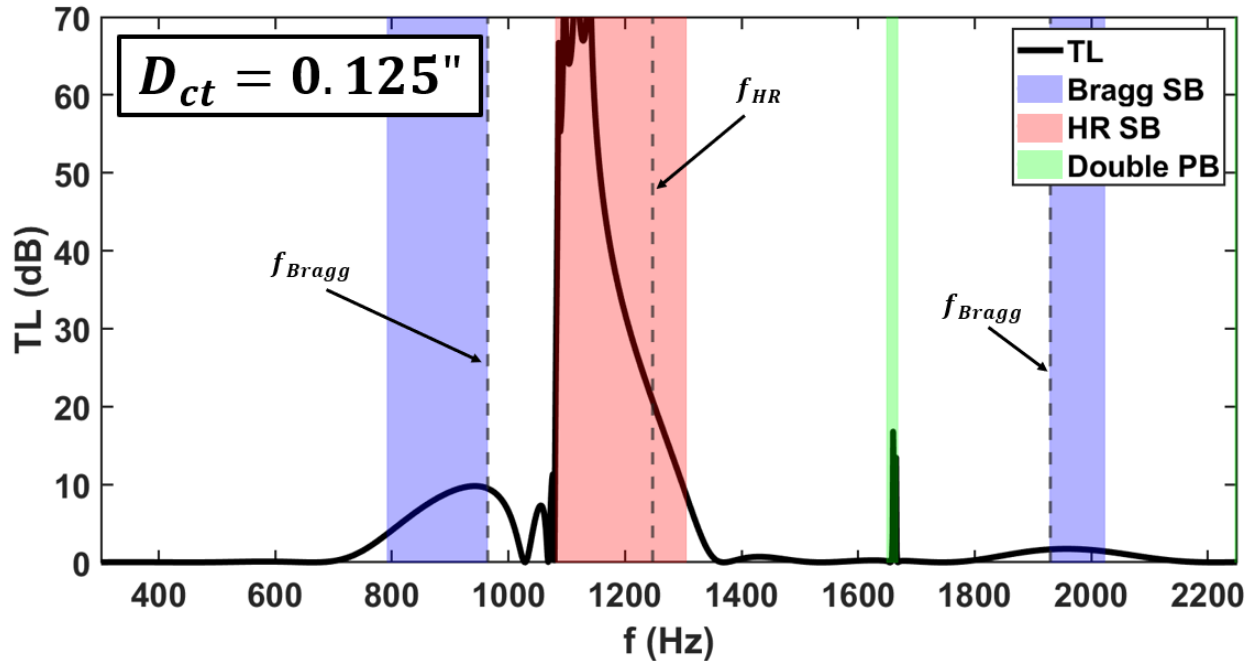


Figure 108. Coupling Tube Diameter = 0.125 in.

The coupling tube diameter in this case is 0.125 in. which is 0.25 in. less than the baseline case. Since the Bragg frequencies only depend on the resonator spacing, they remain constant. Since the coupling tube has a much smaller diameter than the height of the cavity (which is 1.0 in.), the energy cannot propagate through the coupling tubes as easily, and the system becomes more like an array of classical Helmholtz resonators; hence, the double propagation band is thin, and the transmission loss in the Helmholtz stop band approaches one central resonant peak. The next value of the coupling tube diameter is 0.375 in. (which is the baseline case), and the results are plotted in Figure 109.

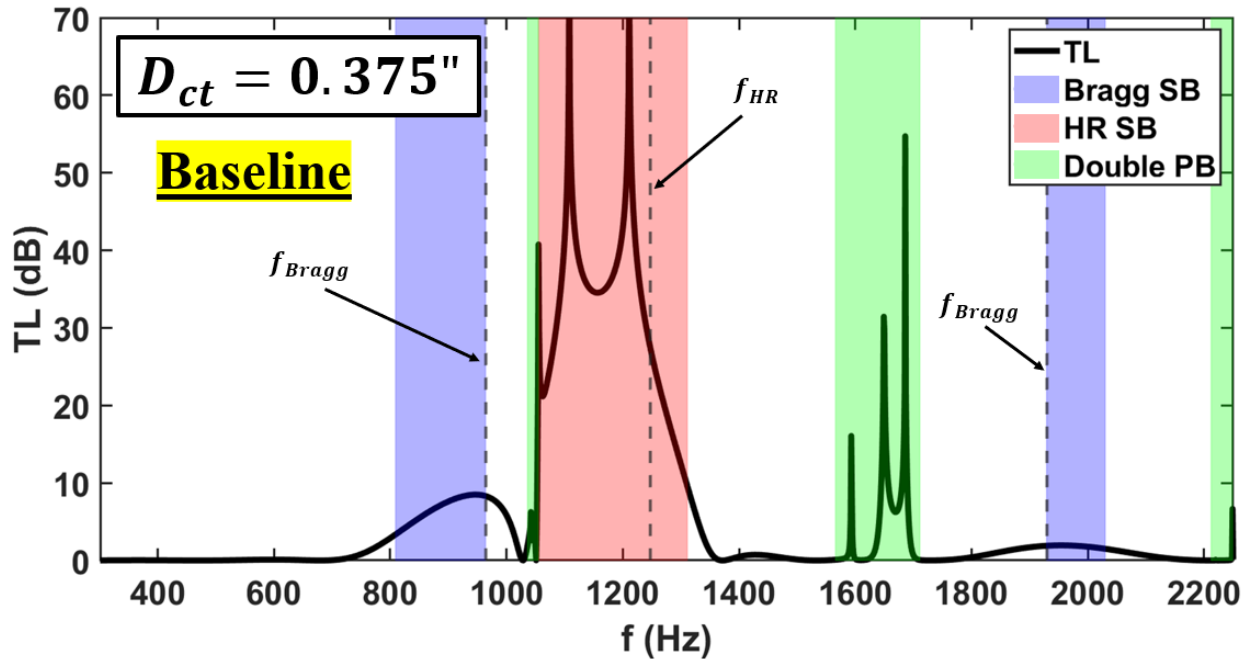


Figure 109. Diameter of Coupling Tube = 0.375 in.

The coupling tube diameter is now 0.375 in. As a result, more energy can transmit through the coupling tubes than in the previous case. Because more energy can go through the coupling tubes, more waves can travel through the coupled-resonator waveguide, and thus there are more opportunities for destructive interference with the waves in the main duct. The double propagation band thus gets wider and the transmission loss within the band increases. The Helmholtz resonator is now influenced by the increased diameter of the coupling tubes, and thus no longer approaches one resonant peak, and instead the transmission loss widens in that region. The next value of the coupling tube diameter is 0.625 in., and the results are plotted in Figure 110.

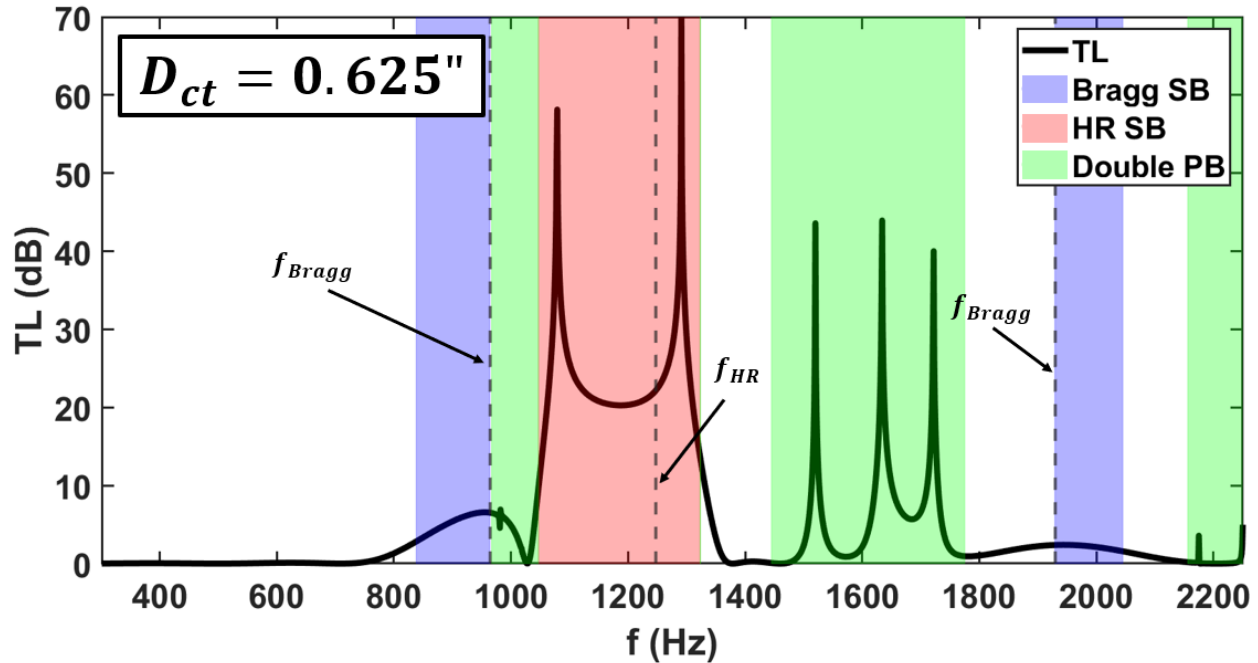


Figure 110. Diameter of Coupling Tube = 0.625 in.

The diameter of the coupling tubes is now 0.625 in. As a result, more energy can transmit through the coupling tube than in previous cases. As such, more destructive interference can occur for a wider range of frequencies, and the double propagation band widens as a result. The transmission loss in the Helmholtz stop band is widening as a result of the coupling tubes. The system is becoming less of an array of classical Helmholtz resonators and more of a waveguide, so the transmission loss in the Helmholtz stop band no longer approaches one singular resonant peak and widens instead. The last value of the coupling tube diameter is 0.875 in., and the results are given in Figure 111.

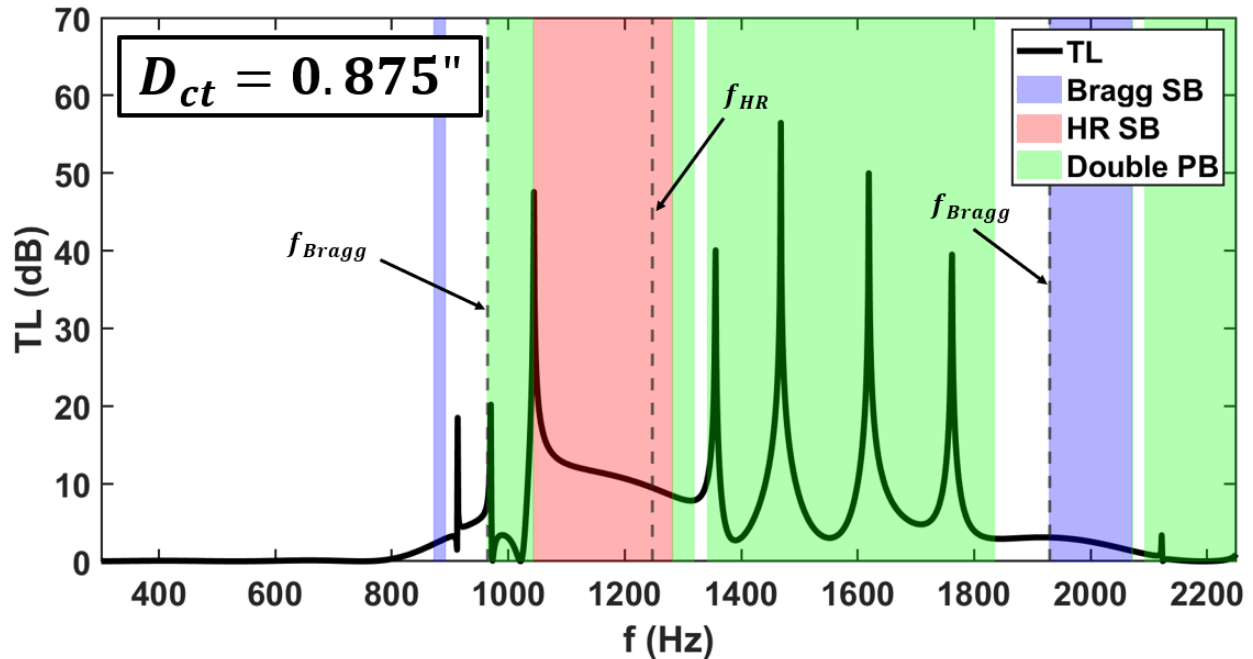


Figure 111. Coupling Tube Diameter = 0.875 in.

The diameter of the coupling tubes is now 0.875 in., which is close to the height of the resonators at 1.0 in. A considerably larger amount of energy can now transmit through the coupling tubes, so the double propagation band is widened. The transmission loss in the double propagation band has also increased considerably because with more energy propagating through the coupling tubes, more destructive interference can occur when the waveguides meet at the resonator necks. The transmission loss in the Helmholtz stop band has decreased in magnitude and is coalescing with the transmission loss in the double propagation band, since the system is becoming more of a waveguide and less of an array of classical Helmholtz resonators. All curves are combined in Figure 112 for reference.

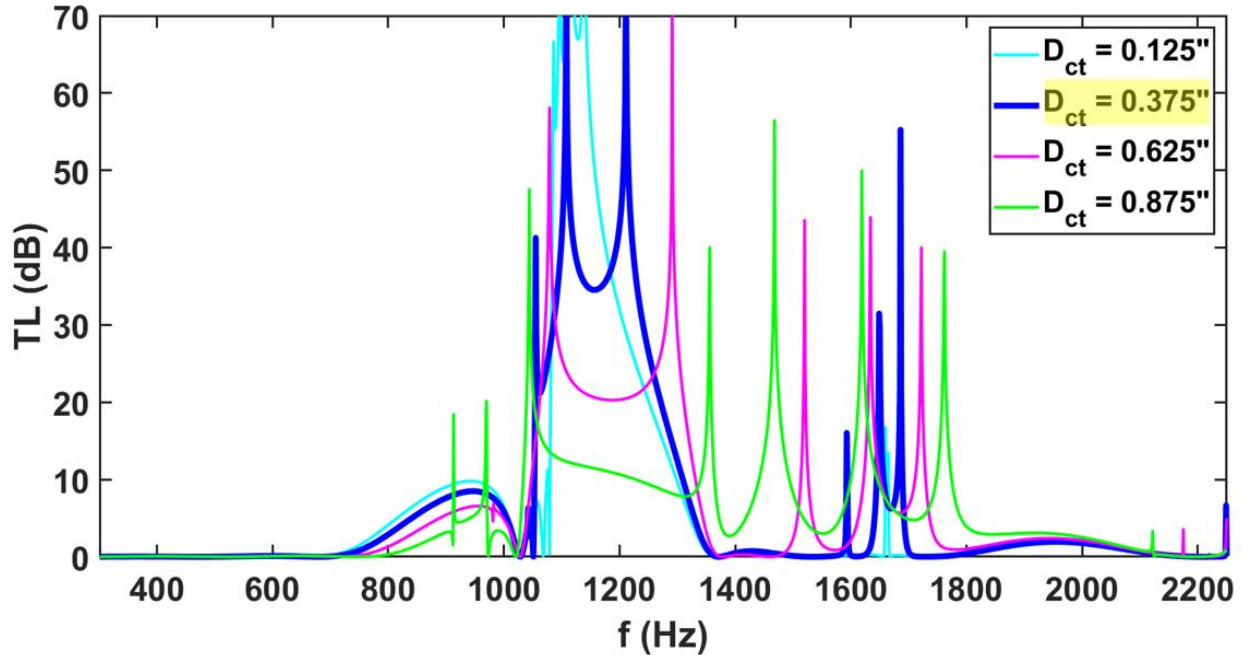


Figure 112. Effect of Coupling Tube Diameter on Transmission Loss - All Plots Combined

In summary, an increase in the coupling tube diameter widens the double propagation band and increases the transmission loss in the band because more energy can travel through the larger diameter coupling tubes which increases the amount of destructive interference when the waves traveling down the two paths meet at the necks of the resonators. The system becomes more of a waveguide and less of an array of classical Helmholtz resonators, so the Helmholtz resonant peak widens and decreases in magnitude.

3.4.7. Change in number of resonators

The next parameter of this study is the number of resonators. The effect of the number of resonators on the transmission loss normalized by the number of resonators TL/N is plotted in Figure 113.

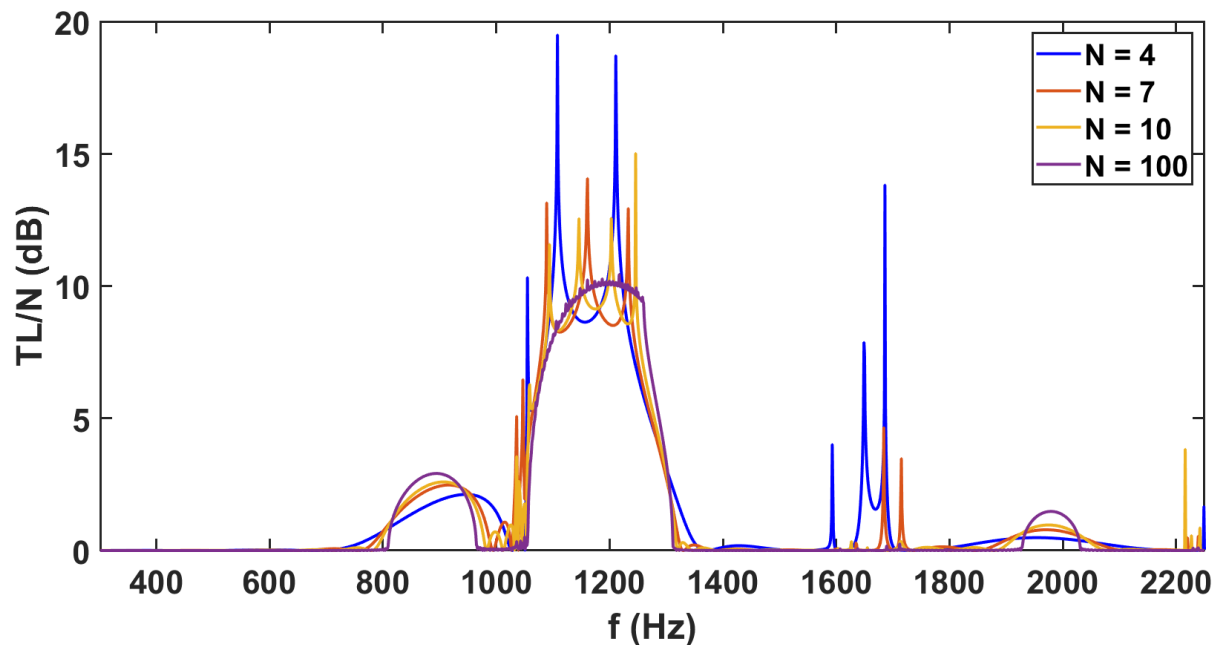


Figure 113. Effect of Number of Resonators on Normalized Transmission Loss for the Connected Resonator System

Like in the case of unconnected resonators, the normalized transmission loss for the connected resonator system does seem to converge as $N \rightarrow \infty$; therefore, it is of interest to obtain an expression for this solution.

Recall that each propagation constant represents a different Bloch wave, a forward and backward-traveling Bloch wave going through the duct and a forward and backward-traveling Bloch wave going through the connected cavities of the resonators. That means that even if one forward-traveling Bloch wave is experiencing a stop-band, the other forward-traveling Bloch wave could be propagating, meaning that power transmission can still occur. Both Bloch waves need to be in a stop-band in order to prevent power transmission through the system. Even if both are in a stop-band, however, the magnitude of the stop-bands can still differ. If one stop-band has an attenuation constant with a higher magnitude, it can stop power transmission more than the other one can; therefore, the limiting factor is the attenuation constant with the lowest magnitude. Given this line of reasoning, the normalized transmission loss as $N \rightarrow \infty$ can again be expressed using the same formula that Wang gave for the unconnected resonator system [16], only this time, the minimum of two forward traveling propagation constants is used (one in the resonator-cavity waveguide, and one in the main duct). Using Wang's reasoning [16], the

normalized transmission loss as the number of resonators approaches infinity can thus be written as

$$\lim_{N \rightarrow \infty} \frac{TL}{N} = 20 \log_{10} |\min(\max|\lambda_{1,2}|, \max|\lambda'_{1,2}|)| \quad (107)$$

Plotting the results of this equation yields the results in Figure 114.

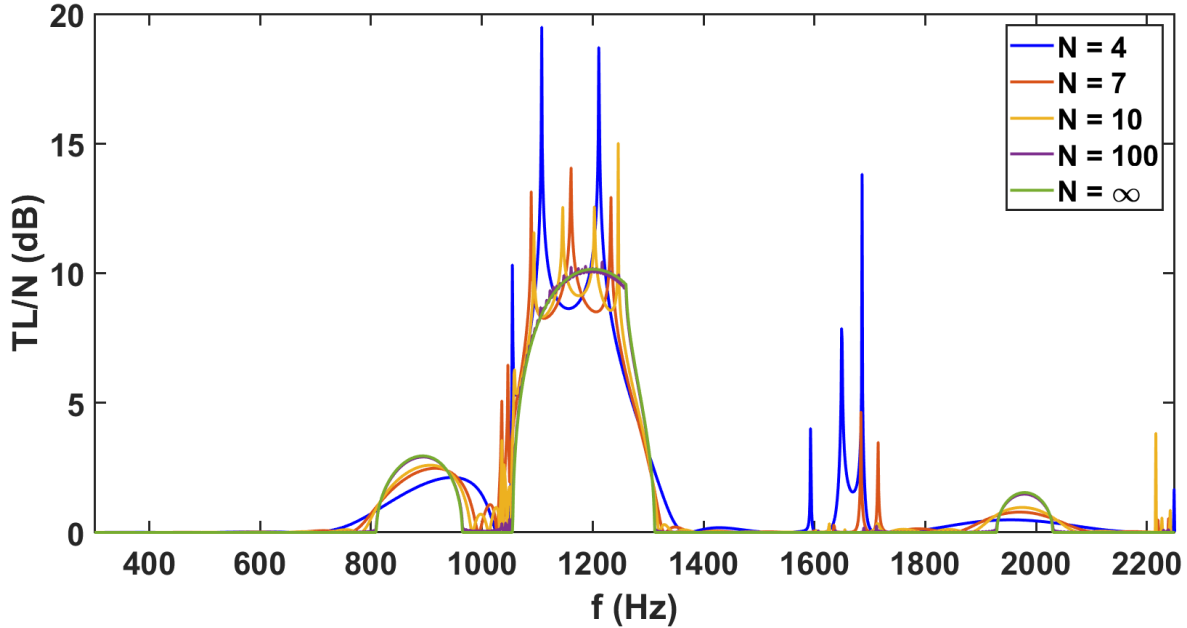


Figure 114. Normalized Transmission Loss TL/N as $N \rightarrow \infty$ for the Connected Resonator System

Because the normalized transmission loss curve for the case of $N \rightarrow \infty$ is close to the $N = 100$ curve, the formula presented for the normalized transmission loss as the number of resonators approaches infinity is considered accurate. The transmission loss also seems to follow the shape of the attenuation constants shown for the infinite system.

Another conclusion based on this study is that as N increases, the peaks in the double propagation band become less prominent. Keeping in mind that the plot shows *normalized* transmission loss, the peaks in the double propagation band are actually still there, but they do not magnify with increasing N as the peaks for stop-bands do. The question “what would happen if the cavity wall is closed every four resonators” is then of interest. This case could be a topic for future work.

3.5. Conclusions

The similarity between the analytical and numerical solutions verifies that a duct lined with periodically-spaced Helmholtz resonators with coupled cavities can accurately be modeled using the transfer-matrix method in conjunction with Bloch wave theory. The results show that transmission loss stop bands from Bragg reflection can be induced by specifically tuning the spacing of the resonators to a multiple of a half-wavelength of the incoming sound waves and that the frequencies of those stop-bands are not altered by the number of resonators. Additional transmission loss has been shown to occur in the double-propagation band for finite systems due to the destructive interference between the waves propagating through the coupled-resonator waveguide and the waves propagating through the main duct when they interact at the interface (i.e., the necks). As the number of resonators approaches infinity, the normalized transmission loss curve aligns with the curves of the smaller of the attenuation constant.

A parameter study revealed that the modification of certain parameters yields desirable effects. By increasing the coupling tube diameter, the transmission loss assumes a more broadband shape without overly sacrificing tonal peaks. By changing either the length of the coupling tube or the spacing of the resonators, the double propagation band can be widened. Based on all of this information, a methodology can be actualized to take advantage of these effects. First, the Helmholtz resonator cavity should be made as large as possible to bring the resonance frequency as low as possible. Then, the resonators should be spaced as far apart as possible to achieve the lowest frequency attenuation possible from Bragg reflection. Next, the spacing could be shortened slightly such that the Bragg peak gets closer to the peak of the resonant frequency of the Helmholtz resonator. As the peaks get closer, the amplitude of the Bragg peak increases. Additional Bragg peaks will occur at higher frequencies that correspond to the next multiple of a half of a wavelength, so those should be considered as well. Then, the resonators can be connected together to achieve transmission loss in the double-propagation band. The coupling tube diameter should then be widened in order to connect all of the peaks together and achieve a broadband response without sacrificing too much tonal transmission loss in the Helmholtz stop band.

The advantages of periodically spaced Helmholtz resonators with cavities connected by coupling tubes shows promise for applications in liner technology. Careful resonator spacing

can even increase transmission loss at frequencies lower than the Helmholtz resonant frequency, and double-propagation bands from coupling the resonators can increase transmission loss in ranges between the peaks. Increasing the diameter of those coupling tubes results in a more broadband transmission loss pattern that does not sacrifice significant amplitude in the Helmholtz stop band.

Based on the analytical and numerical modeling, more practical AMM liner concepts can now be proposed. In practice, liners feature perforated sheets on top of a core of quarter-wave resonators rather than individual Helmholtz resonators, but the same ideas discussed in this paper can still be applied to that geometry. For example, the quarter-wave resonators could be connected together via coupling tubes in the exact same way via perforations in the resonator walls (see Figure 115). Note that to some extent, perforations in resonator walls are present in conventional liners already in the form of drainage slots; perhaps the drainage slots could be optimized to achieve the effects discussed herein.

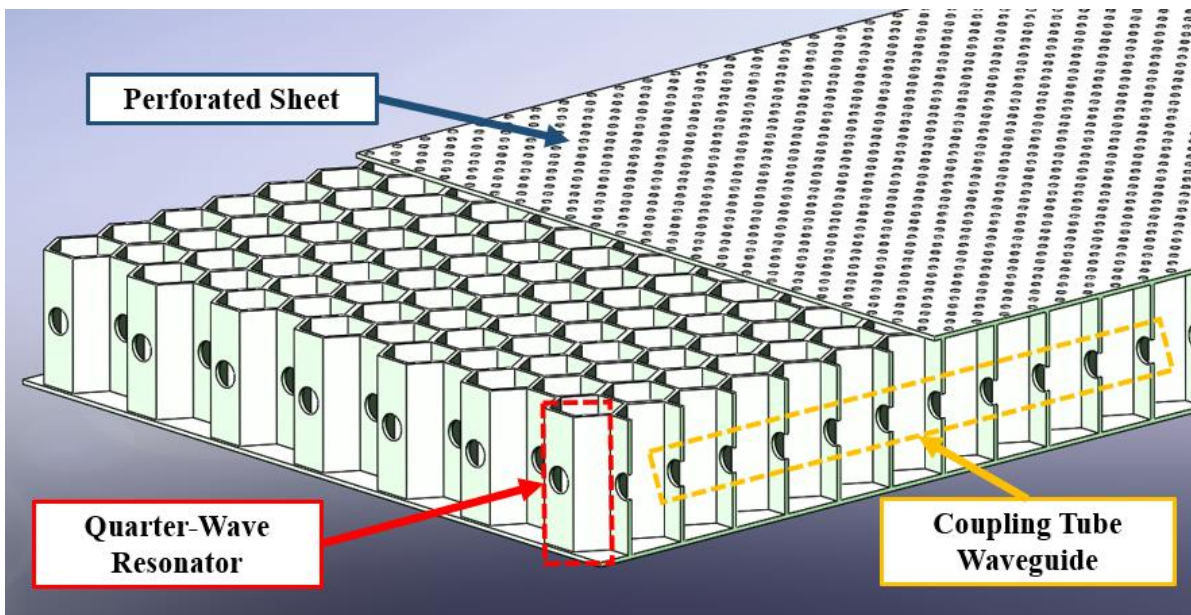


Figure 115. Example of a Practical AMM Liner with Coupled Quarter-Wave Resonators Forming a Waveguide

Recall that Bragg reflection can increase the transmission loss for a resonator spacing that is a multiple of a half of a wavelength. By increasing the spacing of the resonators, Bragg reflection can be induced at lower frequencies (see Figure 116). For this to be effective, a sufficient length in the inlet or aft duct is needed which is not explored herein and is instead left

as future work. Here, rectangular resonators are used for visual simplicity, but hexagonal-shaped resonators can still be used to the same effect. In this example, the cross-sectional area of the coupling tube was increased as well. Recall that increasing the cross-sectional area increases the transmission loss in the double propagation bands which in turn results in more broadband attenuation.

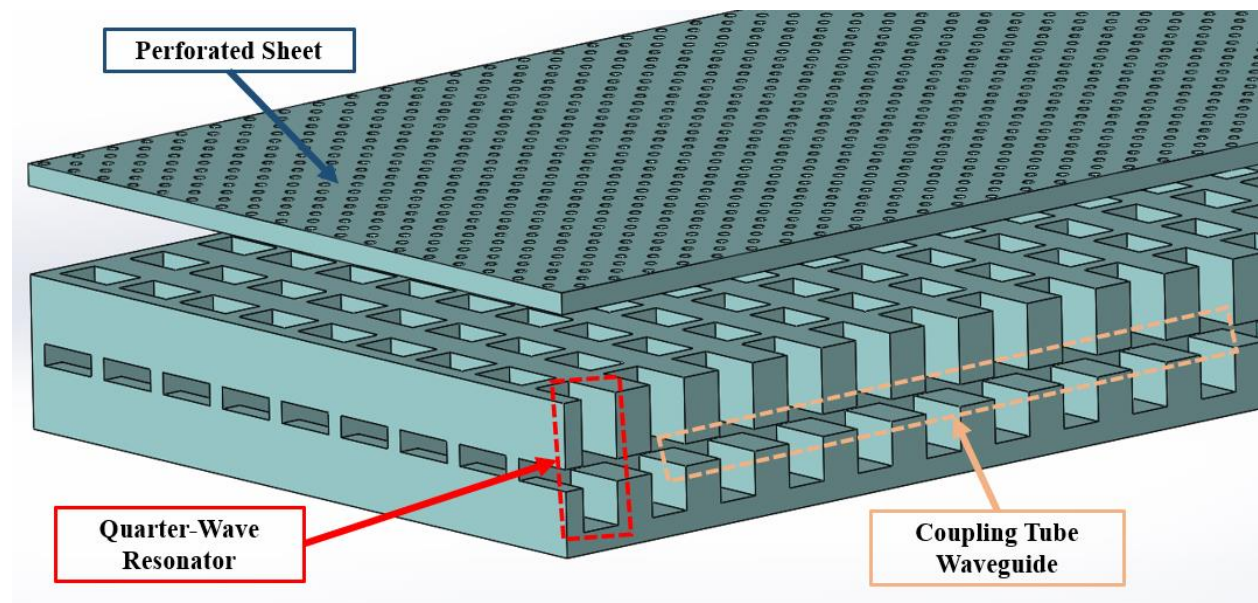


Figure 116. Exploded View of a Practical AMM Liner Example with a Larger Spacing Between the Resonators and Larger Coupling Tube Diameter

Recall from the parameter study that changing the length of the coupling tubes also shifts the frequencies of the double propagation band. In this next example, by moving the coupling tube below the resonators, the coupling tube length can be increased without changing the spacing of the resonators (see Figure 116).

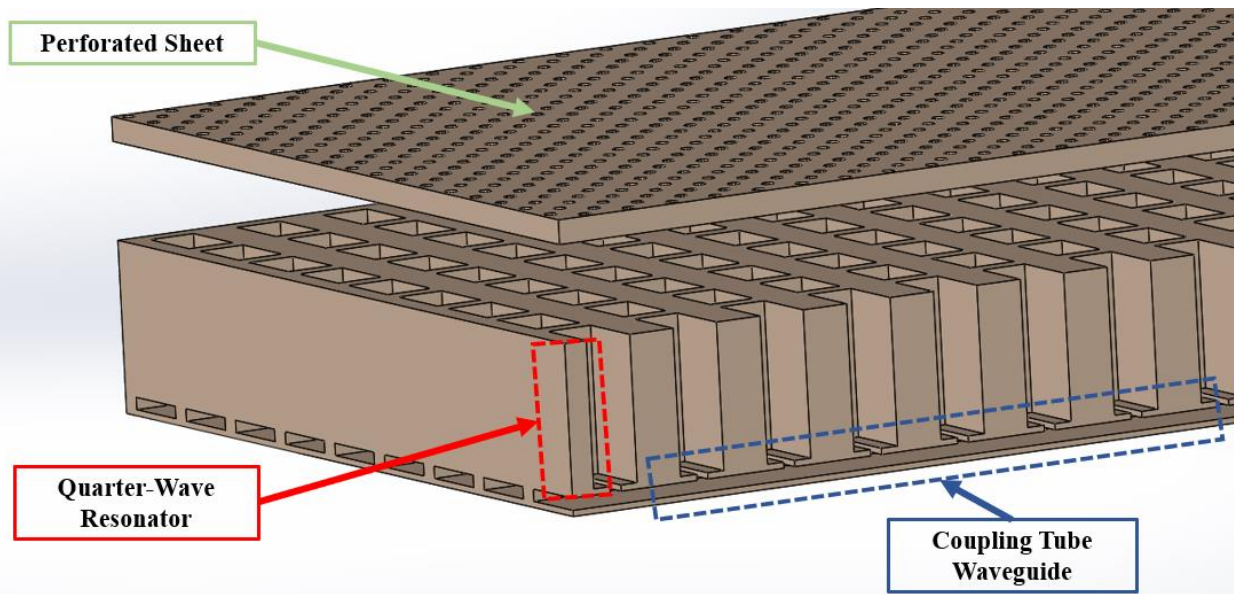


Figure 117. Exploded View of a Practical AMM Liner Example with Coupled Quarter-Wave Resonators Forming a Waveguide Below the Resonators

4. EXPERIMENTAL TESTING AND VALIDATION

The main objective of the experimental testing and validation is to verify that the results predicted in the analytical and numerical studies are possible to achieve in a real acoustic environment representative of an aircraft engine inlet. The analytical and numerical results considered before did not consider damping, viscothermal losses, and other system imperfections that occur in practice, so the results measured are not expected to exactly match the predicted results; rather, the goal is to observe trends. If the trends are found to agree with the predicted results, then the analytical reasoning presented in this paper is further validated. The transmission loss will again be used to evaluate the performance of these systems. The transmission loss is a measurement of how much sound power is reduced by a liner; hence, this measurement relates to an aircraft engine inlet because when a liner is applied to the nacelle, that liner needs to be able to attenuate certain frequencies of sound that are emitted by the engine. The total amalgamation of the modeling and experimental testing results presented herein will thus encompass the groundwork upon which further research and experimentation with this AMM technology can be conducted.

4.1. Experimental setup of impedance tube

An impedance tube is an apparatus used for experimental testing of sound absorbing materials [63]. The particular type of impedance tube used in these experiments is a grazing incidence impedance tube (see Figure 118). In a grazing incidence impedance tube, the liner replaces a portion of one of the inner faces of the duct, and the acoustic waves approaching this liner test section will thus graze the liner. Other kinds of impedance tubes like normal incidence impedance tubes also exist (for example, the NIT at NASA Langley) [11]. Impedance tubes can range from being quite simple to very complex systems. The Grazing Flow Impedance Tube (GFIT) at NASA Langley, for example, has 95 microphones, 18 acoustic drivers, the ability to generate flow up to Mach 0.6 within the duct, and advanced in-situ microphone calibration techniques [11]. All impedance tubes however share some basic requirements: the tube must be of a sufficient length and construction to allow for the propagation of acoustic waves, at least two microphones at different locations along the duct to measure those waves, and some way to process the data from the microphones. Standards such as ISO-10534 [64] or ASTM-E1050 [65]

give more detail as to the specific dimensional requirements of the system depending on the user's application.

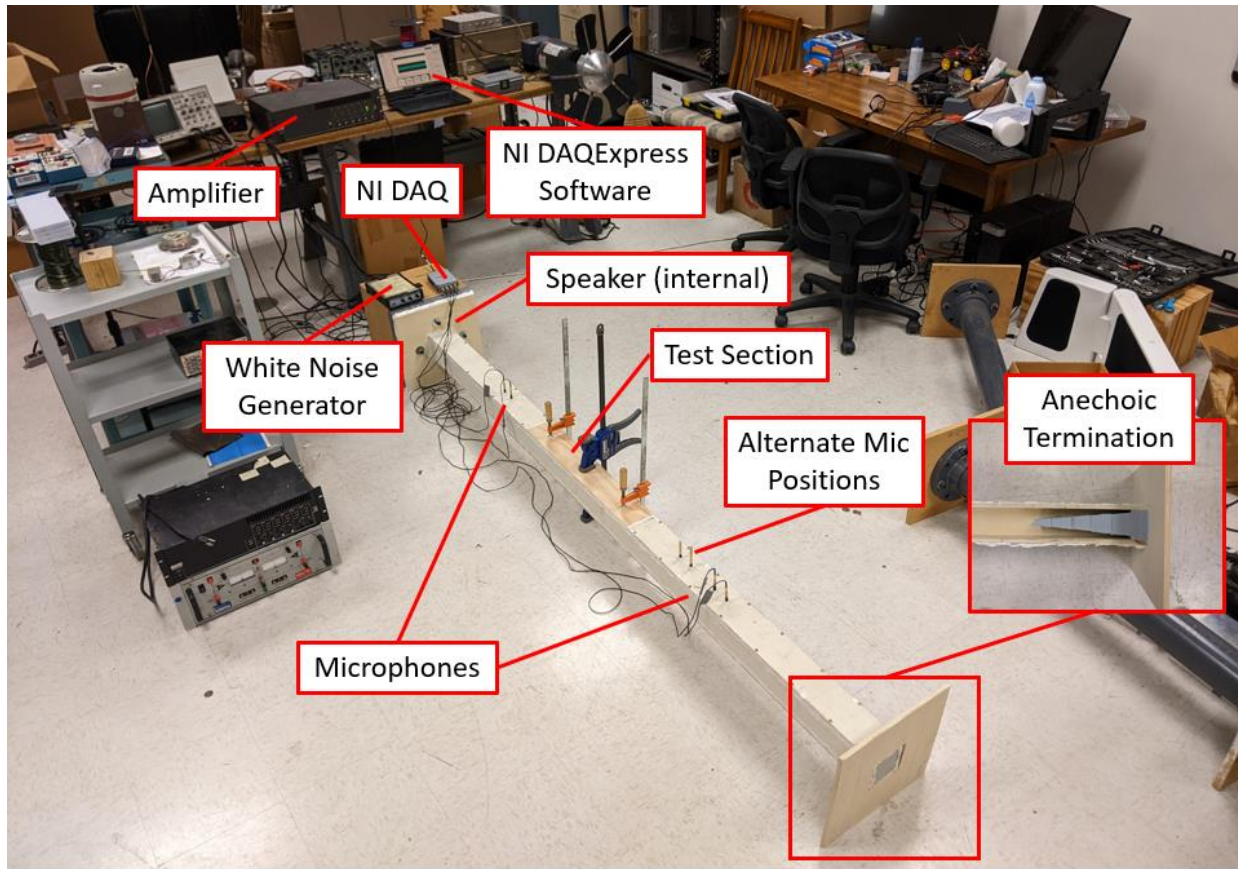


Figure 118. Experimental Setup of Impedance Tube

The grazing incidence impedance tube at the Center for Aerospace Acoustics at the National Institute of Aerospace is a 3"x3"x8' wooden duct with 1/2" walls, a 25" long test section, and six microphone holes – two microphone holes upstream of the test section and four in the downstream section. A diagram showing the dimensions of the four microphone holes used in the experiments are shown in Figure 119 where all dimensions are in inches.

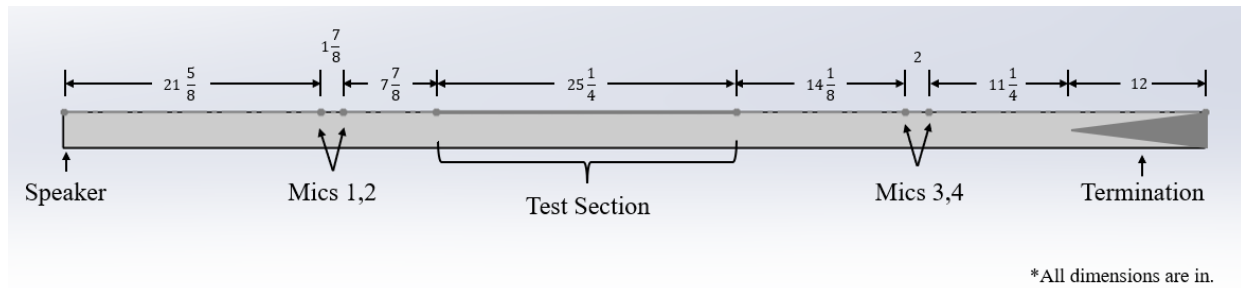


Figure 119. A diagram of dimensions of the impedance tube

For the experiments performed for this research work, four G.R.A.S. Type 40PL microphones were used – two were flush-mounted in the holes of the upstream section, and two were flush-mounted in the two holes furthest from the test section in the downstream section were used. The two furthest holes were used because the coherence between all the microphones was found to be better in that configuration. The other two holes that were not in use were plugged with 5/16” dowels that were sanded down radially to fit as snugly as possible with the holes and then sealed with clay. Each microphone was connected to a National Instruments NI-9234 C Series Sound and Vibration Input Module, using BNC cables. NI DAQExpress software was used to record the data with a 25.6 kHz sampling rate. The microphone sensitivity in NI DAQExpress was manipulated such that the reading from the microphones were all within ± 0.02 dB of the 94 dB 1000 Hz sine wave emitted by the Brüel & Kjær Type Sound Level Calibrator Type 4230 with a 1/4” diameter microphone adapter. An ACO Pacific, Inc. Model 3024 “Very Random”™ Noise Generator was used to generate white noise which was amplified by a Rane MA 6 Multichannel Amplifier before sent to the loudspeaker. The entire tube is sealed including the test section and the microphones to prevent sound from escaping the system. At the end opposite the speaker, a foot-long, wedge-shaped acoustic termination is mounted inside the duct. The termination was created by cutting different sizes of foam and gluing them together into a wedge shape. The waves in the duct will be well absorbed for a wavelength that is four times larger than the length of the termination; hence, with a foot-long termination, good absorption will occur above 281 Hz. Based on the dimensions of the 3”x3” cross-sectional area of the duct, only plane waves are present below 2250 Hz which is the cut-on frequency of the (1,0,0) mode. The working range is thus 281 Hz – 2250 Hz. All other frequency content can be ignored. The inner walls of the duct were painted with two thick coats of polyurethane thus creating a better rigid-walled boundary condition and preventing sound from escaping.

Six different tests were run on the impedance tube with three repeated trials for each – a case with unconnected resonators spaced 4.5” apart, a case with unconnected resonators spaced 7” apart, three cases with connected resonators spaced 7” apart with different diameter coupling tubes, and a hard wall case. The results to be presented are the averaged results across three runs for each system tested. The geometry of the systems are the same geometry presented in the analytical and numerical sections of this work. The resonators were constructed out of MDF – the necks of the resonators were created by cutting 1.5” diameter holes out of a ¼” panel of medium-density fiberboard (MDF) using a hole saw, and the resonators cavities were made by cutting out each of the cavity walls with a circular saw and gluing them together into the shape of the resonator cavity (see Figure 120 and Figure 121). The cavity walls that run perpendicular to the axis of the duct were not glued however so that they could be swapped out with alternate walls used for the connected resonator studies. The walls for the first connected resonator study were the same dimensions as the unconnected study but included a ½” hole drilled out so that a 3/8” I.D. (1/2” O.D.) cross-linked polyethylene (PEX) pipe could be inserted. The PEX tubing was cut with a ratcheting PVC cutter into three 4” long tubes. All of the walls of the resonator and PEX tube interface were held together and sealed using modeling clay. The inside of the resonators as well as the inner face of ¼” boards were painted with two thick coats of polyurethane to create a better rigid-walled boundary condition and prevent sound from escaping. The other two connected-resonator experiments were set up in the exact same way except that larger diameter coupling tubes were used. Once constructed, the test sections were clamped firmly to the duct and clay was placed along all the edges to seal the interfaces.

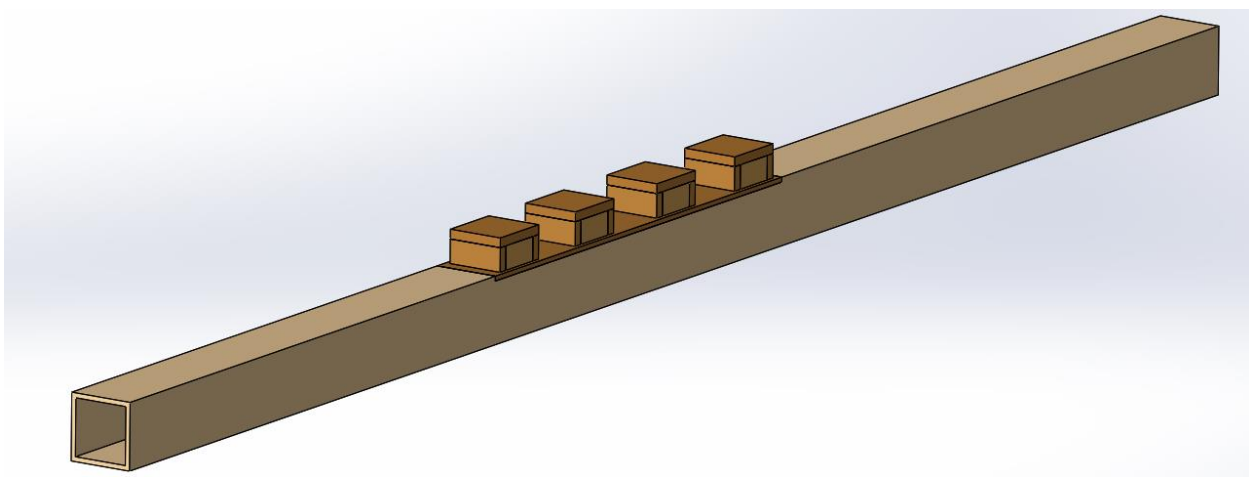


Figure 120. Schematic of the Unconnected Resonators with 7” Spacing Test

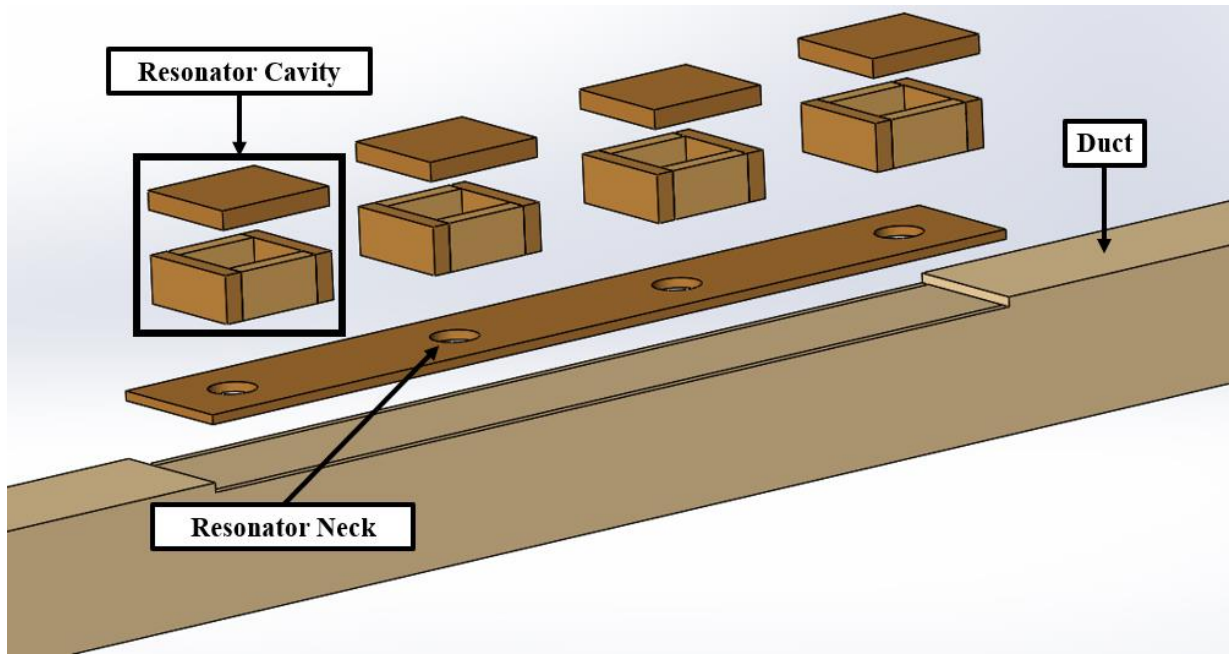


Figure 121. Exploded View Schematic of the Unconnected Resonators with 7" Spacing Test

The first test was the case of unconnected resonators spaced 4.5" apart (see Figure 122).

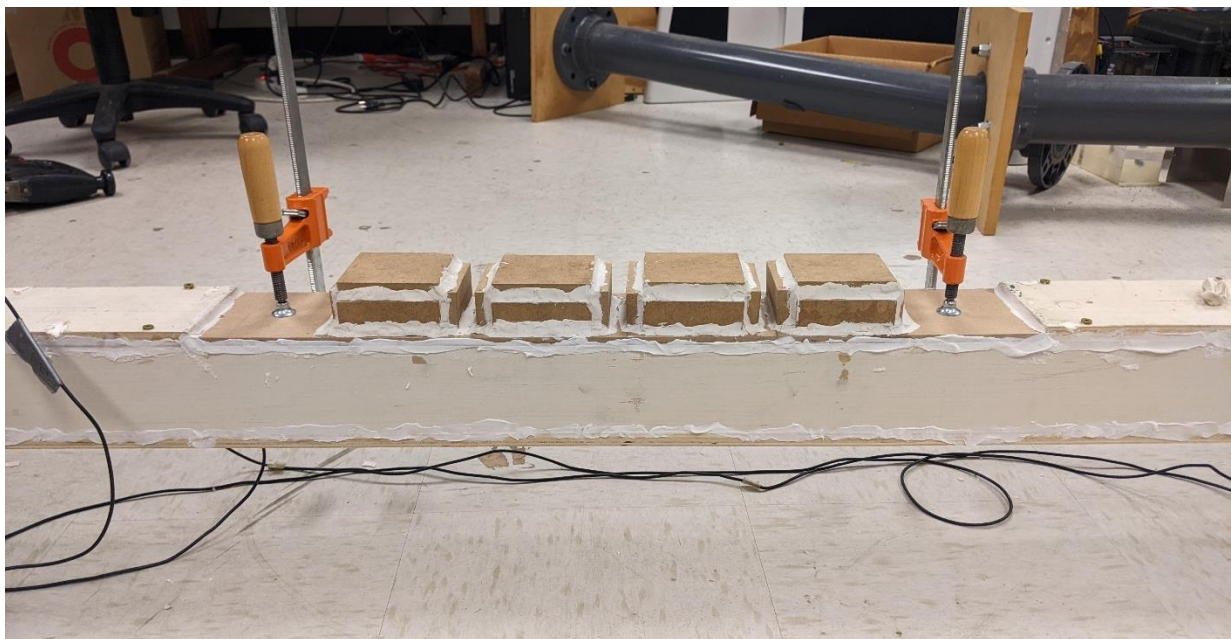


Figure 122. Unconnected Resonators with 4.5" Spacing Test

The purpose of this test was to obtain results for a baseline case. In traditional acoustic liners, the cavities are bordering each other, so in this case, the resonators were of the same geometry as the tests to come, but they were placed as close together as possible such that clay could still fit in between them to seal the system. Given that the spacing is 4.5" Bragg reflection would thus occur at 1500 Hz according to the Bragg reflection formula [23]:

$$f_{Bragg} = m \frac{c}{2L_r}, (m = 1, 2, \dots) \quad (108)$$

The next test was the unconnected resonator system with 7" spacing (see Figure 123).

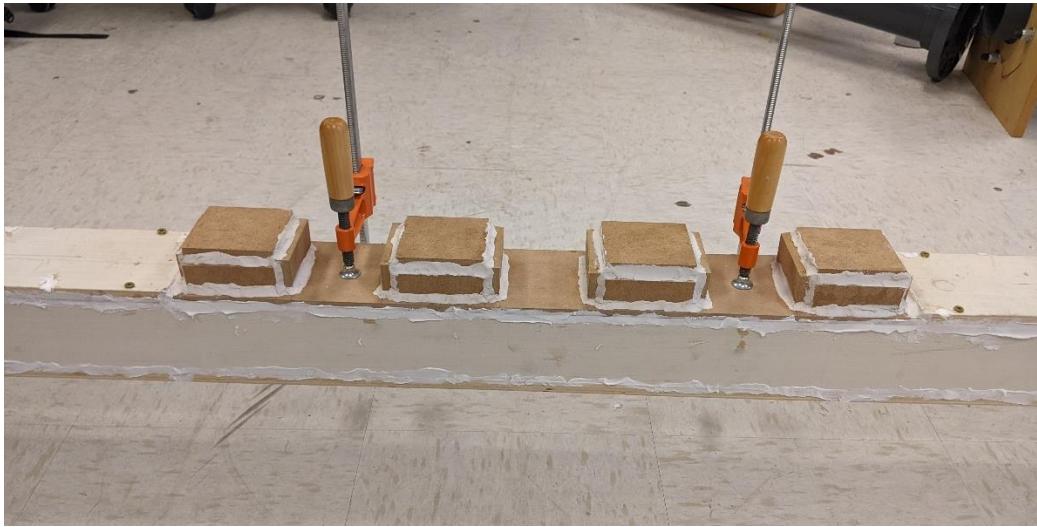


Figure 123. Unconnected Resonators with 7" Spacing Test

This system matches the system described in the analytical and numerical unconnected resonator sections. The purpose of measuring this system is to compare the result to the unconnected resonator system with 4.5" spacing and see how the transmission loss changes. Since these resonators are 7" apart, Bragg reflection should now occur at 964 Hz, which is less than the resonant frequency of the Helmholtz resonator at 1247 Hz [23]. This experiment would then show that spacing the resonators further apart can achieve lower frequency attenuation. The next test is the connected resonators with 7" spacing and a 3/8" coupling tube diameter (see Figure 124).

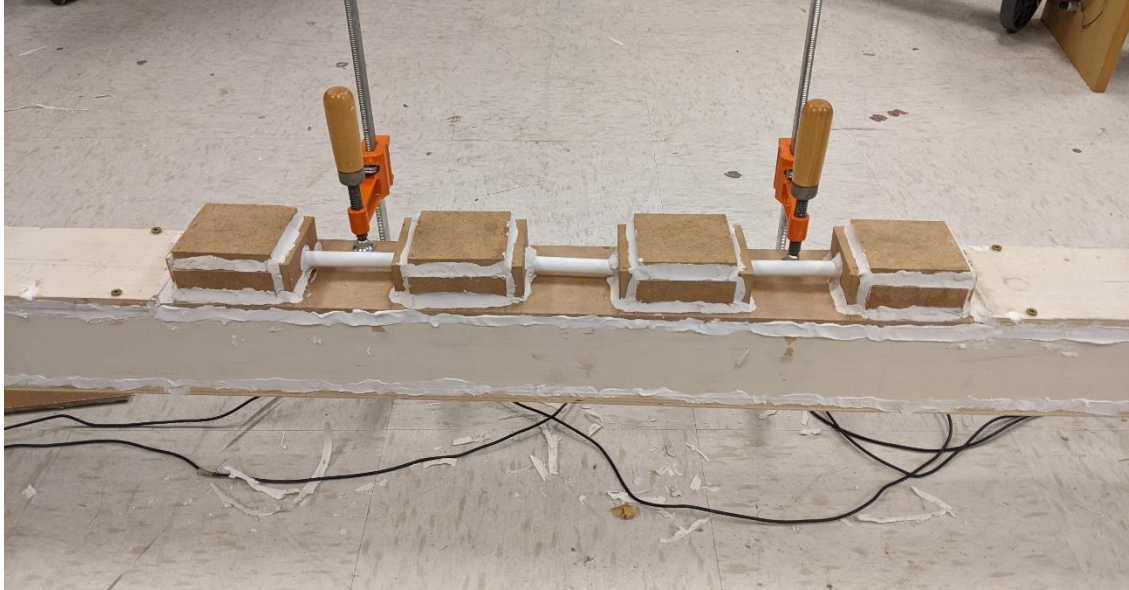


Figure 124. Connected Resonators with 7" Spacing and 3/8" Coupling Tube Diameter Test

The geometry of this test matches the geometry presented in the connected resonator analytical and numerical studies of the prior section. The purpose of this test is to show that the connected resonator system has the same Bragg reflection transmission loss peaks as the unconnected resonator system with the same 7" spacing, but the Helmholtz resonator peak should widen slightly. Also there should be additional transmission loss peaks that appear in the double propagation band that are not evident in the case of the unconnected resonator systems. The next test is the connected resonators with 7" spacing and a 5/8" coupling tube diameter (see Figure 125).

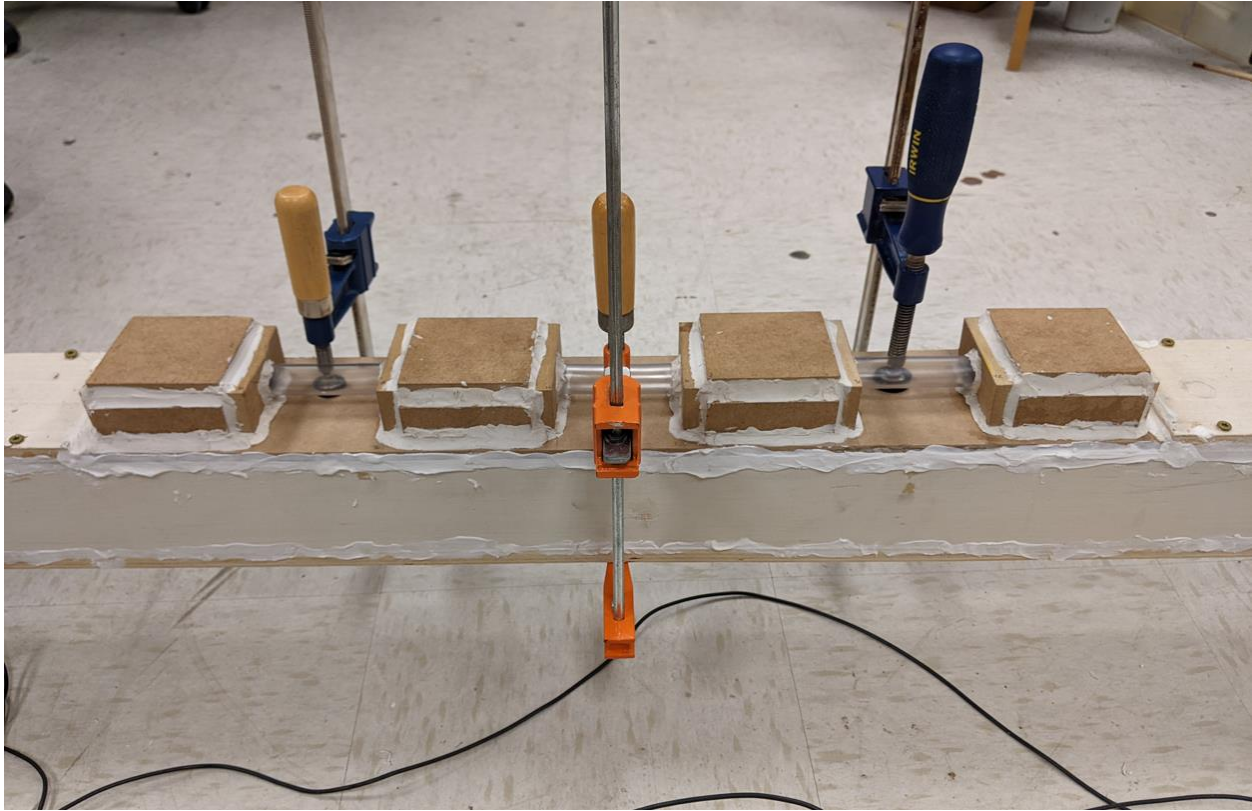


Figure 125. Connected Resonators with 7" Spacing and 5/8" Coupling Tube Diameter Test

The geometry of this test matches the geometry presented in the connected resonator analytical and numerical studies of the prior section except that the coupling tube diameter has been increased to 5/8 in. The purpose of this test is to show that this system will produce an increase in transmission loss in the double propagation band compared to the connected resonator system with 3/8 in. diameter coupling tubes (refer back to the section of the parameter study on coupling tube diameter). The next test is the connected resonators with 7" spacing and a 7/8" coupling tube diameter (see Figure 126).

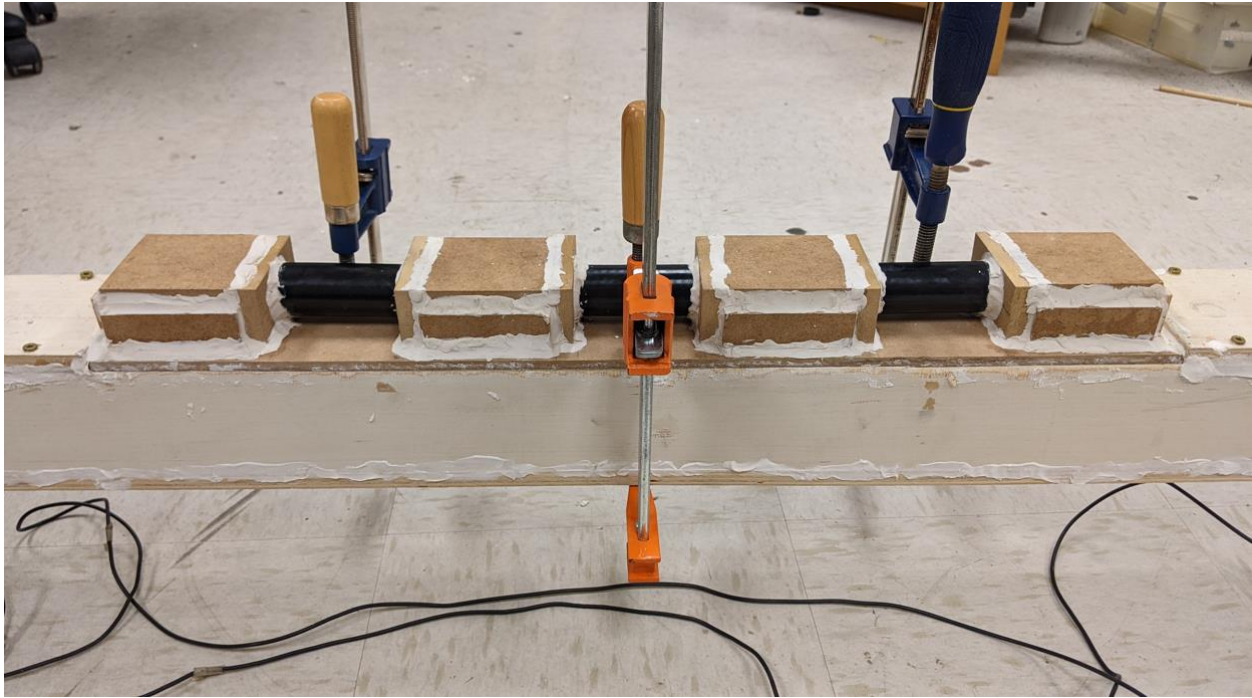


Figure 126. Connected Resonators with 7" Spacing and 7/8" Coupling Tube Diameter Test

The geometry of this test matches the geometry presented in the connected resonator analytical and numerical studies of the prior section except that the coupling tube diameter has been increased to 7/8 in. The purpose of this test is to show that this system will produce an even larger increase in transmission loss in the double propagation band compared to the connected resonator system with 5/8 in. diameter coupling tubes (refer back to the section of the parameter study on coupling tube diameter). The last test is the hard-wall case (see Figure 127).

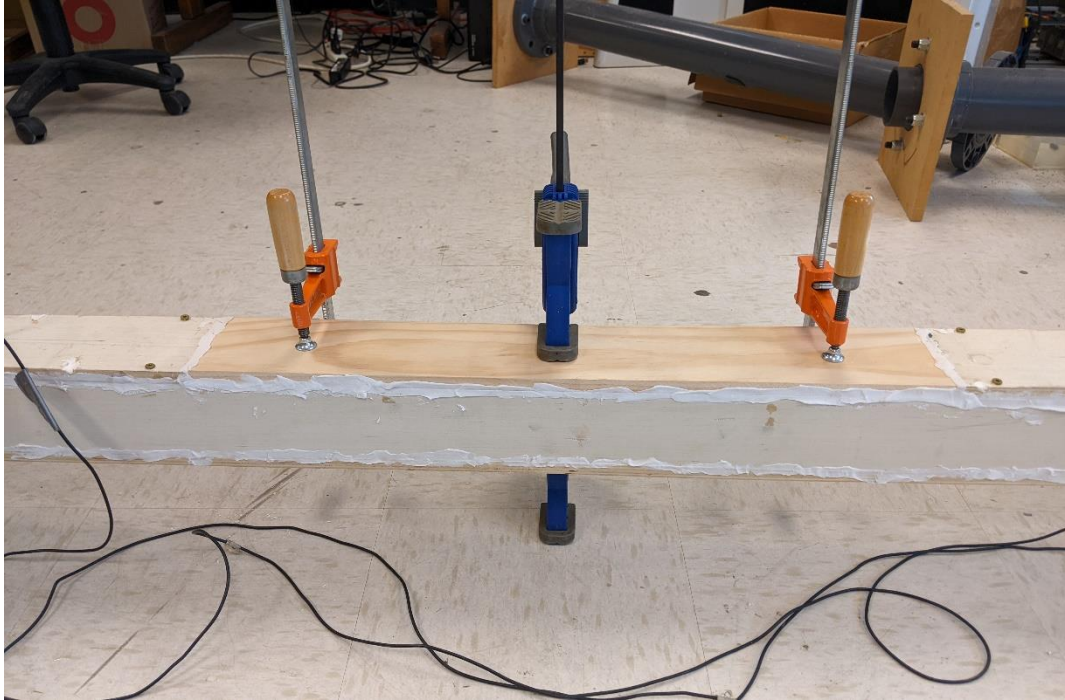


Figure 127. Hard Wall Test

Since the impedance tube is not a perfect system like it was modeled to be, the transmission loss is not going to be exactly zero across all frequencies. Therefore, the purpose of the hard wall test was to see what the transmission loss looks like for this system to account for these imperfections. The hard wall shown in the test section is a $\frac{1}{2}$ " pine board painted with two thick coats of polyurethane, clamped, and sealed with clay.

4.2. Results and validation using impedance tube

The predicted results of the first three tests are shown in Figure 128.

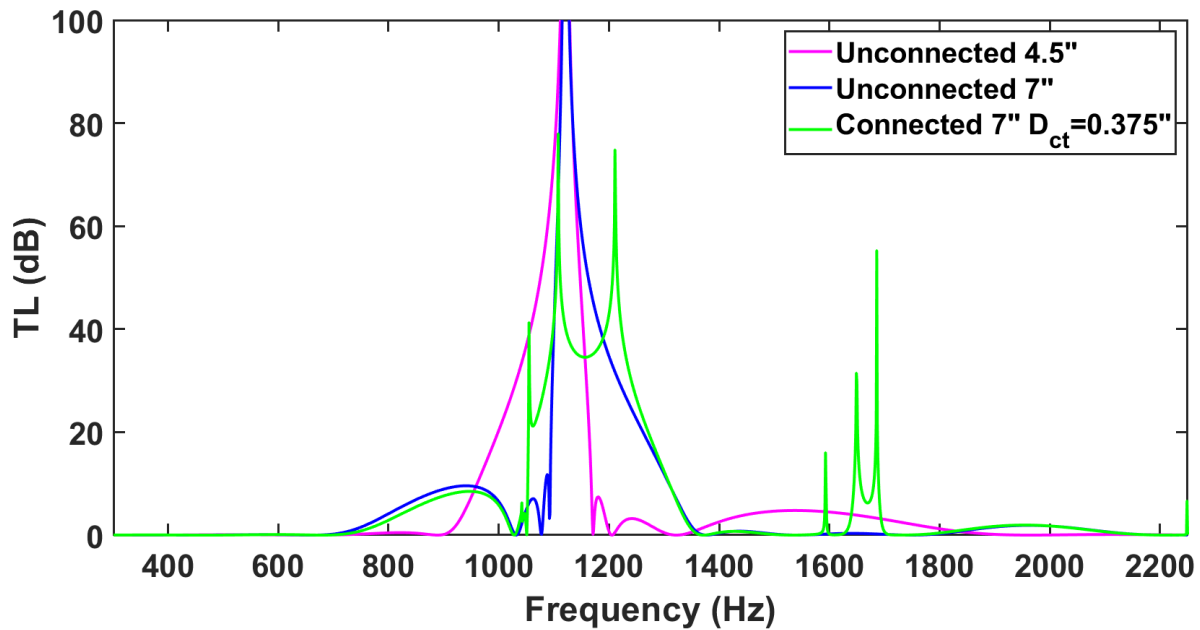


Figure 128. Predicted Results for First Three Impedance Tube Tests

It is shown that the unconnected 4.5" resonators do have the same Helmholtz resonant peak as the unconnected 7" case but without a Bragg-type peak at 964 Hz like the unconnected 7" case. Instead, the Bragg-type peak for the 4.5" resonator case is at 1500 Hz which is much higher. The connected 7" case shows the same Bragg peak at 964 Hz, but a wider shape at the resonant peak of the Helmholtz resonator. The 7" case also has peaks in the double propagation band that the unconnected cases do not have. In fact, the connected resonator system in a way represents the "best of both worlds" scenario – it exhibits the same Bragg peak of the unconnected 7" case *and* double-propagation peaks in the same region as the 4.5" case. The predictions for the three connected resonator cases with varying coupling tube diameters are shown in Figure 129.

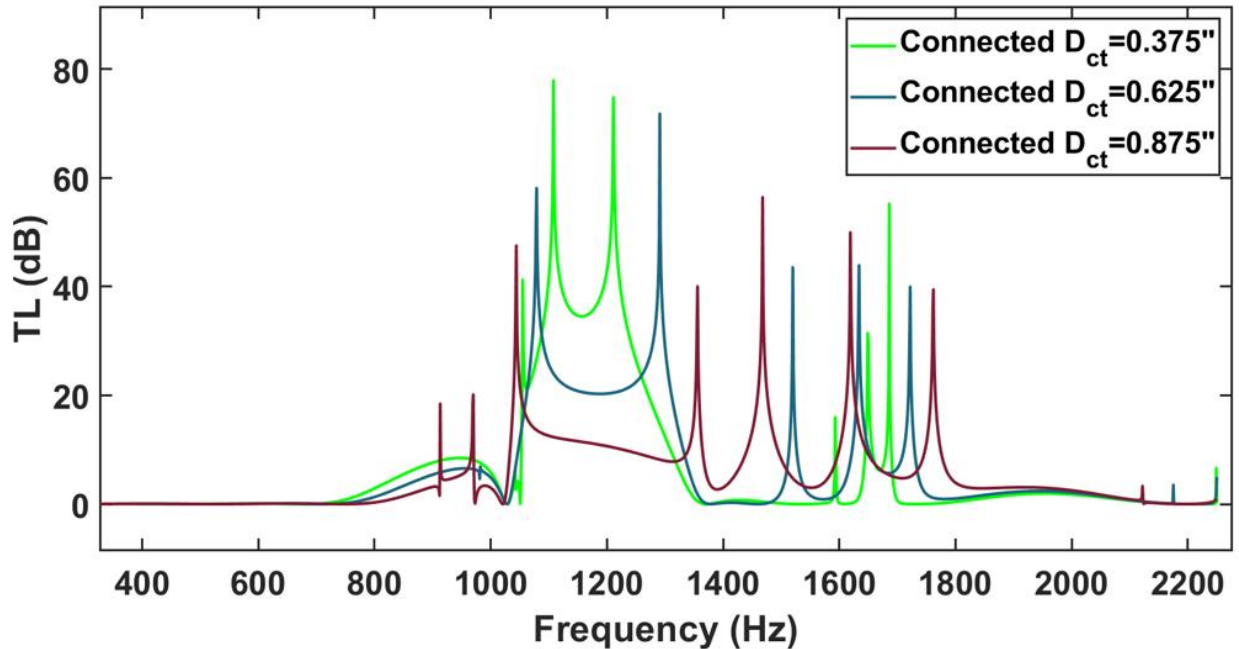


Figure 129. Predicted Results for the Three Connected Resonators Tests

The predictions for these three systems indicate that as the coupling tube diameter increases, the transmission loss in the double propagation band (i.e., 1400-1800 Hz) should increase while the Helmholtz stop band (i.e., 1000-1400 Hz) should decrease. These predictions make sense because as the coupling tube diameter is increased, more energy will be permitted through the coupling tubes; the system will behave more like a waveguide and less like an array of classical Helmholtz resonators. As such, the system will achieve more attenuation through the destructive interference of the waves traveling in the coupled-resonator waveguide combining with the waves traveling through the main duct when they reach the necks of the resonators.

The measurements acquired from NI DAQExpress were processed in a transmission loss MATLAB code that followed the methods presented by B&K [63] and will be summarized briefly here. The variables to follow are defined in Figure 130.

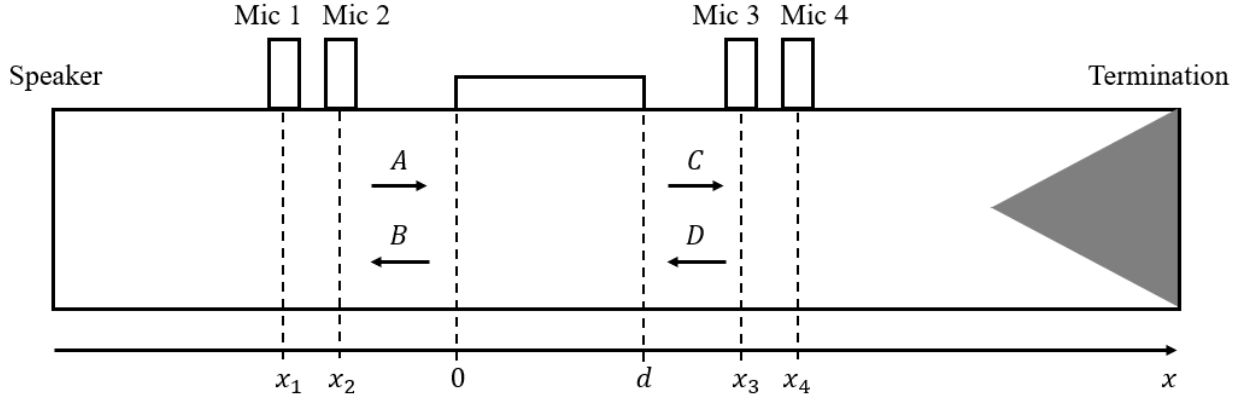


Figure 130. Geometric Definitions used for Measured Transmission Loss Equations

The pressure coefficients of the incident and reflected waves in both the upstream and downstream sections of the tube are found by

$$\begin{aligned}
 A &= \sqrt{G_{rr}} \frac{j(H_{1r}e^{jkx_2} - H_{2r}e^{jkx_1})}{2 \sin k(x_1 - x_2)} \\
 B &= \sqrt{G_{rr}} \frac{j(H_{2r}e^{-jkx_1} - H_{1r}e^{-jkx_2})}{2 \sin k(x_1 - x_2)} \\
 C &= \sqrt{G_{rr}} \frac{j(H_{3r}e^{jkx_4} - H_{4r}e^{jkx_3})}{2 \sin k(x_3 - x_4)} \\
 D &= \sqrt{G_{rr}} \frac{j(H_{4r}e^{-jkx_3} - H_{3r}e^{-jkx_4})}{2 \sin k(x_3 - x_4)}
 \end{aligned} \tag{109}$$

where H_{ir} is the frequency response function between the sound pressures picked up by microphones $i = 1,2,3,4$, and the reference microphone r (which in this case is mic 1), and G_{rr} is the autospectrum of the reference microphone [63]. The pressure coefficients were then used to find the transmission loss using transfer matrix formulation given by

$$\begin{aligned}
 \begin{bmatrix} p \\ v \end{bmatrix}_{x=0} &= \begin{bmatrix} T_{11} & T_{12} \\ T_{21} & T_{22} \end{bmatrix} \begin{bmatrix} p \\ v \end{bmatrix}_{x=d} \\
 p_{x=0} &= A + B \\
 v_{x=0} &= \frac{A - B}{\rho c} \\
 p_{x=d} &= Ce^{-jkd} + De^{jkd} \\
 v_{x=d} &= \frac{Ce^{-jkd} - De^{jkd}}{\rho c}
 \end{aligned} \tag{110}$$

where ρ is the density of air and c is the speed of sound in air [63]. The transfer matrix terms can be found by

$$\begin{bmatrix} T_{11} & T_{12} \\ T_{21} & T_{22} \end{bmatrix} = \frac{1}{p_{x=0}v_{x=d} + p_{x=d}v_{x=0}} \begin{bmatrix} p_{x=d}v_{x=d} + p_{x=0}v_{x=0} & p_{x=0}^2 - p_{x=d}^2 \\ v_{x=0}^2 - v_{x=d}^2 & p_{x=d}v_{x=d} + p_{x=0}v_{x=0} \end{bmatrix} \quad (111)$$

which is the formulation used when the sample adheres to reciprocity (i.e. the determinant of its transfer matrix is 0) [63]. All of the systems used in this study are reciprocal, so the above form may be used. The transmission coefficient can then be written as

$$T_a = \frac{2e^{jkd}}{T_{11} + \frac{T_{12}}{\rho c} + \rho c T_{21} + T_{22}} \quad (112)$$

and finally, the transmission loss is given by

$$TL = 10 \log \frac{1}{|T_a|^2} \quad (113)$$

The impedance tube is not a perfect system, so the results are not exactly the same as what was predicted, but the trends are the same (as will be shown). Again, the differences between the analytical and experimental results are due to factors such as damping, system imperfections, and viscothermal losses. The experimental results for the unconnected resonators with a spacing of 4.5 in. are shown in Figure 131.

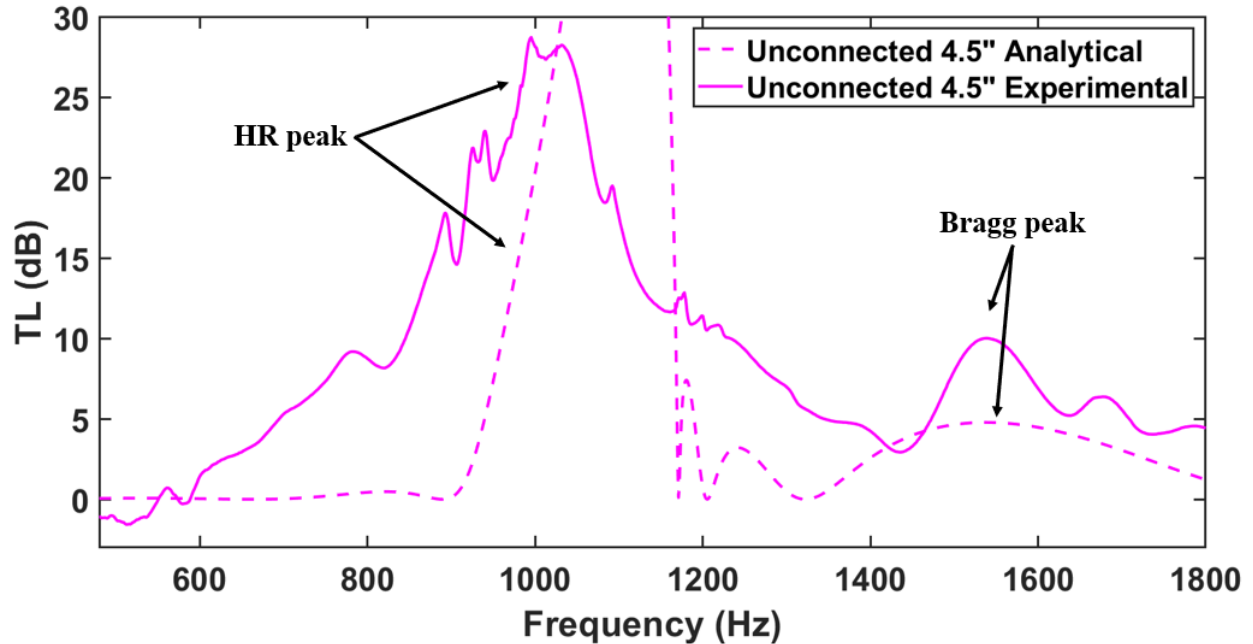


Figure 131. Measured vs Predicted Results for the Unconnected Array with 4.5" Spacing

Based on the predicted results shown before, the unconnected resonators case with 4.5 in. spacing should have one main Helmholtz resonant peak with a smaller Bragg-type peak to the right. Clearly from the experimental results, this is the case; however, the locations of the two peaks do not line up exactly with the predicted locations (again, due to factors such as damping, system imperfections, and viscothermal losses). The experimental results for the unconnected resonators with a spacing of 7 in. are shown in Figure 132.

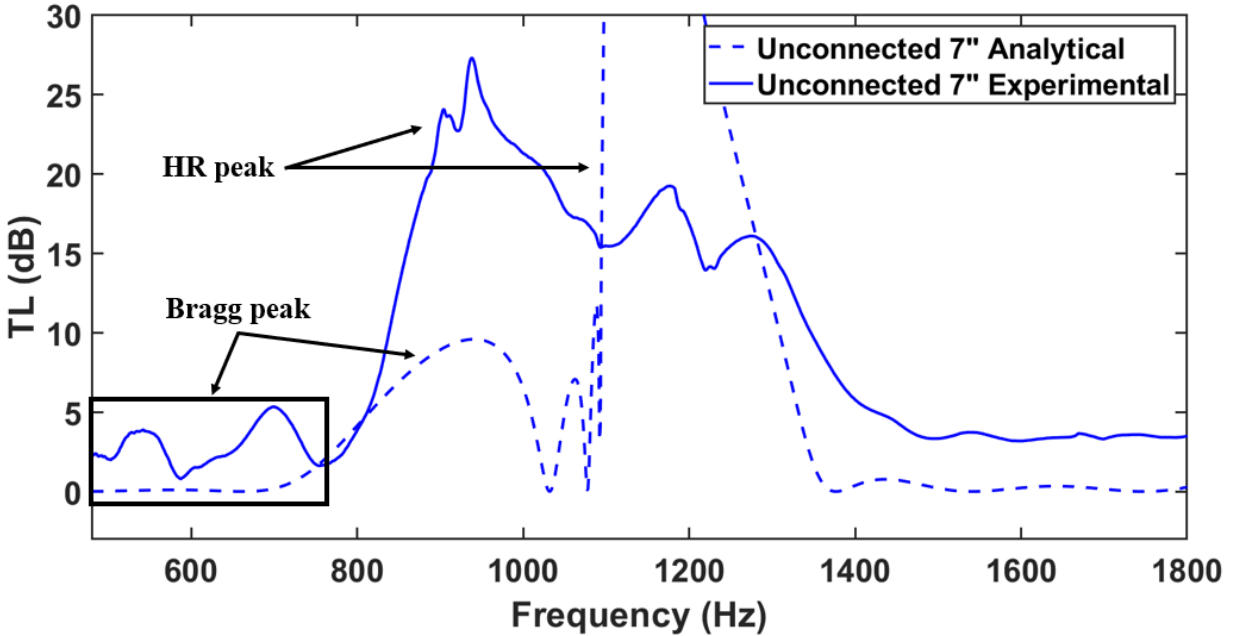


Figure 132. Measured vs Predicted Results for the Unconnected Array with 7" Spacing

Based on the predicted results, the unconnected resonators case with 7 in. spacing should have one main Helmholtz resonant peak with a smaller Bragg-type peak to the left. Clearly from the experimental results, this is the case; however, the locations of the peaks do not line up exactly with the predicted locations because of factors such as damping, system imperfections, and viscothermal losses. The experimental results for the connected resonators with a spacing of 7 in. and 3/8 in. diameter coupling tubes are shown in Figure 133.

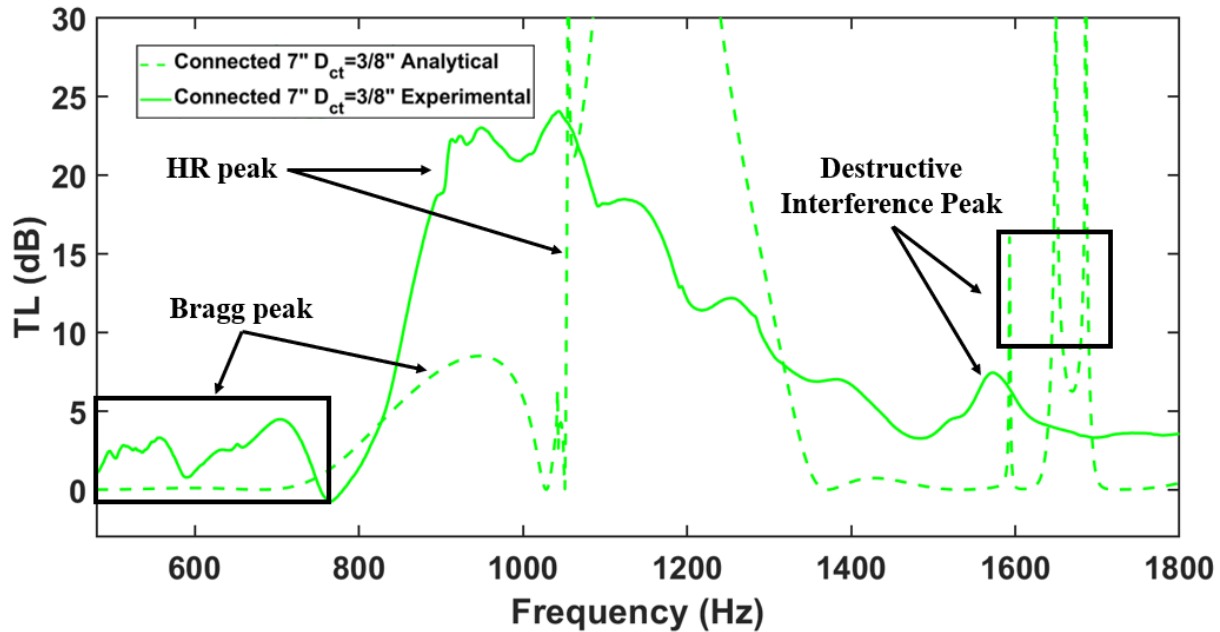


Figure 133. Measured vs Predicted Results for the Connected Array with 7" Spacing and 3/8" Coupling Tube Diameter

Based on the predicted results, the connected resonators case with 7 in. spacing and 3/8 in. diameter coupling tubes should have one main Helmholtz resonant peak with a smaller Bragg-type peak to the left just like the unconnected case; however, this case should also have an addition peak to the right of the Helmholtz resonant peak from the destructive interference of the waves traveling through the waveguide with the waves in the duct. Clearly from the experimental results, this is the case; however, the locations of the peaks do not line up exactly with the predicted locations because of factors such as damping, system imperfections, and viscothermal losses. The results of these three experiments along with the hard wall case are plotted together in Figure 134.

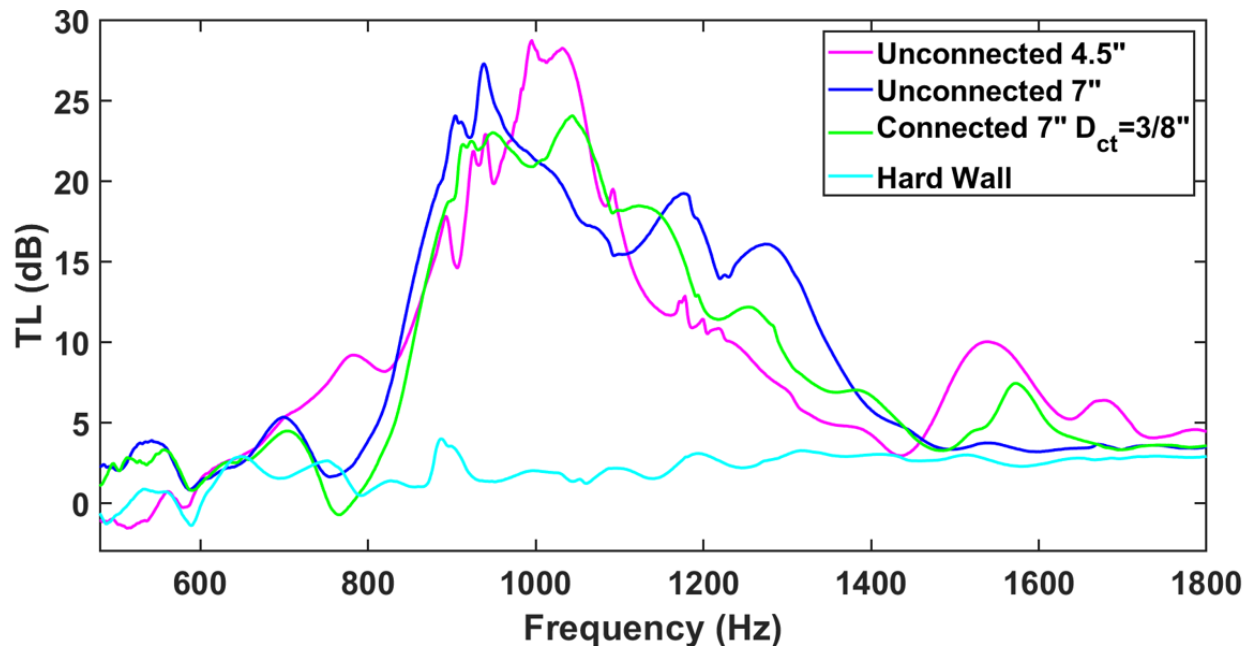


Figure 134. Measured Results of First Three Impedance Tube Tests and the Hard Wall Case

Comparing the measured results with the predicted results indicates that the prediction was accurate, and that these kind of systems can be actualized in real life scenarios. Again, the impedance tube is not a perfect system, so the results are not exactly the same as what was predicted, but the trends are the same. Again these differences are due to factors such as damping, system imperfections, and viscothermal losses. Below 600 Hz, the unconnected 7" and the connected 7" cases both have a high transmission loss peak whereas the unconnected 4.5" case does not. This result occurs because the 7" spacing results in a Bragg-type peak below the Helmholtz resonant peak, while a spacing of 4.5" results in a Bragg-type peak above the Helmholtz resonant peak (at ~1550 Hz). Then, although the unconnected resonator systems attenuate slightly higher than the connected system at the resonant frequency of the Helmholtz resonator, the connected system peak is wider towards the top. Then, the unconnected 4.5" case experiences a peak around 1550 Hz that the unconnected 7" case does not experience which again is because a 4.5" spacing results in Bragg reflection at that frequency. The connected resonator case with 7" spacing however does experience transmission loss at a similar location as the Bragg-type peak of the unconnected 4.5" case due to the double propagation band. The destructive interference in that frequency band for the connected resonator system is what causes the peak rather than Bragg reflection in the case of the unconnected 4.5" case. The connected 7"

case can be thought of as a “best of both worlds” scenario that achieves both sets of peaks from the two systems.

The experimental results for the connected resonators with a spacing of 7 in. and 5/8 in. diameter coupling tubes are shown in Figure 135.

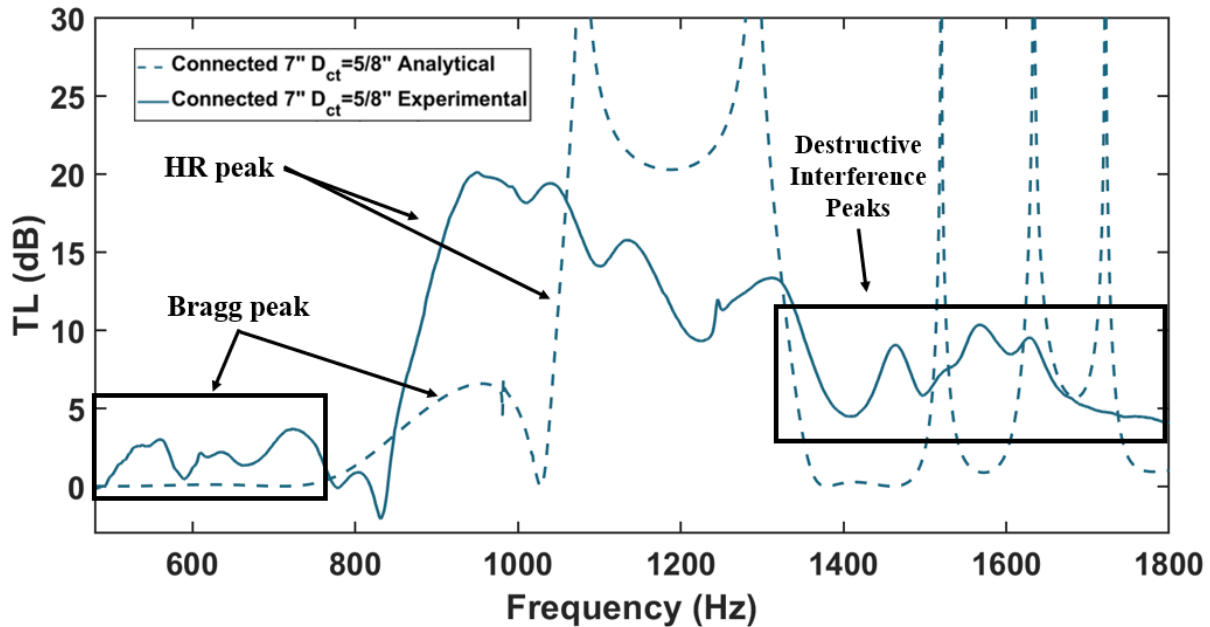


Figure 135. Measured vs Predicted Results for the Connected Array with 7" Spacing and 5/8" Coupling Tube

Based on the predicted results, the connected resonators case with 7 in. spacing and 5/8 in. diameter coupling tubes should have one main Helmholtz resonant peak, a smaller Bragg-type peak to the left of the Helmholtz resonant peak, and additional peaks to the right due to destructive interference between the waves in the coupled-resonator waveguide and the main duct. Clearly from the experimental results, this is the case; however, the locations of the peaks do not line up exactly with the predicted locations because of factors such as damping, system imperfections, and viscothermal losses. The experimental results for the connected resonators with a spacing of 7 in. and 7/8 in. diameter coupling tubes are shown in Figure 136.

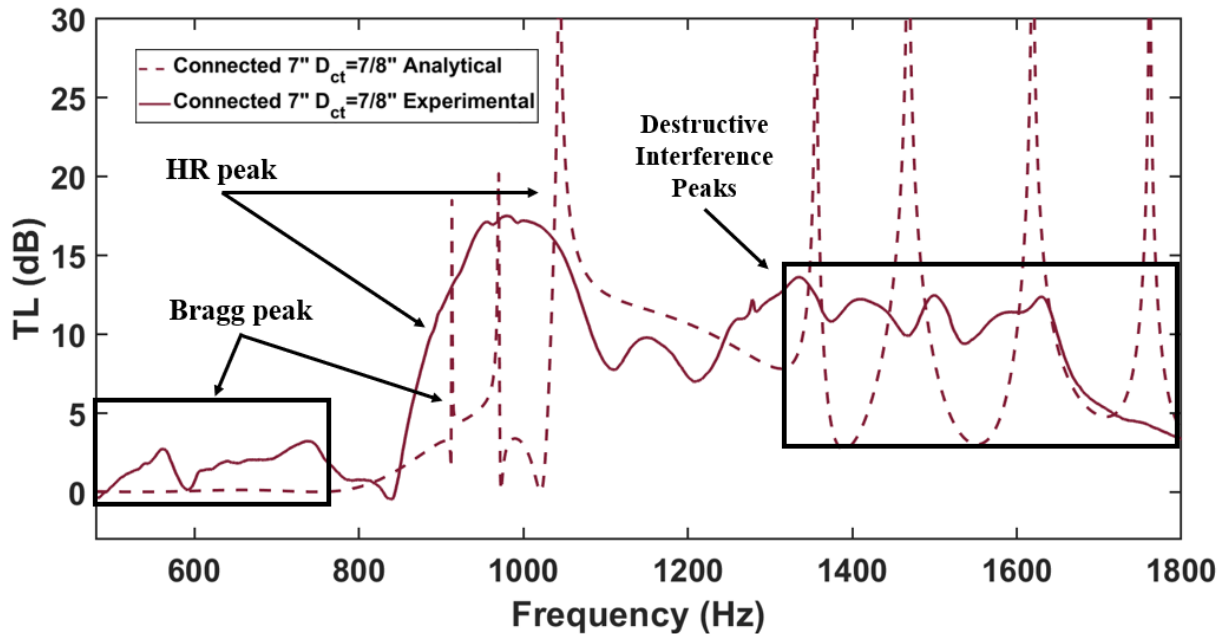


Figure 136. Measured vs Predicted Results for the Connected Array with 7" Spacing and 7/8" Coupling Tube

Based on the predicted results, the connected resonators case with 7 in. spacing and 5/8 in. diameter coupling tubes should have one main Helmholtz resonant peak, a smaller Bragg-type peak to the left of the Helmholtz resonant peak, and additional peaks to the right due to destructive interference between the waves in the coupled-resonator waveguide and the main duct. Clearly from the experimental results, this is the case; however, the locations of the peaks do not line up exactly with the predicted locations because of factors such as damping, system imperfections, and viscothermal losses. The results of the three connected-resonator experiments are plotted together in Figure 137.

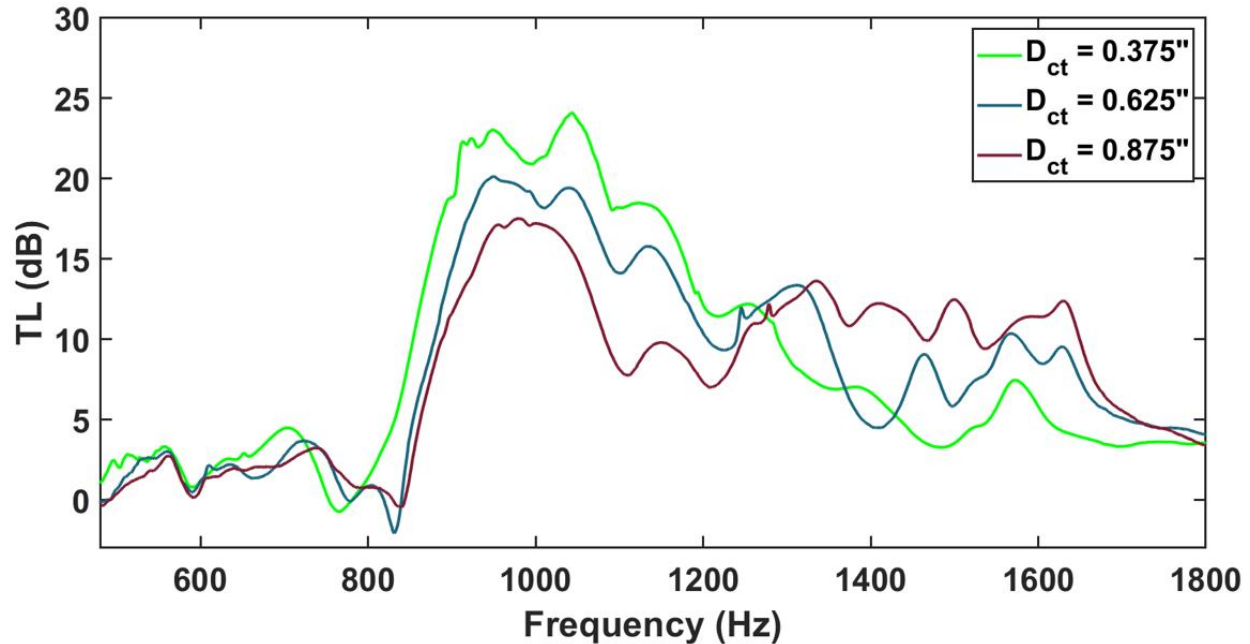


Figure 137. Measured Results of the Three Connected Resonators Systems with Different Diameters

As predicted, when the diameter increases, the transmission loss will increase at the higher frequencies (in the double propagation band) and decrease in the Helmholtz stop band. Recall that this phenomenon occurs because as the diameter of the coupling tubes get wider, more energy can propagate through them, and thus the system has more opportunity to achieve attenuation through the destructive interference of the waves traveling through the coupled-resonator waveguide and the waves in the duct. The wider the coupling tubes become, the more the system behaves like a waveguide, and the less the system behaves like an array of classical Helmholtz resonators, so the Helmholtz resonant peak should decrease as a result. The Bragg-type peaks out in the 500-800 Hz range should remain relatively constant because the spacing of the resonators does not change.

4.3. Conclusions

The results of the experimental testing show that these AMM principles described in the analytical methodology can be actualized. The trends observed in the experimental testing reflected the trends predicted by the analytical and numerical modeling.

An unconnected array of Helmholtz resonators with a 7" spacing was shown to produce transmission loss at frequencies lower than a baseline 4.5" spacing test. An array of Helmholtz

resonators with coupled cavities was shown to produce similar characteristics as the unconnected resonator test with the same spacing; however, the connected case offered key advantages.

One advantage is the widening of the resonant peak of the Helmholtz resonator. This effect would be beneficial if more broadband attenuation was required rather than tonal. Even still, the widened peak still forms around the same tone as the resonant peak of the resonator. This finding could be beneficial in cases where tones shift slightly around a tonal center depending on the operating conditions of the engine.

Another advantage is the transmission loss peaks that emerge in the double-propagation band. These peaks were evident when the spacing of the unconnected resonators was 4.5” (although they resulted from Bragg reflection instead), but were lost in favor of lower transmission loss peaks when the same unconnected system was extended to a 7” spacing; hence, connecting the resonators offers a “best of both worlds” solution that keeps both sets of peaks thus offering greater transmission loss across a wider frequency range including lower frequencies.

By changing the diameter of the coupling tubes, the general shape remained constant except that the transmission loss at higher frequencies increased while the Helmholtz resonant peak decreased. These results were expected because the larger the coupling diameters, the more the system can achieve attenuation through the destructive interference of the waves propagating through the coupled-cavity waveguide and the waves propagating through the main duct.

Through experimental testing and validation, this technology has shown to be beneficial for aerospace applications. Implementation of this kind of AMM technology on liners could lead to a new generation of quieter aircraft.

5. CONCLUSIONS AND FUTURE WORK

5.1. Conclusions

Throughout this research, acoustic metamaterial liner technology has been investigated and found to achieve transmission loss at a wide range of frequencies including low frequencies. Both unconnected and connected arrays of periodically-spaced Helmholtz resonators have been studied as forms of acoustic metamaterials that have proven to achieve transmission loss across a wider range of frequencies. Arrays of periodically-spaced Helmholtz resonators in both a connected and unconnected scheme have been successfully modeled, designed, and tested using analytical, numerical, and experimental techniques. Experiments have been performed using a grazing incidence impedance tube available at the Center for Aerospace Acoustics at the National Institute of Aerospace. These acoustic metamaterials show promise for implementation in acoustic liners for aircraft engine inlets due to their ability to attenuate a wide range of frequencies including low frequencies.

Both the connected and unconnected models were studied by examining the behavior of Bloch waves and Bragg reflection. Bloch wave theory states that a wave propagating through a periodic arrangement of discontinuities is given by a Bloch wave, which is a plane wave modulated by a periodic function. The Bloch wave number is related to a propagation constant for the system. The propagation constant is complex, where the real component is referred to as the attenuation constant while the imaginary component is referred to as the phase constant. The attenuation constant is a measure of how the amplitude of the Bloch wave changes from cell to cell, while the phase constant is a measure of the phase difference of the wave between the cells. By making dispersion plots, the attenuation and phase constants can be studied to determine how they change with frequency. At some frequencies known as “stop bands,” the attenuation constant is non-zero, indicating that the Bloch wave is evanescent at that frequency and thus sound attenuation occurs. Stop bands are created by local resonance or from a phenomenon called “Bragg reflection.” Bragg reflection occurs when the spacing of the periodic discontinuities is a multiple of a half of a wavelength. At these frequencies, the wave that gets reflected at the discontinuity is out of phase with the incident wave which leads to destructive

interference. If the discontinuities are periodically spaced, then this destructive interference will amplify consecutively across the cells leading to a high transmission loss.

An array of periodically-spaced Helmholtz resonators in the unconnected configuration was shown to be effective at attenuating frequencies other than the resonant frequency of the Helmholtz resonator. With enough spacing, the system can experience high transmission loss in frequencies even lower than the resonant frequency of the Helmholtz resonator. Aligning Helmholtz resonators periodically introduces Bragg reflection into the system which occurs when the spacing is a multiple of a half of a wavelength.

Furthermore, the transfer matrix method used in conjunction with Bloch wave theory has been shown to be an excellent method for analytically modeling this system in both the infinite case and the finite case. Dispersion plots for the infinite case were derived and the stop-band behavior was presented. The transmission loss has been analytically derived and reduced to a simple form that is easy to manipulate and quick to compute.

The analytical solution has been shown to be effective even when the number of resonators is high, and the limit of the normalized transmission loss was shown to converge to a function of the attenuation constant when the number of resonators approached infinity. The results of numerical modeling in Actran confirmed that the analytical formulations developed in this work are accurate. Using the analytical approach is thus a much quicker method than doing numerical modeling yet just as accurate; hence, the analytical model is effective when conducting parameter studies on specific geometries.

An array of periodically-spaced Helmholtz resonators in the connected configuration was shown to be effective at attenuating a wide range of frequencies. The connected system was shown to exhibit the same low frequency Bragg-type transmission loss shown in the unconnected system while also offering advantages not present in the unconnected case. First, the resonant peak due to the Helmholtz resonator geometry was shown to widen since the inclusion of the coupling tubes impacts the resonant behavior. This effect would be particularly advantageous in scenarios in which tonal noise shifts slightly as a result of engine operating conditions. Another advantage is the system's ability to generate transmission loss from the interaction of the Bloch waves traveling through the duct and coupled-cavity waveguide. This region in which the waves

destructively interfered with one another was identified as a “double propagation band,” and was shown to exist in dispersion plots of the infinite connected resonator system.

The transfer matrix method used in conjunction with Bloch wave theory was again shown to be an effective approach for modeling these types of systems. Unlike the unconnected resonator case, these transfer matrices are 4th-order, leading to two pairs of propagation constants instead of one pair. The propagation constants were shown to exhibit separate stop-band behavior that resulted in transmission loss for the system in regions where two stop-bands overlapped. These regions were identified as “absolute” stop-bands and the normalized transmission loss plot was shown to converge to a function of the smaller of the two attenuation constants as the number of resonators approached infinity. To maintain the definition of a unit cell, half of a coupling tube had to be included on both sides of the first and last resonators despite not having another resonator to connect to; however, a case of non-cellular ends (leaving out the half-coupling tube on the ends of the first and last cell of the system) was also presented and compared to a completely cellular system. Plotting the results of both revealed that the systems are quite similar, and in the interest of efficiency, use of the completely cellular solution is suggested, especially in cases with a high number of resonators. In cases where accuracy is valued higher than computation speed, an alternative formulation was presented for the non-cellular ends case. The results of numerical modeling in Actran showed that the analytical formulations developed in this work are in fact accurate. Using the analytical approach is thus a much quicker method than doing numerical modeling yet just as accurate; hence, the analytical model is effective when conducting parameter studies on specific geometries.

A parameter study was performed for an array of periodically-spaced Helmholtz resonators with coupled cavities. Different parameters were varied while the others were held constant in order to better understand how each parameter affects the system. Parameters that were examined include the resonator neck diameter, the resonator neck length, the cavity height, the coupling tube length, the cavity length in the axial dimension, the diameter of the coupling tubes, and the number of resonators. Modifying the properties of the resonator like the neck diameter, neck length, and cavity height yielded expected results. Generally speaking, the only part of the transmission loss plots that changed as a result of modifying these parameters was the location and shape of the resonant peak of the Helmholtz resonator. Modifying the coupling tube

length, the coupling tube diameter, and the cavity length in the axial dimension modified the length of the double propagation band and thus the transmission loss peaks contained therein. When the diameter of the coupling tube was made larger, all the peaks seemed to collectively increase and coalesce yielding a broad transmission loss plot. Increasing the resonators was found to increase the transmission loss within the stop-bands but not within the double propagation band.

Experimental testing and validation showed that this type of AMM can be physically developed and tested on grazing flow impedance tubes. The results from the testing validate the trends of the analytical and numerical modelling presented. Cases were compared with different resonator spacing and with connected and unconnected configurations. The connected configuration was shown to exhibit the low frequency transmission loss shown by the unconnected resonators spaced further apart as well as the high frequency transmission loss shown by the closely-spaced unconnected resonators. As a result, the connected resonator configuration showed the most potential for high broadband transmission loss.

The main conclusions of this thesis are:

- An aircraft engine liner can be modeled as an array of Helmholtz resonators using the transfer-matrix method in conjunction with Bloch wave theory.
- Increasing the spacing of the resonators induces Bragg reflection at lower frequencies.
- Connecting the array of resonators together via coupling tubes broadens the main peak of the Helmholtz resonant frequency.
- Connecting the array of resonators together via coupling tubes also creates frequency bands referred to herein as “double propagation bands” where waves propagate through both the coupled-resonator cavities and destructively interfere with the waves propagating through the main duct upon reaching the interface between the two (i.e., the necks of the resonators)
- This coupled-resonator system can also be effectively modeled via the transfer-matrix method in conjunction with Bloch wave theory

- Increasing the length of the coupling tubes, the length of the cavities, and the diameter of the coupling tubes all modify the location of the double-propagation bands as well as the transmission loss within those bands.
- Increasing the diameter of the coupling tubes has the greatest effect on the transmission loss in the double propagation band. The wider the diameter of the coupling tubes, the more that waves are able to propagate through the coupled-resonator cavities and destructively interfere with the main duct when they meet at the necks of the resonators.

5.2. Future work

Future work will focus on applying this technology to more complex representations of aircraft engine inlets. Consideration of larger duct diameters, smaller resonators, a presence of flow and damping, are all areas in which the modeling can improve in complexity.

Future work will also involve the development of optimization algorithms where the optimal geometry of the system will be determined in order to achieve attenuation in the desired frequency bandwidth. More precise testing could be conducted on similar systems by using the acoustic impedance test rigs available at NASA Langley like the Grazing Flow Impedance Tube (GFIT) [11].

Further exploration of the double propagation band is also warranted. The fact that the transmission loss does not increase in this zone as the number of resonators increases gives rise to questions. Perhaps the destructive interference would increase if every fourth coupling tube was closed off for example. Alternatively, further research could be done in the modification of the coupling tubes. Perforated diaphragms could be added inside the tubes to induce damping or even microporous acoustic foam.

Given that the 4th-order transfer matrix approach used in conjunction with Bloch wave theory proved to be an accurate method in modeling the connected resonator system, higher order transfer matrices could potentially be employed to account for additional coupled resonator cavity waveguides stacked on top of one another for example. Adding an additional degree of freedom would thus add another pair of Bloch waves which could have interesting effects.

APPENDIX

A. MATLAB Codes

A.1. MATLAB Code for the Analytical Calculation of the Propagation Constants and Transmission Loss of the Unconnected Resonator System

```
%% Housekeeping
clc; clear; close all

tStart = tic; % start timer

%% Constants
c = 343; % speed of sound in m/s
rho = 1.225; % air density in kg/m^3

%% Parameters for Measurement
N = 4; % number of resonators

P_in = 1; % input pressure (Pa)

% Frequency Range
min_freq = 301;
step = 1;
max_freq = 2250;

f = min_freq:step:max_freq;
wavelength = c./f;

%% Experimental Setup Parameters

% Duct Inputs
Sd = (3*.0254)*(3*.0254); % cross-sectional area of duct in m^2

% Liner Inputs
Lr = 7 * .0254; % distance between resonators
Dn = 1.5 * 0.0254; % diameter of neck in meters
Ln = 0.25 * 0.0254; % actual length of neck (hole in wood)
Vc = 3 * 0.0254 * 2.3562 * 0.0254 * 1 * 0.0254; %resonator cavity volume (L*W*H)

% End Correction
end_cor = 0.017; % end correction

Sn = Dn^2/4*pi; %resonator neck area
LnEff = Ln + end_cor; % effective neck length m

%% Cut-on Frequencies
f_co_d = c/(2*sqrt(Sd)); % for rectangular waveguide (Kinsler pg 254)
f_co_n = 100/(Dn/2); % for cylindrical waveguide (Kinsler pg 255)

%% Frequencies of Interest
f_HR = c/(2*pi)*sqrt(Sn/(Vc*LnEff)); % HR resonant frequency
f_Bragg_1 = 1*pi/Ln*c/(2*pi); % frequency of stop band
```

```

f_Bragg_2 = 2*pi/Lr*c/(2*pi); % frequency of stop band

%% Initialize Loop Variables
lams = zeros(2,length(f));
Gammas = zeros(2,length(f));
TL = zeros(1,length(f));
Norm_TL_inf = zeros(1,length(f));

%% Loop Through Frequencies
for i = 1:length(f)
w = 2*pi*f(i); % angular frequency
k = w/c; % wavenumber
Zr = 1j*w*rho*LnEff/Sn - 1j*rho*c^2/(w*Vc); % Impedance of resonator
Zd = rho*c/Sd; % Impedance of duct

A = cos(k*Lr);
B = -1j*Zd*sin(k*Lr);
C = -1j/Zd*sin(k*Lr);

% Define eigenvalue 1 of T matrix
lam1 = (2*A*Zr - B + (B*(4*C*Zr^2 - 4*A*Zr + B))^(1/2))/(2*Zr);

% Define propagation constant
Gamma = log(lam1);

% Define the eigenvectors
v01 = (A-exp(Gamma))/(C-A/Zr);
v02 = (A-exp(-Gamma))/(C-A/Zr);

% Solve for the transmission loss
X = cosh(Gamma*N) + ((-v01*v02+Zd^2)*sinh(Gamma*N))/(Zd*(v01-v02));
TL(i) = 20*log10(abs(X));
Norm_TL_inf(i) = 20*log10(abs(max(abs(exp(Gamma)),abs(exp(-Gamma)))));

% Define the propagation constants
Gammas(:,i) = [Gamma -Gamma];

disp(f(i));
end

fprintf("The Helmholtz stop band is " + num2str(f_HR) + " Hz." + newline)
fprintf("The first Bragg stop band is " + num2str(f_Bragg_1) + " Hz." + newline)
fprintf("The second Bragg stop band is " + num2str(f_Bragg_2) + " Hz." + newline)

%% Plot Transmission Loss Analytical Solution and Numerical Solution
props_real = real(Gammas);
props_imag = imag(Gammas);

ActranTL_sep = importdata('Fuller_Simple_Array_Actran.csv');
ActranTL_sep = ActranTL_sep(2:end);

figure
yyaxis left

```

```

plot(f,TL,'b', 'LineWidth',2)
hold on
plot(1:20:2250,ActranTL_sep,'-k', 'LineWidth',2)
xlabel('f (Hz)', 'FontSize', 24, 'Fontweight','Bold')
ylabel('TL (dB)', 'FontSize', 24, 'Fontweight','Bold')
xlim([min_freq max_freq]);
ylim([0 120])
hold on
yyaxis right
ylabel("\Gamma", 'FontSize', 24, 'Fontweight','Bold')
plot(f,props_real(1,:), '-','LineWidth',2, 'Color',[0 1 0])
hold on
plot(f,props_real(2,:), '-','LineWidth',2, 'Color',[0 1 0])
hold on
plot(f,props_imag(1,:), '-','LineWidth',2, 'Color',[1 0 1])
hold on
plot(f,props_imag(2,:), '-','LineWidth',2, 'Color',[1 0 1])
ylim([0 2*pi]);
yticks([0 pi/2 pi 3*pi/2 2*pi]);
yticklabels({'0', '\pi/2', '\pi', '3\pi/2', '2\pi'})
legend('Analytical', 'Actran', "Re(\Gamma)", "", "Im(\Gamma)")
set(gca, 'FontSize',22, 'FontWeight', 'Bold', 'LineWidth',1.5);
hold off

```

%% Analytical Transmission Loss and Propagation Constants

```

figure
yyaxis left
plot(f,TL,'b', 'LineWidth',3)
xlabel('f (Hz)', 'FontSize', 24, 'Fontweight','Bold')
ylabel('TL (dB)', 'FontSize', 24, 'Fontweight','Bold')
xlim([min_freq max_freq]);
ylim([0 120])
hold on
yyaxis right
ylabel("\Gamma", 'FontSize', 24, 'Fontweight','Bold')
plot(f,props_real(1,:), '-','LineWidth',2, 'Color',[0 1 0])
hold on
plot(f,props_real(2,:), '-','LineWidth',2, 'Color',[0 1 0])
hold on
plot(f,props_imag(1,:), '-','LineWidth',2, 'Color',[1 0 1])
hold on
plot(f,props_imag(2,:), '-','LineWidth',2, 'Color',[1 0 1])
ylim([0 2*pi]);
yticks([0 pi/2 pi 3*pi/2 2*pi]);
yticklabels({'0', '\pi/2', '\pi', '3\pi/2', '2\pi'})
legend('TL', "Re(\Gamma)", "", "Im(\Gamma)")
set(gca, 'FontSize',22, 'FontWeight', 'Bold', 'LineWidth',1.5);
hold off

```

%% Just Propagation Constants

```

figure
plot(f,props_real(1,:), '-','LineWidth',2, 'Color',[0 1 0])
hold on
plot(f,props_real(2,:), '-','LineWidth',2, 'Color',[0 1 0])
hold on

```

```

plot(f,props_imag(1,:), '-','LineWidth',2,'Color',[1 0 1])
hold on
plot(f,props_imag(2,:), '-','LineWidth',2,'Color',[1 0 1])
xlabel('f (Hz)', 'FontSize', 24, 'Fontweight','Bold')
xlim([min_freq max_freq]);
ylabel("\Gamma", 'FontSize', 24, 'Fontweight','Bold')
ylim([0 3*pi/2]);
yticks([0 pi/2 pi 3*pi/2 2*pi]);
yticklabels({'0', '\pi/2', '\pi', '3\pi/2', '2\pi'})
%xline(f_HR); % HR resonant frequency
%xline(f_Bragg_1); % frequency of stop band
%xline(f_Bragg_2);
legend("Re(\Gamma)", "", "Im(\Gamma)")
set(gca, 'FontSize',22, 'FontWeight', 'Bold', 'LineWidth',1.5);
hold off

%% Plot Normalized Transmission Loss of Infinite Case
figure
plot(f, Norm_TL_inf, 'b', 'LineWidth',2)
xlabel('f (Hz)', 'FontSize', 24, 'Fontweight','Bold')
ylabel('TL (dB)', 'FontSize', 24, 'Fontweight','Bold')
xlim([min_freq max_freq]);
%ylim([0 120])
set(gca, 'FontSize',22, 'FontWeight', 'Bold', 'LineWidth',1.5);
hold off

%% Output TL vector to CSV files

filename = inputdlg('Enter export filename');%prompt user to enter export filename
writematrix(TL/N, strcat('C:\Users\benhubinger\Documents\UGG program\MATLAB
Codes\', filename{1}, '.csv')) %export data

```

A.2. MATLAB Code for the Analytical Calculation of the Propagation Constants and Transmission Loss of the Connected Resonator System

```

%% Housekeeping
clc; clear; close all

tStart = tic; % start timer

%% Constants
c = 343; % speed of sound in m/s
rho = 1.225; % air density in kg/m^3

%% Parameters for Measurement
N = 4; % number of resonators

```

```

P_in = 1; % input pressure (Pa)

% Frequency Range
min_freq = 301;
step = 1;
max_freq = 2250;

f = min_freq:step:max_freq;

%% Experimental Setup Parameters

% Duct Inputs
Sd = (3*.0254)*(3*.0254); % cross-sectional area of duct in m^2

% Liner Inputs
Lr = 7 * .0254; % distance between resonators
Dn = 1.5 * 0.0254; % diameter of neck in meters
Ln = 0.25 * 0.0254; % actual length of neck (hole in wood)
Lc = 1.5 * 0.0254; % half length of cavity
Lct = (Lr-2*Lc)/2; % half length of coupling tube
Vc = Lc*2 * 2.3562 * 0.0254 * 1 * 0.0254; % Volume of cavity (L*W*H)
Dc = 0.375 * 0.0254; % diameter of connecting tube in meters

% End Corrections
end_cor_n = 0.0125; % end correction for neck
end_cor_c = 0.0008; % end correction for connecting tube

Sn = Dn^2/4*pi; %resonator neck area
LnEff = Ln + end_cor_n; % effective neck length m

%% Cut-on Frequencies
f_co_d = c/(2*sqrt(Sd)); % for rectangular waveguide (Kinsler pg 254)
f_co_n = 100/(Dn/2); % for cylindrical waveguide (Kinsler pg 255)
f_co_c = 100/(Dc/2); % connecting tube

%% Impedances
Zc = rho*c/(Vc/(2*Lc)); % impedance of resonator cavity
Zct = rho*c/(Dc^2/4*pi); % impedance of coupling tube
Zd = rho*c/Sd;

%% Frequencies of Interest
f_HR = c/(2*pi)*sqrt(Sn/(Vc*LnEff)); % HR resonant frequency
f_Bragg_1 = 1*c/(2*Lr); % frequency of duct stop band
f_Bragg_2 = 2*c/(2*Lr); % frequency of duct stop band

%% Initialize Loop Variables
lams = zeros(4,length(f));
Gamma_vals = zeros(4,length(f));
TL = zeros(1,length(f));
Norm_TL_inf = zeros(1,length(f));

%% Loop Through Frequencies
for i=1:1:length(f)
w = 2*pi*f(i);
k = w/c;

```

```

Zn = 1j*w*rho*LnEff/Sn; % impedance of the neck (assumed to be a mass)

% Transfer Matrix Tc for cavity radius
Tc = [cos(k*Lc) -1j*Zc*sin(k*Lc) 0 0;
      -1j*sin(k*Lc)/Zc cos(k*Lc) 0 0;
      0 0 cos(k*Lc) -1j*Zd*sin(k*Lc);
      0 0 -1j*sin(k*Lc)/Zd cos(k*Lc)];

% Transfer Matrix Tct for half of connecting tube
Tct = [cos(k*(Lct+end_cor_c)) -1j*Zct*sin(k*(Lct+end_cor_c)) 0 0;
       -1j*sin(k*(Lct+end_cor_c))/Zct cos(k*(Lct+end_cor_c)) 0 0;
       0 0 cos(k*Lct) -1j*Zd*sin(k*Lct);
       0 0 -1j*sin(k*Lct)/Zd cos(k*Lct)];

%% Submatrix Definitions

TM_tube = Tc*Tct*Tct*Tc;
TR = Tc*Tct;

T1 = [TM_tube(1,1) TM_tube(1,2); TM_tube(2,1) TM_tube(2,2)];
T2 = [TM_tube(3,3) TM_tube(3,4); TM_tube(4,3) TM_tube(4,4)];
TR1 = [TR(1,1) TR(1,2); TR(2,1) TR(2,2)];
TR2 = [TR(3,3) TR(3,4); TR(4,3) TR(4,4)];

%% Calculate Transmission Loss

A1 = TM_tube(1,1);
A2 = TM_tube(3,3);
B1 = TM_tube(1,2);
B2 = TM_tube(3,4);
BR1 = TR(1,2);
AR1 = TR(1,1);
BR2 = TR(3,4);
AR2 = TR(3,3);

% Define propagation constants
Gamma_vals(1,i) = acosh((- (4*A1^2*Zn^2 - 8*A1*A2*Zn^2 - 4*A1*B1*Zn + 4*A1*B2*Zn +
4*A2^2*Zn^2 + 4*A2*B1*Zn - 4*A2*B2*Zn + B1^2 + 2*B1*B2 + B2^2)^(1/2) - B2 - B1 +
2*A1*Zn + 2*A2*Zn)/(4*Zn));
Gamma_vals(2,i) = -acosh((- (4*A1^2*Zn^2 - 8*A1*A2*Zn^2 - 4*A1*B1*Zn + 4*A1*B2*Zn +
4*A2^2*Zn^2 + 4*A2*B1*Zn - 4*A2*B2*Zn + B1^2 + 2*B1*B2 + B2^2)^(1/2) - B2 - B1 +
2*A1*Zn + 2*A2*Zn)/(4*Zn));
Gamma_vals(3,i) = acosh(((4*A1^2*Zn^2 - 8*A1*A2*Zn^2 - 4*A1*B1*Zn + 4*A1*B2*Zn +
4*A2^2*Zn^2 + 4*A2*B1*Zn - 4*A2*B2*Zn + B1^2 + 2*B1*B2 + B2^2)^(1/2) - B2 - B1 +
2*A1*Zn + 2*A2*Zn)/(4*Zn));
Gamma_vals(4,i) = -acosh(((4*A1^2*Zn^2 - 8*A1*A2*Zn^2 - 4*A1*B1*Zn + 4*A1*B2*Zn +
4*A2^2*Zn^2 + 4*A2*B1*Zn - 4*A2*B2*Zn + B1^2 + 2*B1*B2 + B2^2)^(1/2) - B2 - B1 +
2*A1*Zn + 2*A2*Zn)/(4*Zn));

Gamma = Gamma_vals(1,i);
GammaP = Gamma_vals(3,i);

Q1 = cosh(Gamma)-A1;
Q1_p = cosh(GammaP)-A1;
Q2 = cosh(Gamma)-A2;

```

```

Q2_p = cosh(GammaP)-A2;

z1 = 1/Q1*BR1*cosh(Gamma/2);
z1_p = 1/Q1_p*BR1*cosh(GammaP/2);
z2 = 1/Q2*BR2*cosh(Gamma/2);
z2_p = 1/Q2_p*BR2*cosh(GammaP/2);

h1 = 1/Q1*AR1*sinh(Gamma/2);
h1_p = 1/Q1_p*AR1*sinh(GammaP/2);
h2 = 1/Q2*AR2*sinh(Gamma/2);
h2_p = 1/Q2_p*AR2*sinh(GammaP/2);

Z_hat = z2*h1_p/det([h1 h1_p; -h2 -h2_p]);
Z_hat_p = z2_p*h1/det([h1 h1_p; -h2 -h2_p]);

Z_A = Z_hat*coth(N*Gamma) - Z_hat_p*coth(N*GammaP);
Z_B = Z_hat/sinh(N*Gamma) - Z_hat_p/sinh(N*GammaP);

% Calculate Transmission Loss
X = ((Z_A+Zd-Z_B)*(Z_A+Zd+Z_B))/(2*Z_B*Zd);
TL(i) = 20*log10(abs(X));
Norm_TL_inf(i) = 20*log10(abs(min(max(exp(Gamma),exp(-Gamma)),max(exp(GammaP),exp(-GammaP))))));

disp(f(i))
end

fprintf("The Helmholtz stop band is " + num2str(f_HR) + " Hz." + newline)
fprintf("The first Bragg stop band is " + num2str(f_Bragg_1) + " Hz." + newline)
fprintf("The second Bragg stop band is " + num2str(f_Bragg_2) + " Hz." + newline)

%% End Timer
tEnd = toc(tStart);
fprintf('%d minutes and %f seconds\n', floor(tEnd/60), rem(tEnd,60));

%% Transmission Loss Plotting

% Import Actran Results
actranTL =
importdata('Square_Fuller_GIT_Test_4_connected_resonator_post_NASA_pres.csv');
actranTL = actranTL(2:end);

% Import analytical separated resonators
sep_res = importdata('test.csv');

% Plot Analytical and Actran
figure
plot(f,TL,'b','LineWidth',2)
xlabel('f (Hz)', 'FontSize', 24, 'FontWeight','Bold')
ylabel('TL (dB)', 'FontSize', 24, 'FontWeight','Bold')
xlim([min_freq max_freq]);
hold on
plot(1:length(actranTL),actranTL,'k','LineWidth',2)
legend('Analytical','Actran')
set(gca, 'FontSize',22, 'FontWeight', 'Bold', 'LineWidth',1.5);

```

```

hold off

%% Propagation Constant Plotting
props_real = real(Gamma_vals);
props_imag = imag(Gamma_vals);

figure
yyaxis left
plot(f,TL,'b','LineWidth',2)
xlabel('f (Hz)', 'FontSize', 24, 'Fontweight','Bold')
ylabel('TL (dB)', 'FontSize', 24, 'Fontweight','Bold')
xlim([min_freq max_freq]);
ylim([0 70])
hold on
yyaxis right
plot(f,props_real(1,:), '-','LineWidth',2, 'Color',[0 1 0])
hold on
plot(f,props_real(2,:), '-','LineWidth',2, 'Color',[0 1 0])
hold on
plot(f,props_imag(1,:), '-','LineWidth',2, 'Color',[1 0 1])
hold on
plot(f,props_imag(2,:), '-','LineWidth',2, 'Color',[1 0 1])
hold on
plot(f,props_real(3,:), '--','LineWidth',2, 'Color',[0 1 0])
hold on
plot(f,props_real(4,:), '--','LineWidth',2, 'Color',[0 1 0])
hold on
plot(f,props_imag(3,:), '--','LineWidth',2, 'Color',[1 0 1])
hold on
plot(f,props_imag(4,:), '--','LineWidth',2, 'Color',[1 0 1])
hold off
ylim([0 2*pi]);
ylabel("\Gamma", 'FontSize', 24, 'Fontweight','Bold')
yticks([0 pi/2 pi 3*pi/2 2*pi]);
yticklabels({'0', '\pi/2', '\pi', '3\pi/2', '2\pi'})
set(gca, 'FontSize',22, 'FontWeight', 'Bold', 'LineWidth',1.5);
ylabel("\Gamma", 'FontSize', 24, 'Fontweight','Bold')
legend(["TL", "Re(\Gamma)", "", "Im(\Gamma)", "", "Re(\Gamma)", "", "Im(\Gamma)"])

figure
plot(f,props_real(1,:), '-','LineWidth',2, 'Color',[0 1 0])
hold on
plot(f,props_real(2,:), '-','LineWidth',2, 'Color',[0 1 0])
hold on
plot(f,props_imag(1,:), '-','LineWidth',2, 'Color',[1 0 1])
hold on
plot(f,props_imag(2,:), '-','LineWidth',2, 'Color',[1 0 1])
hold on
plot(f,props_real(3,:), '--','LineWidth',2, 'Color',[0 1 0])
hold on
plot(f,props_real(4,:), '--','LineWidth',2, 'Color',[0 1 0])
hold on
plot(f,props_imag(3,:), '--','LineWidth',2, 'Color',[1 0 1])
hold on
plot(f,props_imag(4,:), '--','LineWidth',2, 'Color',[1 0 1])

```

```

hold off
xlim([min_freq max_freq]);
ylim([0 3*pi/2]);
ylabel("\Gamma", 'FontSize', 24, 'FontWeight', 'Bold')
yticks([0 pi/2 pi 3*pi/2 2*pi]);
yticklabels({'0', '\pi/2', '\pi', '3\pi/2', '2\pi'})
set(gca, 'FontSize', 22, 'FontWeight', 'Bold', 'LineWidth', 1.5);
ylabel("\Gamma", 'FontSize', 24, 'FontWeight', 'Bold')
legend(["Re(\Gamma)", "", "Im(\Gamma)", "", "Re(\Gamma)", "", "Im(\Gamma)"])

%% Normalized Transmission Loss Plot for Infinite System

figure
yyaxis left
plot(f, Norm_TL_inf, 'b', 'LineWidth', 2)
xlabel('f (Hz)', 'FontSize', 24, 'FontWeight', 'Bold')
ylabel('TL (dB)', 'FontSize', 24, 'FontWeight', 'Bold')
ylim([0 max(Norm_TL_inf)])
xlim([min_freq max_freq]);
hold on
yyaxis right
plot(f, props_real(1,:), '-', 'LineWidth', 2, 'Color', [0 1 0])
hold on
plot(f, props_real(2,:), '-', 'LineWidth', 2, 'Color', [0 1 0])
hold on
plot(f, props_imag(1,:), '-', 'LineWidth', 2, 'Color', [1 0 1])
hold on
plot(f, props_imag(2,:), '-', 'LineWidth', 2, 'Color', [1 0 1])
hold on
plot(f, props_real(3,:), '--', 'LineWidth', 2, 'Color', [0 1 0])
hold on
plot(f, props_real(4,:), '--', 'LineWidth', 2, 'Color', [0 1 0])
hold on
plot(f, props_imag(3,:), '--', 'LineWidth', 2, 'Color', [1 0 1])
hold on
plot(f, props_imag(4,:), '--', 'LineWidth', 2, 'Color', [1 0 1])
hold off
ylim([0 2*pi]);
ylabel("\Gamma", 'FontSize', 24, 'FontWeight', 'Bold')
yticks([0 pi/2 pi 3*pi/2 2*pi]);
yticklabels({'0', '\pi/2', '\pi', '3\pi/2', '2\pi'})
set(gca, 'FontSize', 22, 'FontWeight', 'Bold', 'LineWidth', 1.5);
ylabel("\Gamma", 'FontSize', 24, 'FontWeight', 'Bold')
legend(["TL", "Re(\Gamma)", "", "Im(\Gamma)", "", "Re(\Gamma)", "", "Im(\Gamma)"])

%% Output to CSV

filename = inputdlg('Enter export filename'); %prompt user to enter export filename
writematrix(TL, strcat('C:\Users\benhubinger\Documents\UGG program\MATLAB
Codes\', filename{1}, '.csv')) %export data

```

A.3. MATLAB Code for the Analytical Calculation of the Propagation Constants and Transmission Loss of a High Number of Connected Resonators with Non-Cellular Ends

```
%% Housekeeping
clc
clear
close all

tStart = tic; % start timer

%% Constants
c = 343; % speed of sound in m/s
rho = 1.225; % air density in kg/m^3

%% Parameters for Measurement
N = 100; % number of resonators

P_in = 1; % input pressure (Pa)

% Frequency Range
min_freq = 301;
step = 1;
max_freq = 2250;

f = min_freq:step:max_freq;

%% Experimental Setup Parameters

% Duct Inputs
Sd = (3*.0254)*(3*.0254); % cross-sectional area of duct in m^2

% Liner Inputs
Lr = 7 * .0254; % distance between resonators
Dn = 1.5 * 0.0254; % diameter of neck in meters
Ln = 0.25 * 0.0254; % actual length of neck (hole in wood)
Lc = 1.5 * 0.0254; % half length of cavity
Lct = (Lr-2*Lc)/2; % distance between edge of cavity to midpoint of connecting tube
Vc = Lc*2 * 2.3562 * 0.0254 * 1 * 0.0254; % Volume of cavity (L*W*H)
Dc = 0.375 * 0.0254; % diameter of connecting tube in meters

% End Corrections
end_cor_n = 0.0125; % end correction for neck
end_cor_c = 0.0008; % end correction for connecting tube

Sn = Dn^2/4*pi; %resonator neck area
LnEff = Ln + end_cor_n; % effective neck length m

%% Cut-on Frequencies
f_co_d = c/(2*sqrt(Sd)); % for rectangular waveguide (Kinsler pg 254)
f_co_n = 100/(Dn/2); % for cylindrical waveguide (Kinsler pg 255)
f_co_c = 100/(Dc/2); % connecting tube
```

```

%% Impedances
Zc = rho*c/(Vc/(Lc*2)); % impedance of cavity
Zct = rho*c/(Dc^2/4*pi); % impedance of coupling tube
Zd = rho*c/Sd;

%% Frequencies of Interest
f_HR = c/(2*pi)*sqrt(Sn/(Vc*LnEff)); % HR resonant frequency
f_Bragg_1 = 1*pi/Ln*c/(2*pi); % frequency of duct stop band
f_Bragg_2 = 2*pi/Ln*c/(2*pi); % frequency of duct stop band

%% Initialize Loop Variables
lams = zeros(4,length(f));
TL = zeros(1,length(f));
TL_inf = zeros(1,length(f));
x0 = [1;1;1;1;1;1;1];

%% Loop Through Frequencies
for i=1:length(f)
w = 2*pi*f(i);
k = w/c;
Zn = 1j*w*rho*LnEff/Sn; % impedance of the neck (assumed to be a mass)

% Transfer Matrix Tn for neck
Tn = [1 0 0 0;
      -1/Zn 1 1/Zn 0;
      0 0 1 0;
      1/Zn 0 -1/Zn 1];

% Transfer Matrix Tc for cavity radius
Tc = [cos(k*Lc) -1j*Zc*sin(k*Lc) 0 0;
      -1j*sin(k*Lc)/Zc cos(k*Lc) 0 0;
      0 0 cos(k*Lc) -1j*Zd*sin(k*Lc);
      0 0 -1j*sin(k*Lc)/Zd cos(k*Lc)];

% Transfer Matrix Tct for half of connecting tube
Tct = [cos(k*(Lct+end_cor_c)) -1j*Zct*sin(k*(Lct+end_cor_c)) 0 0;
       -1j*sin(k*(Lct+end_cor_c))/Zct cos(k*(Lct+end_cor_c)) 0 0;
       0 0 cos(k*Lct) -1j*Zd*sin(k*Lct);
       0 0 -1j*sin(k*Lct)/Zd cos(k*Lct)];

% Cell Transfer Matrix
TM_cell = Tct*Tc*Tn*Tc*Tct;

%% Generate eigenvalues and eigenvectors of Cell Transfer Matrix

[V_unsort, D] = eig(TM_cell);

%% Organize Eigenvalues (and corresponding eigenvectors)

% Step 1: Organize eigenvalues into a matrix called "lams"
lams_unsort = [D(1,1); D(2,2); D(3,3); D(4,4)];

% Step 2: Generate a matrix containing the inverses of the lams
lams_inv = 1./lams_unsort;

```

```

% Step 3: Group the eigenvalues that are inverses of each other
lams(1,i) = lams_undef(1);
V(:,1) = V_undef(:,1);
lams(2,i) = lams_undef(round(lams_undef(1),5)==round(lams_inv(:),5)); %finds the
index of the inverse lam that corresponds to lam 1 then reassigns the value contained
within the lam matrix corresponding to that index to lam2
V(:,2) = V_undef(:,round(lams_undef(1),5)==round(lams_inv(:),5));
idcs = find(round(lams_undef(1),5)~=round(lams_inv(:),5)); %finds index 1 and the
indices that haven't been used yet
idcs = [idcs(2) idcs(3)]; % eliminates index 1
lams(3:4,i) = lams_undef(idcs); %groups lams 3 and 4
V(:,3) = V_undef(:,idcs(1));
V(:,4) = V_undef(:,idcs(2));

%% Calculate Transmission Loss

TM_babc = Tc*Tn*Tc*Tct;
TM_inv = inv(Tc)*inv(Tn)*inv(Tc)*inv(Tct);
lam_1 = lams(1,i);
lam_2 = lams(2,i);
lam_3 = lams(3,i);
lam_4 = lams(4,i);
v_1 = V(:,1);
v_2 = V(:,2);
v_3 = V(:,3);
v_4 = V(:,4);

syms a1 b1 c1 d1 A B P_out

vec_1st_cell = a1*v_1 + b1*v_2 + c1*v_3 + d1*v_4;
vec_last_cell = a1*lam_1^(N-2)*v_1 + b1*lam_2^(N-2)*v_2 + c1*lam_3^(N-2)*v_3 +
d1*lam_4^(N-2)*v_4;
vec_in = TM_inv*vec_1st_cell;
vec_out = TM_babc*vec_last_cell;

eqn1 = vec_in(3) == P_in;
eqn2 = vec_in(3) == A + B;
eqn3 = vec_in(4) == A/Zd - B/Zd;
eqn4 = vec_in(2) == 0;
eqn5 = vec_out(3) == P_out;
eqn6 = vec_out(4) == P_out/Zd;
eqn7 = vec_out(2) == 0;

eqns = [eqn1 eqn2 eqn3 eqn4 eqn5 eqn6 eqn7];
vars = [a1 b1 c1 d1 A B P_out];

sol = solve(eqns,vars);

X = sol.A/sol.P_out;

TL(i) = 20*log10(abs(X));

disp(f(i))
end

```

```

fprintf("The Helmholtz stop band is " + num2str(f_HR) + " Hz." + newline)
fprintf("The first Bragg stop band is " + num2str(f_Bragg_1) + " Hz." + newline)
fprintf("The second Bragg stop band is " + num2str(f_Bragg_2) + " Hz." + newline)

%% End Timer
tEnd = toc(tStart);
fprintf('%d minutes and %f seconds\n', floor(tEnd/60), rem(tEnd,60));

%% Transmission Loss Plotting

% Import Actran Results
actranTL =
importdata('Square_Fuller_GIT_Test_4_connected_resonator_post_NASA_pres.csv');
actranTL = actranTL(2:end);

% Import analytical separated resonators
sep_res = importdata('test.csv');

% Plot Analytical and Actran
figure(1)
plot(f,TL,'b','LineWidth',2)
xlabel('f (Hz)', 'FontSize', 24, 'Fontweight','Bold')
ylabel('TL (dB)', 'FontSize', 24, 'Fontweight','Bold')
xlim([min_freq max_freq]);
hold on
plot(1:length(actranTL),actranTL,'k','LineWidth',2)
legend('Analytical','Actran')
set(gca,'FontSize',22,'FontWeight','Bold','LineWidth',1.5);
y_ax_dis = get(gca,'ylabel'); % handle to the label object
p = get(y_ax_dis,'position'); % get the current position property
p(1) = 200.4194; % specify xposition,
set(y_ax_dis,'position',p) % set the new position
hold off

%% Propagation Constant Plotting

props = log(lams);

props_real = real(props);
props_imag = imag(props);

prop_mark_size = 4;
prop_real_color = "g";
prop_imag_color = "m";

figure(2)
scatter(f,props_real(1,:),prop_mark_size,prop_real_color,"filled")
hold on
scatter(f,props_real(2,:),prop_mark_size,prop_real_color,"filled")
hold on
scatter(f,props_real(3,:),prop_mark_size,prop_real_color,"filled")
hold on
scatter(f,props_real(4,:),prop_mark_size,prop_real_color,"filled")
hold off

```

```

ylim([0 2*pi]);
ylabel("Re(\Gamma)", 'FontSize', 24, 'FontWeight', 'Bold')
set(gca, 'FontSize', 22, 'FontWeight', 'Bold', 'LineWidth', 1.5);

figure(3)
scatter(f, props_imag(1,:), prop_mark_size, prop_imag_color, "filled")
hold on
scatter(f, props_imag(2,:), prop_mark_size, prop_imag_color, "filled")
hold on
scatter(f, props_imag(3,:), prop_mark_size, prop_imag_color, "filled")
hold on
scatter(f, props_imag(4,:), prop_mark_size, prop_imag_color, "filled")
hold off
ylim([0 2*pi]);
ylabel("Im(\Gamma)", 'FontSize', 24, 'FontWeight', 'Bold')
yticks([0 pi/2 pi 3*pi/2 2*pi]);
yticklabels({'0', '\pi/2', '\pi', '3\pi/2', '2\pi'})
set(gca, 'FontSize', 22, 'FontWeight', 'Bold', 'LineWidth', 1.5);

figure(4)
yyaxis left
plot(f, TL, 'b', 'LineWidth', 2)
xlabel('f (Hz)', 'FontSize', 24, 'FontWeight', 'Bold')
ylabel('TL (dB)', 'FontSize', 24, 'FontWeight', 'Bold')
xlim([min_freq max_freq]);
hold on
yyaxis right
scatter(f, props_real(1,:), prop_mark_size, prop_real_color, "filled")
hold on
scatter(f, props_real(2,:), prop_mark_size, prop_real_color, "filled")
hold on
scatter(f, props_real(3,:), prop_mark_size, prop_real_color, "filled")
hold on
scatter(f, props_real(4,:), prop_mark_size, prop_real_color, "filled")
hold on
scatter(f, props_imag(1,:), prop_mark_size, prop_imag_color, "filled")
hold on
scatter(f, props_imag(2,:), prop_mark_size, prop_imag_color, "filled")
hold on
scatter(f, props_imag(3,:), prop_mark_size, prop_imag_color, "filled")
hold on
scatter(f, props_imag(4,:), prop_mark_size, prop_imag_color, "filled")
hold off
ylim([0 2*pi]);
ylabel("\Gamma", 'FontSize', 24, 'FontWeight', 'Bold')
yticks([0 pi/2 pi 3*pi/2 2*pi]);
yticklabels({'0', '\pi/2', '\pi', '3\pi/2', '2\pi'})
set(gca, 'FontSize', 22, 'FontWeight', 'Bold', 'LineWidth', 1.5);
%y_ax_dis = get(gca, 'ylabel'); % handle to the label object
%p = get(y_ax_dis, 'position'); % get the current position property
%p(1) = 2350; % specify xposition,
ylabel("\Gamma", 'FontSize', 24, 'FontWeight', 'Bold')
legend(["TL", "Re(\Gamma)", "", "", "", "Im(\Gamma)"])
%% Housekeeping
clc

```

```

clear
close all

tStart = tic; % start timer

%% Constants
c = 343; % speed of sound in m/s
rho = 1.225; % air density in kg/m^3

%% Parameters for Measurement
N = 100; % number of resonators

P_in = 1; % input pressure (Pa)

% Frequency Range
min_freq = 301;
step = 1;
max_freq = 2250;

f = min_freq:step:max_freq;

%% Experimental Setup Parameters

% Duct Inputs
Sd = (3*.0254)*(3*.0254); % cross-sectional area of duct in m^2

% Liner Inputs
Lr = 7 * .0254; % distance between resonators
Dn = 1.5 * 0.0254; % diameter of neck in meters
Ln = 0.25 * 0.0254; % actual length of neck (hole in wood)
Lc = 1.5 * 0.0254; % half length of cavity
Lct = (Lr-2*Lc)/2; % distance between edge of cavity to midpoint of connecting tube
Vc = Lc*2 * 2.3562 * 0.0254 * 1 * 0.0254; % Volume of cavity (L*W*H)
Dc = 0.375 * 0.0254; % diameter of connecting tube in meters

% End Corrections
end_cor_n = 0.0125; % end correction for neck
end_cor_c = 0.0008; % end correction for connecting tube

Sn = Dn^2/4*pi; %resonator neck area
LnEff = Ln + end_cor_n; % effective neck length m

%% Cut-on Frequencies
f_co_d = c/(2*sqrt(Sd)); % for rectangular waveguide (Kinsler pg 254)
f_co_n = 100/(Dn/2); % for cylindrical waveguide (Kinsler pg 255)
f_co_c = 100/(Dc/2); % connecting tube

%% Impedances
Zc = rho*c/(Vc/(Lc*2)); % impedance of cavity
Zct = rho*c/(Dc^2/4*pi); % impedance of coupling tube
Zd = rho*c/Sd;

%% Frequencies of Interest
f_HR = c/(2*pi)*sqrt(Sn/(Vc*LnEff)); % HR resonant frequency
f_Bragg_1 = 1*pi/Lr*c/(2*pi); % frequency of duct stop band

```

```

f_Bragg_2 = 2*pi/Lr*c/(2*pi); % frequency of duct stop band

%% Initialize Loop Variables
lams = zeros(4,length(f));
TL = zeros(1,length(f));
TL_inf = zeros(1,length(f));
x0 = [1;1;1;1;1;1;1];

%% Loop Through Frequencies
for i=1:1:length(f)
w = 2*pi*f(i);
k = w/c;
Zn = 1j*w*rho*LnEff/Sn; % impedance of the neck (assumed to be a mass)

% Transfer Matrix Tn for neck
Tn = [1 0 0 0;
      -1/Zn 1 1/Zn 0;
      0 0 1 0;
      1/Zn 0 -1/Zn 1];

% Transfer Matrix Tc for cavity radius
Tc = [cos(k*Lc) -1j*Zc*sin(k*Lc) 0 0;
      -1j*sin(k*Lc)/Zc cos(k*Lc) 0 0;
      0 0 cos(k*Lc) -1j*Zd*sin(k*Lc);
      0 0 -1j*sin(k*Lc)/Zd cos(k*Lc)];

% Transfer Matrix Tct for half of connecting tube
Tct = [cos(k*(Lct+end_cor_c)) -1j*Zct*sin(k*(Lct+end_cor_c)) 0 0;
       -1j*sin(k*(Lct+end_cor_c))/Zct cos(k*(Lct+end_cor_c)) 0 0;
       0 0 cos(k*Lct) -1j*Zd*sin(k*Lct);
       0 0 -1j*sin(k*Lct)/Zd cos(k*Lct)];

% Cell Transfer Matrix
TM_cell = Tct*Tc*Tn*Tc*Tct;

%% Generate eigenvalues and eigenvectors of Cell Transfer Matrix
[V_unsort, D] = eig(TM_cell);

%% Organize Eigenvalues (and corresponding eigenvectors)

% Step 1: Organize eigenvalues into a matrix called "lams"
lams_unsort = [D(1,1); D(2,2); D(3,3); D(4,4)];

% Step 2: Generate a matrix containing the inverses of the lams
lams_inv = 1./lams_unsort;

% Step 3: Group the eigenvalues that are inverses of each other
lams(1,i) = lams_unsort(1);
V(:,1) = V_unsort(:,1);
lams(2,i) = lams_unsort(round(lams_unsort(1),5)==round(lams_inv(:,5))); %finds the
index of the inverse lam that corresponds to lam 1 then reassigns the value contained
within the lam matrix corresopnding to that index to lam2
V(:,2) = V_unsort(:,round(lams_unsort(1),5)==round(lams_inv(:,5)));

```

```

idcs = find(round(lams_unsort(1),5)~=round(lams_inv(:,5))); %finds index 1 and the
indices that haven't been used yet
idcs = [idcs(2) idcs(3)]; % eliminates index 1
lams(3:4,i) = lams_unsort(idcs); %groups lams 3 and 4
V(:,3) = V_unsort(:,idcs(1));
V(:,4) = V_unsort(:,idcs(2));

%% Calculate Transmission Loss

TM_babc = Tc*Tn*Tc*Tct;
TM_inv = inv(Tc)*inv(Tn)*inv(Tc)*inv(Tct);
lam_1 = lams(1,i);
lam_2 = lams(2,i);
lam_3 = lams(3,i);
lam_4 = lams(4,i);
v_1 = V(:,1);
v_2 = V(:,2);
v_3 = V(:,3);
v_4 = V(:,4);

syms a1 b1 c1 d1 A B P_out

vec_1st_cell = a1*v_1 + b1*v_2 + c1*v_3 + d1*v_4;
vec_last_cell = a1*lam_1^(N-2)*v_1 + b1*lam_2^(N-2)*v_2 + c1*lam_3^(N-2)*v_3 +
d1*lam_4^(N-2)*v_4;
vec_in = TM_inv*vec_1st_cell;
vec_out = TM_babc*vec_last_cell;

eqn1 = vec_in(3) == P_in;
eqn2 = vec_in(3) == A + B;
eqn3 = vec_in(4) == A/Zd - B/Zd;
eqn4 = vec_in(2) == 0;
eqn5 = vec_out(3) == P_out;
eqn6 = vec_out(4) == P_out/Zd;
eqn7 = vec_out(2) == 0;

eqns = [eqn1 eqn2 eqn3 eqn4 eqn5 eqn6 eqn7];
vars = [a1 b1 c1 d1 A B P_out];

sol = solve(eqns,vars);

X = sol.A/sol.P_out;

TL(i) = 20*log10(abs(X));

disp(f(i))
end

fprintf("The Helmholtz stop band is " + num2str(f_HR) + " Hz." + newline)
fprintf("The first Bragg stop band is " + num2str(f_Bragg_1) + " Hz." + newline)
fprintf("The second Bragg stop band is " + num2str(f_Bragg_2) + " Hz." + newline)

%% End Timer
tEnd = toc(tStart);
fprintf('%d minutes and %f seconds\n', floor(tEnd/60), rem(tEnd,60));

```

```

%% Transmission Loss Plotting

% Import Actran Results
actranTL =
importdata('Square_Fuller_GIT_Test_4_connected_resonator_post_NASA_pres.csv');
actranTL = actranTL(2:end);

% Import analytical separated resonators
sep_res = importdata('test.csv');

% Plot Analytical and Actran
figure(1)
plot(f,TL,'b','LineWidth',2)
xlabel('f (Hz)', 'FontSize', 24, 'Fontweight','Bold')
ylabel('TL (dB)', 'FontSize', 24, 'Fontweight','Bold')
xlim([min_freq max_freq]);
hold on
plot(1:length(actranTL),actranTL,'k','LineWidth',2)
legend('Analytical','Actran')
set(gca,'FontSize',22,'FontWeight','Bold','LineWidth',1.5);
y_ax_dis = get(gca,'ylabel'); % handle to the label object
p = get(y_ax_dis,'position'); % get the current position property
p(1) = 200.4194; % specify xposition,
set(y_ax_dis,'position',p) % set the new position
hold off

%% Propagation Constant Plotting

props = log(lams);

props_real = real(props);
props_imag = imag(props);

prop_mark_size = 4;
prop_real_color = "g";
prop_imag_color = "m";

figure(2)
scatter(f,props_real(1,:),prop_mark_size,prop_real_color,"filled")
hold on
scatter(f,props_real(2,:),prop_mark_size,prop_real_color,"filled")
hold on
scatter(f,props_real(3,:),prop_mark_size,prop_real_color,"filled")
hold on
scatter(f,props_real(4,:),prop_mark_size,prop_real_color,"filled")
hold off
ylim([0 2*pi]);
ylabel("Re(\Gamma)", 'FontSize', 24, 'Fontweight','Bold')
set(gca,'FontSize',22,'FontWeight','Bold','LineWidth',1.5);

figure(3)
scatter(f,props_imag(1,:),prop_mark_size,prop_imag_color,"filled")
hold on
scatter(f,props_imag(2,:),prop_mark_size,prop_imag_color,"filled")

```

```

hold on
scatter(f,props_imag(3,:),prop_mark_size,prop_imag_color,"filled")
hold on
scatter(f,props_imag(4,:),prop_mark_size,prop_imag_color,"filled")
hold off
ylim([0 2*pi]);
ylabel("Im(\Gamma)", 'FontSize', 24, 'Fontweight', 'Bold')
yticks([0 pi/2 pi 3*pi/2 2*pi]);
yticklabels({'0', '\pi/2', '\pi', '3\pi/2', '2\pi'})
set(gca, 'FontSize',22, 'FontWeight', 'Bold', 'LineWidth',1.5);

figure(4)
yyaxis left
plot(f,TL, 'b', 'LineWidth',2)
xlabel('f (Hz)', 'FontSize', 24, 'Fontweight', 'Bold')
ylabel('TL (dB)', 'FontSize', 24, 'Fontweight', 'Bold')
xlim([min_freq max_freq]);
hold on
yyaxis right
scatter(f,props_real(1,:),prop_mark_size,prop_real_color,"filled")
hold on
scatter(f,props_real(2,:),prop_mark_size,prop_real_color,"filled")
hold on
scatter(f,props_real(3,:),prop_mark_size,prop_real_color,"filled")
hold on
scatter(f,props_real(4,:),prop_mark_size,prop_real_color,"filled")
hold on
scatter(f,props_imag(1,:),prop_mark_size,prop_imag_color,"filled")
hold on
scatter(f,props_imag(2,:),prop_mark_size,prop_imag_color,"filled")
hold on
scatter(f,props_imag(3,:),prop_mark_size,prop_imag_color,"filled")
hold on
scatter(f,props_imag(4,:),prop_mark_size,prop_imag_color,"filled")
hold off
ylim([0 2*pi]);
ylabel("\Gamma", 'FontSize', 24, 'Fontweight', 'Bold')
yticks([0 pi/2 pi 3*pi/2 2*pi]);
yticklabels({'0', '\pi/2', '\pi', '3\pi/2', '2\pi'})
set(gca, 'FontSize',22, 'FontWeight', 'Bold', 'LineWidth',1.5);
%y_ax_dis = get(gca,'ylabel'); % handle to the label object
%p = get(y_ax_dis,'position'); % get the current position property
%p(1) = 2350; % specify xposition,
ylabel("\Gamma", 'FontSize', 24, 'Fontweight', 'Bold')
legend(["TL", "Re(\Gamma)", "", "", "", "Im(\Gamma)"])

```

A.4. MATLAB Code for the Calculation of the Measured Transmission Loss of a High Number of Connected Resonators with Non-Cellular Ends

```

%% Housekeeping

```

```

clc; clear; close all

%% Import Test
ImportFile = 'HardWall_Thick_Board_Run_1.csv'; % import data file name
fprintf("Importing Data...")
M = readmatrix(ImportFile,'Range','A5'); % Start importing at Cell A4 to skip text
information
clc
Time = M(:,1);
PaChannelZero = M(:,2);
PaChannelOne = M(:,4);
PaChannelTwo = M(:,6);
PaChannelThree = M(:,8);
Fs = 1/(M(2,1)-M(1,1)); % determine collection rate (Hz)

%% Calculate the autospectrum and phase for each signal

NFFT = 16384; % number of points segmented (assuming value must be a power of 2)
overlap = 0.75;
window = hann(NFFT);

[PSD00, freq, phase0] = PSDfun(PaChannelZero,PaChannelZero>window,overlap,NFFT,Fs);
[PSD11, ~, phase1] = PSDfun(PaChannelOne,PaChannelOne>window,overlap,NFFT,Fs);
[PSD22, ~, phase2] = PSDfun(PaChannelTwo,PaChannelTwo>window,overlap,NFFT,Fs);
[PSD33, ~, phase3] = PSDfun(PaChannelThree,PaChannelThree>window,overlap,NFFT,Fs);

%% Check against MATLAB pwelch() function

% Using pwelch()
[pxx2, f] = pwelch(PaChannelTwo>window,overlap*NFFT,NFFT,Fs);
figure
fBin = f(2)-f(1);
plot(f,pxx2,'b')
xlim([0 2250])
xlabel('Frequency (Hz)', 'FontSize', 24, 'FontWeight','Bold')
ylabel('Auto Power Spectral Density')
set(gca, 'FontSize',22, 'FontWeight', 'Bold', 'LineWidth',1.5);

% Compare to my function result
hold on
plot(freq,PSD22,'g')
legend('MATLAB function','own function')
hold off

% check maximum difference between built in function and own function
max(abs(pxx2-PSD22))

%% Calculate the cross-spectrum for each signal

[PSD01, freq, ~] = PSDfun(PaChannelZero,PaChannelOne>window,overlap,NFFT,Fs);
[PSD02, ~, ~] = PSDfun(PaChannelZero,PaChannelTwo>window,overlap,NFFT,Fs);
[PSD03, ~, ~] = PSDfun(PaChannelZero,PaChannelThree>window,overlap,NFFT,Fs);
[PSD12, ~, ~] = PSDfun(PaChannelOne,PaChannelTwo>window,overlap,NFFT,Fs);
[PSD13, ~, ~] = PSDfun(PaChannelOne,PaChannelThree>window,overlap,NFFT,Fs);
[PSD23, ~, ~] = PSDfun(PaChannelTwo,PaChannelThree>window,overlap,NFFT,Fs);

```

```

%% Check against MATLAB cpsd() function

% Using cpsd
[pxx23, f] = cpsd(PaChannelTwo,PaChannelThree>window,overlap*NFFT,NFFT,Fs);
figure
plot(f,abs(pxx23),'b')
xlim([0 2250])
xlabel('Frequency (Hz)', 'FontSize', 24, 'FontWeight', 'Bold')
ylabel('Cross Power Spectral Density')
set(gca, 'FontSize', 22, 'FontWeight', 'Bold', 'LineWidth', 1.5);

% Compare to my function result
hold on
plot(freq,abs(PSD23),'g')
legend('MATLAB function', 'own function')
hold off

% check maximum difference between built in function and own function
max(abs(pxx23-PSD23))

%% Calculate the coherence between each signal using my code and mscohere()

[cxy01, f] = mscohere(PaChannelZero,PaChannelOne>window,overlap*NFFT,NFFT,Fs);
[cxy02, ] = mscohere(PaChannelZero,PaChannelTwo>window,overlap*NFFT,NFFT,Fs);
[cxy03, ~] = mscohere(PaChannelZero,PaChannelThree>window,overlap*NFFT,NFFT,Fs);
[cxy12, ~] = mscohere(PaChannelOne,PaChannelTwo>window,overlap*NFFT,NFFT,Fs);
[cxy13, ~] = mscohere(PaChannelOne,PaChannelThree>window,overlap*NFFT,NFFT,Fs);
[cxy23, ~] = mscohere(PaChannelTwo,PaChannelThree>window,overlap*NFFT,NFFT,Fs);

coherence01 = abs(PSD01).^2./(PSD00.*PSD11);
coherence02 = abs(PSD02).^2./(PSD00.*PSD22);
coherence03 = abs(PSD03).^2./(PSD00.*PSD33);
coherence12 = abs(PSD12).^2./(PSD11.*PSD22);
coherence13 = abs(PSD13).^2./(PSD11.*PSD33);
coherence23 = abs(PSD23).^2./(PSD22.*PSD33);

%% Check own code against mscohere()

% Using mscohere
figure
plot(f,abs(cxy23),'b')
xlim([0 2250])
xlabel('Frequency (Hz)', 'FontSize', 24, 'FontWeight', 'Bold')
ylabel('Coherence')
set(gca, 'FontSize', 22, 'FontWeight', 'Bold', 'LineWidth', 1.5);

% Compare to my function result
hold on
plot(freq,abs(coherence23),'g')
legend('MATLAB function', 'own function')
hold off

max(abs(cxy23-coherence23))

```

```

%% Plot all four autopowers

figure
plot(freq,10*log10(abs(PSD00*fBin)/4e-10))
hold on
plot(freq,10*log10(abs(PSD11*fBin)/4e-10))
hold on
plot(freq,10*log10(abs(PSD22*fBin)/4e-10))
hold on
plot(freq,10*log10(abs(PSD33*fBin)/4e-10))
legend('Mic 1','Mic 2','Mic 3','Mic 4')
xlim([0 2250])
xlabel('Frequency (Hz)', 'FontSize', 24, 'Fontweight','Bold')
ylabel(' SPL (dB) (Pa_{Ref} = 2e^{-5} Pa)')
set(gca,'FontSize',22,'FontWeight','Bold','LineWidth',1.5);
hold off

%% Plot all four phases

figure
plot(freq,phase0)
xlim([0 2250])
xlabel('Frequency (Hz)', 'FontSize', 24, 'Fontweight','Bold')
ylabel('Phase (rad)')
set(gca,'FontSize',22,'FontWeight','Bold','LineWidth',1.5)

hold on
plot(freq,phase1)
hold on
plot(freq,phase2)
hold on
plot(freq,phase3)
hold off
legend('Mic 1','Mic 2','Mic 3','Mic 4')

%% Plot all six coherences

figure
plot(freq,abs(coherence01))
hold on
plot(freq,abs(coherence02))
hold on
plot(freq,abs(coherence03))
hold on
plot(freq,abs(coherence12))
hold on
plot(freq,abs(coherence13))
hold on
plot(freq,abs(coherence23))
xlim([0 2250])
xlabel('Frequency (Hz)', 'FontSize', 24, 'Fontweight','Bold')
ylabel('Coherence')
set(gca,'FontSize',22,'FontWeight','Bold','LineWidth',1.5)
legend('Mics 1&2','Mics 1&3','Mics 1&4','Mics 2&3','Mics 2&4','Mics 3&4')
hold off

```

```

%% B&K Experimental TL Calculation Method before Calibration

% Distances of microphones 1-4 from front of test sample (see B&K Fig. 1)
x1 = -9.75*.0254; %m
x2 = -7.875*.0254; %m
x3 = 39.375*.0254; %m
x4 = 41.375*.0254; %m

% Calculate more PSDs necessary for next step
[PSD10, ~, ~] = PSDfun(PaChannelOne,PaChannelZero>window,overlap,NFFT,Fs);
[PSD20, ~, ~] = PSDfun(PaChannelTwo,PaChannelZero>window,overlap,NFFT,Fs);
[PSD30, ~, ~] = PSDfun(PaChannelThree,PaChannelZero>window,overlap,NFFT,Fs);

% Uncalibrated Transfer Functions
Grr = PSD00*fBin;
H1r = PSD00./PSD00;
H2r = PSD00./PSD10;
H3r = PSD00./PSD20;
H4r = PSD00./PSD30;

modalH1r =
modalfrf(PaChannelZero,PaChannelZero,Fs,hann(NFFT),0.75*NFFT,'Est','H2','Sensor','dis
');
modalH2r =
modalfrf(PaChannelOne,PaChannelZero,Fs,hann(NFFT),0.75*NFFT,'Est','H2','Sensor','dis
');
modalH3r =
modalfrf(PaChannelTwo,PaChannelZero,Fs,hann(NFFT),0.75*NFFT,'Est','H2','Sensor','dis
');
modalH4r =
modalfrf(PaChannelThree,PaChannelZero,Fs,hann(NFFT),0.75*NFFT,'Est','H2','Sensor','di
s');

% verify own function is correct
% Using modalfrf
figure
plot(f,abs(modalH2r),'b')
xlim([0 2250])
xlabel('Frequency (Hz)', 'FontSize', 24, 'FontWeight', 'Bold')
ylabel('FRF')
set(gca, 'FontSize',22, 'FontWeight', 'Bold', 'LineWidth',1.5);

% Compare to my function result
hold on
plot(freq,abs(H2r),'g')
legend('MATLAB function','own function')
hold off

max(abs(modalH2r-H2r))

rho = 1.225;
d = 0.64135;
c = 343; % speed of sound
f_max = 2250; % max frequency of interest

```

```

[~,length_max] = min(abs(f_max-f)); % calculates the length of the frequency vector
up to the max frequency of interest
w = 2*pi*f; % angular frequency
k = w/c; % wavenumber

A = sqrt(Grr)*1j.*(H1r.*exp(1j*k*x2)-H2r.*exp(1j*k*x1))./(2*sin(k*(x1-x2)));
B = sqrt(Grr)*1j.*(H2r.*exp(-1j*k*x1)-H1r.*exp(-1j*k*x2))./(2*sin(k*(x1-x2)));
C = sqrt(Grr)*1j.*(H3r.*exp(1j*k*x4)-H4r.*exp(1j*k*x3))./(2*sin(k*(x3-x4)));
D = sqrt(Grr)*1j.*(H4r.*exp(-1j*k*x3)-H3r.*exp(-1j*k*x4))./(2*sin(k*(x3-x4)));

Px0 = A+B;
Vx0 = (A-B)/(rho*c);
Pxd = C.*exp(-1j*k*d) + D.*exp(1j*k*d);
Vxd = (C.*exp(-1j*k*d) - D.*exp(1j*k*d))/(rho*c);

T11 = 1./(Px0.*Vxd+Pxd.*Vx0) .* (Pxd.*Vxd+Px0.*Vx0);
T12 = 1./(Px0.*Vxd+Pxd.*Vx0) .* (Px0.^2-Pxd.^2);
T21 = 1./(Px0.*Vxd+Pxd.*Vx0) .* (Vx0.^2-Vxd.^2);
T22 = 1./(Px0.*Vxd+Pxd.*Vx0) .* (Pxd.*Vxd+Px0.*Vx0);

Ta = 2*exp(1j*k*d)./(T11 + T12/(rho*c) + rho*c*T21 + T22); % eq 11 in B&K

Ra = (T11+T12/(rho*c)-rho*c*T21-T22)./(T11+T12/(rho*c)+rho*c*T21+T22); % eq 12 in B&K

TL = 10*log10(1./(abs(Ta)).^2);

% Plot transmission loss

figure
plot(f,TL, 'b')
xlabel('Frequency (Hz)', 'FontSize', 24, 'Fontweight','Bold')
ylabel('TL (dB)')
xlim([0 f_max])
ylim([0 40])
set(gca,'FontSize',22,'FontWeight','Bold','LineWidth',1.5);
y_ax_dis = get(gca,'ylabel'); % handle to the label object
p = get(y_ax_dis,'position'); % get the current position property
p(1) = -150; % specify xposition,
set(y_ax_dis,'position',p) % set the new position

figure
plot(f,1-abs(Ra), 'b')
xlabel('Frequency (Hz)', 'FontSize', 24, 'Fontweight','Bold')
ylabel('Reflection Coefficient')
xlim([0 f_max])
ylim([0 1.1])
set(gca,'FontSize',22,'FontWeight','Bold','LineWidth',1.5);
y_ax_dis = get(gca,'ylabel'); % handle to the label object
p = get(y_ax_dis,'position'); % get the current position property
p(1) = -150; % specify xposition,
set(y_ax_dis,'position',p) % set the new position

%% Output Coefficients for Two_Load_Method

```

```

%filename='Coefficients_without_termination';
%save(filename,'A','B','C','D')

%% Output TL for Separate-Connected Comparison

%filename='Test_Con_Run_3';
%save(filename,'f','TL')

%% PSD Function

function [psd, freq, phase] = PSDfun(PaChannelX,PaChannelY>window,overlap,NFFT,Fs)

%calculating window sliding step for iteration
winsize = length(window);
step = winsize - overlap*NFFT;
iter = 1 + (length(PaChannelX) - winsize)/step;

%start and end index of first window/segment
istart = 1;
iend = istart + winsize - 1;

fftX_no_win = zeros(NFFT,iter);
fftY_no_win = zeros(NFFT,iter);
fftX_win = zeros(NFFT,iter);
fftY_win = zeros(NFFT,iter);

%start calculating fft for each window
for i=1:iter

    fftX_no_win(:,i) = fft(PaChannelX(istart:iend),NFFT);
    fftY_no_win(:,i) = fft(PaChannelY(istart:iend),NFFT);

    %apply window and calculate fft
    fftX_win(:,i) = fft(PaChannelX(istart:iend).*window,NFFT);
    fftY_win(:,i) = fft(PaChannelY(istart:iend).*window,NFFT);

    %move to next window segment
    istart = istart + step;
    iend = iend + step;
end

%obtain scale to create modified periodogram
scale = 1/(Fs*sum(window.*window));

%averaging window result and apply the scaling
psd = zeros((NFFT/2)+1,1);
for i=1:iter
    psd = psd + fftX_win(1:(NFFT/2)+1,i).*conj(fftY_win(1:(NFFT/2)+1,i));
end

psd = psd.*scale./iter;

%multiply by 2 except dc and nyquist component
psd(2:end-1) = psd(2:end-1).*2;

```

```
freq = (Fs*(0:NFFT/2)/NFFT)'; % compute frequency

% To get phase, use angular (phase) averaging technique
Xcomp = abs(fftX_no_win).*cos(angle(fftX_no_win));
Ycomp = abs(fftX_no_win).*sin(angle(fftX_no_win));

Xsum = sum(Xcomp,2);
Ysum = sum(Ycomp,2);

Xnorm = Xsum./norm(Xsum);
Ynorm = Ysum./norm(Ysum);

phase = atan2(Ynorm,Xnorm);
phase = phase(1:(NFFT/2)+1);

end
```

BIBLIOGRAPHY

- [1] “Continuous Lower Energy, Emissions, and Noise (CLEEN) Program | Federal Aviation Administration.” [Online]. Available: https://www.faa.gov/about/office_org/headquarters_offices/apl/eee/technology_saf_operations/cleen. [Accessed: 10-Apr-2023].
- [2] “AATT Technical Challenges | NASA,” 28-Apr-2016. [Online]. Available: <https://www.nasa.gov/aeroresearch/programs/aavp/aatt/technical-challenges/>. [Accessed: 10-Apr-2023].
- [3] M. Basner *et al.*, “Aviation Noise Impacts: State of the Science,” *Noise Health*, vol. 19, no. 87, p. 41, Mar. 2017.
- [4] C. Clark *et al.*, “Exposure-effect relations between aircraft and road traffic noise exposure at school and reading comprehension: The RANCH project,” *Am. J. Epidemiol.*, vol. 163, no. 1, pp. 27–37, 2006.
- [5] B. L. . Miller, Nicholas P.; Czech, Joseph J.; Hellauer, Kurt M.; Nicholas, “Analysis of the Neighborhood Environmental Survey,” 2021.
- [6] J. Abbott, “Aerodynamic Performance of Scarf Inlets,” New Orleans, Louisiana, 1979.
- [7] L. J. Heidelberg, D. G. Hall, J. E. Bridges, and M. Nallasamy, “A unique ducted fan test bed for active noise control and Aeroacoustics research,” *2nd AIAA/CEAS Aeroacoustics Conf.*, no. June 1996, 1996.
- [8] K. B. M. Q. Zaman, J. E. Bridges, and D. L. Huff, “Evolution from ‘tabs’ to ‘chevron technology’ - A review,” *Int. J. Aeroacoustics*, vol. 10, no. 5–6, pp. 685–710, 2011.
- [9] “Acoustic Exhaust Technology Demonstrator CLEEN III Consortium Public Industry Day | Collins Aerospace.” [Online]. Available: <https://www.faa.gov/media/25821>. [Accessed: 10-Apr-2023].
- [10] G. Ma and P. Sheng, “Acoustic metamaterials: From local resonances to broad horizons,” *Sci. Adv.*, vol. 2, no. 2, 2016.
- [11] M. G. Jones, D. Nark, B. Howerton, and M. C. Brown, “A Review of Acoustic Liner Experimental Characterization at NASA Langley,” 2020.
- [12] L. F. Kinsler, A. R. Frey, A. B. Coppens, and J. V. Sanders, *Fundamentals of Acoustics*, 4th ed. John Wiley & Sons, Inc., 2000.
- [13] R. Sugimoto, J. Astley, and P. Murray, “Low frequency liners for turbofan engines,” in *20th International Congress on Acoustics, ICA 2010*, 2010.
- [14] H. A. Kramers and G. H. Wannier, “Statistics of the Two-Dimensional Ferromagnet.,” *Phys. Rev.*, vol. 60, pp. 252–276, 1941.

- [15] M. Pachebat and J. Kergomard, “Propagation of acoustic waves in two waveguides coupled by perforations. II. Analysis of periodic lattices of finite length,” *Acta Acust. united with Acust.*, vol. 102, no. 4, pp. 611–625, 2016.
- [16] X. Wang and C. M. Mak, “Acoustic performance of a duct loaded with identical resonators,” *J. Acoust. Soc. Am.*, vol. 131, no. 4, p. EL316-EL322, 2012.
- [17] J. Yu, M. Ruiz, and H. W. Kwan, “Validation of Goodrich perforate liner impedance model using NASA langley test data,” *14th AIAA/CEAS Aeroacoustics Conf. (29th AIAA Aeroacoustics Conf.)*, no. May, 2008.
- [18] A. Ali, A. Mitra, and B. Aïssa, “Metamaterials and Metasurfaces: A Review from the Perspectives of Materials, Mechanisms and Advanced Metadevices,” *Nanomaterials*, vol. 12, no. 1027, 2022.
- [19] P. Flowers, K. Theopold, R. Langley, and W. R. Robinson, *Chemistry 2e*. 2019.
- [20] C. Kittel, *Introduction to Solid State Physics*, 8th ed. John Wiley & Sons, Inc., 2005.
- [21] L. Solymar, D. Walsh, and R. R. A. Syms, *Electrical Properties of Materials*, 10th ed. Oxford: Oxford University Press, 2019.
- [22] D. J. Griffiths, “Introduction to Electrodynamics.” Prentice-Hall, 1999.
- [23] W. H. Bragg and W. L. Bragg, “The Reflection of X-rays by Crystals,” *Proc. R. Soc.*, vol. A, pp. 428–438, 1913.
- [24] L. Brillouin, *Wave Propagation in Periodic Structures*. McGraw-Hill Book Company, Inc., 1946.
- [25] I. Newton, “Principia Mathematica.” 1686.
- [26] D. Broglie, “RECHERCHES SUR LA THEORIE DES QUANTA,” 1924.
- [27] M. PLANCK, “On the Theory of the Energy Distribution Law of the Normal Spectrum,” *Dtsch. Phys. Gesellschaft*, 1900.
- [28] E. Schrödinger, “An Undulatory Theory of the Mechanics of Atoms and Molecules,” *Phys. Rev.*, vol. 28, no. 6, pp. 1049–1070, 1926.
- [29] G. W. Hill, “On the Part of Motion of the Lunar Perigee which is Function of the Mean Motions of the Sun and Moon,” *Acta Math*, vol. 8, no. 1, pp. 1–36, 1886.
- [30] G. Floquet, “Sur les équations différentielles linéaires à coefficients périodiques,” *J. Crelle*, vol. 12, pp. 47–88, 1883.
- [31] F. Bloch, “Über die Quantenmechanik der Elektronen in Kristallgittern,” *Zeitschrift für Phys.*, vol. 52, no. 7–8, pp. 555–600, 1929.

- [32] X. Wang and C.-M. Mak, “Wave propagation in a duct with a periodic Helmholtz resonators array,” *J. Acoust. Soc. Am.*, vol. 131, no. 2, pp. 1172–1182, 2012.
- [33] D. J. Mead, “Free wave propagation in periodically supported, infinite beams,” *J. Sound Vib.*, vol. 11, no. 2, pp. 181–197, 1970.
- [34] D. J. Mead, “A General Theory of Harmonic Wave Propagation in Linear Periodic Systems with Multiple Coupling,” *J. Sound Vib.*, vol. 27, no. 2, pp. 235–260, 1973.
- [35] C. E. Bradley, “Acoustic Bloch Wave Propagation in a Periodic Waveguide,” THE UNIVERSITY OF TEXAS AT AUSTIN, 1990.
- [36] N. Sugimoto and T. Horioka, “Dispersion characteristics of sound waves in a tunnel with an array of Helmholtz resonators,” *J. Acoust. Soc. Am.*, vol. 97, no. 3, pp. 1446–1459, 1995.
- [37] C. R. Fuller, “Propagation and Reactive Attenuation of Low Frequency Sound in Hard-Walled Ducts with and without Flow,” University of Adelaide, 1978.
- [38] C. Fuller and T. D. Saux, “Sound absorption using poro-elastic acoustic meta materials,” in *Inter-Noise 2012*, 2012.
- [39] Z. Liu *et al.*, “Locally resonant sonic materials,” *Science (80-.)*, vol. 289, no. 5485, pp. 1734–1736, 2000.
- [40] M. Hirsekorn, “Small-size sonic crystals with strong attenuation bands in the audible frequency range,” *Appl. Phys. Lett.*, vol. 84, no. 17, pp. 3364–3366, 2004.
- [41] A. Slagle, “Low Frequency Noise Reduction using Novel Poro-Elastic Acoustic Metamaterials,” Virginia Polytechnic Institute and State University, 2014.
- [42] F. Cervera *et al.*, “Refractive Acoustic Devices for Airborne Sound,” *Phys. Rev. Lett.*, vol. 88, no. 2, p. 4, 2002.
- [43] X. Hu, C. T. Chan, and J. Zi, “Two-dimensional sonic crystals with Helmholtz resonators,” *Phys. Rev. E - Stat. Nonlinear, Soft Matter Phys.*, vol. 71, no. 5, pp. 1–4, 2005.
- [44] D. Torrent, A. Håkansson, F. Cervera, and J. Sánchez-Dehesa, “Homogenization of Two-Dimensional Clusters of Rigid Rods in Air,” *Phys. Rev. Lett.*, vol. 96, no. 20, pp. 1–4, 2006.
- [45] D. Torrent and J. Sánchez-Dehesa, “Acoustic metamaterials for new two-dimensional sonic devices,” *New J. Phys.*, vol. 9, no. 323, 2007.
- [46] N. Fang *et al.*, “Ultrasonic metamaterials with negative modulus,” *Nat. Mater.*, vol. 5, no. 6, pp. 452–456, 2006.
- [47] Z. Yang, J. Mei, M. Yang, N. H. Chan, and P. Sheng, “Membrane-Type Acoustic

- Metamaterial with Negative Dynamic Mass,” *Phys. Rev. Lett.*, vol. 101, no. 20, pp. 1–4, 2008.
- [48] A. Baz, “The structure of an active acoustic metamaterial with tunable effective density,” *New J. Phys.*, vol. 11, 2009.
- [49] S. A. Cummer and D. Schurig, “One path to acoustic cloaking,” *New J. Phys.*, vol. 9, no. 45, 2007.
- [50] H. Chen and C. T. Chan, “Acoustic cloaking in three dimensions using acoustic metamaterials,” *Appl. Phys. Lett.*, vol. 91, no. 18, pp. 1–3, 2007.
- [51] S. A. Cummer *et al.*, “Scattering Theory Derivation of a 3D Acoustic Cloaking Shell,” *Phys. Rev. Lett.*, vol. 100, no. 2, pp. 1–4, 2008.
- [52] M. Farhat, S. Enoch, S. Guenneau, and A. B. Movchan, “Broadband Cylindrical Acoustic Cloak for Linear Surface Waves in a Fluid,” *Phys. Rev. Lett.*, vol. 101, no. 13, pp. 1–4, 2008.
- [53] B. I. Popa, L. Zigoneanu, and S. A. Cummer, “Experimental Acoustic Ground Cloak in Air,” *Phys. Rev. Lett.*, vol. 106, no. 25, pp. 1–4, 2011.
- [54] “ActranVI 2021 User’s Guide.” 2020.
- [55] “Actran 2021 User’s Guide - Volume 2 Extended DAT (EDAT) Input File Syntax.” 2020.
- [56] M. Bern and P. Plassmann, “Mesh Generation,” *Handb. Comput. Geom.*, 2000.
- [57] H. Djojodihardjo and K. A. A. Rahim, “Two-dimensional CFD simulation for visualization of flapping wing ornithopter studies,” *ARPN J. Eng. Appl. Sci.*, vol. 10, no. 21, pp. 10018–10026, 2015.
- [58] T. Schönfeld, P. Weinerfelt, and C. B. Jenssen, “Algorithms for the Automatic Generation of 2-D Structured Multi-Block Grids.” .
- [59] S. Singh, “Tonal noise attenuation in ducts by optimising adaptive Helmholtz resonators,” University of Adelaide, 2006.
- [60] K. Saine, E. Komi, and Z. Gao, “Actran – Powerful Vibro-Acoustic Finite Element Software.” .
- [61] Ansys, “ANSYS ICEM CFD 12.1 Help Manual.” 2023.
- [62] “Actran 2021 User’s Guide - Volume 1 Installation, Operations, Theory and Utilities,” vol. 1. .
- [63] J. S. Bolton, T. Yoo, and O. Olivieri, “Measurement of Normal Incidence Transmission Loss and Other Acoustical Properties of Materials Placed in a Standing Wave Tube,” 2007.

- [64] “ISO 10534-2,” *Int. Stand.*, 1998.
- [65] “ASTM E1050-19 - Standard Test Method for Impedance and Absorption of Acoustical Materials Using a Tube, Two Microphones and a Digital Frequency Analysis System,” *ASTM International*, 2019. [Online]. Available: <https://webstore.ansi.org/Standards/ASTM/ASTME105019>. [Accessed: 28-Sep-2020].